UNICA

UNIVERSITÀ
DEGLI STUDI
DI CAGLIARI

Ph.D. DEGREE IN

Innovation Sciences and Technologies

Cycle XXXV

TITLE OF THE Ph.D. THESIS

Innovative Apatite/Bioactive Glass-based materials for biomedical applications

Scientific Disciplinary Sectors

ING-IND/24, ING-IND/22

Ph.D. Student: Damiano Angioni

Supervisor Prof. Ing. Roberto Orrú

Final exam. Academic Year 2021/2022
Thesis defence: April 2023 Session


Damiano Angioni gratefully acknowledges the Sardinian Regional Government for the financial support of his PhD scholarship (P.O.R. Sardegna F.S.E. - Operational Programme of the Autonomous Region of Sardinia, European Social Fund 2014-2020 - Axis III Education and training, Thematic goal 10, Investment Priority 10ii), Specific goal 10.5.

Abstract

Musculoskeletal-related problems are nowadays one of the main concerns in healthcare, due to tumors, traumatology, osteoporosis and others pathologies, especially considering ageing populations. These diseases and induced defects affect millions of people worldwide. An important scientific effort was dedicated, in the past decades, to the development of bone-grafts materials as alternatives to allo- and autografts, due to the drawbacks associated with the employment of the latter ones (as for instance, transmission complications as well as immunological rejection and morbidity).

Scientific research focused on synthetic bone graft displaying suitable properties is an actual hot topic. In this context, calcium phosphates (in particular hydroxyapatite) and bioactive glasses, recently gained much attention due to their characteristics as promising materials for the treatment of non-self-healing bone defects. Indeed, they display biocompatibility, good bioactivity and non-toxicity. Despite these, clinical application of hydroxyapatite- and bioactive glass-derived materials is still limited, and further development of such materials is needed.

The main aim of this work is then to contribute to solve some of the drawbacks displayed by these classes of materials (related to their composition, synthesis and manufacturing), to provide possible useful insights about how to limit/overcome them. In the present thesis, beyond the state of the art, it was attempted to tackle various problems related to the development of innovative materials for hard tissue engineering.

Keywords:*Bone repair; Calcium phosphates; Bioactive glasses; Spark Plasma Sintering; Bioac-*

tivity; Solution Combustion Synthesis; Electrospinning.

Outline

The present thesis is organised as follows. An introduction describing human bone tissues and the fundamentals of bone repair will be provided in Chapter 1. The main classes of materials currently employed will be presented, with a particular focus on Hydroxyapatite and bioactive glasses, being the main ones investigated in the context of this work. A brief description of the bioactivity mechanisms, and its assessment, will follow, together with a discussion on the sintering process, with particular emphasis on the Spark Plasma Sintering (SPS) technique, used in this thesis. This Chapter is intended to give a general description of the state of the art in this field, and a coherent framework for the reserach activity presented in the next chapters.

Chapter 2 contains the outcome of the research activity regarding the densification and characterization of a novel glass formulation (BGMS10), containig Sr and Mg, which are known to provide beneficial effects in biomedical applications.

Taking advantage of the properties of BGMS10 glass, its combination with Hydroxyapatite powders to obtain bulk composite materials is investigated in Chapter 3, together with the assessment of the effect produced by a ball-milling treatment of the composite mixture on the mechanical and biological properties of the related bulk products.

Chapter 4 is focused on the combination of Solution Combustion Synthesis (SCS) and Spark Plasma Sintering (SPS) for the production of bulk nanostructured Apatite-Tricalcium phosphate composites and their detailed characterization.

The result obtained in a 6 month research period as visiting Ph.D. student at the Imperial College of London (UK), under the supervision of Prof. Julian R. Jones, will be presented in

Chapter 5. Specifically, this work was aimed to the obtainment of sol-gel derived amorphous glass fibres by electrospinning.

In the last Chapter, general conclusions will be drawn, together with an overview of the main results achieved during the Ph.D. research programme.

Contents

Chapter 1

Introduction

1.1 Human bone tissue

Human bones are mineralized and hierarchical biological tissues composed by both organic and inorganic parts. Among the mineralized tissues, enamel, dentine, and cementum can be also found, possessing unique chemical composition and structure [1]. Bone is a general term used to indicate different kind of tissues with specific morphology and functions; such classification is briefly presented in what follows.

1.1.1 Functions and structure

The human skeleton system consists of 206 bones and connective tissues, like ligaments, tendons, and cartilage. It is generally aimed to provide structural support (Figure 1.1) [2], but it also displays other important functions [3, 4] :

- *Mechanical*: the skeleton acts as support against gravity and stresses, also providing points of attachment for muscles and tendons;
- *Protective*: it fences vital organs and soft tissues;
- *Hematopoietic*: bone provides an environment for hematopoiesis (production of red and white blood cells in bone marrow);

- *Metabolic*: bones are responsible for maintaining mineral homeostasis, acting as storage for inorganic elements like calcium, phosphorus, and magnesium (among others), crucial for ordinary body functioning.

Classification of bones can arise from anatomy and structure, together with the above-mentioned functions; a representation of this is given in Figure 1.1, and briefly described in what follows.

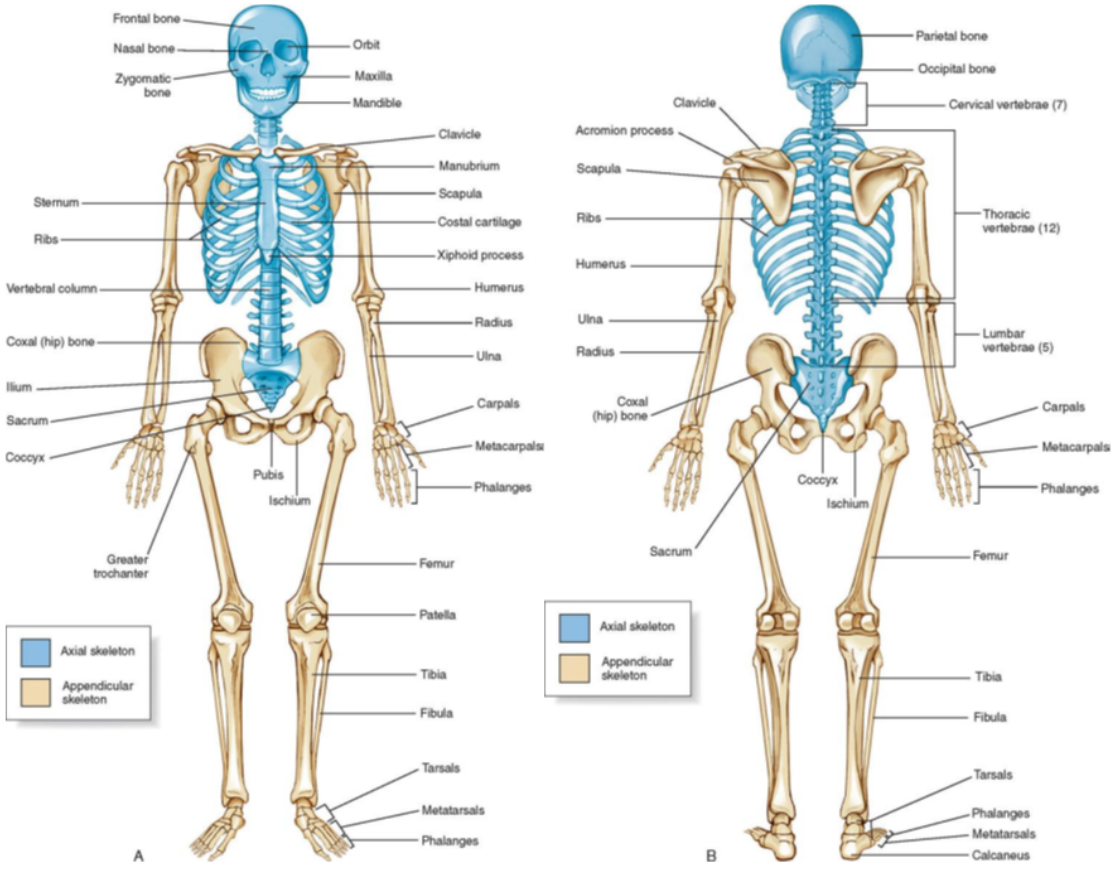

Figure 1.1: Human Skeletal System (axial and appendicular bones) [2].

A possible division is between axial skeleton and appendicular skeleton. The first one, comprised of approximately 80 bones, is mainly devoted to their protective function as well as their supporting one. As seen in Figure 1.1, cranium, facial bone, ribs, and vertebral column are examples of axial skeleton bones. As for the bones of the appendicular skeleton,

they are located symmetrically in the human body and are necessary for balance, stability, and locomotion functions, among others.

Regarding the morphology, more specifically shape, another subclassification is between long (humerus, radius, femur, tibia, etc.), short (carpus, patella, tarsus, etc.), flat (hip, nasal bone et al.), irregular (maxilla, vertebrae, etc.), and sesamoid bones, which are embedded into tendons, such as patella.

As for the structural viewpoint, they are subdivided into microscopic and macroscopic. For the microscopic category the two types are woven and lamellar bones [4]. The first one, considered primary and immature, is observed in fetus development and also during the remodeling process in adults. It possesses low mechanical resistance, due to collagen fibres arrangement (whose function will be described later in this Chapter). The second group, is typical of mature form of adult bones and shows strong mechanical properties [5].

The macroscopic classification divide bones in trabecular (or spongy or cancellous) and cortical (compact or cortex) [6]. Despite the fact that the composition of the two is identical [7], they differ by microstructure and porosity, so that mechanical properties are also diverse, as reported in Table 1.1.

Bone type	**Tensile strength** ***(MPa)***	**Young's Modulus (GPa)**	**Compressive strength (MPa)**	**Fract. toughness (MPa m$^{1/2}$)**	**Porosity (%)**	**Density (g/cm^3)**
Cortical	≈ 150	3-30	130-180	2-12	< 30	1.7-2
Cancellous	60-160	0.02-0.5	2-12	0.1-0.8	$50-90$	0.15-1

Table 1.1: Mechanical properties of human cortical and cancellous bone. Adapted from [8–12].

The cortical bone, schematically represented in Figure 1.2, is formed by closely packed multiple columns, called osteons or Haversian canals. The latter ones consist of lamellae (concentric layers) surrounding the whole canals and providing vascular connections. Approximately the 80% of skeleton weight is due to cortical bones.

The cancellous bone, less dense and stiff due to its high porosity, possesses a greater surface

area. It forms the interior of vertebrae and long bones, with the main functions of creating a network and space for blood vessels and marrow.

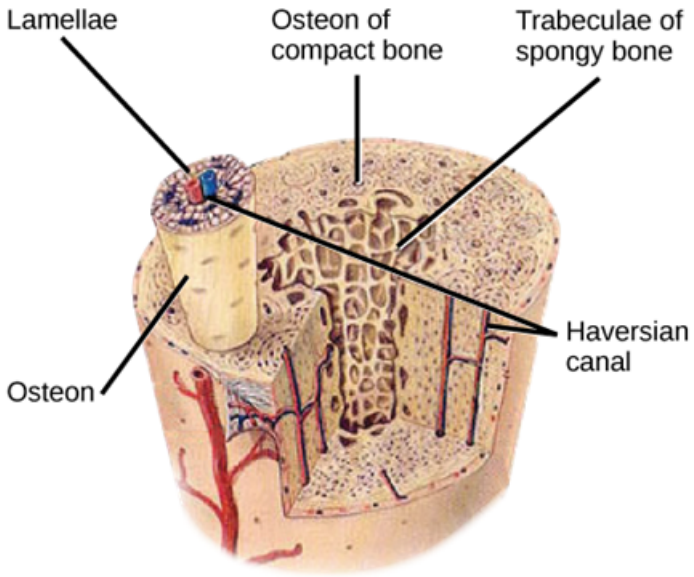

Figure 1.2: Schematic cross section of the structure of compact and cancellous bone. Reproduced from [13].

1.1.2 Composition

Bone is a heterogeneous hierarchical composite material composed of 50 to 70% of bone mineral, 20 to 40% of organic matrix, 5 to 10% of water, and approximately 3% of lipids [4].
The very first and easier distinction regarding bone composition is between cells and extracellular matrix (ECM).
The dynamics of bone growth, modelling and remodeling during life is coordinated by the activities of cells, namely osteoblasts, osteocytes, osteoclasts, and bone lining cells [14,15]. Bone growth, modelling and remodeling processes are discussed in more detail in subsection 1.2.1.
Each type of bone cell plays a specific role:

- *Osteoblasts* are approximately 4-6% of all bone cells, are located on the surface of the bone, and are responsible for bone formation process [16];

- *Osteocytes* are approximately 95% of bone cells. They are involved in bone development [17,18] and in the final part of bone formation process. Some of the osteoclasts turn into osteocytes and integrate into the bone matrix;

- *Osteoclasts* are responsible for the dissolution and adsorption of bone tissue. Anomalous growth of such cells can cause an unbalance between bone formation and adsorption, which causes a decrease in bone density, thus favouring fractures occurrence [19];

- *Bone lining cells* are thought to be involved in both processes of bone formation and resorption [20].

The ECM, schematically described in Figure 1.3, is formed by an organic and an inorganic part. The organic fraction, between 20 to 40% bone structure, is mainly composed of collagenous proteins, primarily (85-90%) type I Collagen, and non-collagenous proteins. Type I collagen is involved in the process of mineralization of bone's inorganic part [21–23], i.e. the apatite mineral.

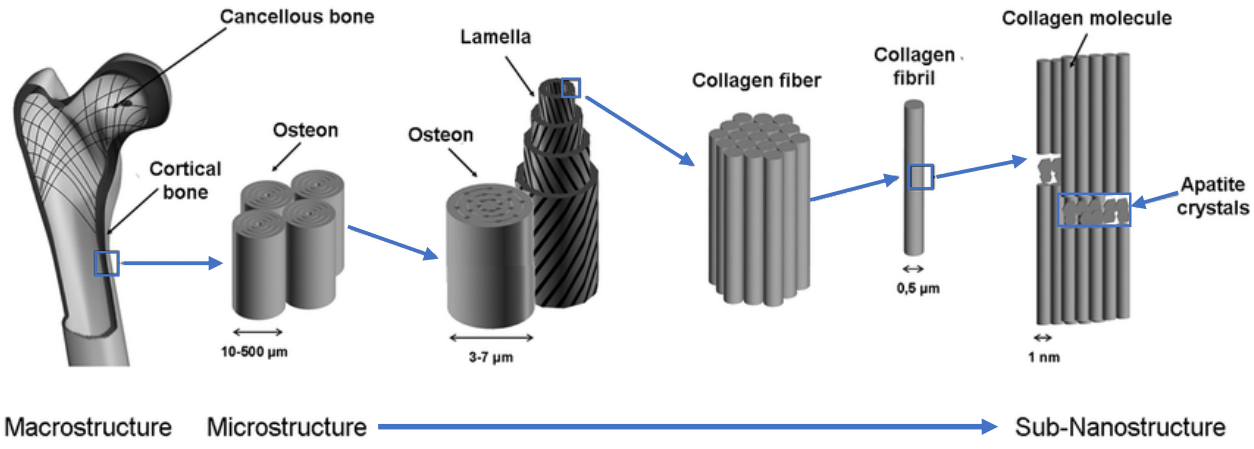

Figure 1.3: Schematic rapresentation of hierarchical structure of the ECM. Adapted from [24].

The latter one, also known as biological apatite, is the main inorganic phase in bone structure. Firstly analysed by X-Ray Diffraction (XRD) in 1926 by De Jong [25], bone mineral was

found to be similar to geological calcium hydroxyapatite, described by the following formulation:

$$Ca_{10}(PO_4)_6(OH)_2 \tag{1.1}$$

which, in this work, will be referred to as HA or stoichiometric apatite.

However, as more studies were performed on such materials, noteworthy chemical composition and crystal structure differences between bone mineral, geological apatite, and synthetic one, arose. From the structural point of view, the biological apatite crystals are significantly smaller, with dimensions, measured by atomic force microscopy (AFM), of 1-4 nm thickness, 8-15 nm wideness, and 20-35 nm length [26–28]. In addition, as for the composition, it was evidenced that the bone mineral presents anionic/cationic substitutions together with vacancies in its structure. Furthermore, biological apatite was found to be calcium and hydroxyl deficient carbonated apatite [29–31]. The carbonation level was estimated to be between 3 and 9 wt% [30, 32], being CO_3^{2-} ions present as substituents in PO_4^{3-} site, referred as B-type substitution, and in OH^- sites, referred as A-type substitution [33,34]. The site of substitution depends on the examined mineralised tissue: bone mineral is mainly characterised by B-type substitution, while enamel by both A and B types. Moreover, the PO_4^{3-} sites can be occupied by phosphate ions HPO_4^{2-} [30,35].

Additionally, other ions have been found to be present in various amounts in biological apatite's structure, such as Mg^{2+}, Na^+, Cl^-, F^-, K^+, Sr^{2+}, and others [36,37]. Typical compositions of the mineral part of calcified tissues in the human body are summarized in Table 1.2.

Composition [wt%]	Enamel	Dentine	Cementum	Bone	HA
Ca	36.5	35.1	≈ 35	34.8	39.6
P	17.7	16.9	≈ 16	15.2	18.5
Ca/P	1.63	1.61	≈ 1.65	< 1.67	1.67
Na	0.5	0.6	-	0.9	-
Mg	0.44	1.23	0.5-0.9	0.72	-
K	0.08	0.05	-	0.03	-
CO_3^{2-}	3.5	5.6	-	7.4	-
F	0.01	0.06	Up to 0.9	0.03	-
Cl	0.3	0.01	-	0.13	-
$P_2O_7^{4-}$	0.022	0.1	-	0.07	-
Total inorganic	97	70	60	65	100
Total organic	1.5	20	25	25	-
Water	1.5	10	15	10	-

Table 1.2: Inorganic phases composition of adult human calcified tissues. Adapted from [38].

A more representative chemical formula for biological apatite, reported in Equation 1.2, has then been proposed by LeGros [30]:

$$Ca_{8.3}(PO_4)_{4.3}(CO_3, HPO_4)_{1.7}(OH)_{0.3} \tag{1.2}$$

Despite this, the actual composition of bone mineral is still debated. The reason for such controversial lies in the fact that, in order to properly analyse the chemical composition of the inorganic part, one has to entirely remove the organic fraction, without affecting the first one. Thus, several other studies were devoted to the investigation of bone composition, and further measures revealed a significant amount of water, with increasing concentration of Ca and Mg close to bone crystal surfaces [39–41]. This is consistent with the fact that such ions can be involved in ion exchange processes and enter the extracellular fluids very rapidly [42, 43]. A recent study based on advanced solid-state nuclear magnetic resonance (ssNMR), carried out on the freshly extracted bone kept in its native hydration state, confirmed a model where apatite nanocrystals are covered by a highly hydrophilic disordered mineral layer that consists of Ca^{2+}, HPO_4^{2-}, CO_3^{2-} ions, and water [44]. Authors identified this layer as amorphous calcium phosphate (ACP)-related phase rather than OCP [45]. Additionally, the core/shell model

was confirmed for apatite particles in dentine [46–48]. A comprehensive formula in this sense, representing the average ionic composition between the core and the shell, has been more recently proposed by Euw et al.(2019) [35], reported in Equation 1.3, which is based on NMR analysis on a 2-years-old sheep bone tissue sample:

$$Ca_{7.5}(PO_4)_{2.8}(CO_3)_{0.6}(HPO_4)_{2.6}(OH)_{0.2} \tag{1.3}$$

1.2 Fundamentals of bone repair

In this section the current needs of materials research regarding bone repair will be discussed. First, a brief introduction about the clinical problem is given, to then proceed with the classification and requirements for materials for bone repair and regeneration.

1.2.1 Remodelling and self-regeneration

Bone is a dynamic tissue that adjusts its structure over a lifetime. Once formed, bone grows and adapts its shape by remodelling as a response to physiologic or mechanical stimuli. Interestingly, during the human lifetime, the mass of bone tissue in the skeletal system is totally deposited and resorbed, in normal conditions, every five to six years [49]. During this renewing process, resorption and formation are two uncoupled pathways, happening on distinct surfaces [4].

The remodelling cycle, described in Figure 1.4, consists of five steps:

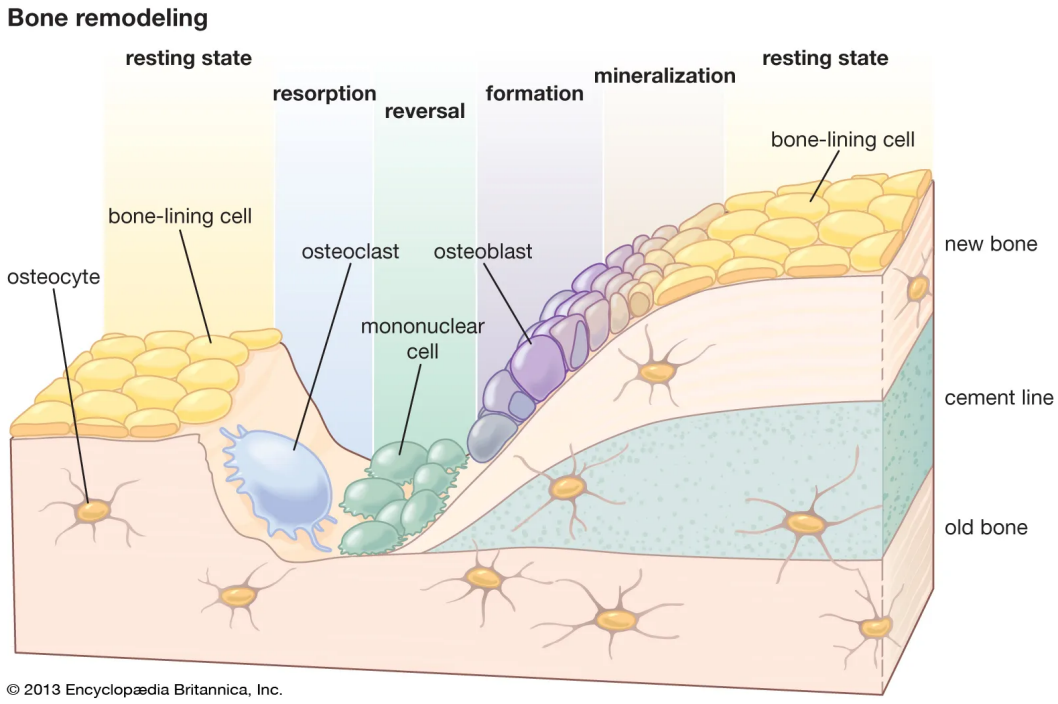

Figure 1.4: Schematic description of the bone remodeling process. Source: Encyclopaedia Britannica.

- *Activation*, starting by a signal triggered by osteocytes;
- *Resorption*, in which the osteoclasts are recruited responding to the signal triggered by osteocytes;
- *Reversal* step, characterised by the disappearance of osteoclast;
- *Formation* phase, which occurs when the osteoclasts are completely replaced by osteoblasts;
- *Mineralization*, that includes the terminal differentiation of osteoblasts and the mineralization phase of new tissue.

Once the process is complete, the bone surface is maintained until a new remodeling process starts.

Except for natural remodelling, bone possesses also self-healing properties, in case of traumatic events. The schematization of such process is represented in Figure 1.5.

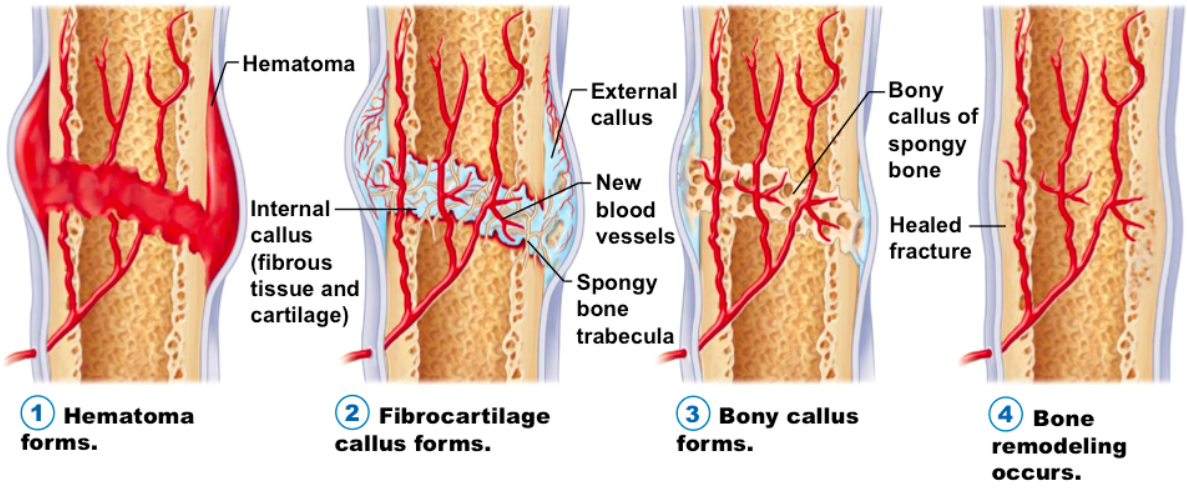

Figure 1.5: Schematic description of bone self-healing process. Source: `http://msgallagherlhs.weebly.com/fracture--repair.html`.

The self-healing process starts with the formation of a hematoma, followed by the development of a fibrocartilage callus, then replaced by bone callus, which is finally remodelled to

bone tissue. Each of the previously mentioned steps involves intervention of different cellular and molecular events. However, when the damage overcomes a critical size, called critical-size defect (CSD), the natural healing process is hindered; under such conditions the cells cannot migrate from one side to the other of the damage. The CSD has not a unique identified dimension [50], and is technically defined as a heal which is not healed spontaneously during the patient's lifetime [51].

Such large bone defects are most commonly caused by accidental or pathological situations, like fractures, infection, osteoporosis, metabolic bone disease, inflammatory arthritis, osteonecrosis, tumours, and rheumatoid arthritis [52, 53].

In addition, the risk of fractures increases with age, due to the reduced release of hormones and other agents involved in bone regeneration, so that the process of bone fracture healing is negatively affected as well [54].

1.2.2 Clinical needs and materials for bone repair

As mentioned in the previous section, many pathologic factors can influence bone remodelling and self-healing, without considering accidental damages. For instance, an average of 1.5 million of fractures per year were reported by U.S. Department of Health and Human Services to be caused by bone-related diseases [55]. As for Italy, bone-diseases related femur fractures in 50+ aged people were reported to be approximately 90 thousand per year, up to 2014. Given the previous data, it is not hard to believe that bone is the second most transplanted tissue all over the world, only after blood [56]. Every year, more than two million of people undergo different bone grafting procedure, including knee and hip replacement, spinal fusion, reconstructive maxillofacial, and others [57, 58]. Extending lifespan expectancy provides an indication of the fact that this market is going to expand; the global bone grafts and substitutes market reached a valuation of US$ 3.06 Bn in 2020, and is expected to reach US$ 4.44 Bn by the end of 2028 [`urly.it/3rbpb`, accessed December 17th,2022].

On the basis of the actual need, the research is very active in this field. Among the various, it is

important to mention Tissue Engineering (TE), which is, according to the currently accepted definition *an interdisciplinary field that applies the principles of engineering and life sciences toward the development of biological substitutes that restore, maintain, or improve tissue function or a whole organ* [59]. Another important issue is related to the concept of biomaterial, for which there are different accepted definitions. The first one was given by the American National Institute of Health in 1984 and described biomaterial as *any substance or combination of substances, other than drugs, synthetic or natural in origin, which can be used for any period of time, which augments or replaces partially or totally any tissue, organ or function of the body, in order to maintain or improve the quality of life of the individual.* Additionally, in the Consensus Conference of the European Society for Biomaterials (1986), it was stated that biomaterial is *a nonviable material used in a medical device, intended to interact with biological systems.*

During the II Conference on Biomaterials, Chester, UK (1991) [60], biomaterial was defined as a material designed to interface with biological system to evaluate, support or replace any tissue, organ or body function. More recently, another formal definition of biomaterial was provided, i.e. *a material designed to take a form that can direct, through interactions with living systems, the course of any therapeutic or diagnostic procedure* [61, 62].

In this regard, the ideal substitutes for CSDs should provide an environment that mimics the natural healing process of the bone. More precisely, it should possess ostoegenesis (the capacity to stimulate bone formation), and angiogenesis (the capacity to stimulate the formation of vascular connection) properties, be resistant from the mechanical point of view, and provide integration with host tissue.

The materials traditionally applied for the treatment of CSD are usually differentiated by the donor source:

- *Autologous* or *Autogeneous* bone graft is the current gold standard for this kind of procedure [63, 64]. The bone graft in this case is harvested by the patient's own body. The advantage of such a source for bone grafting lies in the possession of all essential el-

ements for successful bone repair. For instance, autogenous bone is osteoconductive and osteoinductive with very low immune-related risks. During the healing process, autologous bone is usually replaced by the newly forming bone. However, there are various issues and risks associated with the use of autologous bone, like: high percentage of donor site morbidity [65,66], difficulties in shaping the bone graft, limited quantity of the material, infections, and neurovascular injury [67], not to mention the case of pediatric and elderly patients, for which autogenous bone availability is significantly limited;

- *Allogenic* bone graft, can either be derived from cadavers or living donors. They represent an alternative approach to the autologous bone and need to be processed to remove all living cellular components, to avoid host-versus-graft immune response. However, this procedure alters the biological properties of allograft, resulting in the osteoconductive mineral basis for bone healing, but lacking the osteogenic properties of autologous bone. The main drawbacks associated with the use of allogeneic bone are the inherent risk of infection transmission, and the possibility to induce unfavourable host immune response, which lead to the rejection and requirement of additional operations [68, 69];

- *Xenogenic* bone graft are derived by animal species other than humans, like coral, cattle, horses, and pigs. Skeleton of corals, for example, consisting of calcium carbonate ($CaCO_3$), can be used as a natural source of HA. Generally, this type of material is relatively slowly resorbable in physiological conditions. It also must undergo to specific treatments for deproteinization, meaning that all organic components should be chemically removed. Despite its high biocompatibility, the main disadvantages include brittleness and difficulty in handling, together with limited availability and risk of infections [70].

Alternatives for the abovementioned source are synthetic materials, developed to overcome the drawbacks of the natural sources previously presented, which will be described in the following section.

1.2.3 Requirements for synthetic materials

Synthetic materials display different advantages with respect to the substitutes presented above. First, the possibility to control their chemical composition and structure, which is crucial to tune the specific biological response of the living host tissue. This holds also true for the mechanical properties, that can be specifically designed, and more generally tuned. Lastly, their availability in terms of quantity is not limited by the donor, but just by production limitations. Synthetic bone grafts must possess the following characteristics [71]:

- be:

  a. *biocompatible*, i.e. be able to perform its desired function with respect to a medical therapy, not only without eliciting any undesirable or systemic effects in the recipient or beneficiary of that therapy, but also generating the most appropriate beneficial cellular or tissue response in that specific situation, thus optimizing the clinically relevant performance of the therapy [72];

  b. *bioactive*, i.e. create direct biochemical bonds with the tissues;

  c. *osteoinductive*, i.e. promoting bone formation;

  d. able to bond to the bone without soft tissue encapsulation;

- *osteoconductivity*, to act as a template for bone growth, with an interconnected and appropriate porous structure that allows cell migration and vascularisation;

- biodegradability, or safely degradable in the body with a controllable rate to match the one of bone regeneration growth [73];

- have mechanical properties similar to those of the host bone;

- be produced by a process that allows the scaffold to be shaped in accordance with the defect shape and be up-scalable for commercialisation;

- be sterilisable and meet the regulatory requirements for clinical use.

There are several commercialized synthetic bone grafts and products available on the market, with very few of them matching all the criteria listed above. In the following section a classification of the biomaterials is presented, together with the description of their properties and advantages and disadvantages associated to their usage.

1.2.4 Synthetic materials

Materials used for bone grafting are usually classified into four main groups: metals, polymers (natural and synthetic), bioceramics/bioactive glasses, and combinations of two or more of the previous, namely, biocomposites.

The first three of them possess different properties that can in turn determine their applications. However, these materials are able to mimic biological tissues only to a certain extent on their own, especially in case of complex structures like bones. For this reason, the combination of them in composites, which combine the properties of two or more biomaterials, represent a promising approach to overcome the current limitations of single-phase materials. In the following paragraphs a description of each class will be presented.

1.2.4.1 Metals and alloys

Elemental metals involved in biomaterials currently used for medical implant manifacturing include Fe, Cr, Co, Ni, Ti, Ta, Mo and W. They possess a combination of favourable mechanical properties, such as tensile strength, fracture toughness and fatigue strength, which are required for load bearing or strain applications. In addition, they are relatively non-cytotoxic, at least in limited quantities. On the other hand, one of the main drawbacks of metallic biomaterials is the fact that metal cannot mechanically match bone properties, due to the dramatically different Young's moduli [63], possibly causing bone to become gradually weaker and prone to fracture (stress shielding effect). Another crucial issue related to the use of metals for grafts is corrosion when in contact with the physiological environments. As a result, loss of the structural integrity of the implant, accompanied by the release of toxic elements

in high amount, can occur [74, 75]. Nonetheless metals are usually employed in orthopaedics to replace load-bearing bones [76], for instance, in case of total hip joint replacement. Other important fields of application of metallic biomaterials are dentistry and orthodontics.

1.2.4.2 Polymers

Both natural and synthetic polymers are long-chain molecules that consist of a large number of small repeating units. Their main advantages are the excellent biocompatibility and customizable properties, such as the possibility of tuning the degradation rate depending on the specific application [76, 77], not to mention their flexibility, elasticity, and controllable chemistry. The latter one allows for the promotion of cell attachment, proliferation, and differentiation through the use of bio-functional molecules [78, 79]. Therefore, they are widely applied in field of tissue engineering and regenerative medicine. Natural polymers can mimic the components present in ECM. Some examples are collagen, heparin, chitosan, gelatine, hyaluronan, alginate, and cellulose: all of them are biopolymers that can be derived from natural sources.

Synthetic polymers are relatively more versatile and can be also used to successfully incorporate drugs. General examples of widely studied polymers for biomedicine are Poly(methyl methacrylate) (PMMA), Polyacrylamide (PAM), Polyacrylic acids (PAA), Polyethylene (PE), Polytetrafluoroethylene (PFTE), Polyethylene terephthalate (PET), Poly(Epsilon-Caprolactone) (PCL), Polyvynil Chloride (PVC) , Poly(Lactic-co-Glycolic acid) (PLGA), among the others. The application of polymers, especially natural ones, is currently limited because of stability issues at high temperatures (possibly occurring during materials processing or sterilization), their propensity to swell when in contact with organic fluids, and to strength limitations.

1.2.4.3 Bioceramics and bioactive glasses

According to the definition given by Hench, *bioceramics are those ceramics used for the repair and reconstruction of diseased or damaged parts of the musculoskeletal system* [8]. They are a broad class of materials employed in bone grafting and dentistry.

Bioceramics constitute a subset of biomaterials that can display either a crystalline structure or an amorphous nature. This class includes oxides (Alumina, Zirconia, etc.), calcium phosphates (HA, Tricalcium phosphates, amorphous calcium phosphates, etc.), Bioactive glasses (BG e.g., Bioglass®, S53P4, etc.) [32, 80, 81], as well as their composites. Figure 1.6 contains several examples of applications of bioceramics, glasses and composites. As evident, bioceramics can be employed in many ways, and a variety of them has been commercialized for use as a medical implant of some sort [82].

Such materials can be used in different forms as coatings, powders, granules (as bone filling), as well as porous scaffolds, and solid components (for the reconstruction of middle ear ossicles or in parts of joint prosthesis).

According to their in-vivo response bioceramics can be categorized, into the following subtypes:

- *Bioinert*: they possess a modest interaction with the body. For instance, Al_2O_3 and ZrO_2 have been employed due to their high chemical stability *in-vivo* as well as high mechanical strength, but at the same time for the minimal adverse response they produce in the surrounding physiological environment [83–85]. On the other hand, the possibility of encapsulation by fibrous material has to be considered before their practical usage. In addition, a problem related to the low temperature degradation of zirconia-based implants was evidenced [86, 87];

- *Bioactive*: the bioceramic directly bond to bones, without generating fibrillar connective tissue between them. So, they are bioactive in the sense that *elicit a specific biological response at the interface of the material which results in the formation of a bond between*

the tissues and the material [88]. HA and bioactive glasses belong to this category;

- *Resorbable*: thus gradually (and possibly completely) degraded over time, permitting bone in- growth and replacement of the artificial material with the natural tissue [31,89]. In this case, the dissolution rate should match the kinetic of the new bone formation. Such need can make the design of such materials tricky, since generally, bone formation is slower, with respect to ceramic resorption.

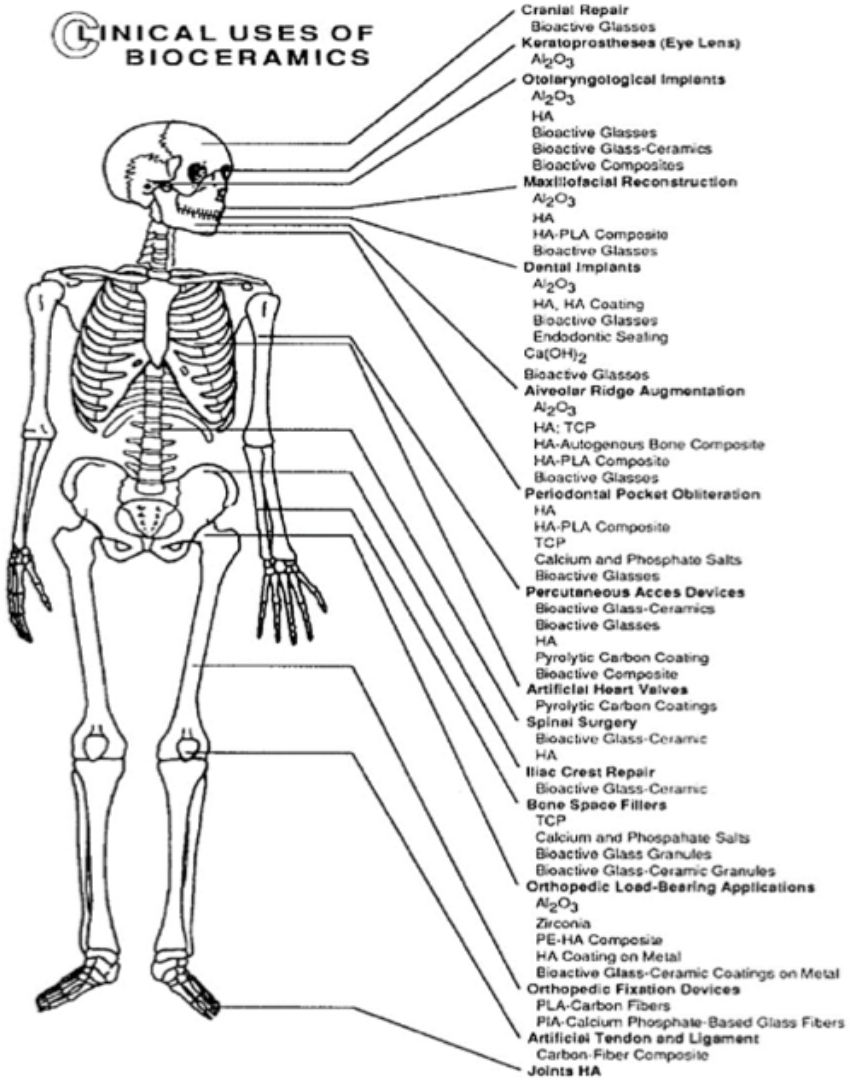

Figure 1.6: Examples of applications of bioceramics, bioactive glasses, and biocomposites [90].

Among the bioceramics used as bone substitute materials, calcium phosphates (CaP) have

drawn great interest due to their similarity with the mineral component of human bone [91]. In addition, owing to their good biocompatibility, osseointegration and osteoconduction, they have been extensively employed for the last 40 years for hard tissue repair and regeneration, both in orthopaedics and dentistry [92]. Some of the most widely employed CaPs are reported in Table 1.3.

Compound	Abbreviation	Formula	Ca/P
Monocalcium phosphate monohydred	MCMP	$Ca(H_2PO_4)\cdot H_2O$	0.5
Dicalcium phosphate dihydred	DCPD	$CaHPO_4\cdot 2H_2O$	1
Octacalcium phosphate	OCP	$Ca8H_2(PO_4)_6\cdot 5H_2O$	1.33
α-Tricalcium phophate	α-TCP	$\alpha - Ca3(PO_4)_2$	1.5
β-Tricalcium phophate	β- TCP	$\beta - Ca3(PO_4)_2$	1.5
Amorphous calcium phosphate	ACP	$Ca_9(PO_4)_6$	1.2-2.2
Hydroxyapatite	HA	$Ca_{10}(PO_4)_6(OH)_2$	1.67
Fluorapatite	FA	$Ca_5(PO_4)_3F$	1.67

Table 1.3: Widely studied calcium phosphates with corresponding chemical formula and Ca/P ratio. Adapted from [91].

Among the most commonly investigated members of this group of ceramics, HA, β-tricalcium phosphate (β-TCP) and their combination i.e., biphasic calcium phosphate (BCP), play a major role [91–93].

Bioactive glasses have also attracted a significant interest in bone-related applications. This is due to their extraordinary capacity to bond to tissues and stimulate bone formation. Because of their properties and applications, the following sections will be concentrated on the description of HA and bioactive glasses, main protagonists of the present work. Indeed, the major part of the experimental chapters is focused on them, either as standalone materials or when combined to form biocomposites.

1.2.4.3.1 Hydroxyapatite (HA)

HA, whose chemical formula has been indicated in Equation 1.1 (subsection 1.1.2) is a complex phosphate of calcium with a Ca/P ratio equal to 1.67. Among the family of CaP-based

compounds, HA have been extensively explored for biomedical applications, due to its morphological features, physicochemical and biological properties [94–98].
As described in subsection 1.1.2, HA shares similarities to inorganic component of bone tissue from structural and compositional point of view; therefore, for a long period of time, it was exploited as a model system to mimic the biomineralization process [99, 100].
Due to the features listed above, HA-based ceramics present a series of advantages [101]:

- excellent biocompatibility;
- bioactivity: indeed, it supports nucleating sites for the precipitation of apatite crystals in culture medium [102];
- non-inflammatory behaviour, non-immunogenicity;
- high osteoconductive and osteoinductive properties.

The suggested model mechanism of interaction between synthetic HA and bone tissue, is represented in Figure 1.7.

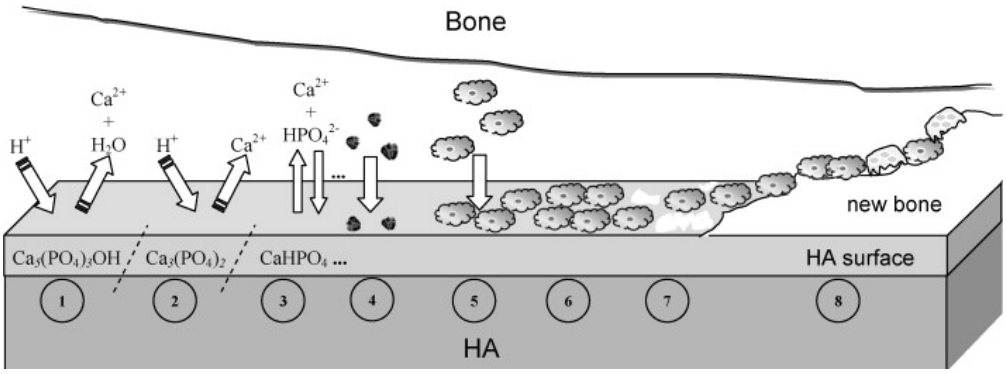

Figure 1.7: Schematization of the proposed interaction process occurring on the surface of implanted HA. Reproduced from [103].

The process, consisting in 8 subsequent steps, starts with the solubilization of the hydroxyapatite surface (1-2) and proceeds with the achievement of the equilibrium condition between physiological fluids and the modified surface of hydroxyapatite (3). Then, adsorption

of proteins and organic material (4), and cell adhesion and proliferation (5-6), occur. Lastly, the beginning of new bone formation mechanisms described in subsection 1.2.1 (7) leads, after some time, to the completion of the process, resulting in new formed bone (8).

Currently, the main drawbacks limiting the applications of HA are mainly the rather low resorption rate in-vivo and mechanical properties.

As for the first one, it has to be specified that, under physiological conditions, (body temperature, pH and body fluids composition), HA is the most stable CaP ceramic [104]. For this reason, it resorbs not adequately in-vivo (below 10 wt.% per year [105]), at a significantly slower rate than that of the growth of newly formed bone tissue. A possible solution about that, is the use of nano-sized apatites, whose composition, morphology and properties entail enhanced resorbability, and much higher bioactivity than microsized ones [106].

Another option to overcome such drawback is the use of apatites more similar to the natural one (either calcium deficient HA or carbonated apatites, whose solubility is higher compared to stoichiometric HA [107, 108]), or the use of HA in combination with more soluble CaPs, like the β polymorph of tricalcium phosphate (β-TCP), to obtain the so called biphasic calcium phosphate (BCP). The latter one has been highly studied and employed in several commercial products [38]. An additional possibility is to combine HA with other kind of materials, particularly Bioactive glasses. This case will be discussed in more details in subsubsection 1.2.4.4. All the compositions involving other ceramics or glasses usually allow for the dissolution rate to be tuned, by suitably adjusting relative proportions of constituents.

Another major limitation of HA-based ceramics concerns their mechanical properties which, depending on the porosity, density, and crystallite size, may vary significantly [109]. In general, HA-based ceramics are brittle and show poor fatigue resistance, making them generally not suitable for load-bearing applications [110].

Despite such drawbaks, HA is widely employed both for clinical applications (craniomaxillofacial reconstruction, spinal surgery, coating in orthopedic -hip joint prosthesis- and dental implants [92, 110–112], among the others) as well as in non-medical ones (including chro-

matography of nucleic acids, proteins, and other biological compounds and for drug delivery purposes [92]). Lastly, it is included in some hygiene products as an addictive to some brands of toothpaste [90].

Apatite-based materials are currently produced by different methods, listed in Table 1.4, along with some peculiar characteristics.

Method	**Processing aspects**			**Powders characteristics**			
	Cost	**Process time [h]**	**Scalability**	**Crystallinity degree**	**Phase purity**	**Size**	**Size distribution**
Solid-state method	low	>24	High	very high	usually low	usually micro	wide
Chemical precipitation	low	>24	High	low	frequently low	usually nano	variable
Hydrolysis	high	<24	-	variable	usually high	variable	variable
Sol-gel	variable	>24	Low	low	variable	nano	narrow
Hydrothermal	high	<24	Medium	very high	usually high	nano or micro	usually wide
Emulsion	high	>24	Medium	low	variable	nano	narrow
Solution Combustion	low	$<<24$	High	low	usually high	usually nano	variable
Biogenic sources	low	-	Variable	variable	usually high	variable	variable

Table 1.4: Comparison of different synthesis methods usually employed for the synthesis of HA. Adapted from [106, 113].

In general, these procedures can be mainly divided into dry and wet methods [114]. The preparation route is of particular importance, since it can affect the morphology and properties of the resulting products. Wet methods, particularly aqueous precipitation, are currently the most employed , given their advantages, such as low processing costs, the possibility to control the morphology and the mean size of powder by the process parameters, as well as up-scalability [113]. In addition, various ions contained in the aqueous solution can be incorporated into the crystal structure, thus allowing doping with suitable elements.

However, one of the main potential disadvantages is the low preparation temperature compared to dry methods, which can result in undesired CaP secondary phases other than HA, and/or the lowering of the crystallinity. Moreover relatively long processing times and different steps are usually associated to wet methods. For example, both aqueous precipitation

and sol-gel synthesis require several days, considering either reaction time and drying; in addition, heat treatment of the obtained products are needed in both cases.
On the other hand, also solid state synthesis consists of different steps, even at high temperatures, implying long processing times. Despite its up-scalability, this route provides well crystallised structures and can result in heterogeneity in its phases composition, given the limited diffusion coefficient of ions in solid phases [106].
The Solution combustion synthesis technique (SCS) is an alternative procedure which, starting from a solution, leads to the formation of the products, in form of powders, by a rapid combustion process. This technique is very versatile [115] and allows for the synthesis of nanoscaled apatites and other CaPs. This process is also up-scalable, making it of particular interest even for large scale production. It will be described in more detail in Chapter 4.

1.2.4.3.2 Bioactive glasses (BGs)

Glasses are amorphous solids without long-range order that are commonly composed of oxides. They are usually Silica-based, but research efforts are also dedicated to glass formulation which are not, like borate- [116, 117] and phosphate-based formulations [71, 118].
Talking about silica-based glasses, those ones used for biomedical applications, named bioactive glasses (BGs), differ from soda-lime glass (commonly used in windows or bottles) by their composition. More specifically, BGs contain less silica and higher amounts of calcium and phosphorus.
The original bioactive glass, also known as Bioglass® 45S5, was developed in 1969 by Professor Larry Hench [119]. The idea to employ glasses and the specific formulation designed by Hench completely revolutionized the field of biomaterials. From that point on, the general trend in bone repair shifted from the development of non-toxic inert biomaterials to the obtainment of bioactive materials, which directly bond to bone and stimulate body response for the generation of natural tissues.
The mechanism for bone bonding between the bioglass and host tissues, which will be de-

scribed in more details in the following subsection 1.2.5, was further attributed to the formation of an hydroxycarbonate apatite (HCA) layer on the surface of the glass, following its initial dissolution.

Other important properties of bioactive glasses include their ability to enhance revascularization, osteoblast adhesion, enzyme activity, and differentiation of mesenchymal stem cells [119].

The composition of the original glass invented by Prof. Hench, further trademarked as Bioglass® 45S5, is: wt.%, 45% SiO_2, 24.5% CaO, 24.5% Na_2O, and 6% P_2O_5 [120].

Depending on the chemical composition of bioactive glass, its biological behaviour, in particular the ability to bond with bone, can vary significantly. In this regard, Figure 1.8 shows the compositional diagram for the Na_2O-CaO-P_2O_5-SiO_2 glass system (6 wt% of P_2O_5) to evaluate possible hard and soft-tissue bonding.

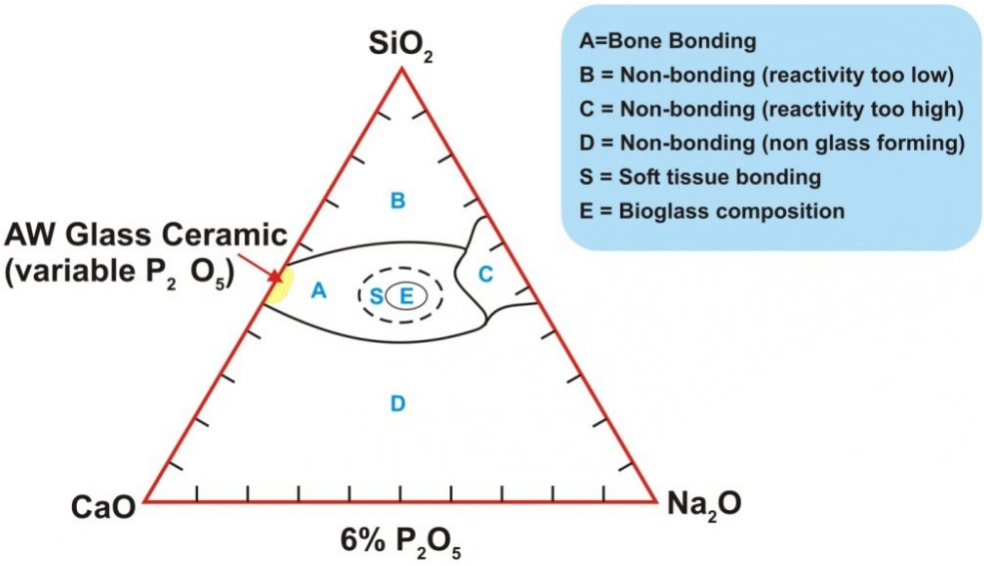

Figure 1.8: Compositional diagram describing Bioactive glass bone bonding ability versus composition. Reproduced from [121].

Region A is the bioactive and bone bonding zone, i.e. glasses with composition which falls within this area can bond to bone. Glass formulation of Region B (soda-lime-like glasses)

behave almost as inert materials and form fibrous morphology at the implant-tissue interface. From the reported phase diagram it is possible to note that the upper limit of Si-content to obtain bone-bonding glasses is 60 wt.% [122]. Region C compositions correspond to resorbable glasses, which disappear within a day, after implantation. Region D is associated to non glass forming materials and are not tested in-vivo. Region E represents the area of 45S5 Bioglass® composition, while Region S contains soft tissue bonding formulations. Even after 50 year span of research on bioactive glasses, 45S5 Bioglass® still represents a gold standard in the field. It has been established that in-vivo 45S5 glass degrades more rapidly, and favours more rapid bone regeneration, unlike the synthetic hydroxyapatite [116].
Given all the described properties, Bioglass® has been employed in several clinical applications (orthopedics, cranial-facial and dental- maxillofacial clinical applications) and commercial products, for instance [123]:

- *Bioglass® Ossicular Reconstruction Prosthesis* (tradename MEP®), which is used to treat conductive hearing loss by replacing the bones of the middle ear;
- *Endosseous Ridge Maintainence Implant* (tradename ERMI), designed to support labial and lingual plates in natural tooth roots and to provide a more stable ridge for denture construction following tooth extraction;
- *PerioGlas®*, initially indicated to restore bone loss caused by periodontal disease, and eventually approved for alveolar ridge augmentation in tooth extraction sites;
- *NovaMin* (GlaxoSmithKline, UK), where Bioglass® is employed in particulate form as an active agent included in the toothpaste to stimulate remineralization of dentine, and reduce tooth ipersensitivity.

Moreover, beyond the bone-related applications, bioactive glasses recently found vast application in biomedicine , such as wound healing, peripheral nerve repair, cardiovascular tissue engineering, gastrointestinal applications, and others (Figure 1.9). In these cases, specific formulations can be required; for example, glass formulations able to bond to soft tissues should

fall within Region S Figure 1.8. Moreover, compositions containing specific ions for therapeutic purposes are also gaining huge scientific interest due to their potential [124]. Furthermore, some applications require specific manufacturing techniques to take full advantage of glass properties, as for instance the obtainment of fibres by electrospinning in the case of wound healing-related applications.

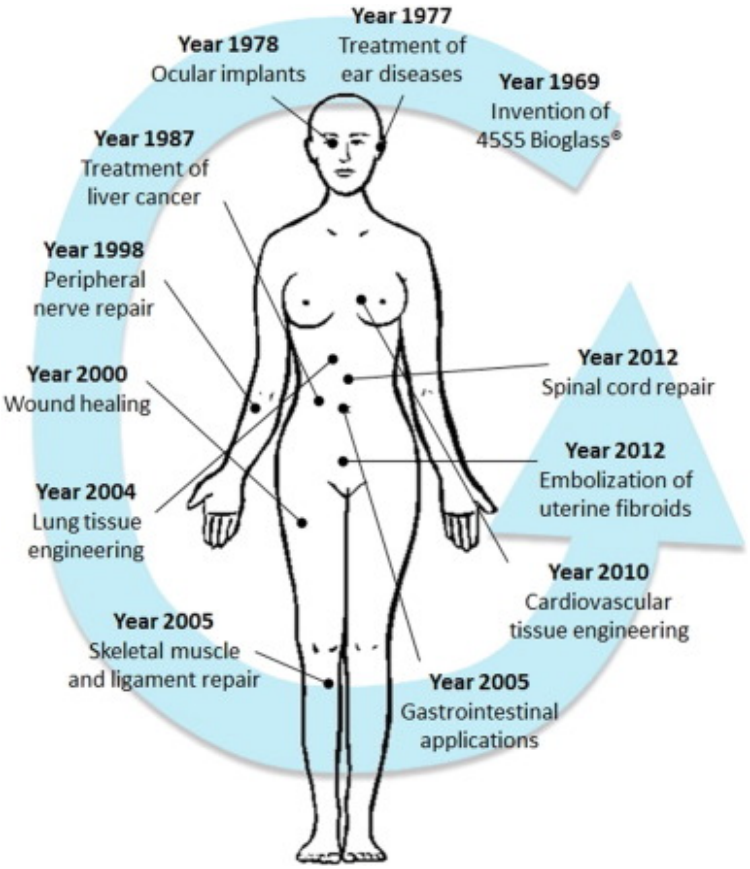

Figure 1.9: Overview of the biomedical applications of bioactive glasses. Reproduced from [124].

The SiO_2-Na_2O-CaO-P_2O_5 system, being so successful, is still used as a template to develop new silica-based formulations [125]. Several modifications have been proposed, also including the presence of other oxides, to improve the characteristics of original Bioglass®. Some of the most common alternative bioactive glasses are 13-93 (wt%, 53% SiO_2, 12% Na_2O, 6% Na_2O, 5% MgO, 4% P_2O_5, 20% CaO), also approved for in-vivo use in Europe, 58S (wt%, 58.2% SiO_2, 9.2% P_2O_5, 32.6% CaO), 77S (mol%, 80% SiO_2, 4% P_2O_5, 16% CaO) and S53P4

(wt%, 53% SiO_2, 23% Na_2O, 20% CaO, 4% P_2O_5). The last one gained particular interest due to its biocompatibility and osteoconductivity, and displays proangiogenic and antibiofilm properties [126–129]. In addition, it was found to be able to inhibit growth of more than 50 strains of clinically relevant bacteria [130–132]. Lastly, good long-term outcomes arose from the treatment of fractures [133, 134]. For all these reasons, S53P4 is an approved material for human application. For instance, Bonalive®, based on S53P4, is currently used in different formats for the treatment of diabetic foot osteomyelitis surgery, bone infection surgery, mastoid surgery, benign bone tumor and spine surgery [https://www.bonalive.com/en, accessed December 18th, 2022].

Despite the advantages demonstrated, bioactive glasses evidenced some common drawbacks. First of all, due to the limited mechanical strength, particularly low fracture toughness, BGs are suitable only for low-load bearing applications.

Another challenging issue is related to the processing of powders, since sintering, or the processes requiring high temperatures in general, usually cause the occurrence of crystallization of the glass. The latter can hinder, or even inhibit, the biological properties of the resulting material, and so it has to be preferentially avoided.

The crystallization (or devitrification) process of 45S5® Bioglass starts at approximately 610°C, while its glass transition temperature is of about 550°C, meaning that the sintering window for this material is quite narrow in terms of temperature range. Even if the effect of the crystallization on the biological properties is still debated in some ways (since it was found that certain crystallization degree might be beneficial in terms of bioactivity [135, 136]), its occurrence was also reported to hinder densification. In general, the limited sintering ability of glass can lead to weaker and less interconnected structures, resulting in bulk materials with the associated formation of micro-cracks and poor mechanical strength [137]. Due to these reasons, one of the main efforts regarding bioactive glasses is to find and assess formulations displaying lower tendency to crystallise, displaying good mechanical and, especially, biological properties. In this sense, new glass formulations have been recently proposed, such as the so called Ca_MIX

(mol%, 47.3% SiO_2, 45.6% CaO, 2.3% Na_2O, 2.3% K_2O, and 2.6% P_2O_5) [138], which was reported to have a crystallization temperature of 880 °C [139]. In addition, Ca_MIX was also able to form an apatite layer in less than 3 days of immersion in SBF, when the amorphous nature was retained during sintering [140]. A further development of the glass composition led to the so called BGMS10 glass formulation (mol %, 47.2% SiO_2, 25.6% CaO, 2.3% Na_2O, 2.3% K_2O, 2.6% P_2O_5, 10.0% MgO, and 10.0% SrO) [141], which was reported to possess a crystallization temperature of 932 °C. During SBF assay HA precipitate was deposited onto glass surface. In addition it was able to induce osteo-differentiation of bone marrow mesenchimal stem cells [142]. The processing of such glass formulation will be discussed in more details in Chapter 2.

Another hot topic about bioactive glass-related research is the introduction of suitable ions into the glass structure, with the aim to improve their properties. Specific metallic ions such as copper, strontium, magnesium, zinc, cobalt, and boron, have emerged as potential therapeutic agents. Some of them have been shown to enhance bone formation due to their stimulating effects on osteogenesis and angiogenesis [143–145]. Others (e.g. copper, zinc, silver) have different effects, like anti-inflammatory and antibiotic capabilities [146, 147]. An important mention is due to magnesium, which is reported to be of extreme importance for several physiological functions (promoting bone formation, protein, and nucleic acid synthesis, adenosine triphosphate metabolism, contraction and relaxation of muscle, normal heart rhythm, and activation of vitamin D) as well as strontium, as potential stimulator for bone formation (via the enhancement of the expression of osteoblast-related genes, promoting differentiation of mesenchymal stem cells and inhibiting the activity of osteoclasts [148]).

Currently, bioactive glasses are mainly synthesised by two techniques: conventional melt quenching [120], and sol-gel [149–151]. The first is a reliable synthesis route of glasses to produce particle dimensions in the micrometer range, usually having superior mechanical properties and flexural strength [152]. On the other hand, the second one allows for the obtainment of glasses showing fine particles and larger specific surface areas, together with superior

porosity and apatite forming ability [152].

1.2.4.4 Composite materials

In general, none of the previously described materials can fulfil all the requirements presented in subsection 1.2.3.

In this context, composite materials are designed and produced to combine the positive features of the materials used to make them, and possibly avoid or limit their drawbacks. The research on composite material is vast and various.

For example, HA-β-TCP composite ceramics, or BCP, are widely investigated as an alternative to pure HA, being such composite more degradable, showing biocompatibility, bioactivity, osteoconductivity, together with capability of carrying and inducing the differentiation of stem cell [153].

Furthermore, HA-BG composites offer the possibility to tune degradation rates, depending on the relative amount of each phase [154–156].

In addition, the presence of the glass has been shown to favour the densification of HA, and also significantly improve the biological response of the resulting composite material.

Beyond the standard combination of the constituents to obtain composite structures with uniform phase distribution, another option is represented by Functionally Graded Materials (FGMs). FGMs consists of one or more different components, engineered to have a varying spatial compositional, or structural profile [157]. FGMs can be divided according to the type of gradient, i.e. compositional and microstructural. Natural biomaterials (for example, allografts) intrinsically have the structure of FGMs. For this reason, this class of materials have been extensively investigated in the last decades for biomedical applications, such as in dental restorations and orthopaedic implants [158–160]. In this context, the study of FGMs based on HA/BG can play an important role. The first months of the candidate's Ph.D. course were partly dedicated to the participation in a study regarding the development of a 5-layered HA/Ca_MIX-based FGM. In the research work, taking advantage of the low tendency to crys-

tallise of the Ca_MIX glass formulation, two different compositions were studied:

- System S1, generally richer in HA, was processed at higher sintering temperature and lower pressure (1000 °C and 16 MPa);
- System S2, richer in BG, was sintered at lower temperature and higher pressure (800 °C and 50 MPa).

The composition of each layer is indicated in Figure 1.10 for both systems.
Nearly fully dense samples were obtained by Spark Plasma Sintering processing (which will be presented in more details in the following chapters). This is confirmed by the low residual porosity of the obtained bulk samples, which was determined to be lower than 10 vol% and 1 vol% for systems S1 and S2, respectively.

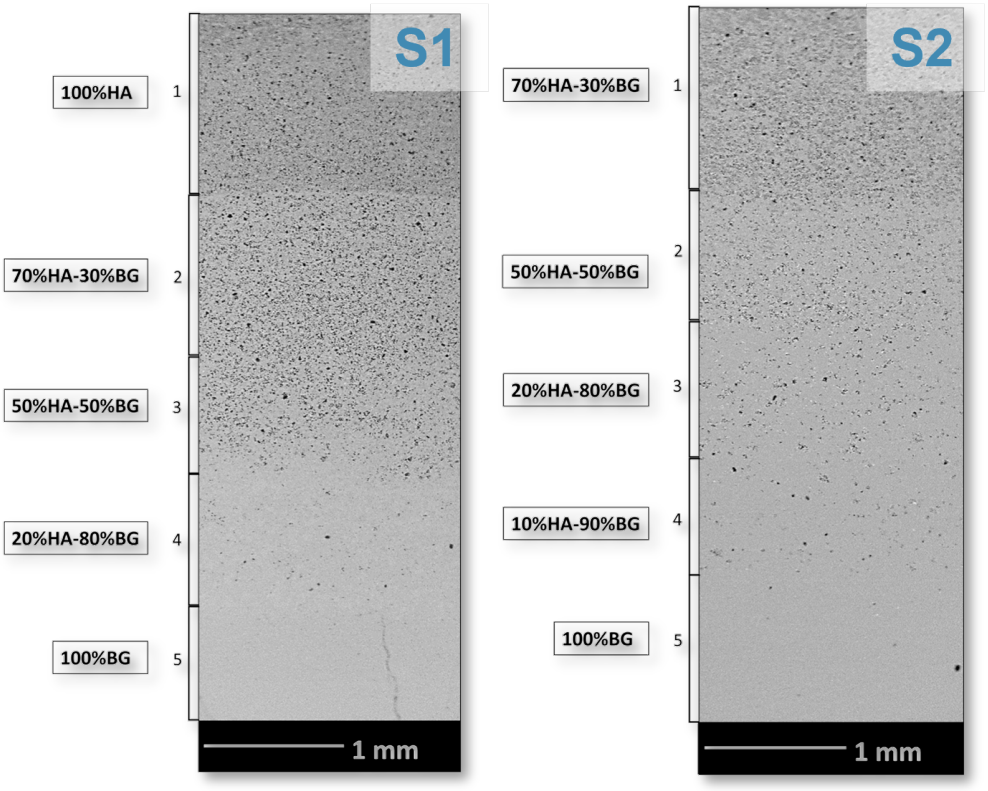

Figure 1.10: Cross sectional SEM images of 5-layered FGM bulk samples with S1 and S2 compositions.

The XRD analysis (Figure 1.11) showed that was possible to preserve the amorphous nature of the glass in system S2 (milder sintering temperature conditions), resulting in an improved amount of HA deposited after 7 days of immersion in SBF (Figure 1.12).

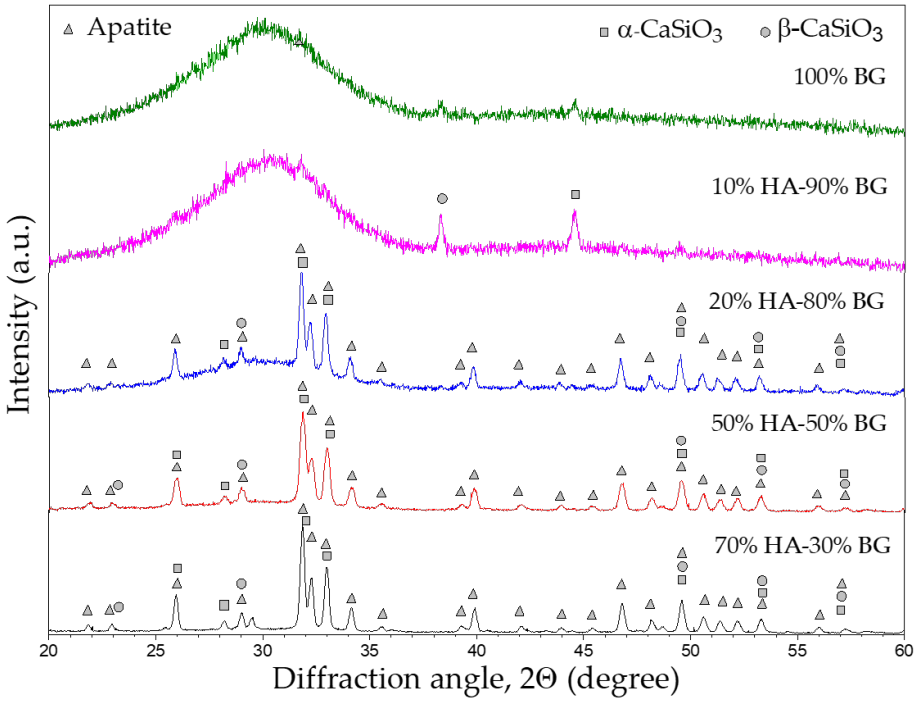

Figure 1.11: XRD patterns of each layer of the S2 composition bulk samples.

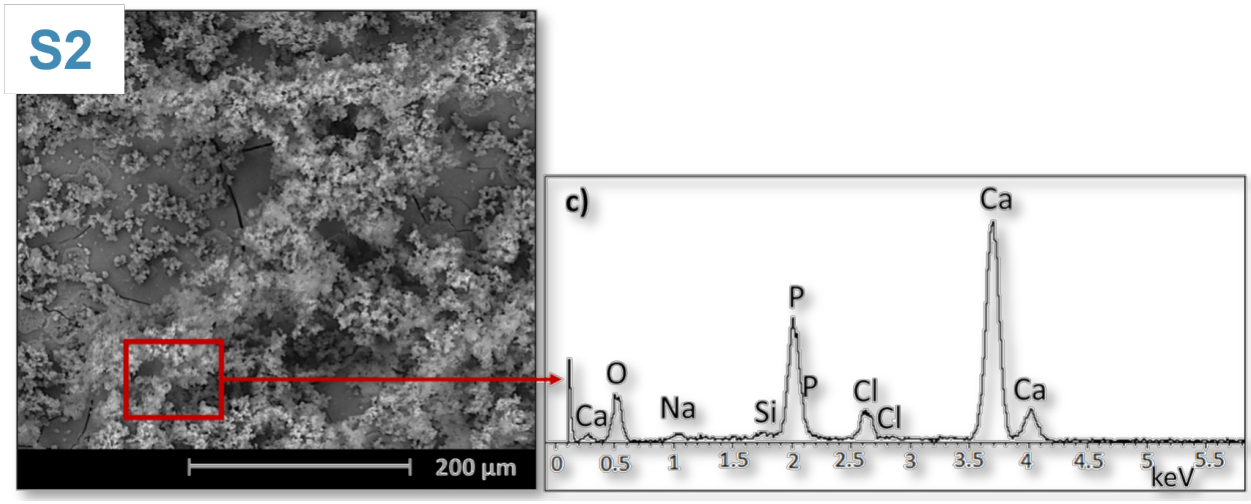

Figure 1.12: SEM micrographs of S2 system sample after 7 days of immersion in SBF, and EDX analysis on the precipitates.

1.2.5 Bone bonding mechanism and bioactivity assessment

The main aspect of bioactivity is the partial dissolution of the investigated material with the associated ions release, and the consequent increase of local concentrations of calcium and phosphate ions. The previous leads to the precipitation of biological apatite onto the surface of ceramics in-vivo. The 12-steps sequence of reaction events involved during the bond formation between bone and a bioactive materials, originally proposed by Hench for the case of bioactive glasses and subsequently modified by Gerhardt and Boccaccini [161], is reported in Figure 1.13:

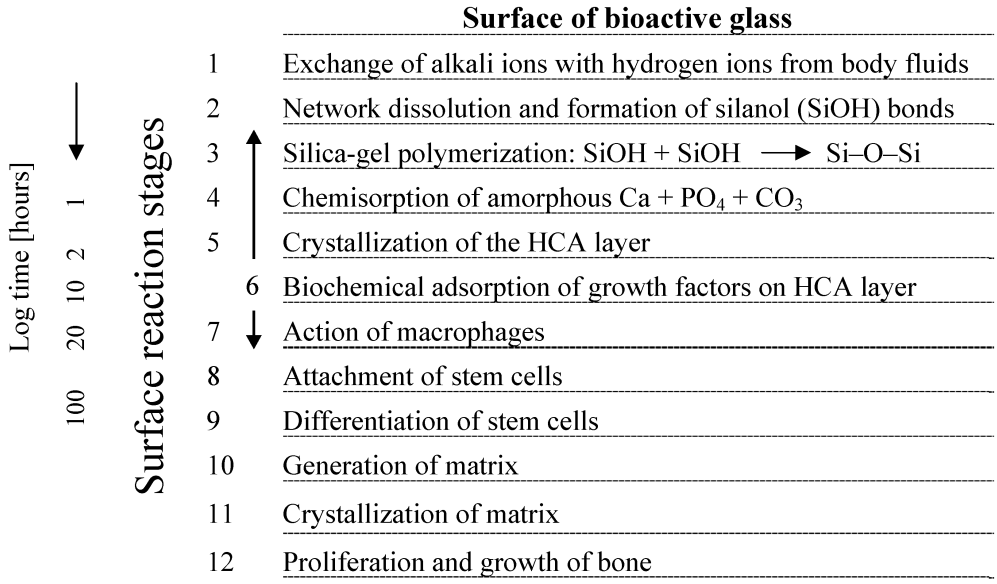

Figure 1.13: Sequence of reactions occurring onto the surface of a bioactive materials once implanted. Reproduced from [161].

Since it is not safe to test new biomaterials directly in-vivo, different methods were proposed to preliminary assess their bioactivity. The first 5 steps indicated in Figure 1.13 involve essentially ion exchange with physiological fluids and the subsequent nucleation of HCA, without noteworthy role played by cells. Therefore, a first approach to test the bioactivity should be the assessment of HCA-forming ability when the material is placed in contact with physiological fluids. Particularly, the idea originally proposed by Kokubo [162] involves the

use of an acellular solution called *Simulated Body Fluid* (SBF), which simulates the fluid of the body, and having an ionic concentration similar to that of human blood plasma (Table 1.5).

	Na^+	K^+	Mg^{2+}	Ca^+	Cl^-	HCO_3^-	HPO_4^{2-}	SO_4^{2-}
Human blood plasma	142	5	1.5	2.5	103	27	1	0.5
SBF	142	5	1.5	2.5	148	4.2	1	0

Table 1.5: Comparison between ions concentration, expressed in mM, of human blood plasma and SBF solution. Reproduced from [163].

Since its proposal, Kokubo's protocol has been considered a useful preliminary method for assessing the potential in-vivo bioactivity of new materials [164]. On the other hand, the reliability of this method depends on the category of investigated bioceramics, as recently pointed out by Bohner and Lemaitre [102]. Thus, the results obtained from SBF assays have to be carefully examined. In any case, when considering specific materials (for instance the ones investigated in this work), the use of the SBF assay still represents an extremely valid first step to test the bioactivity in-vitro across scientific community. Of course, other kind of experiments are necessary to fully assess bioactivity and to support possible positive SBF results. Cellular tests, i.e. studies monitoring and evaluating the in-vitro response of cells to the investigated material are the second step of bioactivity evaluation [111, 165]. The combination of the resulting outcomes can provide a good indication of the biological properties of a newly developed biomaterial.

1.3 Sintering: fundamentals and techniques

This section is aimed to give a general overview about materials processing by sintering. In particular, the principle of the *Spark Plasma Sintering* (SPS) technique adopted in this work will be presented, together with the advantages related to its use.

1.3.1 Sintering

Bioceramics and bioactive glasses processing is an important step involving mechanical and/or thermal treatments of the raw powders or precursors to obtain the final designed product, generally in bulk form. The employed processing technique basically depends on the type of biomaterial and its application.

Among the different manufacturing techniques, sintering is essential when working with ceramics and glasses, being almost the only way to convert powders into bulk samples. Indeed, due to their nature, they cannot be processed by plastic deformation at a macroscopic scale. Sintering allows for the initial powder densification as a consequence of a heat treatment, and/or the application of pressure. It involves the bonding of the particles together into a solid structure by means of mass transport phenomena, mainly occurring at the atomic level, caused by the tendency of ions and atoms to move to compensate the energy differences among their surfaces [126]. Therefore, sintering is an irreversible process in which the reduction of the surface area of the starting powders leads to a decrease of the free energy of the system. Figure 1.14 gives a schematic view of such process, composed by three main steps, conceptually described as follows:

- *Initial stage* or powder rearrangement, a relatively quick process after exposure to high temperatures (of the order of magnitude of minutes, at most), in which the densification level of initial powder increases, up to about 10 vol% (Figure 1.14 a);

- *Intermediate stage* of sintering, which corresponds to an additional increment of powder consolidation, slowly turning to higher density values. This results from the occurrence

of some phenomena, such as neck growth (Figure 1.14 b), the formation of interconnected cylindrical channels by pores and particle centres approaching one another;

- *Final stage*, ideally leading to the progressive and complete elimination of the residual porosity, is usually considered to start whenever the compact powder approaches approximately 95% of the theoretical density (Figure 1.14 c). Strong chemical bonds are established among powders, so that, at the end of the whole process, the loosely initial compacted green bodies are hardened to compact materials.

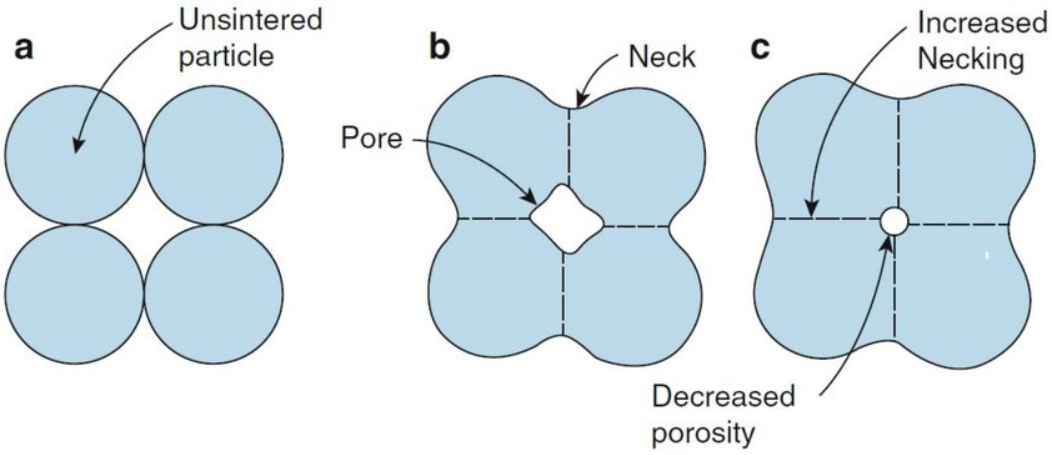

Figure 1.14: Schematic representation of sintering process. Reproduced from [166].

The parameters affecting the densification behaviour previously described are the temperature, the heating rate (or more generally the thermal profile), applied pressure, specimen dimension, powder particle size and porosity, as well as the possible occurrence of phase transformations [167–169].

Of course, the final achieved density and microstructure largely influence mechanical and biological properties of the sintered specimen. The last characteristics, being the result of densification procedure, are strongly dependent on the adopted technique. The general concepts of the two main conventional sintering techniques, i.e. pressureless sintering and pressure-assisted sintering, are briefly described in what follows, together with the innovative Spark Plasma Sintering process, which is employed in the present work.

1.3.1.1 Pressureless sintering (PLS)

This processing route represents the most basic approach to powders sintering. It consists on heating the green body, obtained by the compaction of the powders, without the application of an external pressure. The process can be conducted at constant-rate heating (CRH), rate-controlled sintering (RCS), and two-step sintering (TSS, consisting of a first heating to a temperature T_1, then a cooling to a lower temperature T_2 followed by an holding period at the latter until densification is completed). The microstructure and grain size of the ceramics varies depending on the material and the adopted temperature pattern [170].

To achieve high densification levels, pressureless sintering usually requires high temperatures and long processing times, on the order of magnitude of 24 h. However, the resulting samples usually display residual porosity, and the long processing time, together with the high temperatures, can cause (generally undesired) significant grain and crystallite size growth, not to mention the occurrence of crystallization in the case of bioactive glasses.

1.3.1.2 Pressure assisted sintering

Differently from PLS, pressure assisted techniques involves the application of a pressure during powder heating. Mechanical loads or hydrostatic pressure are well known to influence the consolidation process: since pressure increases the driving force for densification, the required temperature can be significantly reduced with respect to PLS.

The two most widely used pressure-assisted sintering methods are *hot pressing* (HP) and *hot isostatic pressing* (HIP).

In the first one, a mechanical load is applied uniaxially during powder heating. In traditional HP, external elements are used as heating sources (Figure 1.15), so that achievable heating rates are relatively low and, consequently, the process is slow (order of hours) and high energy consuming.

As schematically shown in Figure 1.16, an isostatic pressure (generally using inter gas) is applied during HIP, concurrently to sample heating. [171, 172]. HIP allows to obtain higher den-

sities at low temperatures, compared to HP, and the treatment of complex shapes. However, the equipment/tooling are relatively complex, and the process is more expensive than the sequential approach of compaction followed by conventional sintering [173].

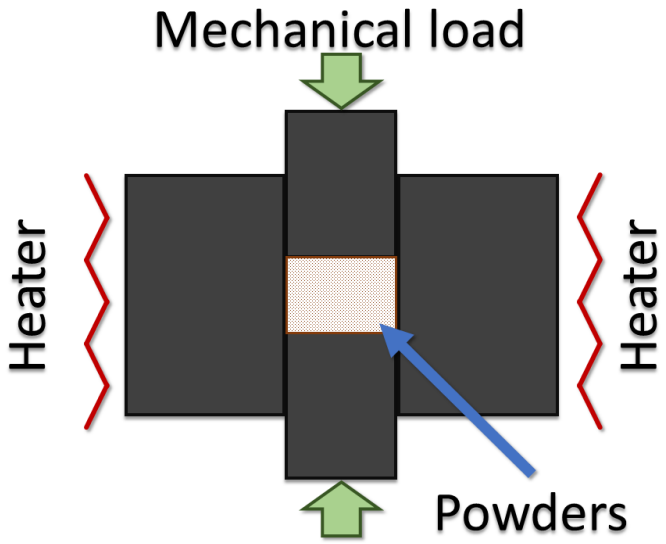

Figure 1.15: Schematic description of conventional hot-pressing technique.

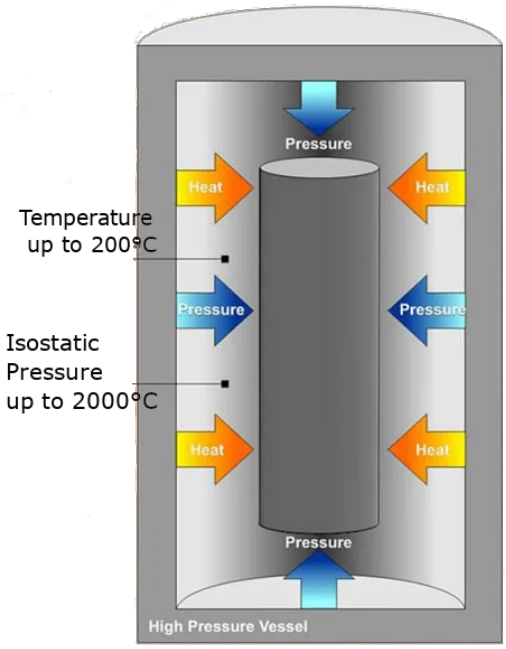

Figure 1.16: Schematic representation of the hot isostatic pressing technique.

1.3.1.3 Spark Plasma Sintering (SPS)

Based on the previous description of conventional sintering techniques, it is evident that they are characterised by some important drawbacks, i.e. the slow heating, long processing times, which both determine high energy consumption. These factors also favour grain growth, making the microstructure of the resulting products typically quite coarse.

To overcome such drawbacks, innovative and more efficient sintering methods were proposed in the last decades, including *Selective Laser Sintering* (SLS), the *Capacitor Discharge Sintering* (CDS), and the *Spark Plasma Sintering* (SPS).

SPS (also known with several alternative names, e.g. *plasma activated sintering, pulse electric current sintering* and *pulse discharge pressure sintering*, etc.) is an advanced pressure-driven technique in which heating is achieved by an electric current flowing through the sample placed inside a conductive mould. A schematic representation of it is reported in Figure 1.17.

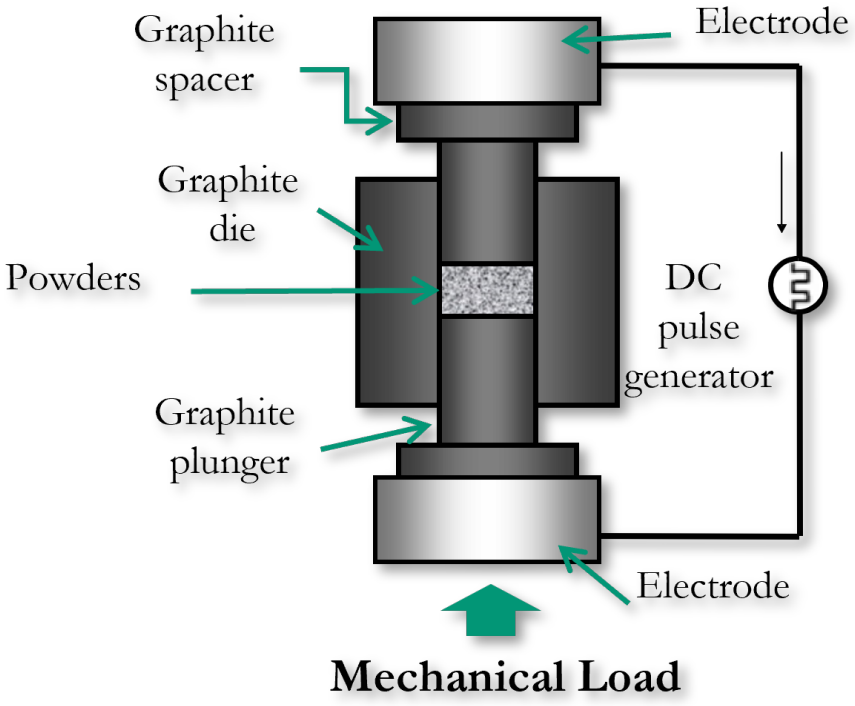

Figure 1.17: Schematic description of the SPS technique.

This technique is an energy-saving technology, particularly due to the short processing times (on the order of minutes) and relatively lower temperature, compared to conventional HP and PLS. Briefly, during a SPS, the powders placed inside a die (typically made of graphite) are rapidly heated by a pulsed DC current which flows through both the die and the sample (depending on its conductivity). The main responsible for powder heating is Joule effect. In addition it has been postulated that the presence of other effects (electromigration, sparks formation, etc.) can promote powder consolidation by SPS [174]. Pressure is simultaneously applied to the processing powders to favour their consolidation.

The most important SPS parameters (temperature, applied load, sample displacement, etc.) can be monitored, giving real-time indications on the ongoing process. However, the thermal expansion of sample, electrodes, graphite blocks, spacers and plungers must be taken into account as factors influencing the measured displacement output, in order to obtain a reliable sample densification behaviour [175].

As summarized in a comprehensive review by Munir and coworkers [176], the use of SPS for the powder consolidation allows to obtain cleaner grain boundaries in sintered materials, a remarkable increase in superplasticity of ceramics, higher permittivity in ferroelectrics, improved magnetic and thermoelectric properties, bonding quality, as well as reduced impurity segregation at the grain boundaries. The peculiar features of the SPS technique are also convenient to process bioceramic and bioactive glasses powders, as will be described in the following chapters. Indeed, the relatively milder sintering conditions adopted during SPS allow to achieve e microstructural characteristics frequently required by biomaterials, i.e. avoid the decomposition of apatites to other undesireable phases, preserve their nanostructure, when originally present in the powders, as well as the amorphous nature of bioactive glasses. For these reasons, the SPS technology has been employed in the present thesis for the obtainment of bulk apatite- and bioactive glass-based materials, as well as their composites.

Chapter 2

Sintering and characterization of an innovative Bioactive Glass containing Sr and Mg (BGMS10)

2.1 Introduction

Owing to their ability to stimulate bone regeneration when interfaced with biological tissues and fluids, bioactive glasses are currently employed in several medical applications [119, 120, 124, 177–181]. In this context, 45S5 Bioglass® has played a prominent role, at least so far [120]. Despite this, negative features are encountered using such glass for obtaining bulk templates for bone regeneration, mostly because of its rapid crystallization tendency at relatively low temperature values (about 600°C), when the corresponding powders are subjected to the required heat treatments [119, 182, 183]. Indeed, a reduced bioactivity is generally displayed by the resulting crystallized sintered products.

For these reasons, as extensively indicated before in this work (Chapter 1), two of the main hot topics regarding BG research are:

- the development of glass formulations displaying a higher crystallization temperature

with respect to standard ones;

- the proper incorporation in glass matrices of ions able to improve the related properties (physical/chemical but also mechanical and biological ones).

In this regard, alternative glass formulations able to guarantee lower tendency to crystallize, and similar, or even higher bioactivity properties with respect to 45S5 Bioglass ®, have been proposed in the literature [138, 140–142, 184–186]. They include a CaO-rich glass (mol. %, 2.3% Na_2O, 2.3% K_2O, 45.6% CaO, 2.6% P_2O_5, and 47.2% SiO_2), generally referred to as BG_ Ca_MIX [138, 140, 184]. More recently, the introduction of strontium and magnesium, which are known to provide beneficial therapeutic effects [139, 148, 187] in bioactive glass, was explored to generate the so called BGMS10 (mol%, 2.3% Na_2O, 2.3% K_2O, 25.6% CaO, 10.0% MgO, 10.0% SrO, 2.6% P_2O_5, and 47.2% SiO_2) [141, 142], Bio_ MS (mol%, 5.0% Na_2O, 31.3% CaO, 5.0% MgO, 10.0% SrO, 2.6% P_2O_5, 46.1% SiO_2) [185] and BGMSN (mol%, 6.1% Na_2O, 31.3% CaO, 5% MgO, 10% SrO, 2.6% P_2O_5, 45% SiO_2) [186] formulations. These three glasses were specifically designed to achieve very high crystallization temperatures, thus possibly avoiding crystallization phenomena upon thermal treatments, being the latter ones necessary for the fabrication of sintered bodies, coatings, scaffolds, etc. To preserve their low crystallization tendency, a high content of CaO was kept in these glasses, i.e. 25.6 mol.% for BGMS10 and 31.3 mol.% for Bio_ MS and BGMSN, respectively. Correspondingly, crystallization temperatures among the highest ever reported in the literature (932°C, 859°C and 851°C, respectively), and, at the same time, outstanding properties in terms of bioactivity and biocompatibility were obtained [142]. These glasses were also tested with an innovative 3D cellular model [142,185], able to mimic their potential clinical application, when human bone marrow mesenchymal stem cells are employed. Furthermore, the reactivity and dissolution behaviour of such materials were confirmed by means of a Molecular Dynamics model [188]. Thus, such bioactive glasses showed a very favourable combination of properties, i.e. excellent biological performances and very high crystallization temperatures at the same time. Therefore, they could be considered very promising for bone tissue engineering and regenerative medicine,

particularly when a thermal treatment is necessary to produce specific devices.

Once the nominal composition of the glass is set, it is very important to achieve the most suitable microstructural characteristics, so that both bioactivity and mechanical properties of the corresponding sintered products are optimized. Since both these characteristics depend on sample porosity (volume percentage, pores size and distribution), the latter one should be maintained the same when the effect produced by other structural parameters, for instance the crystallization level attained during sintering, has to be proved. Unfortunately, such condition is quite difficult to achieve.

To overcome this drawback, a preliminary comparison of mechanical and biological behaviour could be assessed by considering fully dense glass-derived products, so that possible masked effects induced by other difficult-to-control parameters associated with porous bodies are avoided. A strong support in this regard could be provided by the use of SPS technique for powder consolidation. As described in section 1.3.1.3, SPS is a very efficient sintering method and typically permits to obtain dense products in relatively shorter times/milder temperatures compared to conventional sintering methods. In addition, it allows to carefully control processing parameters for hindering devitrification phenomena from the parent glass or obtaining desired crystallization levels. All these advantages were recently exploited to produce nearly full dense 45S5 [135] and BG_ Ca_MIX [140] glass samples as well as HA-BG composites [189], with different degrees of crystallization, and evaluate their behaviour during biological tests in SBF (subsection 1.2.5).

Although bioactive glasses are generally used as porous scaffolds, few examples of their application in dense form are also reported in the literature, for instance for the repair of orbital floors [119]. Some porous bioceramics are also obtained via SPS, by properly selecting the applied pressure/sintering temperature conditions, powder characteristics/pretreatment, porogen agents, etc. [190–193].

The main aim of the investigation presented in this Chapter is the identification of the optimal temperature conditions to fully consolidate BGMS10 powders by SPS. To this, three sets

of differently crystallized dense products are obtained for further characterization. A detailed microstructural analysis is carried out to quantitatively estimate their degree of crystallization, phases content, and crystallites size. Finally, mechanical and biological properties of the bulk samples are evaluated and compared. The obtained results should be considered as a good starting point to provide valuable indications for the subsequent fabrication of porous scaffolds, as well as for further studies regarding BGMS10-containing composite materials, which will be presented later in this work (Chapter 3).

2.2 Experimental materials and methods

2.2.1 Powders

The lab-made BGMS10 bioactive glass powders were obtained by melt-quenching the route at the Department of Engineering "Enzo Ferrari", Università degli Studi di Modena e Reggio Emilia (Italy).
Briefly, the commercial raw powders (SiO_2, $Ca_3(PO_4)_2$, $CaCO_3$, Na_2CO_3, K_2CO_3, $(MgCO_3)_4 \cdot Mg(OH)_2 \cdot 5H_2O$, $SrCO_3$, all reagent grade - Carlo Erba Reagenti, Italy) were weighted, mixed for 2 h in a laboratory shaker (M63a4 - Motori Elettrici Carpanelli, Bologna, Italy) and then melted in a Pt crucible in air. The following thermal cycle was adopted:

- a pre-heating step, from room temperature to 1100°C at a rate of 10°C/min;
- a decarbonation step at 1100°C for 1 h;
- a heating step from 1100°C to 1450°C at a rate of 10°C/min;
- 1h at 1450°C to obtain a homogeneous melt;
- quick quenching of the molten glass in room-temperature water to obtain a frit;
- a drying phase of such frit overnight at 110°C.

The obtained frit was then ground for 20 min in dry conditions in a porcelain jar and sieved to produce a powder with a final grain size lower than $63\,\mu m$ [141].

Particle size distribution was determined by laser light scattering analyser (CILAS 1180, France). The powder morphology was examined by high-resolution scanning electron microscopy (HR-SEM, mod. S4000, Hitachi, Tokyo, Japan). The density of BGMS10 was measured by employing a gas pycnometer (Accupyc II 1340, Micromeritics USA), which provided a value of 2.97 g/cm^3. To assess the thermal behaviour of glass powders, differential thermal analysis (DTA) (Netzsch Differential Thermal Analyzer, DSC 404, Netzsch-Gerätebau GmbH, Selb, Germany) was carried out from room temperature to 1000°C under air flow. The corresponding data obtained at different heating rates, in the range 8-30°C/min, were also used to estimate, according to the Kissinger theory [194], the effective activation energy of the crystallization process (E_C), using the following expression:

$$ln\left(\frac{r}{T_p^2}\right) = -\frac{E_C}{RT_p} + C \tag{2.1}$$

where T_p [K] is the temperature value relative to the exothermic peak in the DTA curve, r the heating rate, and R the universal gas constant.

2.2.2 Bulk samples

Cylindrical samples of about 14.7 mm diameter and 3 mm thickness were produced from BGMS10 powders using the SPS apparatus (515S model, Fuji Electronic Industrial Co., Ltd., Kanagawa, Japan) reported in Figure 2.1. Sintering experiments were carried out in vacuum (about 20 Pa), with a current sequence of 12 ON pulses followed by 2 OFF pulses, and 3.3 ms as characteristic time of single pulse. The temperature was measured using a K-type thermocouple (Omega Engineering Inc., USA) inserted in a small hole drilled on the external surface of graphite, about 1-2 mm far from the processed powders. The die and the plungers shown in Figure 2.2 a) and b), were both made of AT101 graphite (Atal s.r.l., Italy). About 1.5 g of the

powder to be sintered was placed inside a cylindrical die with an external diameter of 35 mm, an inner diameter of 15 mm, and 30 mm high, and between two plungers of 14.7 mm diameter, 30 mm height. To make sample release easier after SPS, a graphite foil with a thickness of 0.13 mm, as the one shown in Figure 2.2 c) (Alfa Aesar, Karlsruhe, Germany), was placed between the powders and the inner walls of die/plungers. In addition, thermal losses from the die were limited by covering it with a 3 mm thick graphite felt (Atal s.r.l., Italy), also shown in Figure 2.2 d). The most important SPS parameters, i.e. temperature, current, voltage between the machine electrodes, applied load and vertical sample displacement, were monitored and recorded during each experiment.

Figure 2.1: Spark Plasma Sintering equipment (model 515S) used in this work.

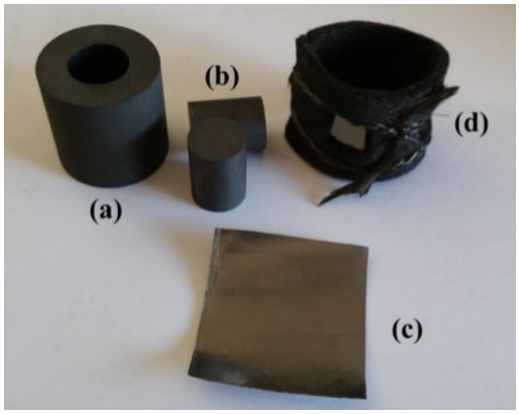

Figure 2.2: a) graphite die, b) plungers, c) foil, and d) felt used for SPS experiments.

Bulk BGMS10-derived samples were prepared at different dwell temperature conditions

(T_D), in the range 650-950°C, whereas holding time (t_D) and mechanical pressure (P) were kept constant equal to 2 min and 16 MPa, respectively. As reported in Figure 2.3, the temperature was first increased at a rate of 50°C/min from the ambient value to 100°C below T_D. The heating rate was then lowered (10°C/min), to minimize overshooting problems, until the dwell temperature was achieved. The sample was isothermally heated for 2 min at T_D, then the temperature was decreased at a rate of 50°C/min down to 300°C, followed by a natural cooling step. For the sake of reproducibility, each experimental run was replicated at least twice.

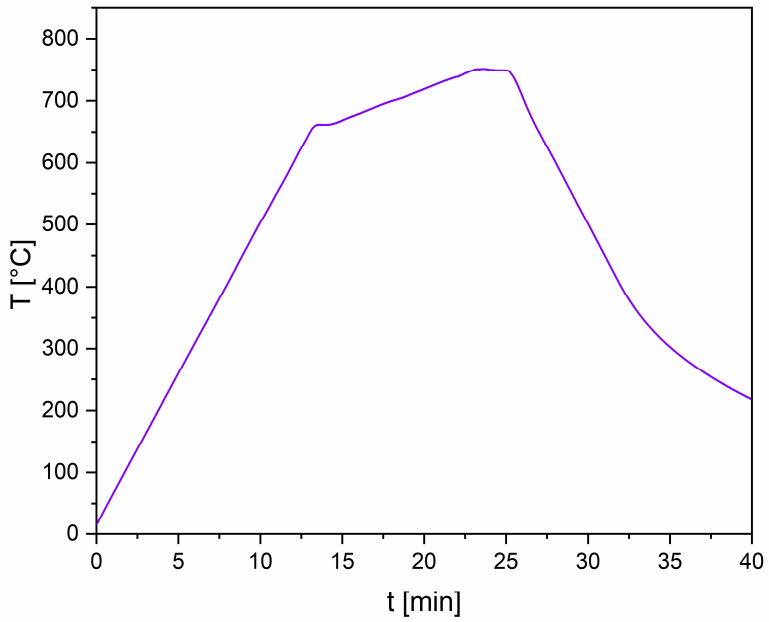

Figure 2.3: Example of temperature profiles adopted during SPS experiments for the consolidation of BGMS10 powders ($T_D = 750$°C).

The densities of polished sintered samples were determined by the Archimedes' method using ethanol as immersing medium.

The amorphous or crystalline nature of the differently SPSed products was first assessed by X-Ray Diffraction (XRD) analysis (Smart Lab rotating anode diffractometer) using a Cu Kα radiation under the following experimental conditions: Range: 10-130°; Step: 0.05°; dwell time:

10 sec. Phases, their amount (wt.%) and the related structural parameters were determined according to the Rietveld method, using the MAUD program [195].

HR-SEM was also used to examine the microstructure of the sintered specimens, after being chemically etched for time intervals up to 5 min using a 1 vol.% HF solution. High-resolution TEM analysis was performed using a FEI TECNAI 200 operating at 200 kV working with a field emission electron gun.

Mechanical properties were evaluated by micro-indentation using an Open Platform equipment (CSM Instruments, Peseux, Switzerland), with a Vickers indenter tip. Such technique was used to determine both Young's modulus and hardness of the products. The SPSed samples, sintered at 750 °C, 850 °C, and 950 °C, were embedded into epoxy resin and then lapped and polished. A maximum load of 100 mN was applied for the indentation process, with a load/unload rate of 200 mN/min. Fifteen measurements were recorded for each SPSed sample, where the load-penetration depth curve was automatically acquired. The Young's modulus was calculated from the unloading part of the load-depth curve according to [196].

The in vitro bioactivity of samples was investigated by soaking them in Simulated Body Fluid, according to the protocol developed by Kokubo [164]. Samples sintered at different temperatures were immersed in SBF solution, being the latter one and the corresponding volume used during the test prepared and calculated according to the aforementioned protocol. The SPSed products were soaked in SBF for 3 and 7 days and stored at 37 °C in an incubator, refreshing the solution every 2 days. After each soaking time, samples were carefully washed with distilled water and then left to dry at room temperature. Bioactivity was then evaluated as the ability of the material to form a surface layer of hydroxycarbonate apatite (HCA), and/or of a silica-gel film (from which HCA nucleates, once in contact with SBF). HCA and silica-gel formation on the surface of sintered samples was detected by means of ESEM (Quanta 2000, FEI Co., Eindhoven, The Netherlands). Moreover, the possible apatite precipitation on the surface of the samples was investigated through micro-Raman spectroscopy using a Jobin-Yvon Raman Microscope Spectrometer (HORIBA Jobin-Yvon S.A.S., Villeneuve d'Ascq, France) with a diode

laser source emitting at 632.8 nm (output power: 20 mW at the sample). A spectra collection of 30 acquisitions of 20 s each was employed.

2.3 Results and discussion

2.3.1 Powders characterization

Particles size measurement of BGMS10 powder by laser light scattering provided the values reported in Table 2.1:

Parameter	Value [μm]
d_{10}	0.83 ± 0.01
d_{50}	4.9 ± 0.1
d_{90}	26.2 ± 0.3
d_{av}	9.4 ± 0.1

Table 2.1: Particle size of BGMS10 powder resulting from laser light scattering.

These data are consistent with SEM observation (Figure 2.4) which indicates that these powders consist of irregular particles with size less than about 25 μm, most of them being aggregates of few micrometres-sized grains.

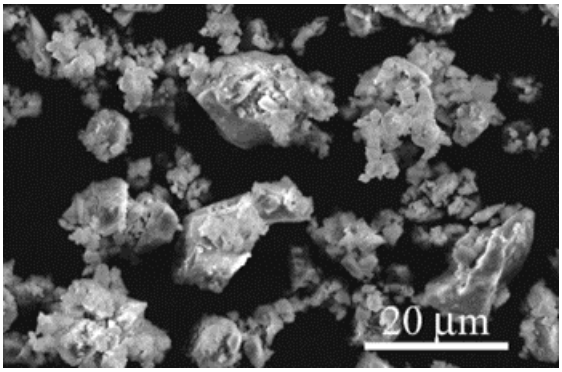

Figure 2.4: SEM images of the BGMS10 powders investigated in the present work.

Three representative DTA curves obtained at different heating rates are plotted in Figure 2.5 a). The characteristic endothermic peak corresponding to the glass transition clearly shifts from about 880 to 920 °C as the test was conducted at progressively higher heating rates.

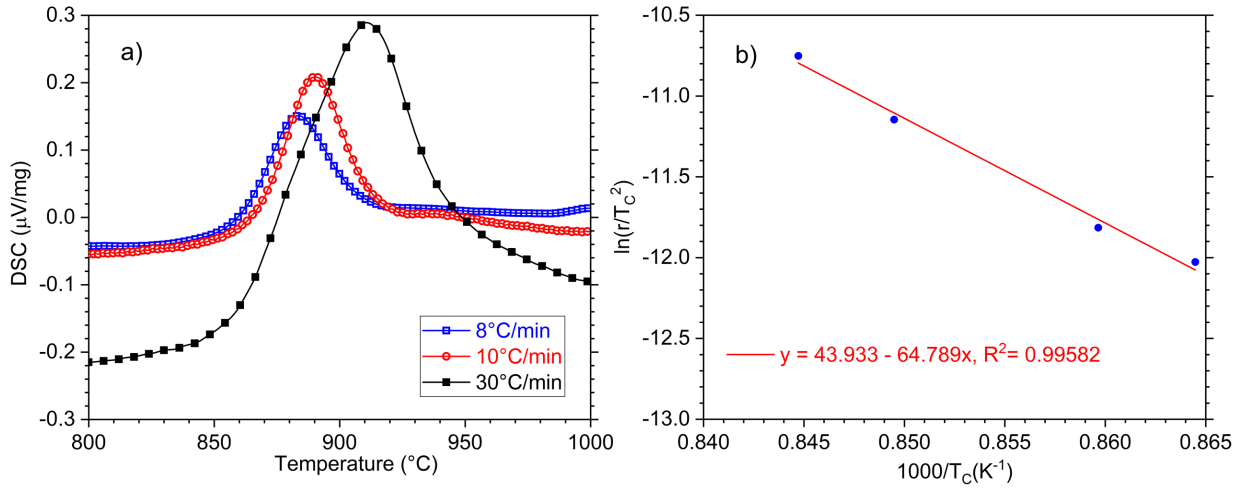

Figure 2.5: DTA curves (a) of BGMS10 powders at different heating rates and (b) corresponding Kissinger plot.

As shown in Figure 2.5 b), by plotting $ln\left(\frac{r}{T_p^2}\right)$ as a function of $\frac{1}{T_p}$ (Kissinger plot) a straight line is obtained, according to Equation 2.1.

The estimated effective activation energy of the crystallization process is 538.9 kJ/mol. The latter value is significantly higher with respect to the range of E_c data reported in the literature for commercial Bioglass® (230-338 kJ/mol) and S53P4 (283-311 kJ/mol) glasses, also determined using the Kissinger method [194]. On the other hand, the E_c value calculated in this work for BGMS10 is very close to that (520.8 kJ/mol) obtained for the BG_ Ca_MIX bioactive glass [138].

The result above provides a further indication of the markedly lower tendency to crystallize of innovative BGMS10 and BG_ Ca_MIX formulations compared to standard bioactive glasses.

2.3.2 Bulk samples

2.3.2.1 Fabrication and structural characterization

As shown in Figure 2.6 a), initial BGMS10 powders are white-coloured. Their consolidation carried out by SPS at different holding temperatures has led to the bulk samples reported in Figure 2.6 b)-g). Sintered samples processed at 650°C (Figure 2.6 b)) maintained the original powder's colour. Conversely, as the holding temperature is increased from 700 to 850 °C, the resulting products progressively change their colour from light to dark grey (Figure 2.6 c)-e)), respectively. Surprisingly, a further increase of the T_D value turns progressively the colour of the sample to white (Figure 2.6 f) and g)).

This outcome might be correlated with the corresponding structural/compositional changes of the glass powders undergoing SPS, as discussed afterwards.

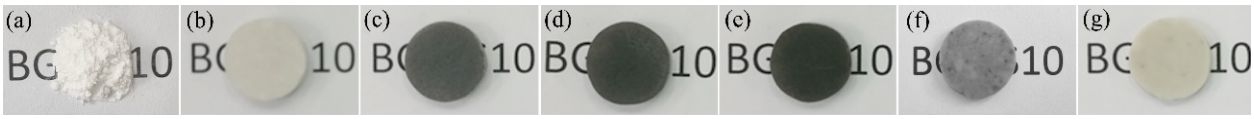

Figure 2.6: Images of **(a)** initial BGMS10 powder and the corresponding bulk samples produced by SPS at different T_D values: **(b)** 650°C, **(c)** 700°C, **(d)** 750°C, **(e)** 850°C, **(f)** 900°C, and **(g)** 950°C.

The effect of the dwell temperature on the density of SPS products is shown in Figure 2.7. The sample obtained at T_D=650°C displays an average relative density equal to about 95 %. Powder densification is progressively improved as the sintering temperature is augmented to 750°C. The absolute density value achieved in the latter case is 2.96 g/cm^3, very close to the theoretical value (2.97 g/cm^3). On the other hand, average relative densities of samples obtained at temperatures above 750°C become progressively lower, albeit their values remain very high, i.e. 99.3% (850°C), 99.0 % (900°C) and 98.6% (950°C).

Structural and compositional characteristics of SPS samples produced in the T_D range 750-950°C are first investigated by XRD analysis (Figure 2.8). The pattern referred to the system prepared at 750 °C presents a typical shape of an amorphous glass. The phase,

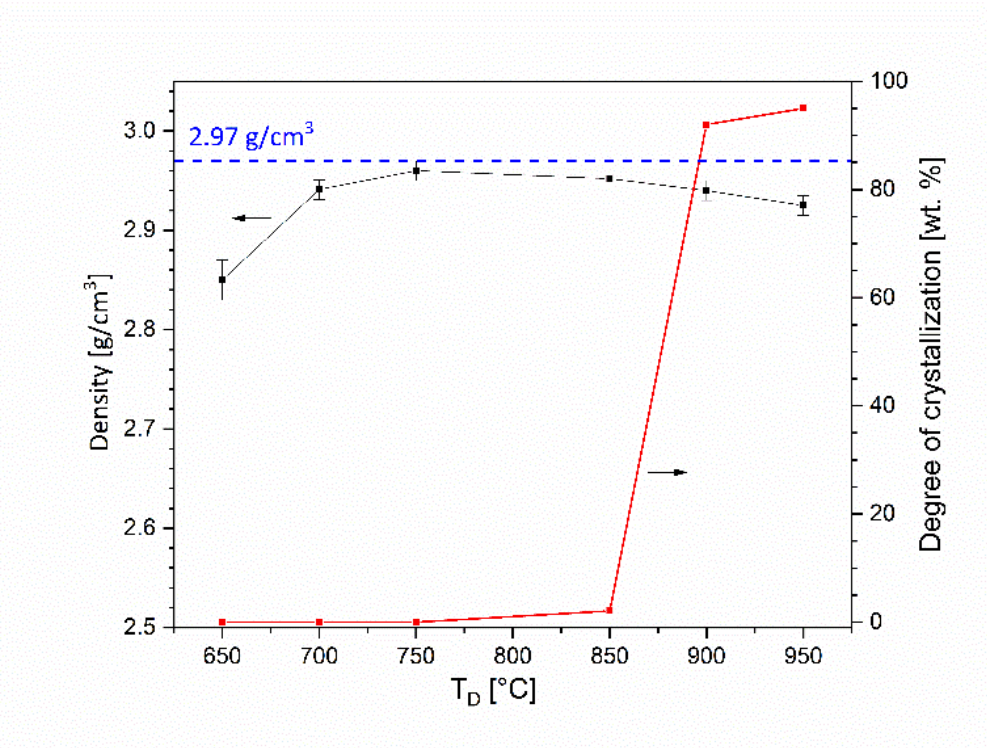

Figure 2.7: Influence of the holding temperature T_D on the density and degree of crystallization of BGMS10 products obtained by SPS (t_D=2 min, P=16 MPa).

named $Ca_{1.5}Na_{2.64}Si_9O_3$, has been computed using a pseudo-crystalline structure factor ($Ca_{1.5}Na_{2.64}Si_9O_3$ phase; symmetry: trigonal; space group: $R-3m$; crystallite size: 20Å; microstrain: 0.03) according to the LeBail approach [197].

Figure 2.8 also evidences that the XRD pattern of the sample sintered at 850°C is still characterized by the halo peak ascribable to the amorphous $Ca_{1.5}Na_{2.64}Si_9O_3$. However, differently from the previous sample, some small Bragg reflections are also observed. The latter ones were then fitted with the two polymorphs of $CaSiO_3$ ($\alpha-CaSiO_3$, Pseudowollastonite, monoclinic $C2/c$ and $\beta-CaSiO_3$, Wollastonite, triclinic $P-1$), whose amount was estimated to be approximately equal to 1.1 and 1.0 wt.%, respectively (Table 2.2). This aspect was further investigated by TEM. The high-magnification TEM image presented in Figure 2.9 a) suggests that the system prepared at 850°C consists of crystalline grains dispersed into an amorphous matrix.

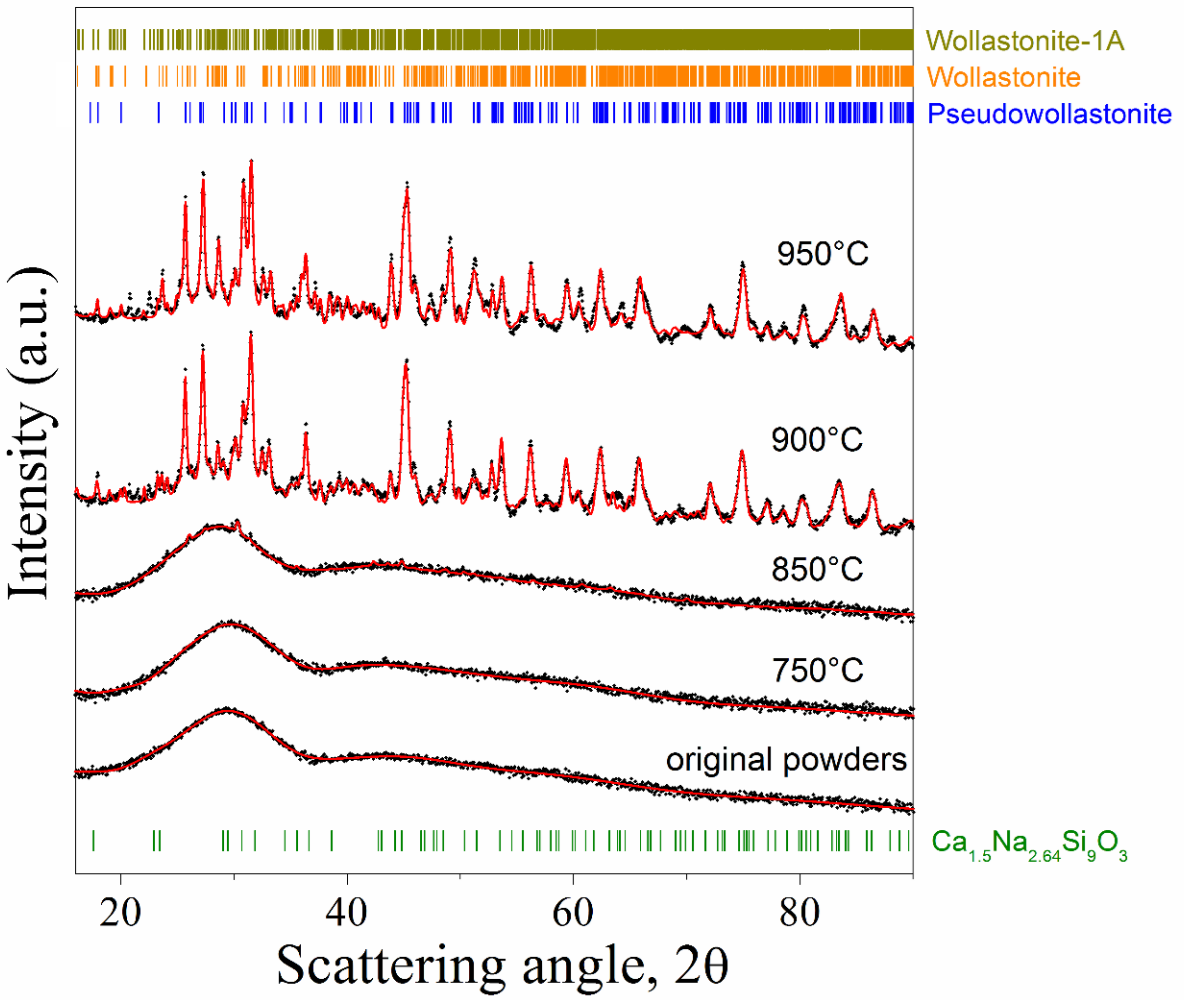

Figure 2.8: XRD patterns (log scale) of BGMS10 samples sintered at various temperatures. Original glass powder data are also shown for the sake of comparison. Black dots are experimental data, the red line is the calculated fit. The bar sequence marks the expected peak position from the values of lattice parameters and space group of the crystallographic phases.

On the other hand, as the temperature was increased to 950 °C, the microstructure of the system, shown in Figure 2.9 b), is characterized by well-defined crystalline grains (average dimension of 900 Å) surrounded by a thin layer of amorphous nature. The Rietveld analysis of the sample prepared at 950°C revealed that it basically consists of two crystalline phases, namely $\alpha - CaSiO_3$ and $\beta - CaSiO_3$ (Figure 2.8). A third phase is represented by the halo of the amorphous glass, apparently still present at this temperature, estimated to be ≈5 wt.% (Table 2.2). There are some additional minor peaks at low diffraction angles, which can be

associated to a second polymorph of wollastonite $1-A$ (triclinic, s.g. $P-1$), which displays an enlarged cell volume (Table 2.2).

Such peculiarity is likely due to the fact that, besides Ca, O and Si, other elements (i.e. Mg and Sr) are also present in the cell of this calcium silicate polymorph. Wollastonite 1-A is also detected by XRD analysis in the sample sintered at T_D=900°C (Figure 2.8 and Table 2.2). The main phases detected at the last temperature condition are still the monoclinic polymorph pseudowollastonite and regular wollastonite, while the residual content of amorphous phase (8 wt.%) is, as expected, in between with respect to those ones of samples sintered at 850°C and 950°C. Although all microstructural parameters and relative amount of each phase estimated by Rietveld method are reported in Table 2.2, the related data are also plotted in Figure 2.7, to better follow the evolution of the degree of crystallization with sintering temperature.

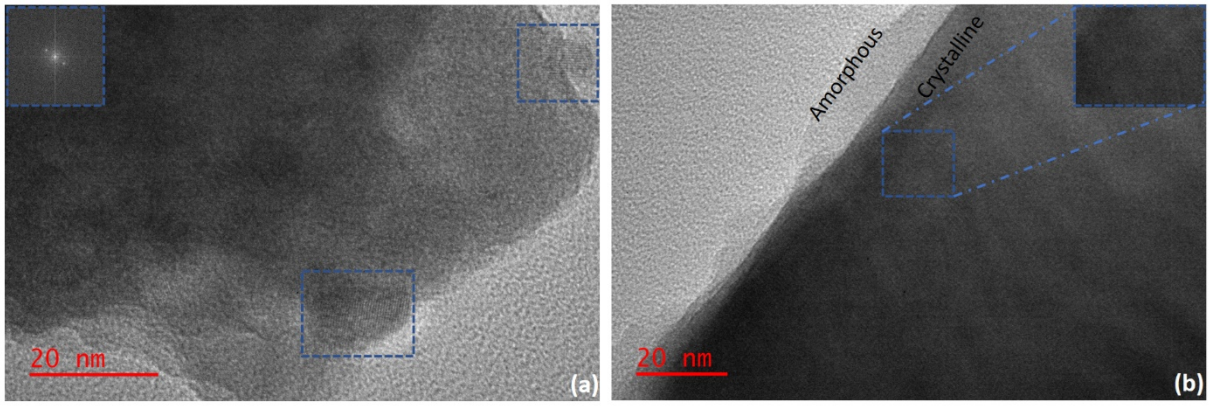

Figure 2.9: Representative HR-TEM images of the BGMS10 samples obtained by SPS at (a) 850 °C and (b) 950 °C. Fast Fourier transform (FFT) of the crystalline grains (marked by blue squares), is displayed in the inset of the left side image. A zoom of crystalline plane is marked by blue square in the right-side image.

In what follows some considerations regarding the changes in disks color depending on the sintering temperature (Figure 2.6) are drawn. The blackening phenomenon is observed to progressively occur if the T_D value is increased in the range 700-850°C, when the resulting products are completely or nearly full amorphous. The obtainment of dark samples by SPS is not so unusual, particularly when considering oxide-based ceramics. This aspect is generally associated either to carbon contamination from the graphite tools surrounding the sample

850 °C									
Phase	**%**	**a**(Å)	**b**(Å)	**c**(Å)	**Angle**(°)	**Space Group**	**Cryst.size** (Å)	**R.m.s. Strain**	**V**(Å^3)
Pseudowollastonite	1.1	6.8567	12.7311	20.0917	β**=90.4**	Mono (C2/c)	650	$9.7 \cdot 10^{-4}$	1753.82
Wollastonite	1.0	7.5454	7.0578	7.1523	α**=89.4** β**=95.6** γ**=103.2**	Triclinic (P-1)	904	$6.0 \cdot 10^{-4}$	369.03
$Ca_{1.5}Na_{2.64}Si_9O_3$	97.9	-	-	-	-	Trigonal (R-3m)	-	-	-
900 °C									
Phase	**%**	**a**(Å)	**b**(Å)	**c**(Å)	**Angle**(°)	**Space Group**	**Cryst.size** (Å)	**R.m.s. Strain**	**V**(Å^3)
Pseudowollastonite	71	6.9345	12.0191	19.7805	β**=90.3**	Mono (C2/c)	780	$1.4 \cdot 10^{-3}$	1644.82
Wollastonite	13	7.8236	7.09035	7.2163	α**=89.2** β**=95.9** γ**=103.1**	Triclinic (P-1)	959	$2.7 \cdot 10^{-3}$	385.03
Wollastonite-1A	8	10.1139	11.0631	7.3142	α**=99.8** β**=101.1** γ**=83.3**	Triclinic (P-1)	892	$7.0 \cdot 10^{-4}$	788.38
$Ca_{1.5}Na_{2.64}Si_9O_3$	8	-	-	-	-	Trigonal (R-3m)	-	-	-
950 °C									
Phase	**%**	**a**(Å)	**b**(Å)	**c**(Å)	**Angle**(°)	**Space Group**	**Cryst.size** (Å)	**R.m.s. Strain**	**V**(Å^3)
Pseudowollastonite	59	6.9269	12.0051	19.7794	β**=90**	Mono (C2/c)	887	$1.5 \cdot 10^{-3}$	1644.82
Wollastonite	32	7.8557	7.0647	7.1579	α**=89.5** β**=95.6** γ**=103.1**	Triclinic (P-1)	968	$1.7 \cdot 10^{-3}$	385.03
Wollastonite-1A	4	10.0815	11.1595	7.2917	α**=99.8** β**=100.9** γ**=83.7**	Triclinic (P-1)	873	$9.0 \cdot 10^{-4}$	791.24
$Ca_{1.5}Na_{2.64}Si_9O_3$	5	-	-	-	-	Trigonal (R-3m)	-	-	-

Table 2.2: Microstructural parameters and amount of each phase present on the SPS product obtained at 850, 900 and 950°C, as estimated by the Rietveld analysis performed on the related XRD pattern (Figure 2.8).

undergoing sintering or to oxygen vacancies generated because of the reducing environment encountered during the sintering process. For instance, oxygen deficiency was the reason provided to explain the dark colour of yttria [198] and barium titanate based [199] ceramics obtained by SPS. The latter motivation is probably also valid to justify the behaviour observed in the present study, since the incorporation of carbon from the graphite die/plungers/foils is expected to enhance as the temperature is increased. In contrast, as shown in Figure 2.6, the sample obtained at 900°C becomes light-grey coloured, with few small dark spots in it, whereas that one sintered at 950°C is completely white. The corresponding increase of the crystallization degree (Figure 2.7 and Table 2.2) supports the hypothesis that samples whitening is likely due to the occurrence of devitrification phenomena from the parent glass. Nevertheless, supplementary investigations are needed to draw final conclusions on this matter.
Bulk samples have also been examined by SEM after being chemically etched. Three representative micrographs of sintered products obtained at 750, 850, and 950 °C are shown in Figure 2.10 a)-c), respectively. The resulting microstructures are quite different, with the presence of very small grains (up to 100 nm sized) observable only for the case of T_D=950°C. No further definite features could be deduced by this analysis.

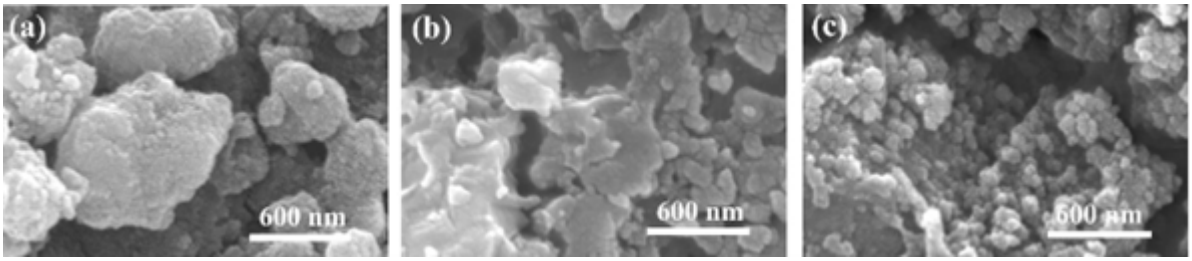

Figure 2.10: SEM micrographs of chemically etched dense BGMS10 products obtained by SPS (2 min/16MPa) at different sintering temperatures: (a) 750°C, (b) 850°C, and (c) 950°C.

The fact that, based on XRD analysis and TEM observation, devitrification phenomena already occurred in samples produced by SPS at T_D=850°C, while the crystallization temperature of BGMS10 was previously reported to be relatively higher, i.e. 932°C [141], can be explained as follows. As reported in section 2.2, during SPS, the temperature is measured using a thermocouple inserted into a small orifice drilled at the centre of the lateral die surface.

Due to the unavoidable presence of thermal gradients across the radial direction, glass powders are very likely exposed to temperatures higher than the prescribed T_D value. Therefore, it is not surprising that the incipient crystallization was observed in SPS samples produced at T_D=850°C.

2.3.2.2 Mechanical properties

The mechanical properties of the SPSed samples produced at different temperatures were evaluated by the microindentation technique. The obtained results are reported in Table 2.3.

T_D [°C]	Hardness [Vickers]	Young's modulus [GPa]
750	672 ± 17	90.9 ± 3.4
850	719 ± 29	92.8 ± 2.2
950	619 ± 47	98.4 ± 5.9

Table 2.3: Mechanical properties of the BGMS10 samples produced by SPS at different temperatures.

It is worth noting that an increase of the sintering temperature corresponds to progressively higher values of Young's modulus. This can be ascribed to the beneficial effect of crystallization achieved in samples sintered at 850 and 950°C. This is consistent with the fact that, usually, crystalline materials are mechanically stronger than their amorphous counterparts [200]. Accordingly, in the present study, XRD analysis evidenced that the BGMS10 product sintered at 750°C was fully amorphous, while samples obtained at 850°C and 950°C were partially and nearly fully crystallized, respectively (Figure 2.7 and Figure 2.8, Table 2.2). In particular, the increase of Young's modulus from 750°C to 950°C can be justified by the presence of wollastonite, which is known to display good mechanical properties [201].

With regard to the hardness data, the sample processed at 950°C has a lower value compared to the other two competitors. A similar behaviour was also observed by Desogus et al. [138] when investigating the BG_ Ca_MIX system and can be explained as follows. Despite the fact that crystallization is expected to improve mechanical properties, the development of crystalline phases also implies changes in specific volumes, which may be responsible for a decrease in compactness and relative density. As a matter of fact, the density values of BGMS10 samples sintered at 750 and 850°C were very close to the theoretical value (99.7 and 99.3 %, respectively). On the other hand, samples sintered at 950°C were only 98.6% dense. So, the negative effect of such density reduction counterbalances the positive effect of the crystallization occurrence.

It is also worth noting that the values of elastic modulus of BGMS10 samples are higher compared to those obtained with 45S5, both sintered using the same SPS technique [138]. The improved mechanical properties of BGMS10 could be explained by the beneficial contribution provided by MgO and SrO, because of their high metal-oxygen bond strength. This confirms that their presence in the glass favours not only biological properties but also mechanical ones. With regard to BG_ Ca_MIX SPSed samples investigated in a previous work [138], the Young's modulus of BGMS10 specimens is relatively higher when amorphous products are compared, i.e. about 91 instead of 65 GPa. On the other hand, the opposite situation is encountered when considering crystallized samples. Indeed, this parameter equals to approximately 98.4 GPa for the BGMS10 product obtained in the present work at 950°C, whereas its average value for mainly crystallized BG_ Ca_MIX specimens consolidated at 850°C was about 120 GPa [138].

Based on the results obtained in this study, it is possible to state that the high consolidation levels obtained by SPS and the beneficial contribution of MgO and SrO, provide good mechanical properties to the resulting BGMS10 glass products.

2.3.2.3 In-vitro characterization

ESEM analyses were performed on samples sintered at 750, 850 and 950°C after 3 and 7 days of immersion in SBF. Figure 2.11 reports the related micrographs. According to Kokubo et al. [164], it is possible to preliminarily evaluate the bone-bonding ability of a given material by studying the precipitation of HCA on the sample after being soaked in SBF, an acellular solution whose ion concentration is similar to that of the human blood plasma. In fact, as already explained in Chapter 1, bioactive glasses, once implanted in the body, bond to bone via the formation of a superficial HCA layer, which mimics the mineral phase of the bone. In this context, the tendency to crystallize of bioactive glasses during thermal treatments is among the reasons that limit the use of these materials, as crystallization is reported to both slow down sintering phenomena during powder consolidation and inhibit the in-vitro and in-vivo bioactivity of the material [202, 203]. In addition, the partial devitrification of the glass can lead to the instability of the implant once placed in the body, since the residual amorphous phase is typically more reactive and is preferentially degraded by physiological fluids [119]. From this point of view, the novel BGMS10 is less prone to crystallize, so that it looks particularly promising. In particular, regarding the in-vitro assessment of bioactivity, samples processed by SPS at lower T_D values, which remained almost amorphous, are expected to be more reactive in SBF than those partly (or widely) crystallized after sintering. ESEM analysis results, shown in Figure 2.11, were substantially consistent with this scenario. In fact, the surfaces of the SPSed samples obtained at 750°C (Figure 2.11 a and d) are characterized by several cracks, which reveal the formation and the subsequent drying of a hydrated silica gel layer. It should be stressed that, as described in Chapter 1, the formation of such layer is among the steps which lead to the nucleation of HCA on the glass surface, as reported in the literature [164]. After 7 days in SBF, the delamination of the silica gel film is even more pronounced (Figure 2.11 d). Moreover, it is possible to observe the presence of phosphorus and calcium rich precipitates, which locally formed on the silica gel film.

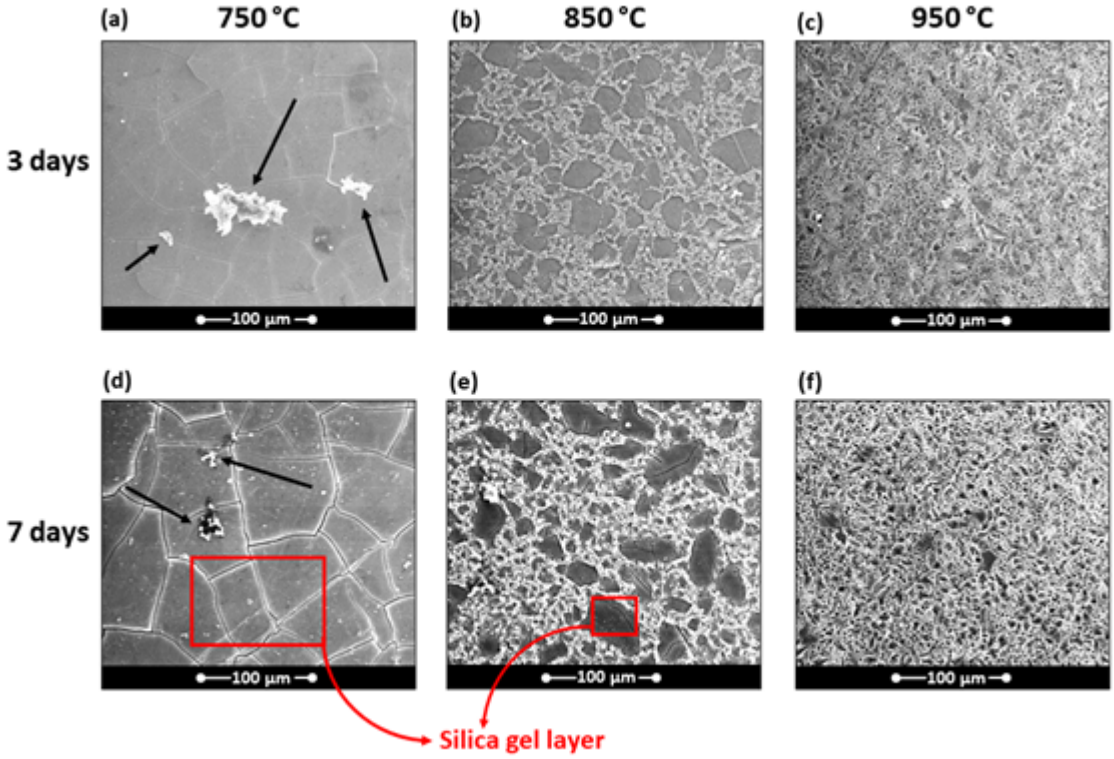

Figure 2.11: ESEM micrographs of the BGMS10 samples, sintered by SPS at different temperatures, after immersion in SBF for 3 and 7 days. Phosphorus and calcium rich precipitates are indicated by black arrows in a) and d).

The precipitation of such aggregates is a further step towards the formation of an HCA layer. Conversely, the observation of the samples sintered at 950°C (Figure 2.11 c and f), which are widely crystallized, did not reveal neither the presence of the gel, nor that of calcium and phosphorus rich precipitates. Finally, regarding the partially crystallized samples obtained at 850°C (Figure 2.11 b) and e), it is possible to note that the formation of silica gel mainly occurs on the residual glassy areas, which appear darker in the micrographs of Figure 2.11.

The nature of the calcium phosphate precipitates observed on the silica gel layer was further investigated by means of Raman spectroscopy. In fact, the possible precipitation of apatite can be easily confirmed by this technique, thanks to the high intensity of the Raman peaks associated to the P-O vibration modes. In addition, since the in-vitro grown apatite is usually carbonated (HCA), Raman spectroscopy can be used to confirm the presence of carbon-

ate groups, as it is sensitive to the C-O vibrational modes. Figure 2.12 shows a Raman spectrum acquired on the phosphorus and calcium rich precipitates found after 7 days in SBF on the samples sintered at 750°C. This analysis reveals that the composition of such precipitates evolves to tend to that one of HCA. To support such statement, some of the typical Raman peaks of the carbonated apatite, which arise from phosphate and carbonate ions, can be clearly identified in Figure 2.12. Moreover, besides the very intense peak found at about $960\,c\,m^{-1}$, which can be ascribed to the symmetric stretching mode ν_1 of the $(PO_4)^{3-}$ group, the other one revealed at $\approx 430\,c\,m^{-1}$ is related to the ν_2 bending mode of the same group. An additional peak emerges from the background between $\approx 550\,c\,m^{-1}$ and $\approx 650\,c\,m^{-1}$. Within this range, it is reported in the literature the presence, for apatite, of a peak ($\approx 600\,c\,m^{-1}$) associated to the ν_4 bending mode of the $(PO_4)^{3-}$ group [204, 205]. Finally, the spectrum shown in Figure 2.12 reveals a peak at about $1070\,c\,m^{-1}$, which can be attributed to the CO_3 groups (symmetric stretching mode ν_1), thus confirming the carbonated nature of the forming apatite [206, 207]. Based on these observations, one should expect an improved biological responsiveness of samples sintered at 750°C, i.e. the ones with the highest reactivity in vitro.

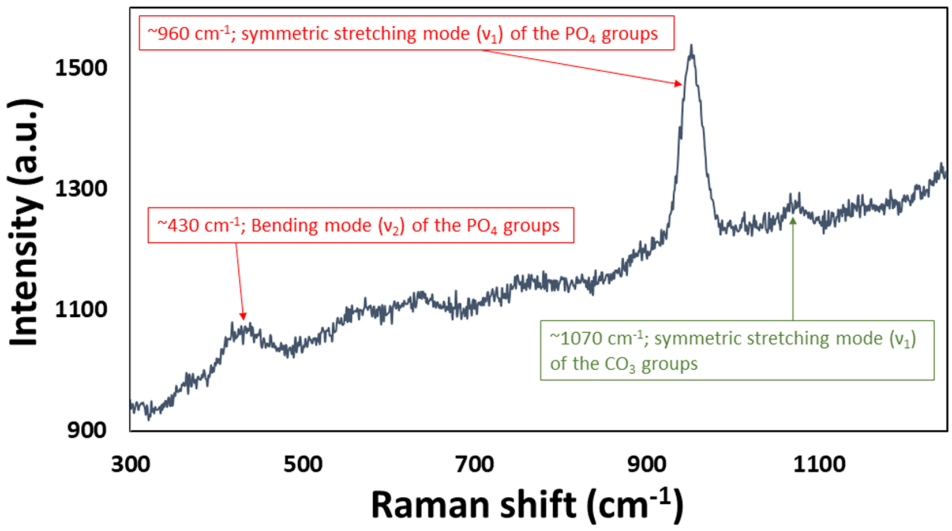

Figure 2.12: Raman spectrum acquired on the phosphorus and calcium rich precipitates which formed on the SPSed samples at 750 °C after 7 days in SBF.

It is apparent that this study represents a first step towards the validation of BGMS10 formulation for potential clinical utilization. Reliable cellular tests should be also carried out to better evaluate the biological response of these materials. In addition, experiments using porous scaffolds, more likely desirable for practical applications, should be also taken into account in future investigations. Also, to expand the possible applications of BGMS10 formulation, suitable methods for the production of bioactive glass coatings (e.g. on metallic prosthesis) should be evaluated [208].

Chapter 3

Development of novel Apatite-BGMS10 composites

3.1 Introduction

It is well recognized that the availability of innovative bioceramics capable to stimulate the repair of biological tissues represents a current need in regenerative medicine [57, 82, 209, 210]. To this aim, in particular for the treatment of bone defects, a useful contribution could derive by the combination of HA with BG with suitable composition. Indeed, even though HA is the most widely exploited ceramic for orthopaedic applications, it displays modest mechanical performance as well as it reacts and interacts rather slowly with biological fluids and tissues. Therefore, its biodegradability and osteoinductivity properties are not satisfying for regenerating tissues at the required rate. The latter characteristics could be improved when HA is coupled with bioactive glasses, which are known to bond tissue to bone more rapidly than other bioceramics [119, 177, 182, 202]. The higher reactivity of such materials, deriving from their intrinsic amorphous nature, is expected to foster both the bioactivity and the biological responsiveness of the resulting composite material. Consequently, the growth rate of the new natural tissue is enhanced. The use of glasses can be further exploited to introduce specific

ions of biological interest (strontium, magnesium, or fluorine, etc.) into the HA lattice, in order to mimic the composition of the biological apatite, which is characterised by several ion substitutions [35, 211]. Finally, the addition of suitable amounts of BG also facilitates the consolidation of HA powders, so that the sintering temperatures required to obtain bulk products are correspondingly milder.

Accordingly, several investigations reported in the literature have been focused on the fabrication and characterization of HA-BG composites [139, 142, 154–156, 189, 207, 212–216]. In most of these studies, the HA and BG are homogeneously distributed across the sample volume [139,142,154–156,207,212,214–216]. However, the possibility to couple these two components to form Functional Graded Materials was also considered [189, 213]. It should be noted that, at least in early studies, the main focus of these works was the mechanical improvement of HA through the addition of calcium phosphate glasses [155], which were preferred due to their chemical similarity to HA. Only subsequently, the opportunity of tuning the HA degradation or improve its bone bonding ability have begun to be explored, together with the production of porous composites (i.e., scaffolds) for bone tissue regeneration and repair. In this context, silicate glasses, in particular 45S5 Bioglass®, were mostly used by virtue of of their high bioactivity. In fact, silicon seems to be essential for bone formation, as it favours the adhesion, proliferation, and differentiation of osteoblast-like cells; silicon supplementation is reported to reduce bone fragility and to increase bone mineral density in several animal models [217,218]. On the other hand, as in the case of pure BGs, heat treatments required to obtain bulk HA/BG composites may lead to the crystallization of the glassy phase to crystallize, thus reducing, or even hampering, both the bioactivity and ion release of the final system [203]. To overcome such drawbacks, different studies have been addressed to the preparation of new silicate BGs less prone to crystallize [141,184]. Such glasses have been used either singularly or in combination with HA to obtain a new generation of ceramic composites, whose biological responsiveness, degradation and mechanical performance can be designed to satisfy specific clinical requirements [207, 214].

In this framework, the effect produced by a ball milling (BM) treatment of the composite powder mixture prior to densification, on the sintering, mechanical and bioactivity behaviour of the resulting bulk material is totally unexplored so far, to the best of the author's knowledge. BM is a well-known and versatile mechanical treatment method able to promote structural transformations in the processing powders, thus permitting the formation of non-equilibrium metastable phases, the synthesis of nanostructured alloys, affecting mixture reactivity, degradation of toxic species, etc. [219]. The produced effects depend on the system, the used equipment (planetary ball mills, attritors, etc.), the adopted operating conditions (rotational speed, processing time, ball to powder or charge ratio, CR, etc.), and it is basically due to the combination of impact and attrition actions involving milling tools and processing powders [219–222]. Apart from HA-BG composite systems, the influence of a mechanical treatment on BG or other bioceramics was also barely studied [222–224]. For instance, Ibrahim et al. [223] employed different milling media made of WC or ZrO_2 for the treatment of BG powders ($Na_2O-CaO-SiO_2-P_2O_5$ system) obtained by melt quenching. Milling was carried out for 18 min using a planetary mill at 500 rpm. Negligeable changes were correspondingly observed on the amorphous silica network glass structure. Similarly, no beneficial effects were noted with an increase of the milling time from 20 to 50 h (planetary ball mill, 300 rpm, CR=10, Argon) when processing $Ti-HA$ composite powders, based on SBF (Simulated Body Fluid) assay and wettability test results conducted on the corresponding sintered samples [225].

Moreover, sol-gel derived bioactive nanomaterials based on the quaternary $MgO-CaO-CuO-SiO_2$ system were ball milled for 6h at different rotational speeds, in the range 300-500 rpm, using a S100 centrifugal ball mill [224]. Bioactivity test results in SBF revealed that apatite formation occurred earlier (after 1 day) when using unmilled powders instead of the milled ones (HA was detected after 3 days). No specific motivation was given by the authors to explain such negative effect of the mechanical treatment on powder bioactivity.

In this Chapter, the effect produced by a ball milling treatment on different compositions of HA-BG composite powders on the densification, mechanical, and in vitro biological be-

haviour is investigated for the very first time in the literature. More specifically, various mixtures consisting of commercial HA and the BGMS10 glass formulation presented in Chapter 2, are ball milled for different time durations. The resulting powders are then consolidated by SPS to provide bulk samples to be characterised. Composition, microstructure, mechanical properties, and the bioactivity behaviour in a SBF solution of the sintered composite products are examined and compared.

3.2 Experimental materials and methods

3.2.1 Powders

Commercial hydroxyapatite (CAPTAL® Hydroxylapatite, Cod. CAPTAL 60-1, Ca/P ratio equal to 1.67, 99% purity, 99% crystallinity) supplied by Plasma Biotal LTD. (UK) was selected as one of the composite constituents. The second one is the lab-made BGMS10 bioactive glass already presented in Chapter 2. The glass has been prepared according to a melt-quenching procedure and subsequently ground to obtain powders with grain size < 63 μm, as described in detail in section 2.2.1 of Chapter 2.

Different ratios of HA/BG powders were mixed to obtain the following three composite formulations:

- 25 wt.% HA and 75 wt.% BGMS10 powder (25HA-75BG)
- 50 wt.% HA and 50 wt.% BGMS10 powder (50HA-50BG)
- 75 wt.% HA and 25 wt.% BGMS10 powder (75HA-25BG)

About 16 g of powder resulting from both HA and BG were mildly mixed in a SPEX 8000 (SPEX CertiPrep, USA) shaker mill, shown in Figure 3.1, using plastic vials and small agate balls (7 mm diam.). The corresponding ball-to-powder weight or charge ratio (CR) was maintained very low, about 0.2. The obtained powders will be considered and referred to as unmilled (t_{BM} = 0 min).

Approximately 2.4 g of the composite mixtures were subsequently mechanically treated, still using the SPEX 8000 device (Figure 3.1), but in agate vial containing two larger agate balls (12 mm diam.) as milling tools, and by setting a CR value equal to 2. The durations of the adopted ball milling treatments were t_{BM}= 30, 60 and 120 min.

Particle size distribution was measured using a laser light scattering analyser (CILAS 1180, France).

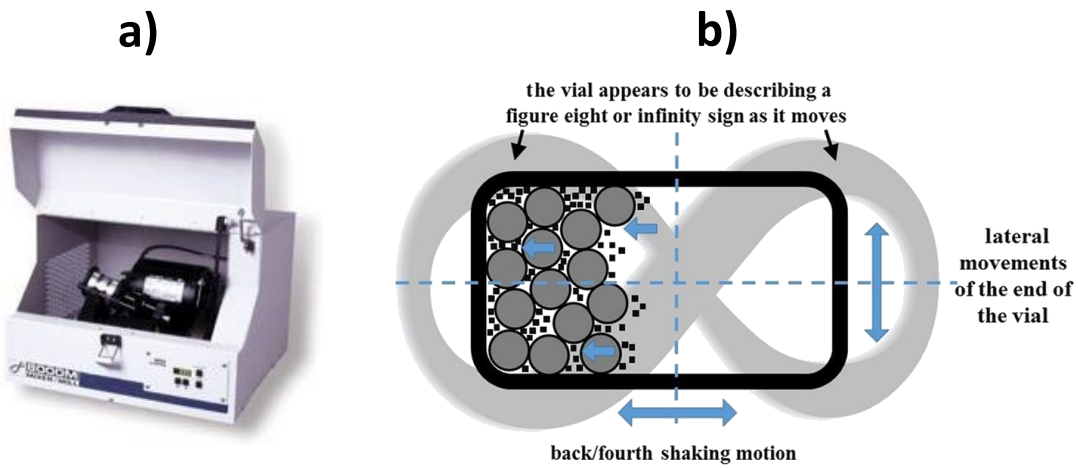

Figure 3.1: a) Ball milling device (SPEX 8000) used in the present study and b) schematical representation of the movement of the vial during the mechanical treatment.

N_2 sorption isotherms were collected with a Sorptomatic 1990 instrument (Fisons Instruments, Milan, Italy) and the corresponding superficial areas were calculated according to the BET method. 800 mg of each sample were placed in a quartz tube and degassed under mild conditions (100 Pa at 180°C for 24 h) to prevent any structural evolution. The dead volume of the quartz tube was evaluated through helium adsorption measurements.

Phases identification and structural characteristics of mixed and milled powders were first investigated by X-ray diffraction analysis (Philips PW 1830, Netherlands) taking advantage of the Rietveld procedure. The acquisition conditions and elaboration software for the Rietveld analysis were the same presented in (Chapter 2).

A FEI TECNAI 200 operating at 200 kV was used for TEM observations. Samples were prepared by dispersing a few milligrams in absolute ethanol using an ultrasonic bath. Finally, one or two drops of the as-obtained suspension were dispersed on a holey carbon supported grid for TEM analysis.

3.2.2 Bulk samples

About 1.56 g of either the unmilled (t_{BM}=0 min) or milled (t_{BM}=30, 60 and 120 min) composite mixtures were placed inside a die cylinder equipped with two plungers both with same spec-

ifications provided in Chapter 2. A graphite foil of 0.13 mm thickness was placed between the powders and the inner walls of die/plungers, as also described in Chapter 2. The die, covered with a 3 mm thick graphite felt, was then inserted in the sintering chamber of the 515S SPS equipment. Temperature was measured using a K-type thermocouple (TC Misure e Controlli S.R.L., Italy).

As reported in Figure 3.2, the temperature was firstly increased at a rate of 50°C/min from the room value to 100°C below the maximum level (T_D). Subsequently, to avoid or attenuate possible overshooting problems, the T_D value was achieved at a lower rate (10°C/min). The sample was isothermally heated for 2 min at T_D, then the temperature was decreased at a rate of 50°C/min down to 300°C, followed by a natural cooling step. As for the applied pressure (P), it was suddenly raised to the maximum value in about 1 min, then maintained constant during the non-isothermal and isothermal heating stages, whereas this parameter was gradually lowered during sample cooling (Figure 3.2).

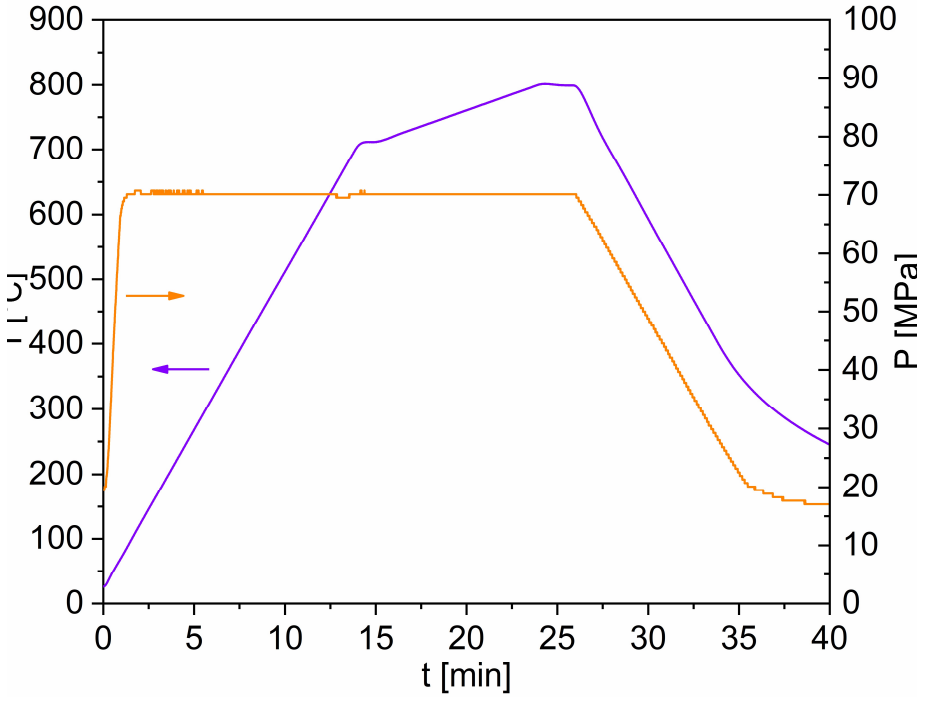

Figure 3.2: Example of temperature and applied pressure profiles adopted during SPS experiments for the consolidation of HA-BGMS10 composite powders (T_D = 800°C, P= 70 MPa).

Bulk composite samples were produced at different dwell temperature and pressure conditions depending on the system composition, in the ranges 750-1200°C and 16-70 MPa, respectively. Before their subsequent characterization, the opposite sides of the sintered specimens were accurately ground/polished using abrasive paper to remove residual impurities from the graphite tools. Cylindrical samples with approximately 14.7 mm diameter and 2.5-3 mm height were finally obtained. For the sake of reproducibility, each experimental condition was replicated at least twice.

The relative density (ρ) of bulk samples was determined by the Archimedes' method. Theoretical densities for the different composites were calculated by means of a rule of mixture [226], using the values of 3.16 and 2.97 g/$c\,m^3$ [227] for HA and BGMS10, respectively. The obtained values are reported in Table 3.1, to which relative densities of the composite samples are referred to.

Composition	Absolute density [$g/c\,m^3$]
0HA-100BG	2.97
25HA-75BG	3.02
50HA-50BG	3.06
75HA-25BG	3.11
100HA-0BG	3.16

Table 3.1: Absolute densities calculated according to the rule of mixture [226]. Data of pure constituents are reported as a reference.

3.2.3 Microstructural characterization and mechanical testing

Scanning electron microscopy (ESEM - Quanta 2000, FEI Co., Eindhoven, The Netherlands) was employed to investigate the microstructure of the sintered disks. Additional studies were also conducted using a high-resolution scanning electron microscopy (HR-SEM, mod. S4000, Hitachi, Tokyo, Japan) equipped with a UltraDry EDS detector (Thermo Fisher Scientific, Waltham, MA, USA).

The mechanical properties of the samples, embedded into resin and mirror polished, were evaluated by micro-indentation technique. Open Platform equipment, with Vickers indenter

tip, (CSM Instruments, Peseux, Switzerland) was employed to measure both the hardness and the Young's modulus of the composites. A load of 500 mN was used during the indentation process, with 1.5 N/min as loading/unloading rate (loading time at maximum load: 15 s). At least fifteen measurements for each sintered disk were obtained. For each indentation, the load-penetration depth curve was automatically recorded. The elastic modulus was then calculated from the indentation load-unloading curves, according to the Oliver and Pharr method [196].

3.2.4 In vitro bioactivity tests

The bioactivity of the obtained composites was investigated by immersing them in SBF, according to the Kokubo protocol [164]. Before using it, the pH of the solution was adjusted to 7.4, as recommended [164]. Each sample was soaked in 25 ml of SBF and stored in plastic flasks at 37°C. The solution was renewed every 48 h. The samples were removed from SBF after 7 and 14 days, properly washed with distilled water and dried at room temperature for 24 h. The possible precipitation of HA on the samples' surface was evaluated by means of both ESEM and micro-Raman spectroscopy. The ESEM was equipped with an Energy Dispersive X-ray microanalysis (INCA, Oxford Instruments, U.K.) and used in low-vacuum conditions, i.e. ≈ 0.5 Torr. Raman spectra were acquired by using a LabRAM HR Evolution spectrometer (Horiba, France) with a diode laser source emitting at 632.8 nm (output power: 21 mW at the sample). Photons scattered by each sample were dispersed by a 1800 lines/mm grating monochromator and then collected by on a CCD camera (a 100x objective was employed as collection optic). A spectra collection setup of ten acquisitions, each of them taking 30 s, was used.

3.3 Results and discussion

3.3.1 Composite powders characterization

The effect produced by the ball milling treatment on the particle size of various HA-BGMS10 the mixtures can be deduced from Figure 3.3. The corresponding d_{10}, d_{50}, d_{90}, and d_{43} parameters are reported in Table 3.2.

From the obtained results, it is possible to state that the BM treatment affects differently the processing powders, depending on the relative amount of each constituent.

Specifically, when considering the 25HA-75BG system (Figure 3.3 a and b) three main classes of particles, corresponding to 1-1.1 μm, 6-7 μm, and approximately 20 μm size can be identified in the unmilled powders (black lines).

A mechanical treatment of 30 min duration produced a decrease of the q3 curve corresponding to the 1-1.1 μm sized particles and, simultaneously, an increase of that of the class at 6-7 μm. This finding can be associated to the occurrence of agglomeration phenomena between the processing powders. However, such behaviour was observed to reverse when the BM time is prolonged to 60 (blue curves) and 120 min (green curves). This outcome indicates that, when the milling time exceeds 30 min, comminution takes place to generate finer particles. All the described changes did not result in a significant variation of the average size d_{43} (Table 3.2).

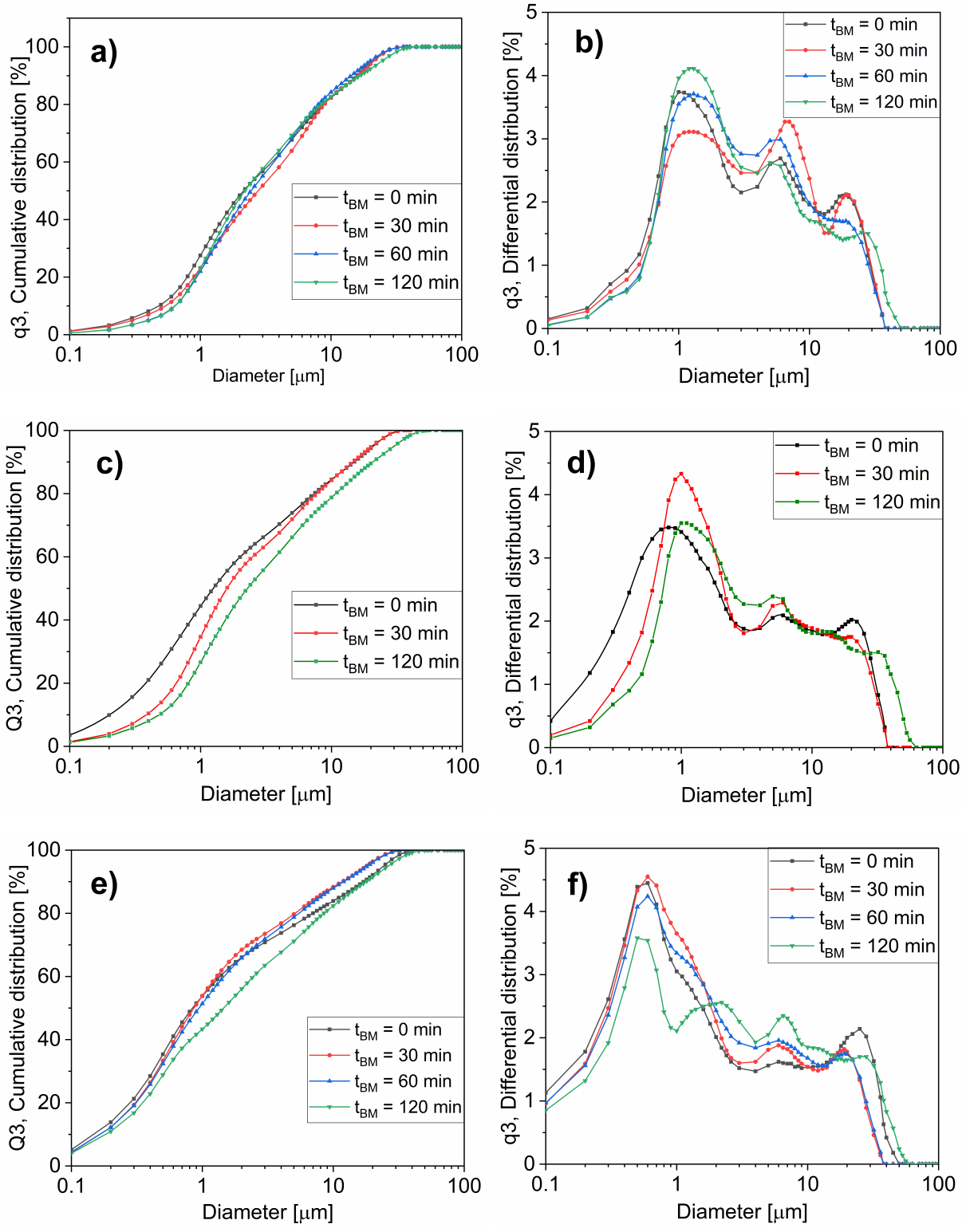

Figure 3.3: Particles size distribution (cumulative and differential curves) of unmilled and milled HA-BGMS10 composite powders: (a)-(b) 25HA-75BG, (c)-(d) 50HA-50BG, (e)-(f) 75HA-25BG.

Considering 50HA-50BG system, both cumulative and differential curves evidence that particles progressively increase their size during milling, to indicate the occurrence of powder agglomeration phenomena. It is likely that the softer HA particles incorporate the glass ones. In addition, the results of this analysis suggest that, when the mechanical treatment is conducted up to 30 min, most of the changes are confined to the lower range of particles size ($< 2.5\ \mu m$). In particular, the maximum value of the q3 curve for milled powders at about 0.8 μm, which represents the higher percentage of particles at that size, is shifted to higher values ($> 1\ \mu m$) and its intensity markedly increases. On the other hand, only small changes in the cumulative and differential curves, compared to the unmilled ($t_{BM} = 0$ min) mixture, can be observed when considering the larger particles size range. Moreover, the measured average size (d_{43}=4.6 μm) did not vary compared to that of untreated powders (Table 3.2). In contrast, when the milling treatment is prolonged to 120 min, powder agglomeration leads to the formation of coarser particles, as manifested by the shifting of both Q3 and q3 curves on the right side as well as by the decreased intensity of the q3 curve maximum at about 1 μm (finer class of particles).

Composition	$\mathbf{t_{BM}}$**[min]**	$\mathbf{d_{10}}$ [μm]	$\mathbf{d_{50}}$ [μm]	$\mathbf{d_{90}}$ [μm]	$\mathbf{d_{43}}$ [μm]
25HA-75BG	0	0.48 ± 0.06	2.15 ± 0.1	16.1 ± 0.5	5.3 ± 0.2
	30	0.51 ± 0.08	2.78 ± 0.07	17 ± 1	5.8 ± 0.4
	60	0.63 ± 0.02	2.47 ± 0.1	14 ± 2	5.1 ± 0.6
	120	0.54 ± 0.01	1.8 ± 0.1	13 ± 3	4.5 ± 0.9
50HA-50BG	0	0.20 ± 0.01	1.25 ± 0.07	15.3 ± 0.3	4.59 ± 0.09
	30	0.37 ± 0.03	1.6 ± 0.1	14 ± 2	4.6 ± 0.6
	60	0.24 ± 0.03	1.65 ± 0.09	14 ± 3	4.7 ± 0.8
	120	0.49 ± 0.02	2.3 ± 0.3	20 ± 4	6.0 ± 1.0
75HA-25BG	0	0.16 ± 0.01	0.85 ± 0.06	16 ± 1	4.4 ± 0.3
	30	0.20 ± 0.01	0.95 ± 0.01	12.06 ± 0.01	3.61 ± 0.01
	60	0.18 ± 0.03	1.0 ± 0.1	14 ± 3	4.1 ± 0.8
	120	0.12 ± 0.06	0.9 ± 0.5	12 ± 8	4 ± 2

Table 3.2: Average particle size distribution parameters of the investigated composition mixtures obtained at different milling conditions.

Finally, when considering the composite mixture richer in HA, i.e. 75HA-25BG, BM treatments up to 60 min duration did not produce noteworthy changes in the Q3 and q3 curves, particularly on the smaller particle size range. In contrast, as the milling time was extended to 120 min, the intensity of the main peak of the q3 curve in the range 0.5-0.6 μm decreases. Correspondingly, the 7 μm sized class of powder increases its relative content. In addition, a new class of particles with size in the range 2-3 μm is formed. All these findings are consistent with the occurrence of agglomeration phenomena favoured by the high content of HA in the composite.

Based on the results described above, it is possible to draw some general conclusions regarding the effect of the BM treatment on particles size of the composite mixtures.

Agglomeration mechanism usually prevails in the entire 0-120 min milling time interval when system containing 50 wt.% or higher contents of HA.

Conversely, agglomeration phenomena are confined only to the 0-30 min range when considering the composite mixture rich in BG, i.e. 25HA-75BG. Indeed, in the latter case, as the mechanical treatment is extended above 30 min, the prevailing content of the hard/fragile BG phase particles comminution.

As a representative example, 50HA-50BG composite powders were further analysed. In particular, textural properties of the unmilled ($t_{BM} = 0$ min) and samples milled at $t_{BM} = 30$ and 120 min have been also investigated by N_2 physisorption. The isotherms of all the samples are depicted in Figure 3.4 a)-c). BET (Brunauer, Emmett, Teller) surface areas vary from 5.0 $m^2 g^{-1}$ for the unmilled ($t_{BM} = 0$ min) to 11.7 and 11.1 $m^2 g^{-1}$ for the systems milled at 30 and 120 minutes, respectively (see Table 3.3).

All the samples show a type II isotherm with a H3 type hysteresis loop typical of macroporous materials. The mechanical processing is found to significantly increase the specific surface area of the system, thus reaching the maximum value after 30 minutes.

Sample	B.E.T. Surface Area $[m^2 g^{-1}]$
HA	5.5
$t_{BM} = 0$ min	5.0
$t_{BM} = 30$ min	11.7
$t_{BM} = 120$ min	11.1

Table 3.3: B.E.T surface area values estimated for the unmilled ($t_{BM} = 0$ min) and milled (t_{BM} = 30 and 120 min) samples. HA has been measured for comparison.

The extension of the specific surface area during the first period of milling is the result of the newly exposed surfaces correspondingly formed, together with the desorption of physisorbed gases, which typically occlude nanopores. As the milling treatment is prolonged particle fracturing is balanced by the formation of agglomerates, and only minor changes in the specific surface area are observed to occur. A similar characterization is currently in progress for 25HA-75BG and 75HA-25BG formulations.

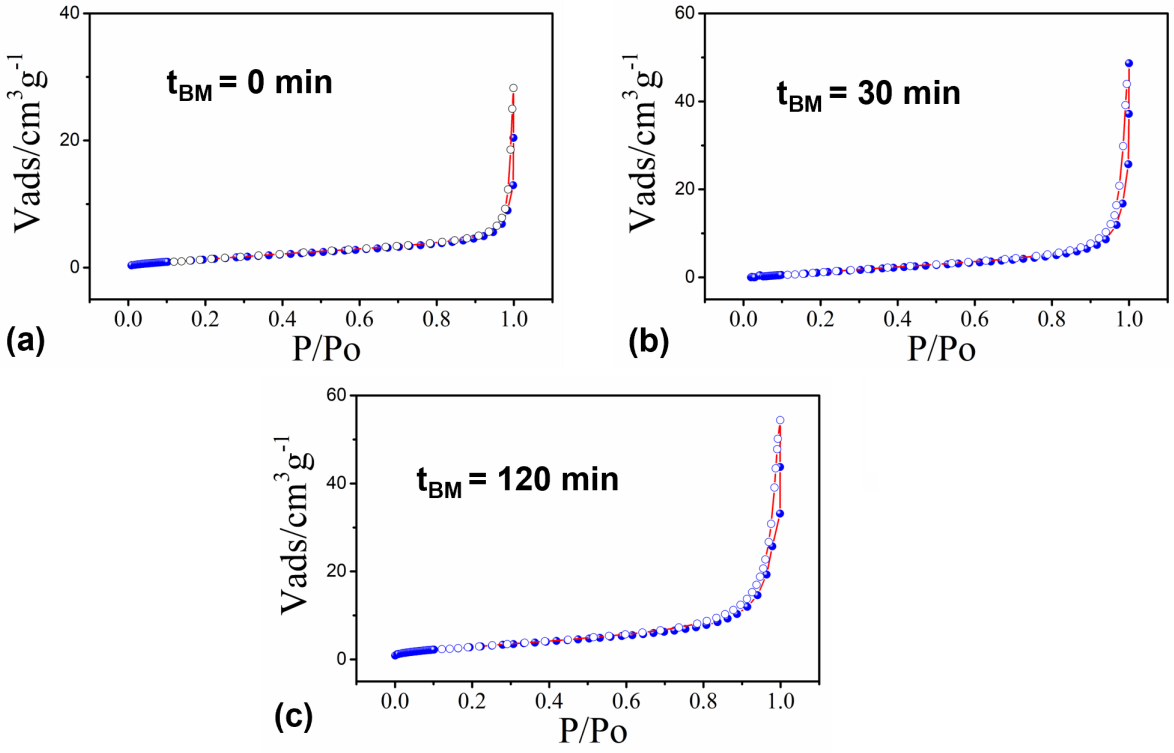

Figure 3.4: N_2 physisorption isotherms of the a) unmilled ($t_{BM} = 0$ min) sample and, milled for 30 b) and 120 minutes c) samples.

Structural and microstructural characteristics of the three formulations of powders are then investigated by XRD analysis (Figure 3.5).

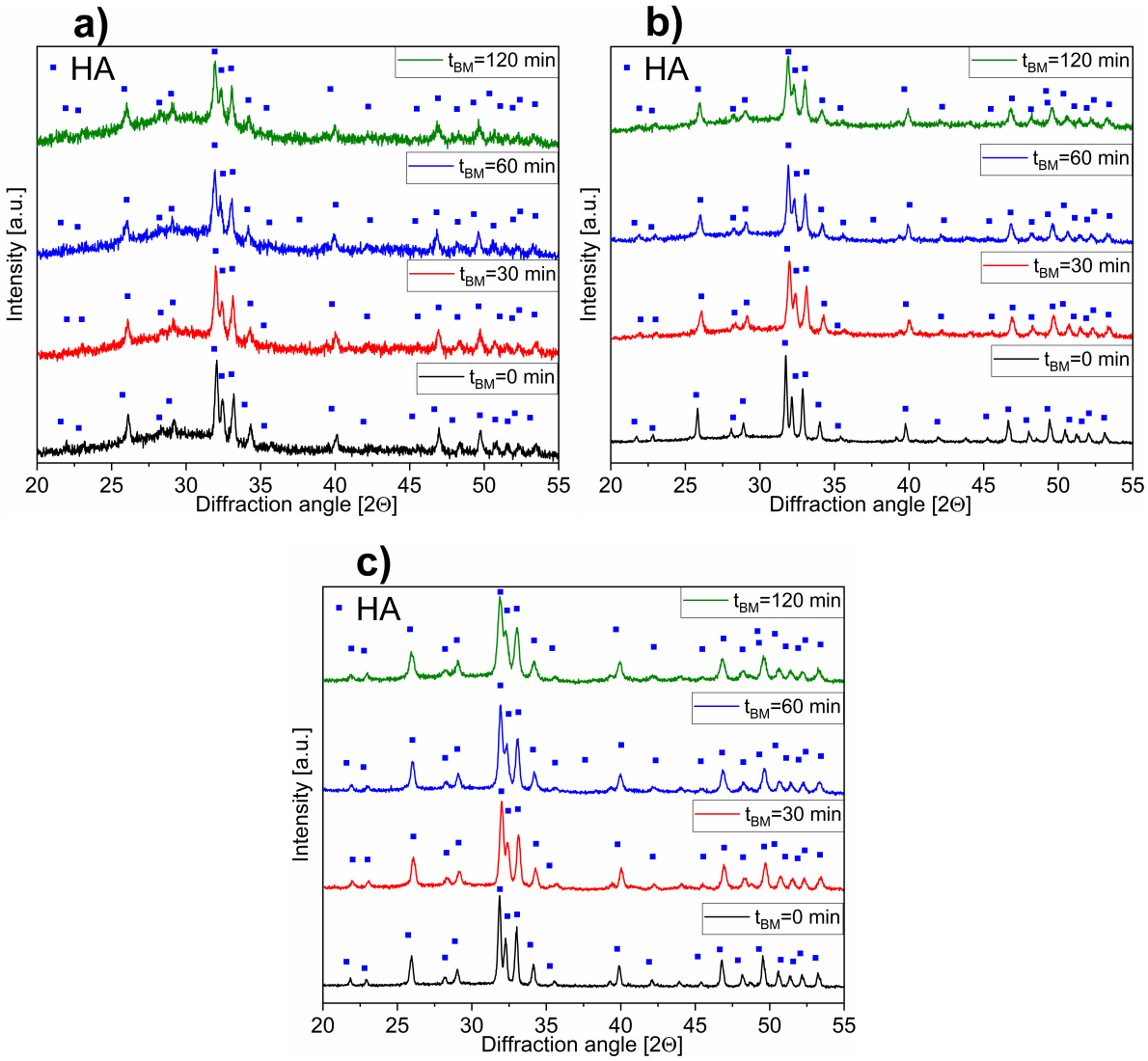

Figure 3.5: XRD patterns of powders as a function of the ball milling time for a) 25HA-75BG, b) 50HA-50BG and c) 75HA-25BG composites.

The patterns in Figure 3.5 show that no changes in power composition occurred after the BM treatment. The only variation is relative to the enlargement of HA's peaks, observed in all cases.

The 50HA-50BG powders were characterised in more detail, and the obtained results are reported in Figure 3.6 and Table 3.4.

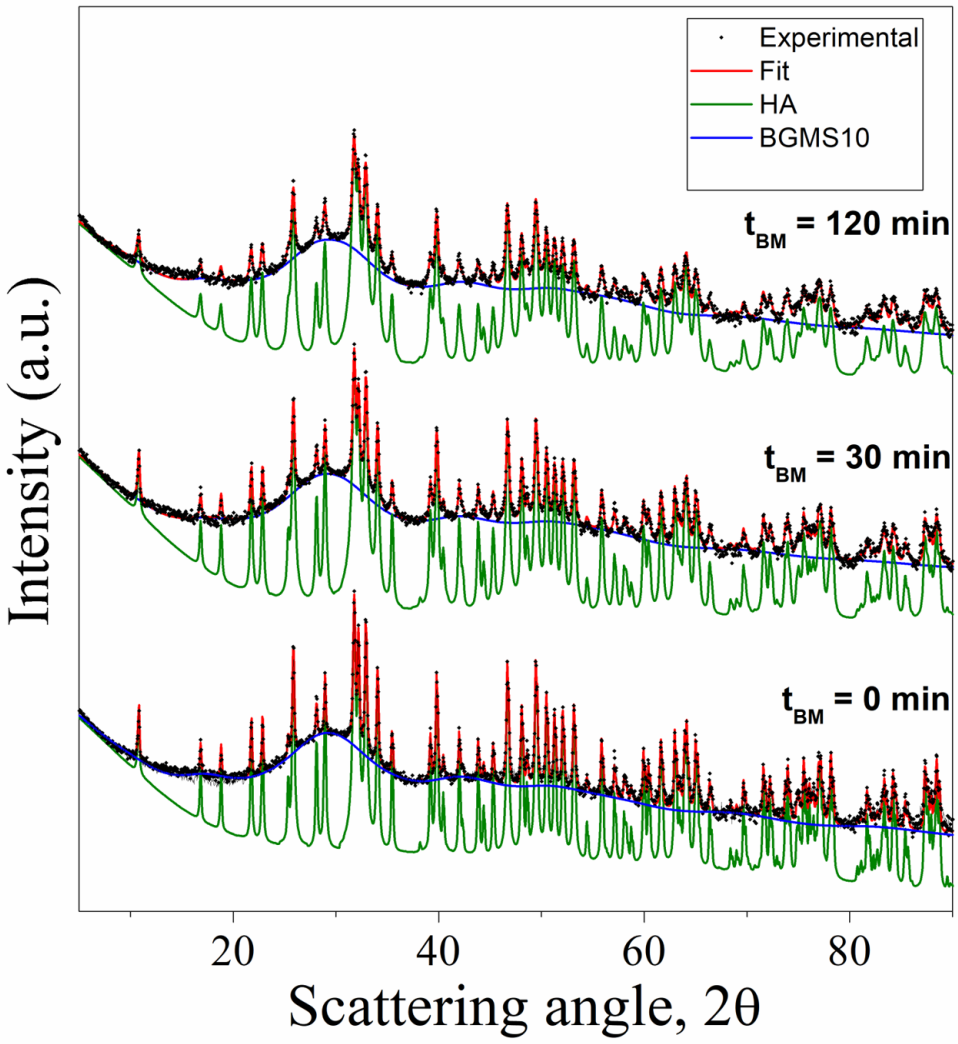

Figure 3.6: XRD patterns (log scale) of unmilled ($t_{BM} = 0$ min) and milled 50HA-50BG samples. The black dots are experimental data, and the red line is the calculated fit. Deconvoluted amorphous BGMS10 and hydroxyapatite phases are indicated by the blue and green full lines.

The pattern referred to the unmilled system shows Bragg reflections ascribable to the hydroxyapatite phase (S.G. $P63/m$) together with a typical shape of an amorphous glass related to the BGMS10. The phase, named as $Ca_{1.5}Na_{2.64}Si_9O_3$, has been computed using a pseudo-crystalline structure factor ($Ca_{1.5}Na_{2.64}Si_9O_3$ phase; symmetry: trigonal; space group: $R-3m$; crystallite size: 20 Å; microstrain: 0.03) according to the LeBail approach [197].

The relative amount of each phase contained in the unmilled ($t_{BM} = 0$ min) composite (46/54 wt.% - HA/BGMS10) is rather consistent with the initial nominal mixture. This holds also

true when considering the milled powders. Figure 3.6 also evidences that the XRD pattern of the sample milled for 30 minutes is still characterised by the halo peak ascribable to the amorphous phase. However, as expected, the hydroxyapatite crystallites size decreased significantly from > 2000 Å to 700 Å (Table 3.4), as a consequence of the mechanical processing. Increasing the milling time up to 120 minutes, both crystalline and amorphous phases are still observed, while the crystallite dimensions of the hydroxyapatite phase further decreased down to 470 Å (Table 3.4).

Unmilled powders (t_{BM}= 0 min)							
Phase	**a**(Å)	**b**(Å)	**c**(Å)	**Content [%]**	**Space Group**	**Cryst.size** (Å)	**Microstrain**
Apatite	9.4231	-	6.8872	46	P63/m	>2000	$3.47 \cdot 10^{-4}$
Amorphous	-	-	-	54	-	-	-
Milled powders (t_{BM}= 30 min)							
Phase	**a**(Å)	**b**(Å)	**c**(Å)	**Content [%]**	**Space Group**	**Cryst.size** (Å)	**Microstrain**
Apatite	9.4235	-	6.8875	48	P63/m	709	$4.14 \cdot 10^{-4}$
Amorphous	-	-	-	52	-	-	-
Milled powders (t_{BM}= 120 min)							
Phase	**a**(Å)	**b**(Å)	**c**(Å)	**Content [%]**	**Space Group**	**Cryst.size** (Å)	**Microstrain**
Apatite	9.4248	-	6.8879	44	P63/m	472	$1.20 \cdot 10^{-4}$
Amorphous	-	-	-	56	-	-	-

Table 3.4: Microstructural parameters and amount of each phase present on the unmilled and differently milled 50HA-50BG powders, as estimated by the Rietveld analysis performed on the related XRD patterns (Figure 3.6).

Furthermore, as emerged from the microstructural parameters here estimated, the cell volume associated with the hydroxyapatite phase increases as the milling treatment was prolonged. Unmilled and milled 50HA-50BG powders were further characterised from the microstructural point of view by TEM. The corresponding images shown in Figure 3.7 suggest that all the three systems consist of agglomerates of particles with different shapes. This finding confirms the formation of an intimate mixture even when HA and BGMS10 were just mixed. Crystalline domains decreased, accordingly to the XRD analysis, when the powders were subject to mechanical milling. No new phase emerged both from TEM and XRD characterization, at least up to this stage of milling. XRD/Rietveld and TEM analyses are currently in progress also for 25HA-75BG and 75HA-25BG formulations.

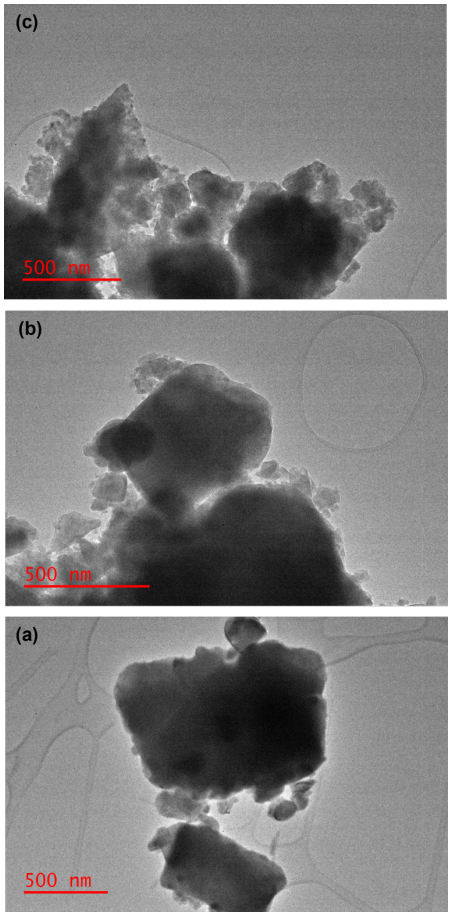

Figure 3.7: Representative TEM images at comparable magnifications of the (a) unmilled (t_{BM} = 0 min), (b) 30, and (c) 120 min milled 50HA-50BG powders.

3.3.2 Bulk samples

3.3.2.1 Fabrication and preliminary characterization

3.3.2.1.1 Unmilled powders

The effect of the holding temperature (P=16 MPa) and the applied pressure (at a fixed T_D, depending on the composite formulation) on the densification of the sintered products was investigated for the case of $t_{BM} = 0$ min, i.e. unmilled composites powders. The resulting densities are reported in Figure 3.8.

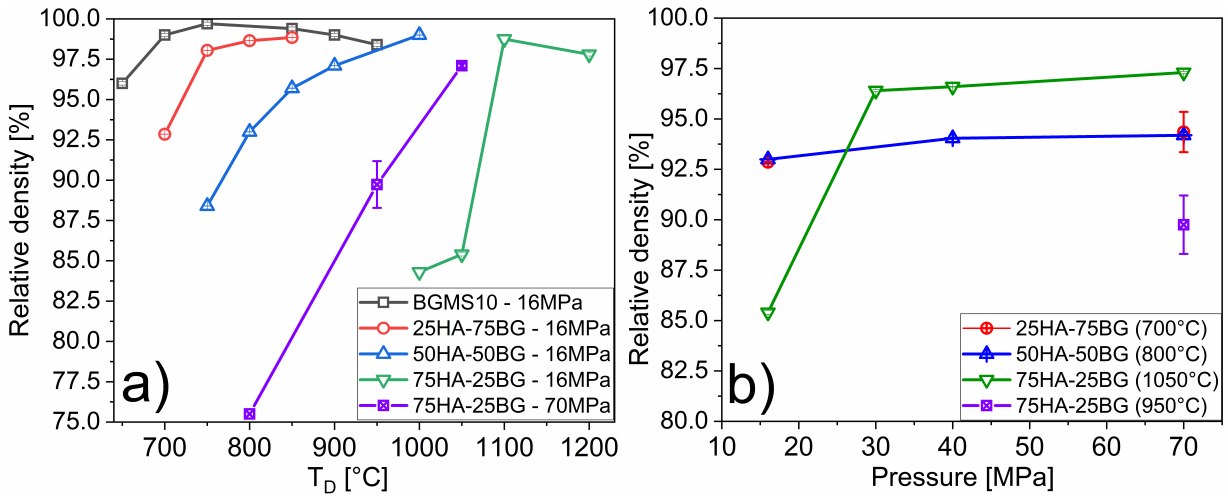

Figure 3.8: Densities of the SPS products from unmilled ($t_{BM} = 0$ min) composite powders as a function of a) the holding temperature and b) the applied pressure. The data relative to the pure glass [227] are reported for the sake of comparison.

As for the 25HA-75BG system, a significant density improvement (from 92.9 to 98.1%) is observed when increasing the temperature from 700 to 750°C (Figure 3.8 a, red line). XRD analysis does not evidenced noteworthy compositional/structural changes (Figure 3.9 a), thus indicating that the glass amorphous characteristic is preserved for sintering temperatures up to 800°C. A slight increase in relative density resulted from a further temperature increment. Indeed, the measured density at 850°C is 98.9%. Correspondingly, some diffraction peaks associable to $\alpha - CaSiO_3$ are detected in the XRD pattern, indicating the occurrence of crystallization phenomena.

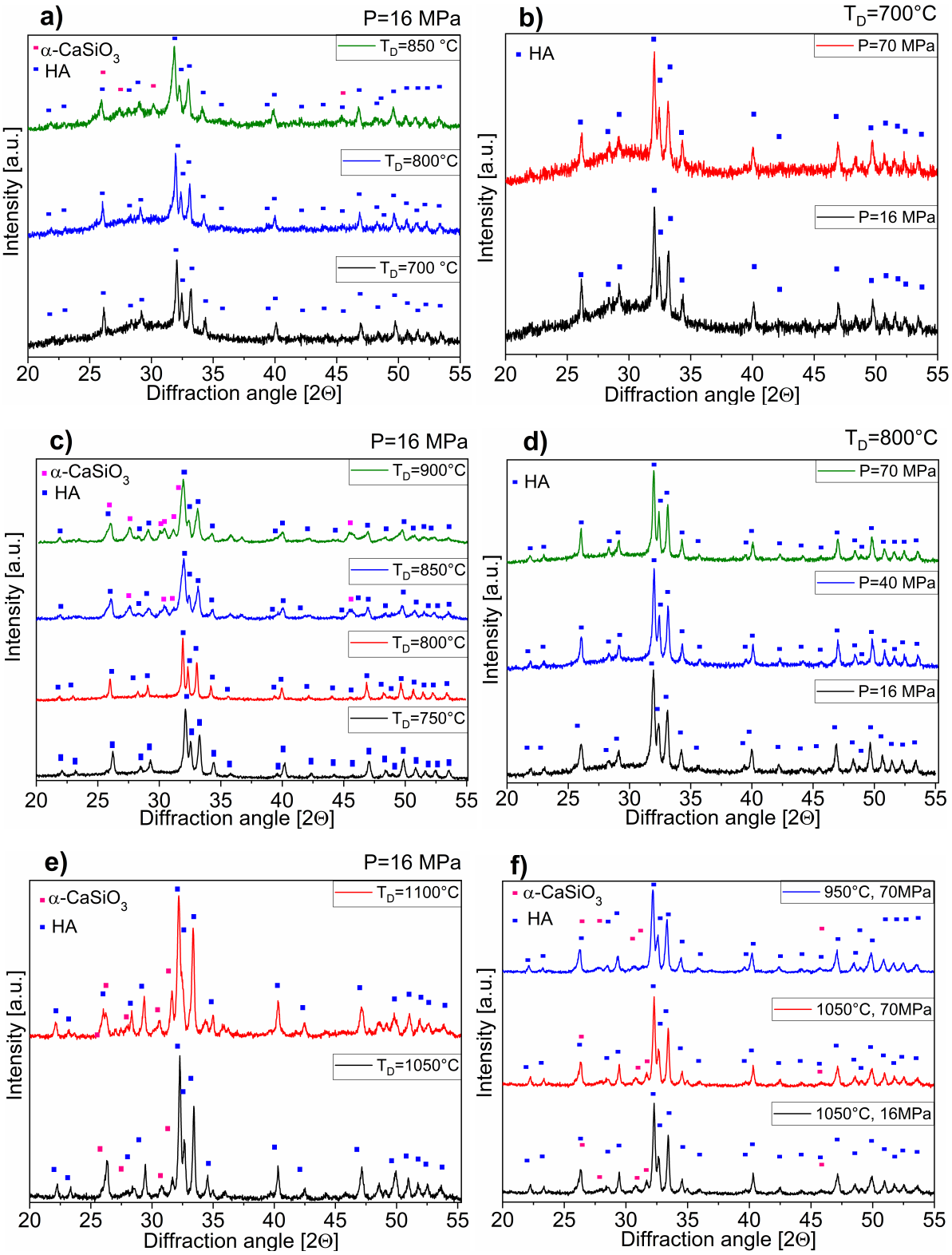

Figure 3.9: XRD patterns of dense composite samples obtained from unmilled powders (t_{BM} = 0 min) under different SPS conditions: a),b) 25HA-75BG, c),d) 50HA-50BG,and e),f) 75HA-25BG formulations.

For the same system, an increase of the applied pressure from 16 to 70 MPa (when operating at T_D=700°C) was found to provide only a slight increase in samples densities, from 92.9 to 94.4% (Figure 3.8). No changes in the composition of the obtained bulk products were also correspondingly observed (Figure 3.9 b), being diffraction peaks associable to the HA the only ones detected together with the glass halo.

As the relative content of HA in the composite is increased to 50 wt.%, the corresponding 50HA-50BG powders are scarcely consolidated at 750°C (about 88.4 % relative density). No evidence of glass crystallization arises from the resulting XRD analysis on the bulk products (Figure 3.9 c). The latter statement holds also true for $T_D = 800$°C, which determined an improvement in sample densification (93%). On the other hand, new peaks ascribed to $\alpha-CaSiO_3$ are detected in the pattern at 850°C, corresponding to a 95.9% dense product. The new crystalline phase formed from the glass was also observed when the holding temperature was raised to 900°C, which also led to an improved product density (97.1%). An even higher density was obtained when the T_D was augmented to 1000°C (99%). Figure 3.8 a) shows that an increase of the mechanical pressure from 16 to 40 MPa at T_D=800°C provided slight improvement of sample density from 93 to 94%, whereas only modest changes (94.2%) were observed when this processing parameter was further raised to 70 MPa. No modifications in product composition were correspondingly obtained (Figure 3.9 d), being hydroxyapatite still the only crystalline phase detected under such conditions. Therefore, when considering 50HA-50BG system, 94% is the maximum relative density obtainable in bulk samples, where the amorphous nature of the glass is preserved. On the other hand, nearly fully dense products with the same nominal composition produced at higher temperature conditions also contained $\alpha-CaSiO_3$ as result of glass crystallization.

The presence of a higher HA percentage in 75HA-25BG composite required the use of higher processing temperatures to reach adequate relative density levels. Indeed, the densification at both 1000 and 1050°C led to poorly densified products, with densities of 84.3 and 85.4%, respectively. A significant improvement on densification is obtained when sintering was car-

ried out at 1100°C, resulting in average densities of 98.8%. A Further increase of the temperature resulted in broken samples, whose density is relatively lower (97.8%) than that obtained at 1100°C. This behaviour, also manifested by the parent glass [227], was justified by the occurrence of crystallization and, especially, ongoing crystalline grains growth, both known to hamper densification. It is worth noting that, since 1000-1100°C are well above glass crystallization temperature, the obtained bulk products also contained $\alpha - CaSiO_3$ (Figure 3.9 e). The effect of the pressure on the densification for this composite formulation is quite interesting. Indeed, differently from the other HA-BG formulations, pressure is observed to have a huge effect on the sintering process, causing an increase of bulk sample's density from 85.4 to 96.4% when this parameter was augmented from 16 to 30 MPa, respectively. A further improvement in powder densification was obtained when the applied pressure was raised to 70 MPa (97.3%). Owing to the latter, the sintering temperature was progressively lowered at 70 MPa to identify the optimal value for achieving proper densification level. However, when operating at 800°C, which allows to avoid glass crystallization, the resulting sample is very low (75.5%), as reported in Figure 3.8 a). In contrast, as the temperature was increased to 950°C, denser samples (89.7%) are obtained. As expected , Figure 3.9 f) shows that crystallization was not avoided under the latter condition, but is retained compared to the cases of 1050 and 1100°C.

3.3.2.1.2 Ball milled powders

The effect produced by a mechanical treatment of the composite powders before their consolidation by SPS was then investigated. Based on the results obtained in paragraph 3.3.2.1.1, the milled powders were all processed by SPS at 70 MPa, whereas the selected temperature conditions depend on the specific composite formulation, i.e. 25HA-75BG at 700°C, 50HA-50BG at 800°C and 75HA-25BG at 950°C. This choice is due to tha fact that, under such conditions, the relative densities achieved for the three composite formulations were similar, in the range 89.8 - 94.2%. In addition, the selected T_D/P values did not produce too highly densifies sam-

ples, so that the effect of the BM treatment is expected to be more evident.

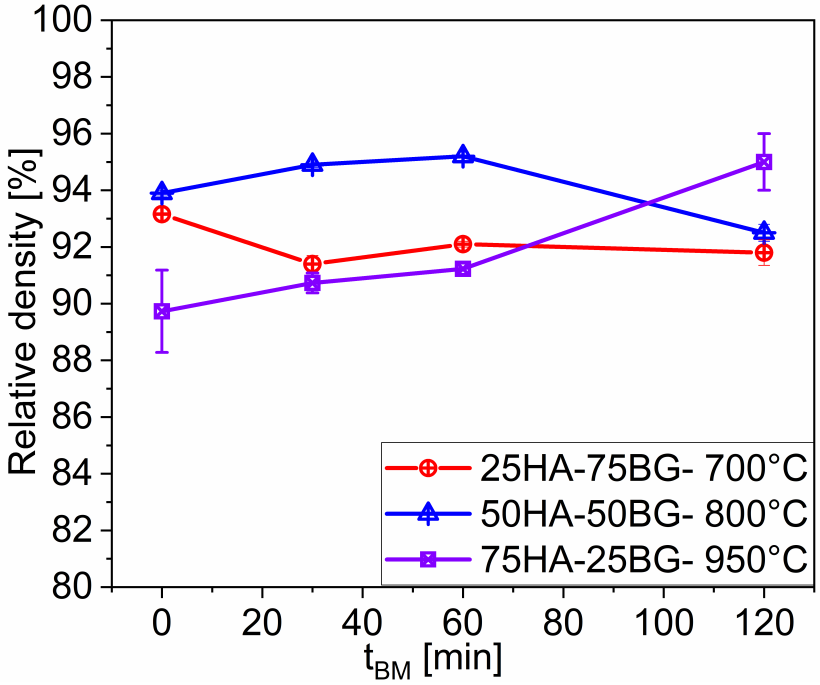

Figure 3.10: Effect of the milling time (t_{BM}) on the density of the three composite products obtained by SPS.

As reported in Figure 3.10, the effect of the milling time on the sample densities varies depending on the assessed composition. Following, a description of the obtained results. For the case of 25HA-75BG system, the relative density decreases from 92.9 to 91.4% as a consequence of a 30 min BM treatment. As the latter one is prolonged to 120 min, a slight density increase (91.8%) is observed. No compositional changes were correspondingly observed by XRD analysis (Figure 3.11). However, the width of HA main peaks progressively increase as the t_{BM} was augmented. This can be associated to the beneficial grains size refinement deriving from the BM process.

When considering the 50HA-50BG composition, a beneficial outcome was obtained after 30 and 60 min ball milling, with an increase of the relative density from 94.2 to 94.7% at 30 min, and 95.2% at 60 min. The interfaces between the two constituents are enhanced by ball milling, so that sintering phenomena are expected to be promoted. In contrast,

when such treatment was extended to 120 min, sintered sample were relatively less dense (92.4%). A possible motivation for such outcome could be that, is spite of the beneficial effect produced by the interface formation, particles become considerable coarser for t_{BM}=120 min (Figure 3.3 and Table 3.2), which is expected to hinder powder consolidation. Another supplementary plausible explanation will be provided afterwards, after examining in detail (subsubsection 3.3.2.2) the composition of SPS product.

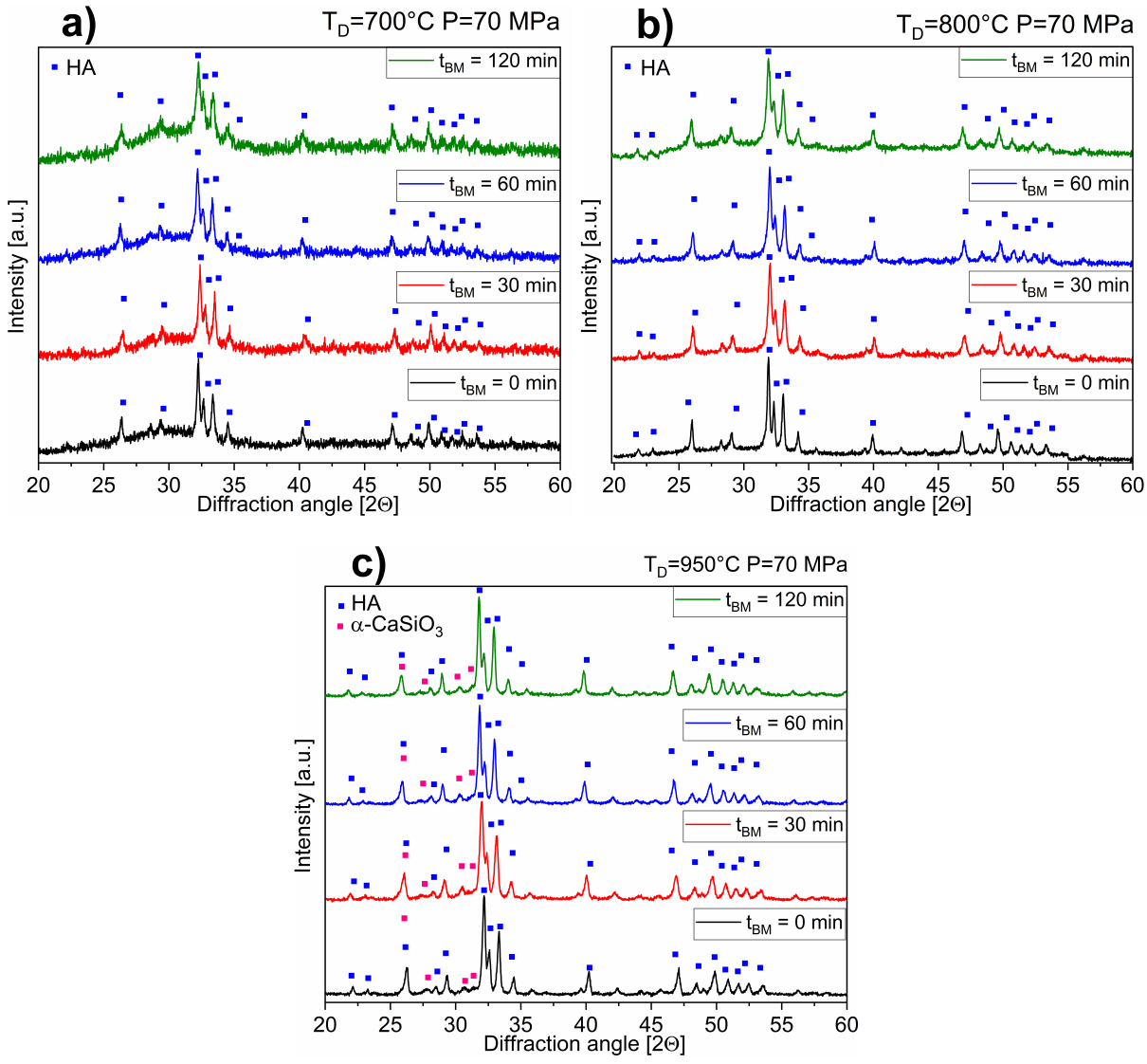

Figure 3.11: XRD patterns of composite samples obtained by SPS from mechanically treated powders: a) 25HA-75BG, b) 50HA-50BG, and c) 75HA-25BG.

The introduction of the milling treatment prior to SPS in the HA-rich composite (75HA-25BG) caused a progressive increase of bulk samples density. Shorter BM times (30 and 60 min) resulted in a modest improvement of the consolidation level (from 89.7 to 91.2%). In contrast, the effect is remarkable (from 89.7 to 95%) for longer treatments. The composition of the resulting bulk samples is not affected by the ball milling treatment, as evidenced by the XRD patterns reported in Figure 3.11 c). Differently from the other two composites, in this case, also the widths of HA peaks are similar, regardless of BM treatment. This can be due to the more severe SPS conditions adopted (950°C) which produce a significant grain growth.
To summarize, it is found that, when the composite powders are preliminarily processed by BM:

- a beneficial effect in terms of product densification is obtained by the HA-rich composite, particularly when operating with high t_{BM};
- a slight density decrease is produced during the early stage of milling (0-30min) in BG rich composites;
- an intermediate situation is encountered when processing 50HA-50BG powders, since the benefits arising during initial 60 min treatment are followed by a density decrease.

To explain such findings, more detailed characterizations are required. So far, this has been carried out for the case of 50HA-50BG composition, by XRD/Rietveld analyses.

3.3.2.2 Detailed characterization of 50HA-50BG composites

A more detailed characterization has been carried out on dense samples of 50HA-50BG composition. XRD/Rietveld analysis, together with mechanical and in-vitro investigation results are reported in what follows. For the sake of brevity, from now on, the investigated bulk samples of the 50HA-50BG will be referred as t_{BM}/T_D-P, to differentiate them depending on the milling (t_{BM}) and sintering (T_D and P) conditions adopted.

3.3.2.2.1 Microstructural characterization

The XRD experimental patterns (black rhombohedral) and the best fit (red line) relative to the SPS products obtained from unmilled ($t_{BM} = 0$ min) and milled powders are shown, on a log scale, in Figure 3.12. Table 3.5 summarizes the structural and microstructural parameters evaluated from the Rietveld analysis applied to these patterns. The 0/800-70 sample obtained starting from the unmilled powders consists of the amorphous glass and crystalline hydroxyapatite phases, with an estimated relative amount of 53 and 47 wt.%, respectively. Similar values for the HA/BGMS10 weight ratio were also obtained for the milled systems processed by SPS (Table 3.5). Moreover, when t_{BM}=30 min (sample 30/800-70), the crystallite sizes of HA keep within nanostructured conditions of 900 Å, just slightly higher than those relative to the starting milled powders, i.e. 709 Å (Table 3.4). Interestingly, similar crystallite dimensions (850 Å) can be achieved for the sintered sample 120/800-70 obtained from the powders milled for 2 hours. This value corresponds roughly twice those of the original milled powders, i.e. 472 Å (Table 3.4). Along to this significant result, which can be linked to the higher reactivity of this set of mechanically processed powders, it is important to highlight that the corresponding XRD pattern presents a second crystalline phase ascribable to SiO_2 (5 wt.%). In this regard, it can be postulated that the prolonged ball milling enhanced the reactivity of BGMS10 powders, thus favouring the nucleation and segregation of quartz from the glass phase. This is in accordance with the trend observed for the volume dimension of the hydroxyapatite crystal lattice which can be distorted by the diffusion of alkali metal cations.

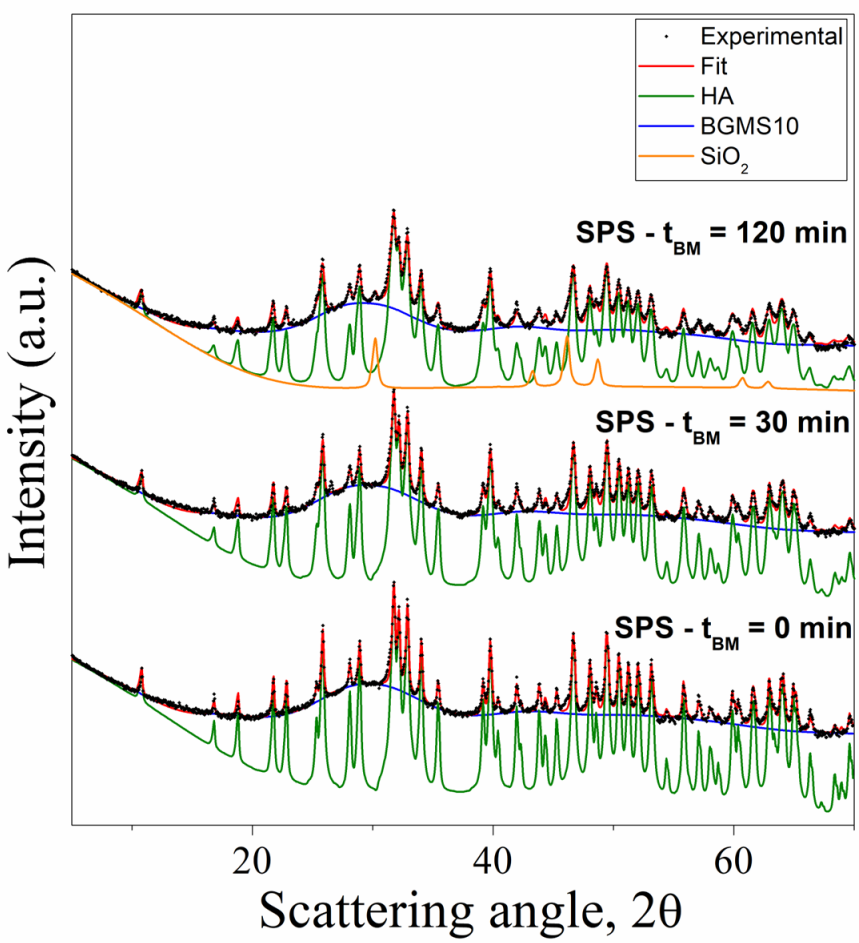

Figure 3.12: XRD patterns (log scale) of dense 50HA-50BG composite samples obtained from the unmilled ($t_{BM} = 0$ min) and milled powders. Black dots are experimental data, and the red line is the calculated fit. Deconvoluted amorphous BGMS10, hydroxyapatite, and quartz (SiO_2) phases are indicated by blue, green, and orange full lines, respectively.

The formation of a crystalline phase during SPS likely provides a plausible explanation for justifying the sample density decrease when the milling treatment was extended from 60 to 120 min (Figure 3.10). Indeed, the occurrence of crystallization phenomena during the consolidation of BGMS10 and other glass powders by SPS was found to correspond to relatively less dense products [138, 227].

The XRD/Rietveld characterization of 25HA-75BG and 75HA-25BG samples obtained by SPS are currently in progress. From the obtained results, it is expected that important information will be deduced to justify the sintering behaviour as well as the corresponding properties.

SPS product (t_{BM}= 0 min)							
Phase	**a**(Å)	**b**(Å)	**c**(Å)	**Content [%]**	**Space Group**	**Cryst.size** (Å)	**Microstrain**
Apatite	9.4254	-	6.8843	47	P63/m	>2000	$5.28 \cdot 10^{-4}$
Amorphous	-	-	-	53	-	-	-
SPS product (t_{BM}= 30 min)							
Phase	**a**(Å)	**b**(Å)	**c**(Å)	**Content [%]**	**Space Group**	**Cryst.size** (Å)	**Microstrain**
Apatite	9.4223	-	6.8819	51	P63/m	900	$5.78 \cdot 10^{-4}$
Amorphous	-	-	-	49	-	-	-
SPS product (t_{BM}= 120 min)							
Phase	**a**(Å)	**b**(Å)	**c**(Å)	**Content [%]**	**Space Group**	**Cryst.size** (Å)	**Microstrain**
Apatite	9.4215	-	6.8830	51	P63/m	850	$4.423 \cdot 10^{-4}$
Amorphous	-	-	-	44	-	-	-
SiO_2	4.1737	-	2.6309	5	P42/mmm	579	$3.83 \cdot 10^{-5}$

Table 3.5: Microstructural parameters and amount of each phase present on the 50HA-50BG bulk composited obtained by SPS (T_D=800°C, P=70 MPa) from unmilled and differently milled powders, as estimated by the Rietveld analysis performed on the related XRD patterns (Figure 3.12).

3.3.2.2.2 Mechanical characterization

SEM images of the surface of the sintered 50HA-50BG composites are shown in Figure 3.13. The samples appear very similar to each other, are adequately consolidated, and possess a dense microstructure, apart from some local defects and residual microporosity. This fact confirms the effectiveness of the sintering protocol and is coherent with the results of the density measurements (Table 3.6). The more detailed SEM-EDS analysis conducted on the 0/850-16 sample (Figure 3.14) evidenced that residual porosity is confined to rounded regions

corresponding to the HA constituent. On the other hand, the glassy counterpart in the composite appears to be fully consolidated.

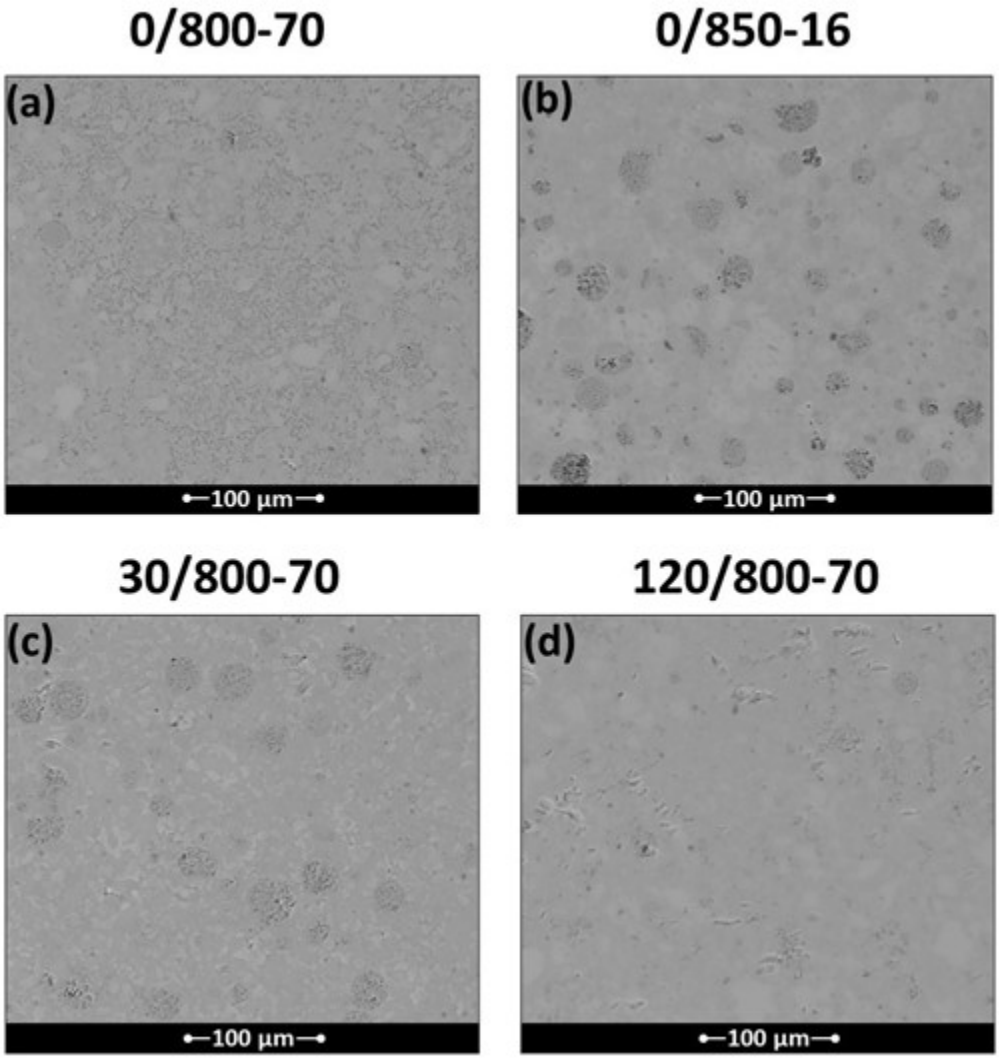

Figure 3.13: The surface of the 50HA-50BG sintered disks.

The mechanical properties of the 50HA-50BG composites (Young's modulus and hardness), as measured by micro-indentation tests, are reported in Table 3.6. In general, the obtained results are analogous or even slightly better than those recently obtained for pure BGMS10 powders sintered by SPS [227], in particular when considering 0/850-16 and 30/800-70 samples. This demonstrates the beneficial contribution exerted by the HA phase in the composite.

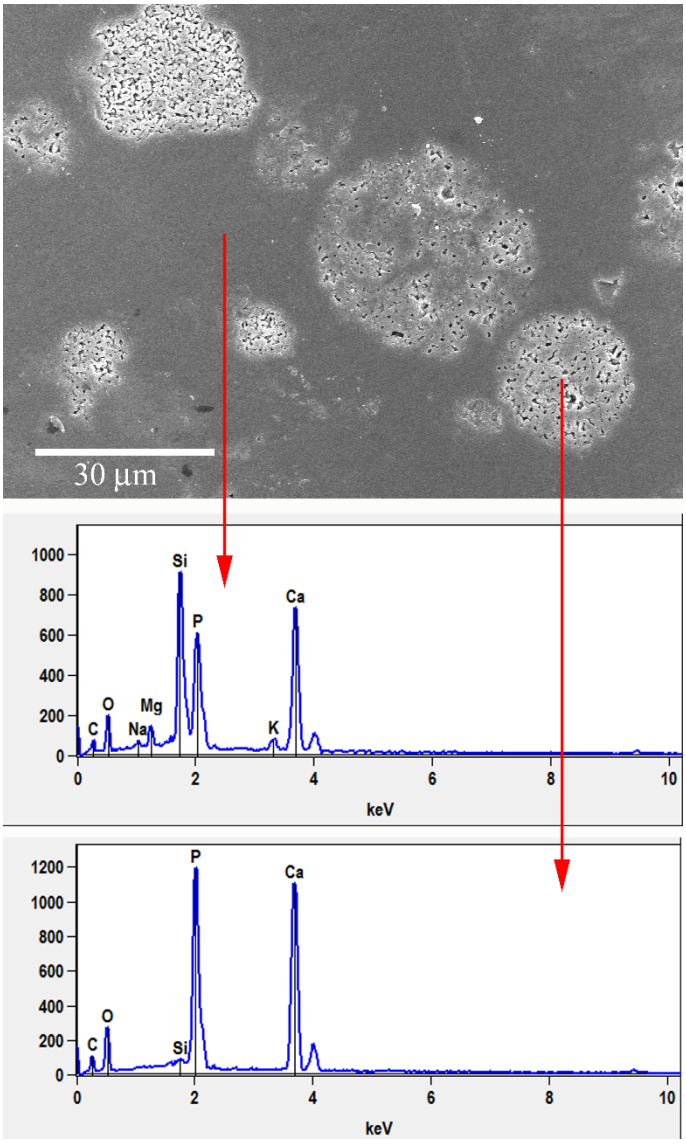

Figure 3.14: SEM micrograph and EDS analysis results related to two different areas (red arrows) of the 0/850-16 sample (50HA-50BG).

It should be stressed that pure HA, when consolidated by SPS, displayed better mechanical properties than BGMS10 products obtained by the same technique [175], although it is not straightforward to compare the performances of such samples, given the different processing parameters adopted to sinter them, i.e. T_D=1200°C (HA) [175], and T_D=750-950°C (BGMS10) [227]. In addition, it should be also noted that the 50HA-50BG composite samples investigated in this work possess lower relative densities (in the range 92.4-95.9%) compared to those resulting from pure HA (fully dense) [175], and BGMS10 (in the range 98.6-

99.6%) [227].

Sample	Relative density $[g/cm^3]$	Young's Modulus (GPa)	Hardness (Vickers)
0/800-70	94.2	95.2 ± 2.5	510 ± 34
0/850-16	95.9	116.4 ± 4.5	698 ± 27
30/800-70	94.7	122.3 ± 3.6	675 ± 38
120/800-70	92.4	98.0 ± 4.6	683 ± 42

Table 3.6: Young's modulus and hardness of the 50HA-50BG composite samples, as determined by micro-indentation tests. The corresponding relative density values are also reported.

The results reported in Table 3.6 reveal an increment of both the local elastic modulus and hardness with increasing holding temperature in the set of samples obtained from unmilled powders (i.e., 0/800-70 and 0/850-16). This fact can be ascribed to the increased density of the samples processed by SPS at higher temperatures and to the progressive crystallization of their glassy phase, with the concurrent formation of $\alpha - CaSiO_3$ (see Figure 3.9). In fact, a slight devitrification of the glass phase is expected to increase the mechanical properties of HA/BG composites, as crystalline phases are usually mechanically stronger than their parent glass [228,229]. Nonetheless, excessive crystallization should be avoided in this kind of samples, as the development of new phases may also imply non-trivial changes in specific volumes, with a reduction of the final density and compactness of the sintered composite [138,227]. Indeed, a density reduction is typically associated to a decrease of the mechanical performance. The differences in the Young's modulus of the 50HA-50BG samples prepared at the same holding temperature (i.e., 800 °C), but with increasing milling times (i.e., 0 min, 30 min and 120 min) of the starting powders, may be also explained in terms of the different degree of density and compactness achieved after sintering (see Figure 3.8, Table 3.6).

3.3.2.2.3 *In-vitro* bioactivity

The bioactivity of the produced 50HA-50BG composite has been evaluated in vitro by immersing the samples in a Simulated Body Fluid solution, which contains an ionic concentration similar to that of human plasma [164].

The results of the SEM analysis performed on the disks after 7 and 14 days in SBF are shown in Figure 3.15. It is evident that the process parameters - in particular, the milling time of the starting powders and the holding temperature- influence the samples' bioactivity in a non-trivial way. After one week, the surface of all the produced composites appeared highly degraded, with a widespread porosity due to the dissolution of the samples and their ionic release. After 14 days in SBF, the composites were characterised by different degrees of bioactivity. In particular, no precipitates ascribable to HA were observed on the surface of the 0/850-16 sample.

This behaviour can be partially attributed to the crystallization of the glass phase with the concurrent formation of $\alpha - CaSiO_3$. Indeed, the latter phase is characterised by a slower in vitro reactivity and, therefore, by a less marked bioactivity compared to that of the parent glass [230]. All the samples produced at a lower holding T_D value (i.e., 800°C) displayed their bioactivity after two weeks of soaking, with different degree of reactivity depending on the milling time. It should be highlighted the extraordinary bioactivity of the 30/800-70 samples, whose surface, already after a week, is markedly degraded and completely covered by white precipitates with the typical morphology of in vitro formed HA. The X-EDS analysis reported in Figure 3.16 confirms the presence of precipitates rich in calcium and phosphorus, with a Ca/P ratio gradually approaching that of stoichiometric HA.

The chemical nature of the globular precipitates formed on the sintered disks after immersion in SBF has been further investigated by means of Raman microscopy. In fact, such technique can be used to locally identify the presence of HA, as the main Raman peaks of the P-O vibrational modes are particularly intense.

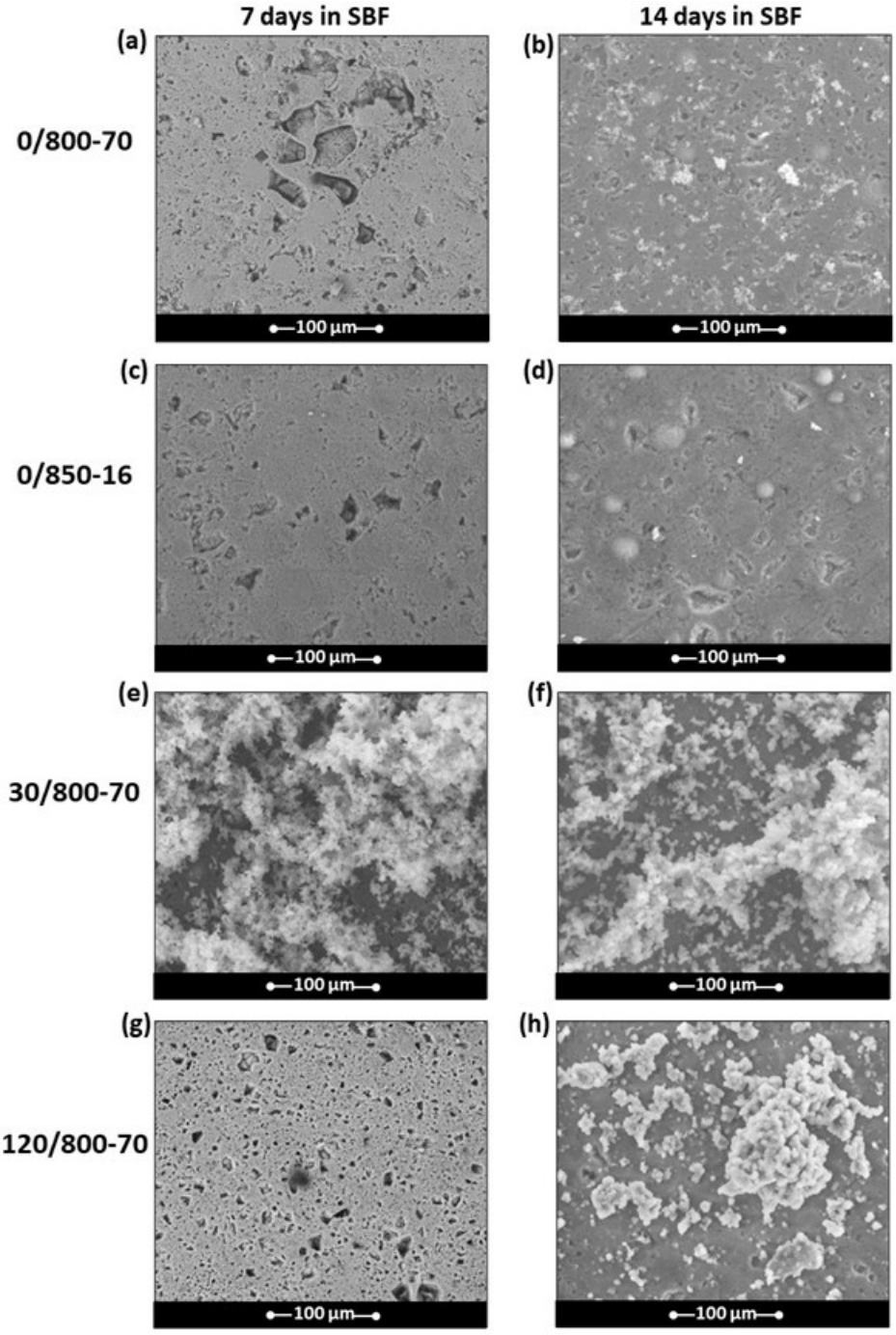

Figure 3.15: SEM images of the sintered 50HA-50BG samples after soaking them in SBF for 7 and 14 days. It should be noted the marked HA precipitation on the 30/800-70 samples already after 7 days of immersion.

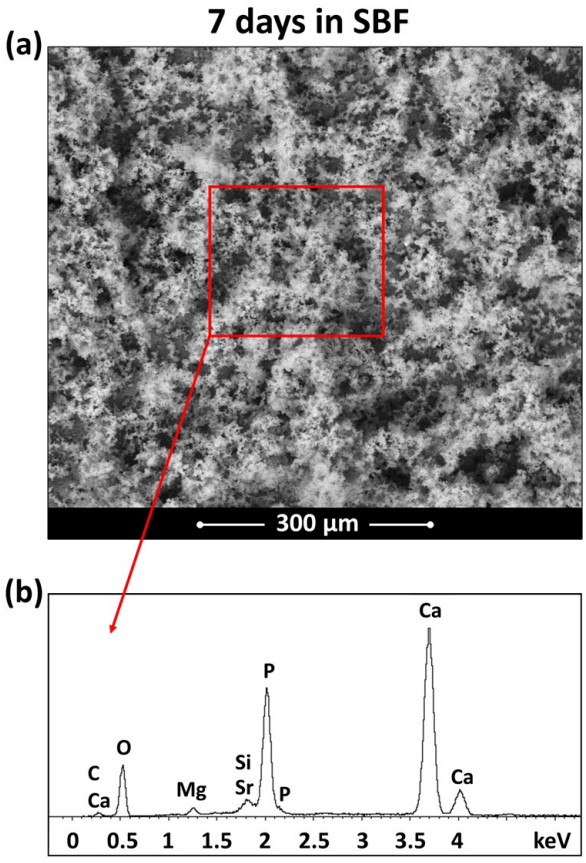

Figure 3.16: (a) HA formed on the 50HA-50BG (30/800-70) sample after 7 days in SBF and (b) results of the X-EDS analysis performed on the area shown in a).

Moreover, since the in vitro grown HA is typically carbonated and the Raman spectroscopy is sensitive to the C-O vibrational modes, the presence of carbonated groups can be also verified. Figure 3.17 reports the Raman spectra acquired on the phosphorus and calcium rich precipitates found on the 30/800-70 samples after 7 and 14 days in SBF. Since the spectra obtained from the other samples are very similar, they are not reported for the sake of brevity. Already after 7 days in SBF, the Raman spectra are dominated by the characteristic peaks of carbonated HA, as reported by the literature [231–233]:

- a very sharp peak at $\approx 960\ c\,m^{-1}$, which is related to the symmetric stretching mode of the PO_4 groups;
- two broad peaks at $\approx$430 $c\,m^{-1}$ and $\approx$590 $c\,m^{-1}$, ascribable to the bending modes of the

same group;

- a broad peak at about 1070 $c\,m^{-1}$, which is imputable to the symmetric stretching mode of the CO_3 groups.

It is then possible to conclude that the precipitates are mainly composed of carbonated HA, thus confirming the marked bioactivity of the produced samples.

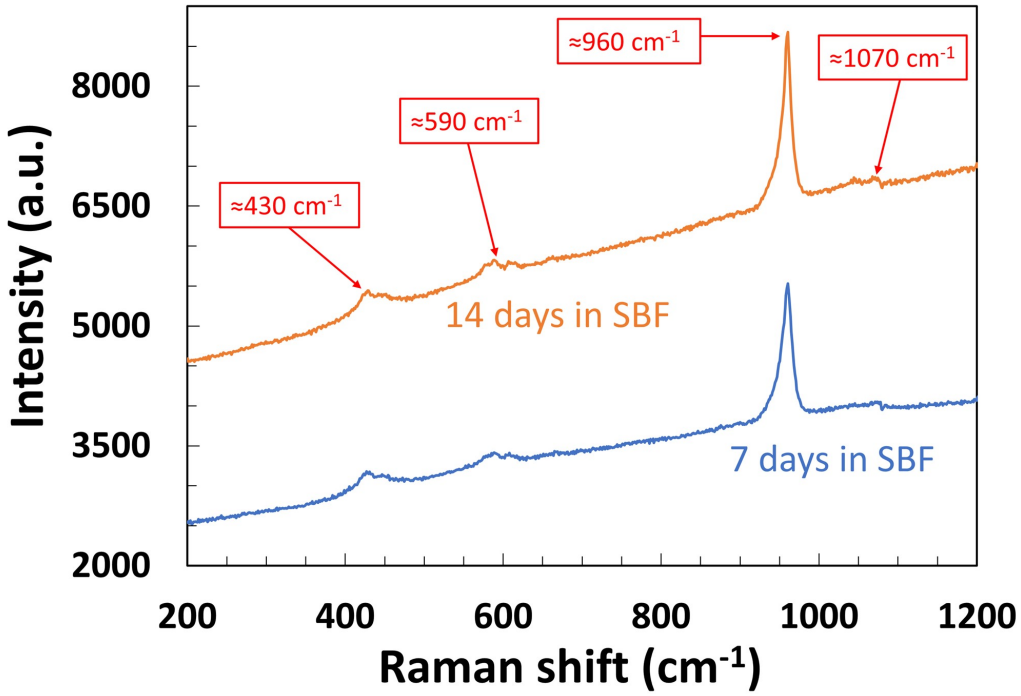

Figure 3.17: Raman spectra acquired on the calcium and phosphorus rich precipitates formed on the 30/800-70 samples after 7 and 14 days in SBF.

To justify the surprisingly different bioactivity behaviour exhibited during in-vitro test by 50HA-50BG sintered samples when the starting composite powders are mechanically treated prior to SPS, some considerations can be made. First, as mentioned in section 3.1, structural changes, as well as the formation of intimate interfaces among the different processed constituents, are induced by BM. This feature also emerges in this work from the analysis of the three sets of powders. A progressive crystallite size refinement of the HA phase from > 2000 Å (untreated) to 700 Å (t_{BM}=30 min), and 470 Å (t_{BM}=120 min), was correspondingly achieved. Although an unavoidable crystallites growth occurred during their heat treatment

by SPS, the samples derived from milled powders were still nanostructured, with crystallite size in the range 85-90 nm. Such fine microstructure corresponds to a broader grain boundary area compared to the unmilled sample, so that composite reactivity, dissolution, and ion-exchange phenomena, as well as the nucleation of the new apatite phase, during SBF test, are expected to be highly favoured.

The formation of intimate composite mixtures induced by the BM treatment, as evidenced by particle size analysis and TEM observation, could also have played a role in the observed enhancement of SPS samples reactivity. The features above could be considered the main factors responsible for the marked bioactivity improvement which came out from SBF test results involving sintered samples prepared using 30 min milled powders. Such considerations are also valid when examining the 120 min milled specimen, since the latter also displays improved HA-forming ability (Figure 3.15 g-h) with respect to the unmilled ($t_{BM} = 0$ min) sample (Figure 3.15 a-b). Nonetheless, product bioactivity was relatively reduced with a prolonged milling treatment. The main structural/compositional difference observed when t_{BM} was increased from 30 to 120 min was the formation of SiO_2 in the SPS products, while very similar HA crystallites size were obtained (90 or 85 nm, respectively). Therefore, the presence of crystalline SiO_2, which is certainly less bioactive than the original glass phase, apparently slows down the apatite-forming ability of the composite.

Based on the results above, it is expected that BM could represent a promising tool, if utilized under proper conditions, for improving the bioactivity of composite systems of potential interest in regenerative medicine.

In addition to the ongoing characterization, involving 25HA-75BG and 75HA-25BG samples, future work will be devoted to a comprehensive biological characterization, to further corroborate the findings of this work. Specifically, other in-vitro tests will be carried out, such as cellular direct and indirect tests. Moreover, an in vivo study will be performed on the most promising composite products, based on the preliminary tests.

Chapter 4

Bulk apatite-tricalcium phosphate nanocomposites from combustion synthesised powders

4.1 Introduction

As described in Chapter 1, due to their peculiar structural/compositional characteristics, similar to the mineral part of bones and teeth, synthetic calcium orthophosphates have attracted a strong interest, during the past 50 years, for biomedical applications [234]. In this regard, the most representative CaP, HA, displays low solubility, i.e. about 0.0003 g/L at 25°C, which makes it biologically stable once introduced into the human body [234]. The latter aspect is not desirable in modern regenerative medicine, where biomaterials capable to be progressively resorbed are required. On the other hand, TCP in both its forms β and α-TCP, have acquired significant importance due to its superior biodegradability, compared to that of HA, associated to its relatively higher dissolution rate [234]. Nonetheless, dissolution should not occur too fast to allow for bone bonding. In this framework, the combination of HA with TCP to generate biphasic composites with suitable resorption rate, under the physiological conditions, in

between that of individual phases was explored [108]. It should be noted that, in this work, the word *composite* is used for HA-TCP ceramics, although this term might be considered not appropriate, as is generally referred to systems consisting of two or more constituents with rather different physico-chemical characteristics, so that *multiphasic calcium phosphates* is often preferable [108]. Nonetheless, as mentioned above, TCP possesses quite different biodegradability properties compared to HA, so that its presence might affect markedly the biological behaviour of the biphasic material.

No matter what terminology is used, the characteristics of these bioceramics depend on the synthesis routes adopted to obtain them. Several methods have been proposed to prepare HA-β-TCP biphasic calcium phosphate (BCP). The latter ones can be produced by heat treatment, above certain temperatures, of other calcium phosphates [175, 235–239], precipitation method [240–243], Pechini based liquid-mix technique [244], microwave irradiation [245], sol-gel [246], combined wet mechano-chemical - solid-state synthesis [247], and solution combustion [115, 248–250].

In this regard, it is important to possibly provide the synthesis product in the form of nanopowders, to better mimic, not only the composition, but also the size of the mineral constituent of hard tissues, i.e. the biological apatite, which is nanocrystalline [251].

Along this line, solution combustion synthesis (SCS) represents a very rapid and powerful technique for the preparation of a wide variety of materials at the nanoscale [115]. SCS is a rapid synthesis process, based on the occurrence of highly exothermic reactions taking place in a liquid or sol/gel media [115]. Specifically, the main reaction involves an organic precursor (fuel) and an oxidizing agent (oxidizer), usually a metal nitrate hydrate [115]. The solution also contains the solvent and other reactants/additives, depending on the system to be synthesised.

The mixture is properly heated until the ignition temperature is reached. The resulting combustion reaction is accompanied by the evolution of a large amount of gases, which determine a significant expansion of the solid products, followed by their fast cooling. The described se-

quence is responsible for the porous and finely dispersed nanostructured powders resulting from the process.

Accordingly, several investigations have been addressed to the synthesis of calcium phosphate-based bioceramic powders by SCS [115, 250]. Such studies basically differ each other from the type of fuel used (glycine, urea, citric acid), heating source (furnace, hot plate, microwave), doping elements (Cr, Al, Sr, Eu), and for the characterization of the combustion synthesised products [250]. In addition, most of them focused on the synthesis of powders and related analysis, whereas, to the best of the author's knowledge, only two investigations also considered their sintering to obtain bulk products [252, 253]. Specifically, the processing route adopted by Canillas et al. (2017) [252], to produce samples consisting of HA (main) and β-TCP (minor) phases, was based on the following four stages:

1. SCS, using urea ($CO(NH_2)_2$) as fuel, $Ca(NO_3)_2 \cdot 4H_2O$ as calcium source/oxidizer, $(NH_4)_2HPO_4$ as phosphate source and HNO_3 as additive;
2. 8h duration milling treatment, for breaking the formed agglomerates;
3. uniaxial pressing at 200MPa of the obtained powders;
4. pressureless sintering for 2 h at 1230°C.

The obtained samples show low residual porosities, i.e. $< 6\%$ (aqueous) and $< 2\%$ (HNO_3). Similarly, the preparation of HA products carried out by Ghosh et al. (2018) [253] involved the following processing steps:

1. SCS, using citric acid ($C_6H_8O_7$) as fuel, $Ca(NO_3)_2 \cdot 4H_2O$ as calcium source/oxidizer, $(NH_4)_2HPO_4$ as phosphate source and HNO_3 as additive;
2. powder calcination up to 1300°C;
3. cold pressing of calcinated powder in presence of 6% PVA;
4. pressureless sintering for at 1200 and 1250°C.

Although both studies evidenced the importance of the obtainment of small grains size of apatite, similar to that present on natural tissues, such information was not reported for the sintered samples. However, it is expected that the adopted sintering temperatures (equal or above 1200°C) during steps 4 are too severe to retain the original grains size of SCSed apatite at the nanoscale. In this sense, a more efficient densification technique to process the powders at milder conditions, is desirable.

To this, the present work is aimed to produce bulk nanostructured apatite-based bioceramics by combining, for the first time for this type of materials, the SCS method with the efficient SPS technology. Specifically, the influence of the fuel to oxidizer ratio (ϕ) on the synthesis reaction ignition and product composition will be initially systematically studied. Then, the effect of the annealing temperature on the compositional and microstructural characteristics of the resulting powders will be analysed in detail with the aim to minimize the presence of secondary phases. Finally, bulk nanostructured biphasic HA-TCP samples will be produced under optimal SPS conditions.

4.2 Materials and methods

4.2.1 Powders synthesis

The procedure adopted for the solution combustion synthesis of apatite, shown in Figure 4.1, was adapted from that proposed by Ghosh et al. (2011) [254]. Aqueous solutions of calcium nitrate tetrahydrate ($Ca(NO_3)_2 \cdot 4H_2O$ >99.0%, Sigma-Aldrich, Italy) and diammonium phosphate ($(NH_4)_2HPO_4$ >99.0%, Sigma-Aldrich, Italy) were prepared with concentrations of 2.72M and 2.09M, respectively. Subsequently, such solutions were combined in proper amounts to match the stoichiometry of the following base reaction:

$$\begin{aligned} 10\,Ca(NO_3)_2 \cdot 4\,H_2O + 6(NH_4)_2HPO_4 + \phi\frac{100}{9}NH_2CH_2COOH + 9O_2 = \\ = Ca_{10}(PO_4)_6(OH)_2 + \frac{194}{9}N_2 + \frac{200}{99}CO_2 + \frac{844}{9}H_2O \end{aligned} \tag{4.1}$$

where ϕ is the fuel to oxidizer ratio. The solution was kept under continuous stirring until a white precipitate is formed. 14M nitric acid solution (70% HNO_3 > 99.99%, Sigma-Aldrich, Italy) was then added dropwise to adjust the pH value to 1, and the resulting clear solution was stirred for 15 min. The fuel, glycine (NH_2CH_2COOH ReagentPlus >99%, Sigma-Aldrich, Italy), was then introduced to the solution in proper quantities, depending on the value of the ϕ parameter (varied in the range 0.7 to 1.4), according to Equation 4.1 [254]. After additional 15 min of stirring, the dehydration phase started. The temperature of the solution was kept in the temperature range 70-80°C for a total time of 20 min, using a heating plate (mod. TK22, Kartell, Italy). The temperature of the plate was then increased to its maximum value of 370°C until the combustion synthesis reaction occurred. The resulting powders were then grounded in an agate mortar and, to remove/reduce undesired secondary phases, subsequently heat treated in a muffle furnace (mod. LT 24/11/B410, Nabertherm, Lilienthal, Germany), at temperatures ranging from 600 to 900°C.

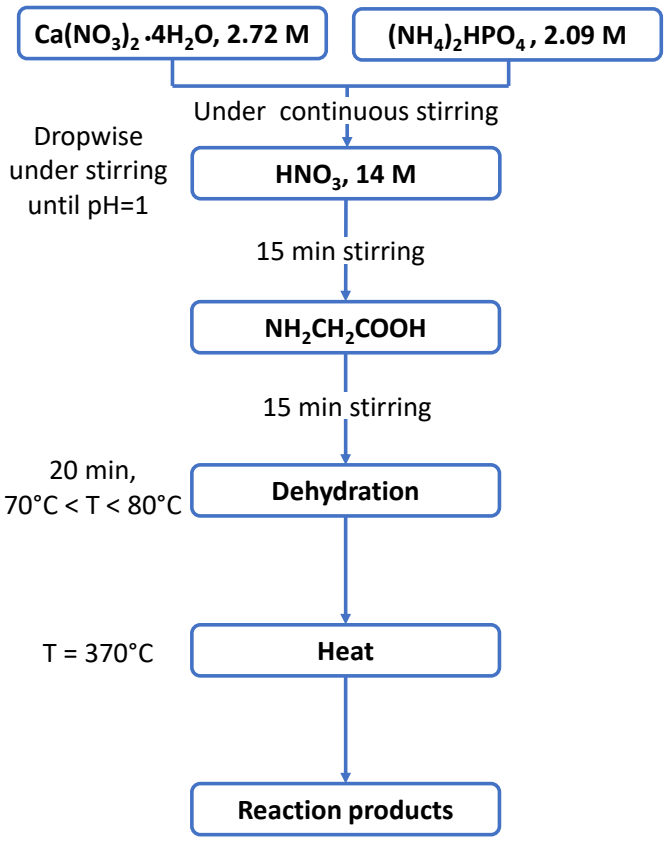

Figure 4.1: Schematic representation of the experimental procedure of solution combustion synthesis of apatite-based powders.

Annealing consisted of heating the powders for 3 h at the holding temperature, which was reached at 5°C/min, whereupon, a natural cooling step. To guarantee the reproducibility of the process, each test was replicated at least twice.

4.2.2 Bulk samples

Powder consolidation was carried out using the SPS equipment 515S model and following the same procedure described in Chapter 2.

The temperature was firstly increased at a rate of 50°C/min from the room value to a level, 100°C below the maximum (T_D). To limit possible overshooting problems, the final T_D value

was then reached at the lower rate of 10°C/min. The 5 min isothermal heating at T_D was followed by temperature decrease at a rate of 50°C/min down to 300°C, followed by a natural cooling step. The applied pressure (P) was raised to 70 MPa in about 1 min, then maintained constant during both non-isothermal and isothermal heating steps, and, finally, gradually reduced during sample cooling. Various bulk samples were produced at different T_D conditions, in the range 750-900°C. They were accurately grounded/polished using abrasive paper, to remove residual impurities from the graphite tools, to provide final cylindrical disks of about 14.7 mm diameter and 2.5-3 mm height. Each experimental condition was replicated at least twice.

4.2.3 Characterization

The composition and microstructure of both the powders and bulk samples was first assessed by X-Ray Diffraction (XRD) analysis (Philips PW 1830, Netherlands) using a Cu Kα radiation, under the following experimental conditions: Range: 10-130°; Step: 0.05°; dwell time: 10 sec. Phases, their amount (wt.%) and the related structural parameters were estimated according to the Rietveld method, using the MAUD program [195].

Raman measurements were carried out using a MS750 spectrograph (sol-instruments, Minsk, Belarus) equipped with 1200-600 gr/mm grating. The laser beam (λ=785 nm), with a power of about 7.5 mW, was focalized by means of Olympus objectives (50x and 100x). Measurements were performed at room temperature, with a spectral resolution of 1 $c\,m^{-1}$. At least ten acquisitions, each resulting from an average of three measures of 120 s, were taken in different parts of each examined sample.

Furthermore, detailed scanning electron microscopy (SEM) and transmission electron microscopy (TEM) analyses were conducted to investigate the composition, morphology, and atomic structure of both powders and SPSed samples. Specifically, a Helios Nanolab 600 instrument (Thermo Fisher Scientific), equipped with a dual electron/ion beam system was used to both acquire secondary-electron SEM images and for the preparation of $\approx$ 70 nm thin

slices for cross-sectional TEM measurements.

Powders and compact samples were coated by an iridium layer (2.5 nm thick) prior to SEM measurements. Secondary electron imaging was conducted in both field-free and field-emission modes.

A Titan 300 TEM equipment (FEI,USA, with resolution: 0.136 nm in scanning mode, information limit: $\approx$ 0.1 nm at high-resolution mode) was employed to examine the synthesised powders. About 0.1 g of the material were sonicated in 10 ml of deionized water for 10 minutes, few drops of it were placed onto a 300 mash Cu TEM grid with lacey carbon films and naturally dried overnight. A cleaning procedure in 20%$O_2 - Ar$ plasma was performed for 1 minute prior to measurements.

Thin slices were prepared for the TEM analysis from bulk samples. A 1 μm thick platinum layer was deposited onto a selected rectangular area of 10 μm x 0.5 μm. Approximately 5 μm deep trenches (with a 52 °base angle) were milled by a gallium beam on both sides of the carbon layer (accelerating voltage: 5 keV, milling current: 27 nA). Then, the slice was lifted from the sample and polished to about 70 nm thickness under an accelerating voltage of 5 keV and a milling current of 700 pA. In this way, a clean cross-section of the samples for TEM images was produced, without milling artifacts. Spectra 300 TEM microscope (Thermo Fisher Scientific, resolution: 50 pm at 300 kV in scanning TEM mode) equipped with GIF Continuum K3 camera (Gatan, to perform low-dose high-resolution imaging in beam-sensitive samples) was used for the TEM analyses of the prepared thin slices. EDS analysis was carried out by an EDS (Bruker) Si(Li) detector (energy resolution of $\approx$ 25 eV at 5.9 keV).

TEM images were then processed by the software ImageJ [255], while TEM-derived diffraction patterns were examined by the software ProcessDiffraction [256]. Finally, all the d-spacing assignment are based on the calculations made by the software VESTA [257]. The density of the bulk samples was measured by the Archimedes' method using ethanol as immersing medium and an Ohaus Explorer Pro (Ohaus Corporation, NJ, USA) analytical balance ($\pm$ 0.0005 g precision) to weight them.

4.3 Results and discussion

4.3.1 Solution combustion synthesis

The effect produced by an increase of ϕ value on the ignition time of the SCS reaction (Equation 4.1) is shown in Figure 4.2 a. The reaction ignition did not occur, at least within 45 min after the beginning of the experiment, for $\phi = 0.7$ or lower values as well as when this parameter equals or exceeds 1.4. Moreover, the condition under which the reaction ignition was observed to occur earlier is $\phi = 1$ (stoichiometric mixture) whereas it took longer time periods for lower of higher values of this parameter. In any case, the process lasted less than 15 min.
The XRD patterns of the synthesised products obtained for different ϕ values are compared in Figure 4.2 b), from which it is possible to note that apatite is always the main phase present in the synthesised products, regardless of the specific ϕ value adopted. In this regard, the relative intensities of the apatite peaks at 32.34 and 33.08 °are coherent with the one of A-type substitution in Carbonated apatite phases (as defined in section 1.1.2). Indeed, while peak intensity at 33.08°in stoichiometric apatite is relatively higher than that at 32.34 °, the opposite occur in carbonated apatite [258].
Apart from apatite, some secondary phases are also present in the synthesised powders, namely TCP (in both α and β forms), $CaCO_3$, $CaHPO_4$, and small amounts of CaO. Due to XRD patterns complexity and wide peaks associated to the nanostructured nature of the synthesised powders, the general trend for the content of secondary phases is not easy to obtain. Nonetheless, it is possible to state that lower amounts of $CaHPO_4$ and $CaCO_3$ are achieved when ϕ is in range 1.0-1.2. In addition, XRD peaks intensity of the TCP phase are minimized when operating at $\phi = 1.1$.
Accordingly, the related powders were characterised in more detail by the Rietveld analysis, to assure of the phases present and estimate quantitatively their amount. The obtained results are reported in Figure 4.3 a and Table 4.1.

The phases identified by this analysis and their relative amounts (wt.%) are: apatite (47.4), $CaHPO_4$ (20.8), $\beta - TCP$ (11.9), $CaCO_3 \cdot 6(H_2O)$ (9.6), α-TCP (6.4), $CaCO_3$ (3.7), and CaO (0.2). However, the presence of possible additional minor phases is not excluded.

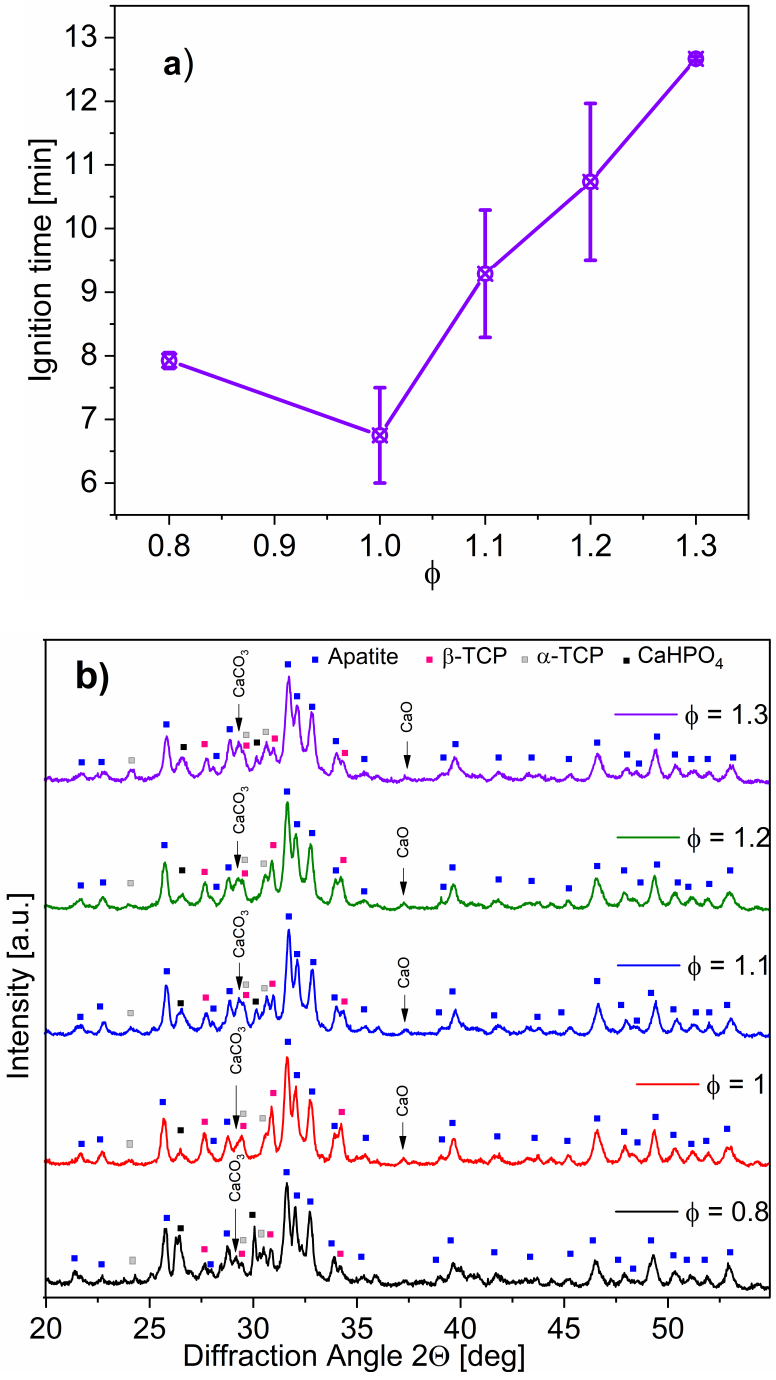

Figure 4.2: Effect of the fuel to oxidizer ratio (ϕ) on a) the ignition time of the SCS reaction, and b) the composition of the resulting products.

Furthermore, the estimation provided by Rietveld analysis for crystallites average size of apatite in SCS powder is approximately 65 nm.

The SCS products obtained for $\phi = 1.1$ were heat treated at different temperatures in the range 600-900°C, and the resulting powders characterised by XRD analysis taking advantage of the Rietveld method. The XRD patterns corresponding to 600 and 700°C are shown in Figure 4.3 b)-c), respectively, whereas microstructural parameters and amount of each phase are reported in Table 4.1. The latter contains the results of all the analysed samples. For the sake of comparison, relative phases amount as well as crystallites size of apatite and β-TCP are plotted in Figure 4.4 a) and b), respectively, as a function of the annealing temperature.

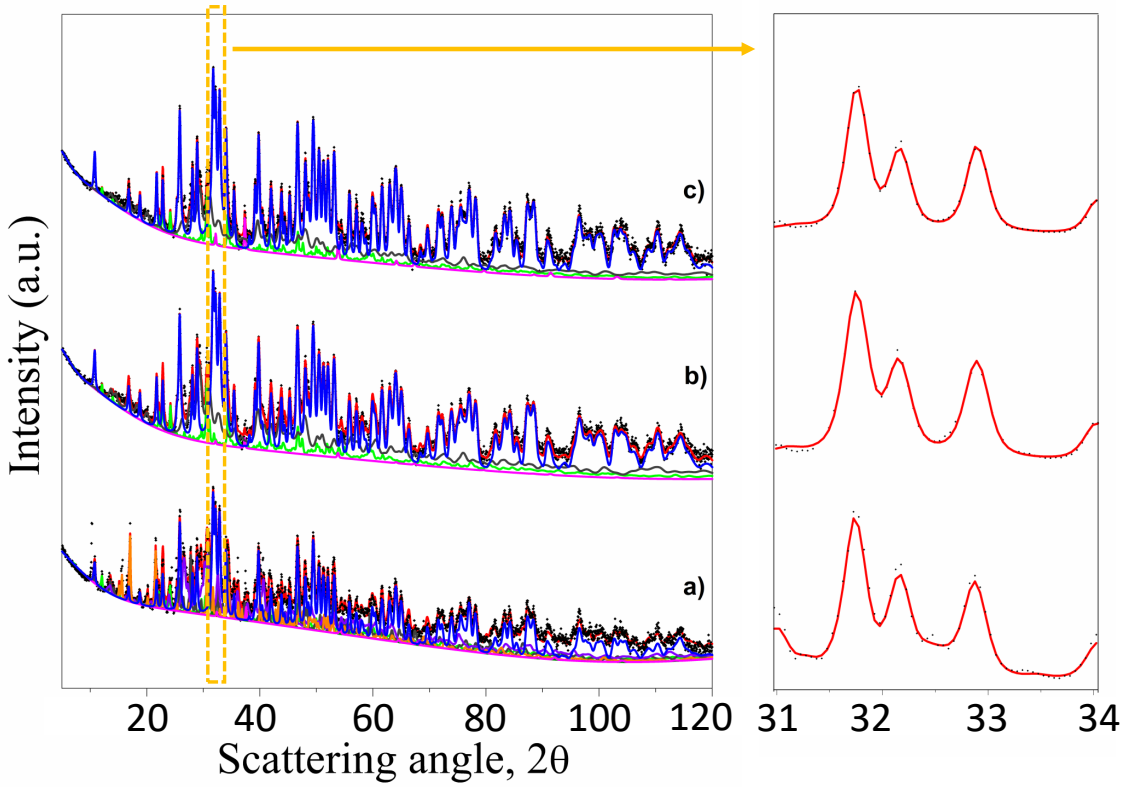

Figure 4.3: XRD patterns (log-scale) of SCSed powders (ϕ=1.1) before (a) and after 3h heat treatment at 600°C (b) and 700 °C (c). Black dots: experimental. Red line: fit. Apatite: Blue line. Calcium oxide (CaO): magenta line. Calcium Carbonate ($CaCO_3$): wine line. Ikaite ($CaCO_3 \cdot 6(H_2O)$): orange line. $CaHPO_4$: violet line. β-TCP: Dark grey. α-TCP: light green line. Details of XRD patterns (linear scale) in the 2Θ range 31-34°are shown on the right side of the figure.

As synthesised powders										
Phase	**%**	**a** [Å]	**b** [Å]	**c** [Å]	α [°]	β [°]	γ [°]	**Space Group**	**Cryst.size** [Å]	**Microstrain**
Apatite	47.4	9.4315	-	6.8874	-	-	-	P63/m	655	$9.99 \cdot 10^{-4}$
β-TCP	11.9	10.4401	-	37.3990	-	-	-	R3c:H	815	$9.17 \cdot 10^{-4}$
CaO	0.2	4.7850	-	-	-	-	-	Fm-3m	898	$7.29 \cdot 10^{-4}$
$CaCO_3$	3.7	6.3499	4.9862	8.0796	-	106.43	-	P21/c:b1	1001	$1.01 \cdot 10^{-4}$
$CaCO_3 \cdot 6H_2O$	9.6	8.6803	8.2867	10.9423	-	108.53	-	C2/c:b1	1467	$5.80 \cdot 10^{-4}$
$CaHPO_4$	20.8	6.8950	6.5678	6.9700	96.47	103.79	89.37	P1	317	$5.21 \cdot 10^{-4}$
α-TCP	6.4	12.8870	27.2800	15.2190	-	126.20	-	P21/c:b3	1000	$6.00 \cdot 10^{-4}$
Heat treated powders - 600 °C										
Phase	**%**	**a** [Å]	**b** [Å]	**c** [Å]	α [°]	β [°]	γ [°]	**Space Group**	**Cryst.size** [Å]	**Microstrain**
Apatite	78.6	9.4276	-	6.8925	-	-	-	P63/m	595	$1.20 \cdot 10^{-3}$
β-TCP	17.4	10.5437	-	36.5052	-	-	-	R3c:H	162	$1.20 \cdot 10^{-3}$
CaO	0.1	4.8159	-	-	-	-	-	Fm-3m	901	$7.24 \cdot 10^{-4}$
α-TCP	3.9	12.9191	27.1543	15.3105	-	126.45	-	P21/c:b3	967	$6.15 \cdot 10^{-4}$
Heat treated powders - 700 °C										
Phase	**%**	**a** [Å]	**b** [Å]	**c** [Å]	α [°]	β [°]	γ [°]	**Space Group**	**Cryst.size** [Å]	**Microstrain**
Apatite	83.0	9.4274	-	6.8906	-	-	-	P63/m	672	$1.10 \cdot 10^{-3}$
β-TCP	13.5	10.5165	-	36.6457	-	-	-	R3c:H	154	$1.20 \cdot 10^{-3}$
CaO	0.3	4.8127	-	-	-	-	-	Fm-3m	900	$7.23 \cdot 10^{-4}$
α-TCP	3.2	12.9088	27.2135	15.2589	-	126.30	-	P21/c:b3	974	$6.11 \cdot 10^{-4}$
Heat treated powders - 800 °C										
Phase	**%**	**a** [Å]	**b** [Å]	**c** [Å]	α [°]	β [°]	γ [°]	**Space Group**	**Cryst.size** [Å]	**Microstrain**
Apatite	72.1	9.4270	-	6.8871	-	-	-	P63/m	949	$6.52 \cdot 10^{-4}$
β-TCP	26.9	10.4379	-	37.4375	-	-	-	R3c:H	1444	$9.26 \cdot 10^{-4}$
CaO	1.0	4.8148	-	-	-	-	-	Fm-3m	983	$6.60 \cdot 10^{-4}$
Heat treated powders - 900 °C										
Phase	**%**	**a** [Å]	**b** [Å]	**c** [Å]	α [°]	β [°]	γ [°]	**Space Group**	**Cryst.size** [Å]	**Microstrain**
Apatite	69.4	9.4258	-	6.8864	-	-	-	P63/m	1128	$4.83 \cdot 10^{-4}$
β-TCP	29.9	10.4382	-	37.4344	-	-	-	R3c:H	1437	$8.00 \cdot 10^{-4}$
CaO	0.7	4.8131	-	-	-	-	-	Fm-3m	1027	$7.32 \cdot 10^{-4}$

Table 4.1: Microstructural parameters and amount of each phase present on the as synthesised and differently heat treated SCSed powders (ϕ=1.1), as estimated by the Rietveld analysis performed on the related XRD patterns (Figure 4.3).

It is found that the larger relative amount of apatite in the product is obtained when the SCSed powders are annealed at 700°C. On the other hand, an increase of the temperature to 800°C or higher values produces the partial transformation of apatite to β-TCP. A marked crystallite growth is also observed when the heat treatment temperature exceeded 700°C.

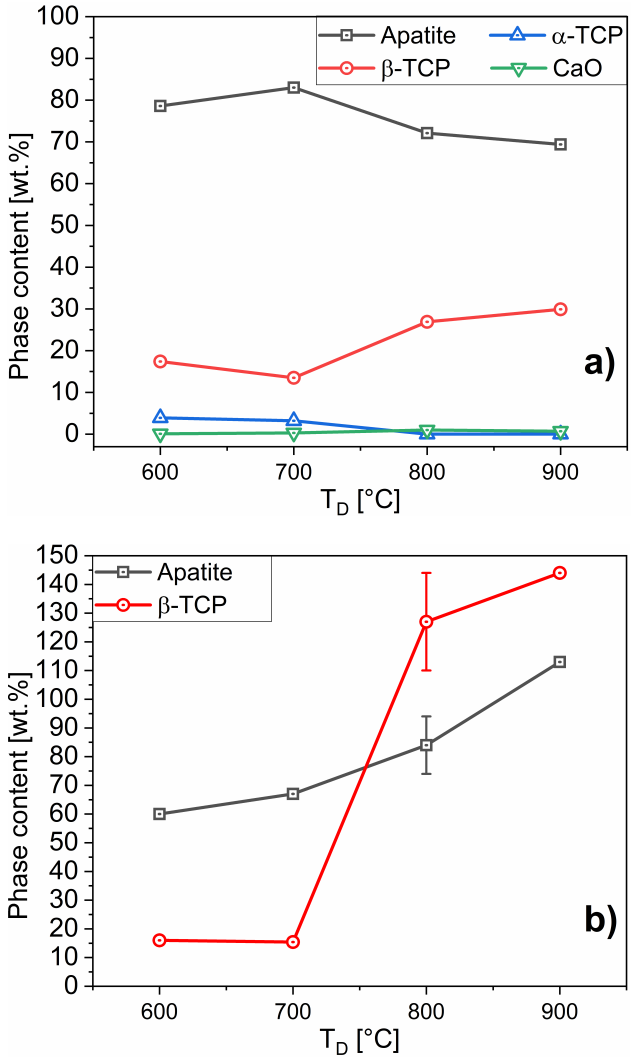

Figure 4.4: Effect of annealing temperature on a) phases amount and b) crystallite size of SCSed products (ϕ=1.1).

Powder samples synthesised with $\phi = 1.1$ before and after their annealing at different temperature conditions have been also examined by Raman analysis. The obtained results are reported and compared in Figure 4.5 a)-b). Figure 4.5 a) indicates that the $\nu_1 - PO_4$ mode at 960 cm^{-1} (main one of apatite) is the most intense in all the reported spectra, supporting the fact that apatite is the principal phase in the as-synthesised powders and well as in the annealed products, regardless the heat-treatment conditions adopted. In addition, as evidenced in Figure 4.5 b), the FWHM of such peak decreases when increasing the annealing temperature, suggesting that crystallites growth takes place.

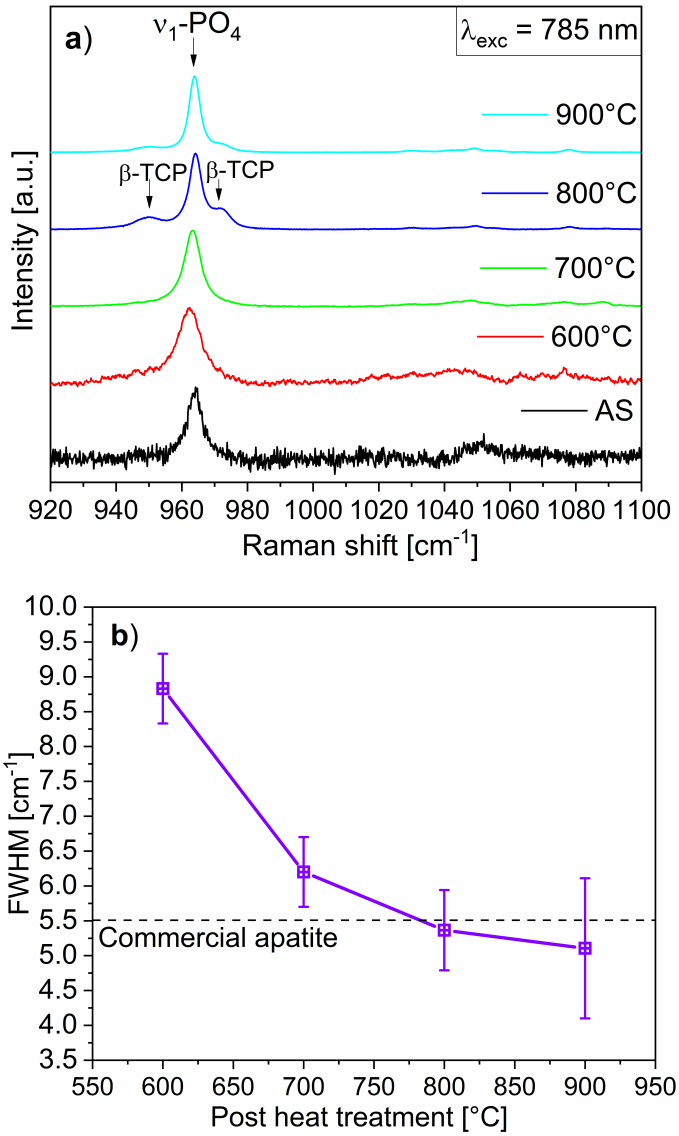

Figure 4.5: (a) Raman spectra of SCSed powders (ϕ=1.1) before and after being heat treated at different temperatures. (b) FWHM of the 960 cm^{-1} peak resulting from fitting procedure as a function of the post heat treatment temperature.

Furthermore, β-TCP peaks are clearly seen in spectra corresponding to samples heat treated at 800 and 900°C. This finding is evidenced in more detail in Figure 4.6 where it is seen that the signal of β-TCP significantly increases when the annealing temperature is augmented from 700 to 800°C. This outcome is consistent with the Rietveld analysis results shown in Figure 4.3 a) and Table 4.1, and can be readily justified by the partial apatite decomposition into β-TCP as annealing temperature levels overcome 700°C. The Raman spectra part enclosed by

the green box in Figure 4.6 displays a reduction of the intensity of the 1086 cm^{-1} peak (calcium carbonate main Raman peak) as the annealing temperature is augmented. This is consistent with the $CaCO_3$ dissociation temperature of approximately 800°C [259]. In this regard, the fact that $CaCO_3$ was not revealed by XRD in samples heat treated at 700°C is likely due to its quantity, since its content is below the detection limit for this analysis.

Another important information is provided by the Raman spectra delimited by the red box in Figure 4.6, which is related to the bands analysed to estimate the carbonation level of apatite. Following Awonusi et al. (2007) [206], a fitting procedure was carried out to calculate the area of the 1075 cm^{-1} peak ($\nu_3 - PO_4$) with respect to the $\nu_1 - PO_4$ one. The obtained results, summarized in Table 4.2, indicate that the heat treatment carried out at 700°C allows the apatite phase to maintain a residual carbonation level of approximately 2 wt.%. On the other hand, treatments conducted at 800°C or higher temperatures apparently lead to apatite decarbonation. It should be noted that carbonation data reported in Table 4.2 refer only to B-type substitution, since the previously cited fitting procedure involves only $\nu_3 - PO_4$ bands.

Heat treatment temperature [°C]	**CO_3 amount [wt/%]**
700	≈2
800	0
900	0

Table 4.2: Estimated CO_3 as a substituent at B-site as a function of post-heat treatment temperature.

Four SEM images relative to the SCSed powders (ϕ=1.1) prior and after being annealed at 700°C are reported in Figure 4.7 a)-c) and Figure 4.7 b)-d), respectively. From these micrographs, it can be clearly seen that the heat treatment provided powders with more defined nanosized grains (Figure 4.7 b-d) compared to the as-synthesised ones (Figure 4.7 a-c). This holds also true for the case of $\phi = 1$ (not shown).

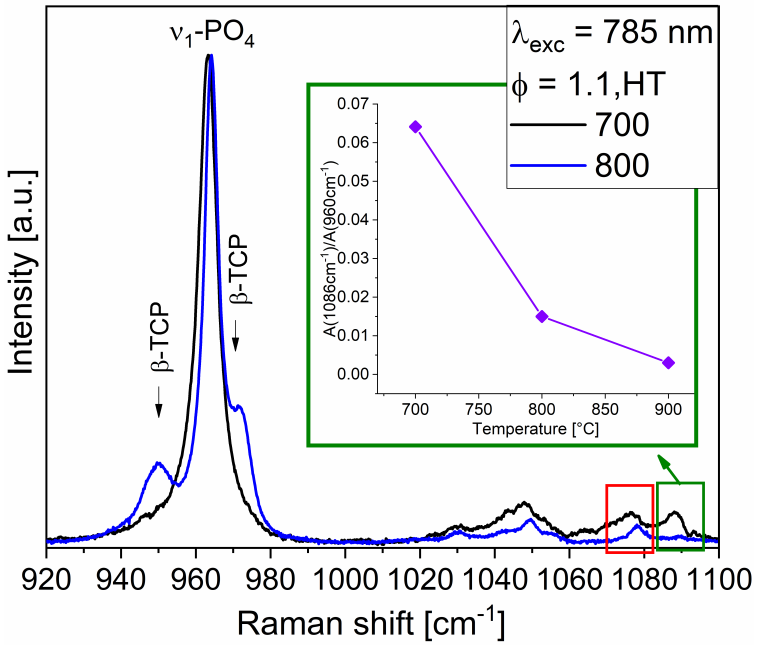

Figure 4.6: Raman spectra of SCSed powders (ϕ=1.1) before and after being heat treated at different temperatures. In the green box, the intensity of 1086 $c\,m^{-1}$ band with respect to the 960 $c\,m^{-1}$ one.

To complete their characterization, untreated and annealed powders have been also examined by TEM. In this regard, it should be noted that stoichiometric compounds (i.e. HA, TCP, etc.) were used as literature data reference for TEM analysis, i.e. all the d-spacing and angles related to each lattice corresponded to stoichiometric formulations, instead of the non-stoichiometric phases possibly formed during SCS.

As for the as-synthesised powders, TEM observations evidenced the presence of two different types of structures, indicated hereto after as Structure 1 and Structure 2, which will be examined in what follows.

A bright-field image of Structure 1 is shown in Figure 4.8 a)-c) along with the corresponding SADP results. Figure 4.8 b) and c) indicate that the obtained diffraction pattern corresponds to an amorphous structure. However, Figure 4.8 c), resulting from longer exposure to the electron beam of the same spatial region, also evidenced some diffraction spots present at different positions. This is assumed to be the result of the occurrence of the partial transition of the amorphous phase to a crystalline one, apparently induced by the electron beam.

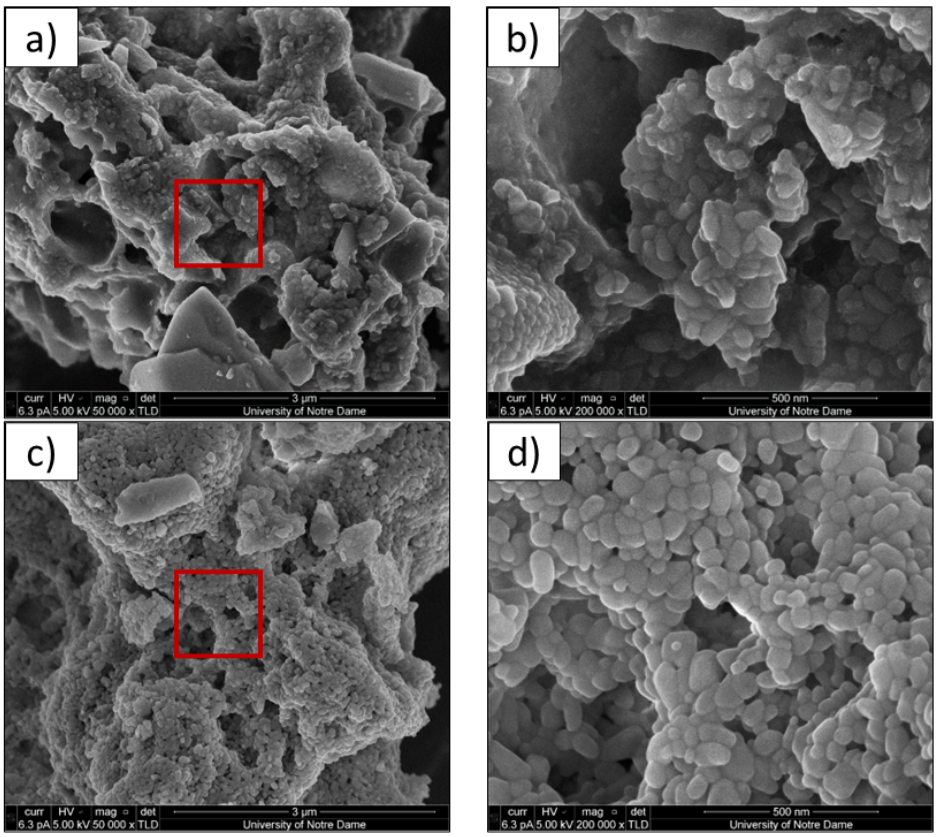

Figure 4.7: General and detailed SEM micrographs of SCSed powders (ϕ=1.1) before (a)-(c) and after (b)-(d) being heat treated at 700°C.

The distance between such diffraction spots was then converted into d-spacing in the direct lattice. The obtained values, indicated in the same figure, are compared to those of HA. The resulting 2.3/2.5 Å values are rather close to (2, 2, 0) and (3, 0, 1) planes' d-spacing (2.35 and 2.52 Å, respectively), while 1.68/1.72 Å values are similar to (0, 0, 4) and (1, 0, 4) planes' d-spacing (1.682 and 1.719 Å, respectively). A bright-field image of Structure 2 and the related diffraction analysis results are reported in Figure 4.9 a)-c). In this case, the crystalline nature of such structure is evident. The corresponding diffraction pattern relative to a grain size of about 1 μm is shown in Figure 4.9 b), while the corresponding diffraction distribution in terms of scattering vector is represented by the red line in Figure 4.9 c). The latter figure also reports the nominal position (vertical lines and relative Miller indices) of scattering vectors of stoichiometric HA and some of β-TCP. The thickness of the vertical lines is proportional to the nominal intensity of the indicated planes' signal.

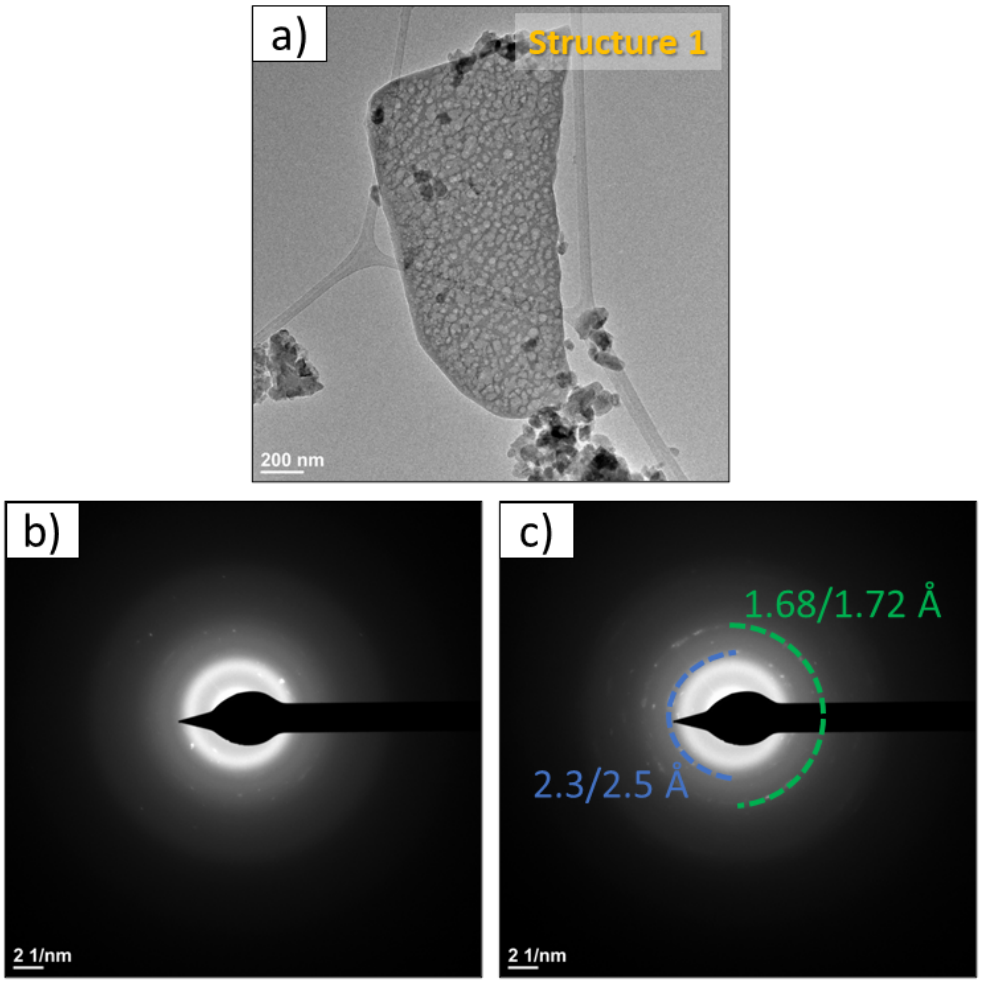

Figure 4.8: a) Low magnification bright field image of Structure 1 type identified in as synthesised powders (ϕ=1.1) and related SADP detected by TEM imaging after relatively shorter b) and longer c) time exposures.

From this figure, it is apparent that the diffraction distribution is well described by the HA structure, with minor amounts of β-TCP. On the other hand, the comparison with nominal values of other possible phases (α-TCP, $CaCO_3$, etc.) did not result in any match.

To provide additional information, high resolution-TEM (HR-TEM) imaging are also provided in Figure 4.12. The angle between m and n directions is 92°. The d-spacing of 2.73 Å, measured by the TEM image above, could be assigned to the (3, 0, 0) planes of the apatite structure (nominal value 2.72 Å), while the d-spacing of 1.72Å could be ascribed to the (0, 0, 4) planes of the same structure (nominal value of 1.72 Å).

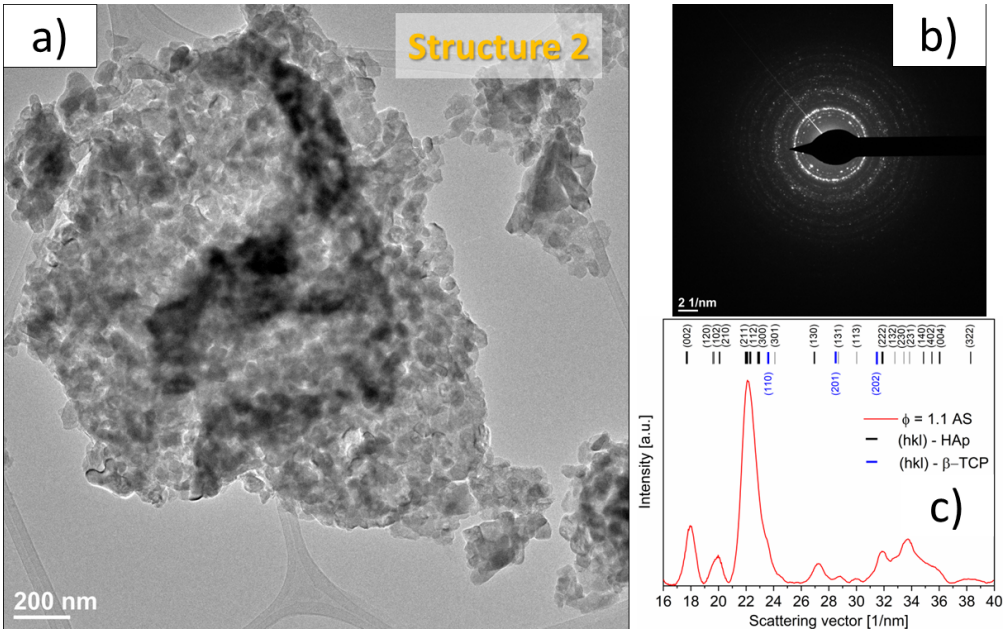

Figure 4.9: a) Bright field image of Structure 2 type identified in as synthesised powders (ϕ=1.1), the related b) electron diffraction pattern, and c) diffraction intensities as a function of the scattering vector.

The calculation of the angle between the previous cited directions (by means of scalar product) is 90°(as quite obvious from the h,k,l indexes), which is compatible with that measured of approximately 91°.

The distance between the atoms across the q and r directions is 3.12 Å. Furthermore, the measured angle between the r and q directions is approximately 57°. Stoichiometric apatite's (1, 2, 0) and (2, 1, 0) planes, with nominal d-spacing of 3.09 Å for both, enclose an angle of 60°. The same analysis was carried out for the case of SCSed products annealed at 700 °C. The results, referred to particles of 1-2 μm size, are reported in Figure 4.11.

Figure 4.11 c) shows the diffraction distribution in terms of scattering vector (red line) and the nominal position (vertical lines and relative Miller indices) of scattering vectors of stoichiometric HA and β-TCP. The thickness of the vertical lines is proportional to the nominal intensity of the indicated planes signal. The diffraction distribution is generally well described by the HA structure, with β-TCP as minor phase. This finding agrees with Rietveld analysis results reported in Table 4.1.

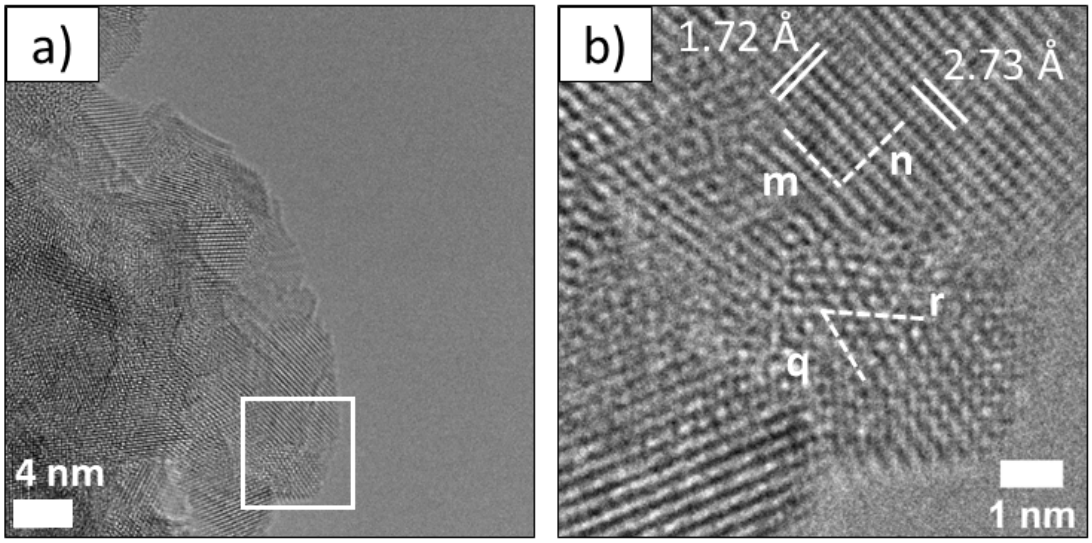

Figure 4.10: (a) HR-TEM imaging of as synthesised powders (ϕ=1.1), and (b) magnification of the area confined by the white box.

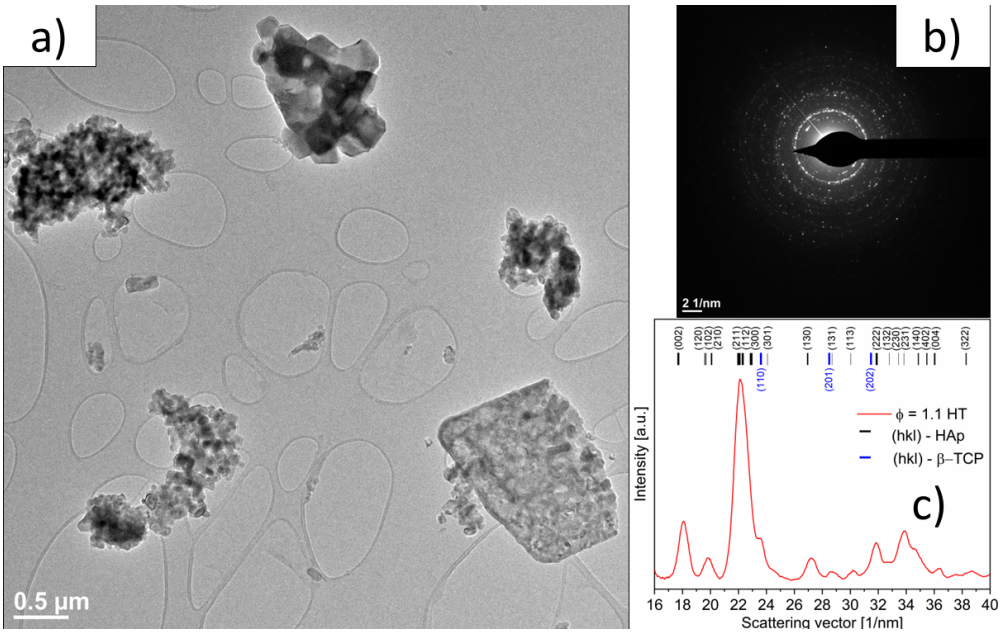

Figure 4.11: a) Bright-field image of SCSed powders (ϕ=1.1) after being heat treated at 700°C, related b) electron diffraction pattern, and c) diffraction intensities as a function of the scattering vector.

The results obtained by the HR-TEM imaging analysis are reported in Figure 4.12. The d-spacing of 3.24 and 3.08 Å measured by the image could be ascribed to the (1, 0, 2) and (2, 1, 0) planes of the apatite structure (nominal value for HA equal to 3.17 and 3.09 Å , respectively). It

should be noted that the calculation of the angle between the previously cited directions (by means of scalar product) is of approximately 61°, which is compatible with that measured of approximately 59°. Moreover, the d-spacing of 2.67 and 2.76 Å determined from TEM images could be related to the (1, 1, 0) and (1, 0, 2) planes of the β-TCP structure (nominal values of 2.70 Å and 2.95 Å , respectively). Also in this case, the calculation of the angle between the latter directions provided a value of 81°, which is compatible with that measured of approximately 86°. To conclude, TEM data confirmed the presence of both crystalline apatite and β-TCP structures in heat-treated samples, further confirming the outcomes of Rietveld analysis.

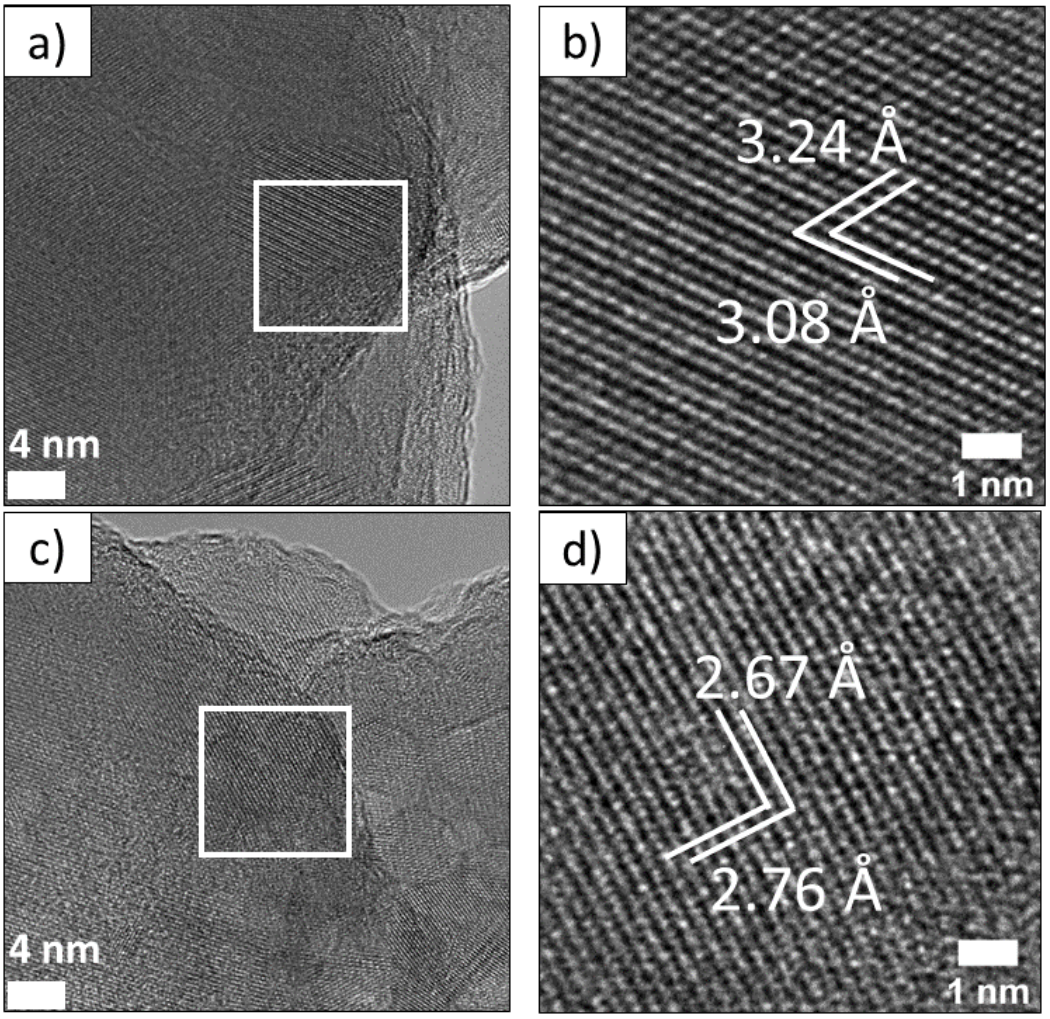

Figure 4.12: HR-TEM imaging of two regions of SCSed powders (ϕ=1.1) after being heat treated at 700°C and magnification of the areas described by white boxes: a)-b) region 1 and c)-d) region 2.

4.3.2 Powder consolidation and bulk products characterization

The SCSed powders heat treated at 700°C were processed by SPS to obtain bulk samples. The XRD patterns of samples sintered at different temperature conditions are shown in Figure 4.13. The detected phases, their content, and the associated microstructural parameters resulting from Rietveld analysis are reported in Table 4.3. The data regarding the phases amounts and crystallite size are also plotted in Figure 4.14 a) and b), respectively, to provide a clear description of the effect of the increasing sintering temperature on such characteristics. In addition, the density values of the samples processed at different temperatures is reported in Figure 4.14 c).

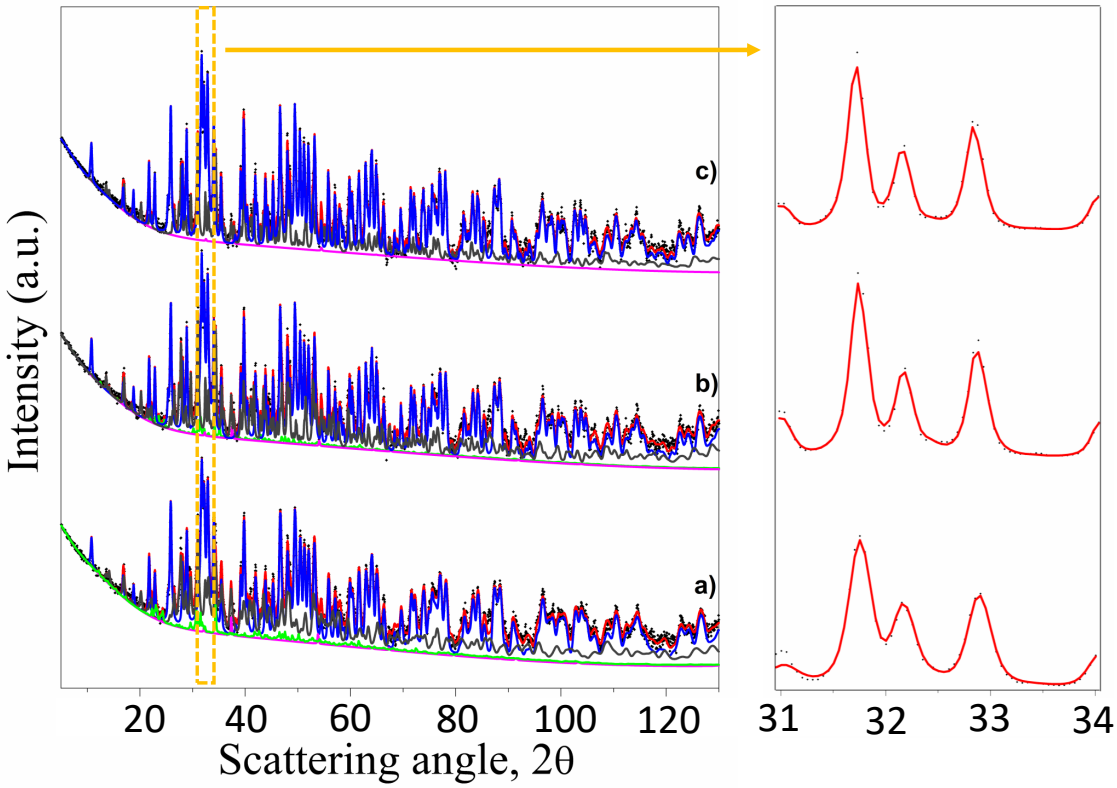

Figure 4.13: XRD patterns (log-scale) of bulk samples obtained at different temperatures by SPS from SCSed powders (ϕ=1.1): (a) 750°C, (b) 850°C, and (c) 900°C. Black dots: experimental. Red line: fit. Apatite: Blue line. Calcium oxide: magenta line. β-TCP: Dark grey. α-TCP: light green line.The fraction of the pattern between 31 and 34 °(yellow dashed box) reported at the right side of the figure. Details of XRD patterns (linear scale) in the 2Θ range 31-34°are shown on the right side of the figure.

SPS product T_D = 750 °C										
Phase	**%**	**a** [Å]	**b** [Å]	**c** [Å]	α [°]	β [°]	γ [°]	**Space Group**	**Cryst.size** [Å]	**Microstrain**
Apatite	76.2	9.4294	-	6.8883	-	-	-	P63/m	676	$1.49 \cdot 10^{-3}$
β-TCP	21.9	10.4379	-	37.4750	-	-	-	R3c:H	364	$1.33 \cdot 10^{-4}$
CaO	0.1	4.8144	-	-	-	-	-	Fm-3m	908	$6.59 \cdot 10^{-4}$
α-TCP	1.8	12.9869	27.0918	14.8861	-	126.5448	-	P21/c:b3	676	$6.36 \cdot 10^{-4}$
SPS product T_D = 850 °C										
Phase	**%**	**a** [Å]	**b** [Å]	**c** [Å]	α [°]	β [°]	γ [°]	**Space Group**	**Cryst.size** [Å]	**Microstrain**
Apatite	76.5	9.4340	-	6.8858	-	-	-	P63/m	783	$3.52 \cdot 10^{-4}$
β-TCP	23.1	10.4279	-	37.4990	-	-	-	R3c:H	761	$2.13 \cdot 10^{-4}$
CaO	0.1	4.7948	-	-	-	-	-	Fm-3m	912	$6.65 \cdot 10^{-4}$
α-TCP	0.3	12.7298	26.3054	14.8115	-	124.5682	-	P21/c:b3	631	$6.47 \cdot 10^{-4}$
Heat treated powders - 900 °C										
Phase	**%**	**a** [Å]	**b** [Å]	**c** [Å]	α [°]	β [°]	γ [°]	**Space Group**	**Cryst.size** [Å]	**Microstrain**
Apatite	77.9	9.4465	-	6.8850	-	-	-	P63/m	1132	$4.68 \cdot 10^{-4}$
β-TCP	22.0	10.4252	-	37.4930	-	-	-	R3c:H	958	$2.20 \cdot 10^{-4}$
CaO	<0.1	4.7522	-	-	-	-	-	Fm-3m	908	$6.27 \cdot 10^{-4}$

Table 4.3: Microstructural parameters and amount of each phase present on bulk samples obtained at different temperatures by SPS from SCSed powders (ϕ=1.1), as estimated by the Rietveld analysis performed on the related XRD patterns (Figure 4.13).

Raman measurements were carried out on the three differently sintered samples,and the associated spectra are reported in Figure 4.15. Also in this case, the ν_1 mode of the phosphate group is the most intense one independently of the sintering temperature, further supporting the major presence of apatite. In addition, β-TCP bands indicate that an increase of this phase occurred after SPS, which is also consistent with the results arising from the Rietveld analysis.

Similarly to the case of SCSed powders, the fitting procedure proposed by Awonusi et al. (2007) [206] was carried out also when considered the SPS samples, to calculate the area of the 1075 cm^{-1} peak ($\nu_3 - PO_4$) with respect to the 960 cm^{-1} one. Accordingly, no residual B-type CO_3^{2-} was detected by means of Raman analysis, to confirm that apatite decarbonation took place during the sintering process. In this regard, an important role is likely played by the environmental conditions (vacuum) adopted to perform SPS experiments, which are expected to favour the occurrence of decarbonation phenomena.

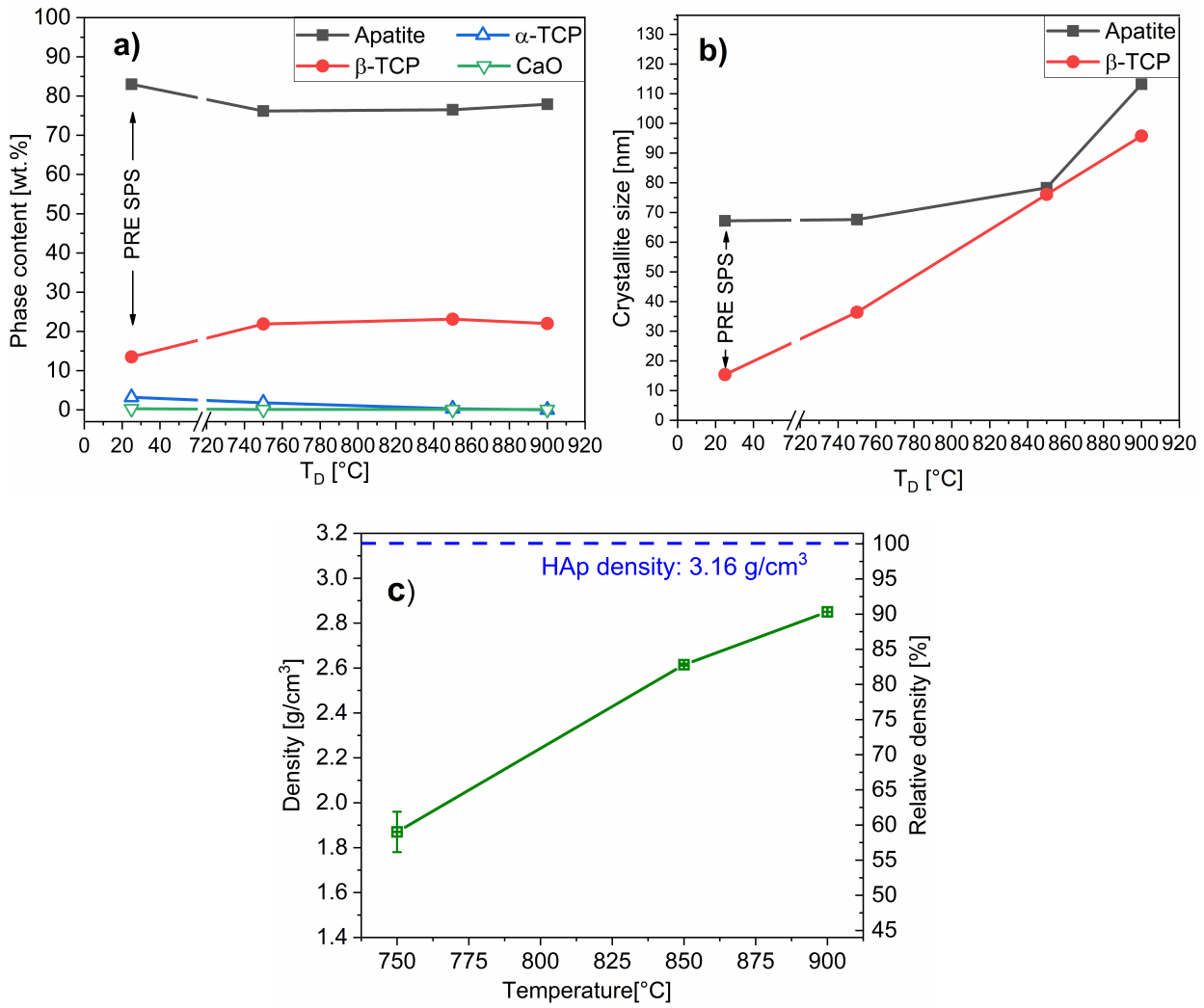

Figure 4.14: Effect of the dwell temperature (T_D) on a) the phases' amount, b) crystallite size, and c) density of SPS products.

SEM observations (Figure 4.16) confirmed that powder sintering is progressively promoted with the dwell temperature increase. Samples obtained at 750°C by SPS are poorly consolidated, with a significant residual porosity, in agreement with the corresponding low relative density values (about 60%, cf. Figure 4.14 c). On the other hand, samples obtained at higher temperatures, particularly at 900°C, displayed a reasonably good densification level, even though porosity was not eliminated, consistently with the resulting SPS product density (90%, cf. Figure 4.14 c).

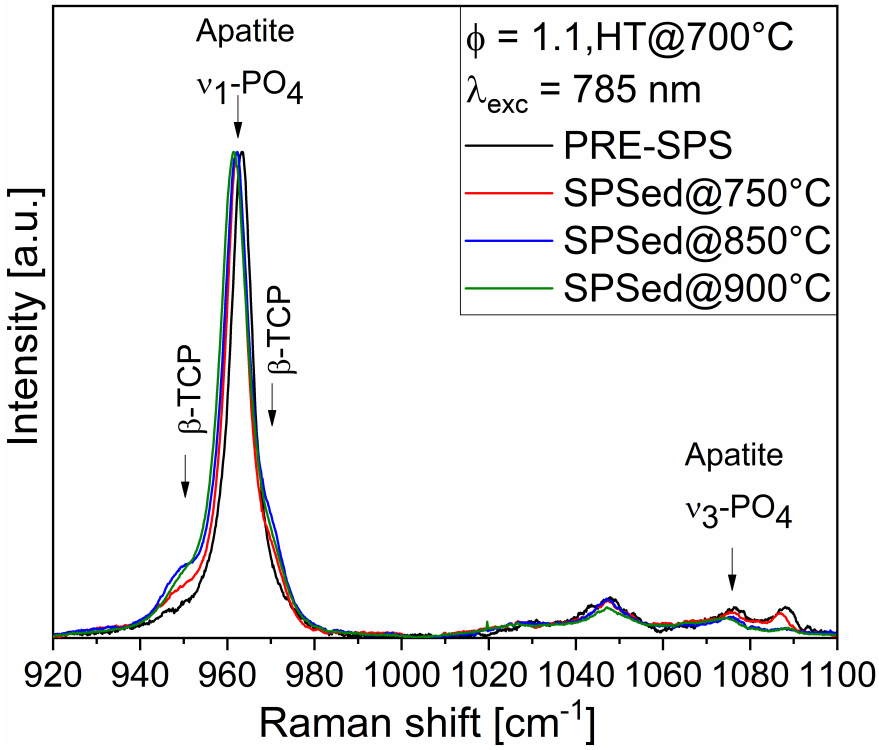

Figure 4.15: Raman spectra of SPSed samples. Each spectrum was obtained by the average of several spectra acquired in different regions of the samples.

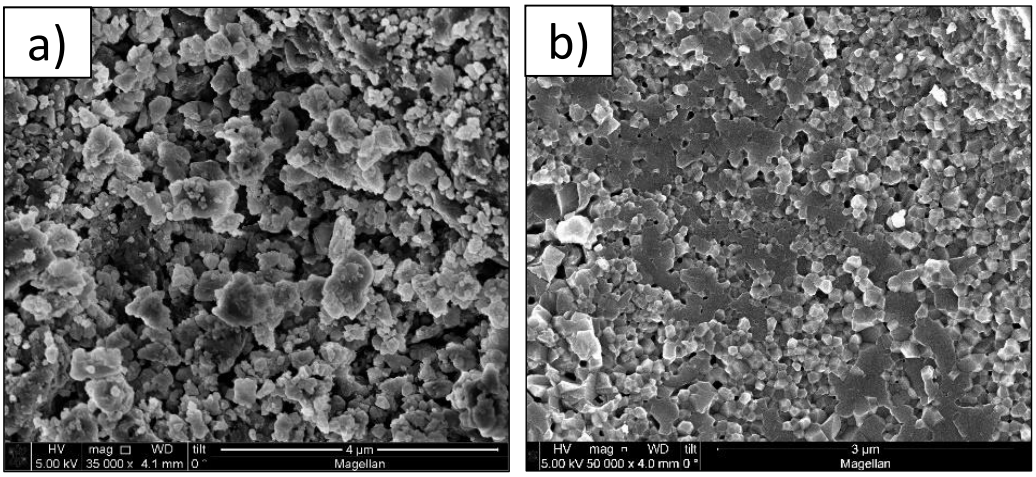

Figure 4.16: SEM micrographs of samples obtained by SPS at 750 a) and 900 °C b) from SCS powders (ϕ=1.1).

A magnification of the SEM image of the latter sample is shown in Figure 4.17 a), which evidences that a uniform microstructure with well-defined grains is obtained. From this mi-

crograph, the grain size distribution was determined, by the measurements on about 900 of them, taking advantage of the ImageJ software [255]. The obtained results are reported in Figure 4.17 b. The mean value resulted to be 115 ± 42 nm, with a median value of 108 nm. The obtained values are quite consistent with the results deriving from the Rietveld analysis, i.e., approximately 115 nm (Table 4.3). Image analysis was also employed to estimate the pores size, which resulted to be of 100 ± 40 nm, based on 30 measures.

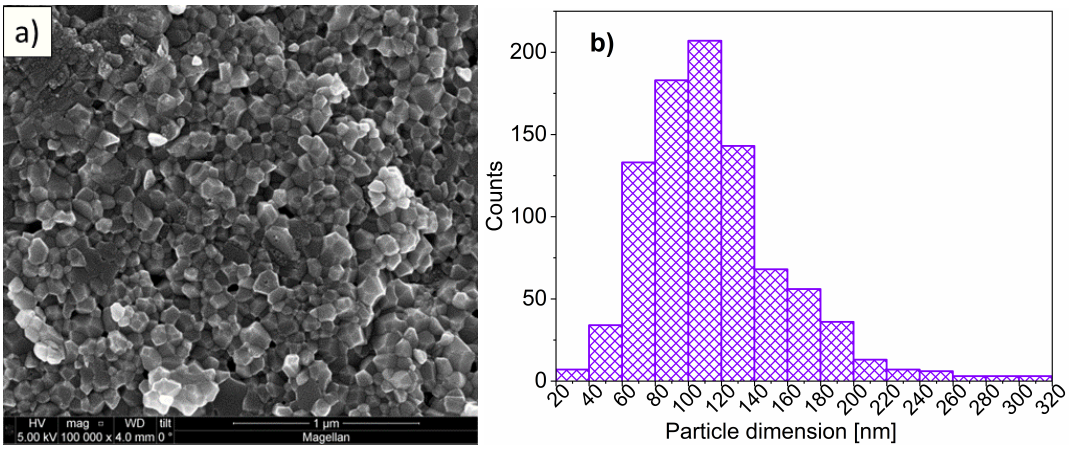

Figure 4.17: SEM micrograph a) and grain size distribution b) of the sample produced by SPS at 900°C.

Additional data are obtained from HR-TEM analysis (Figure 4.18). The use of low intensity electron beam was necessary to prevent the damage of the examined sample, apparently very sensitive to the beam, as evidenced by the spots enclosed in the yellow circle of the image shown in Figure 4.18 a). Secondly, as indicated by the dash lines in the same image, the grains dimension, being of approximately 100 nm, is in line with the previously reported XRD and SEM analyses. This holds also true regarding pore size, on the order of few hundreds of nm (light areas in Figure 4.18 b). Moreover, the SADP measurements resulted in spot-like patterns, as the one shown in Figure 4.18 c). This means that it was not possible to generate a profile, as for the case of powders. In any case, the obtained SADP is clearly due to the polycrystalline nature of the sample.

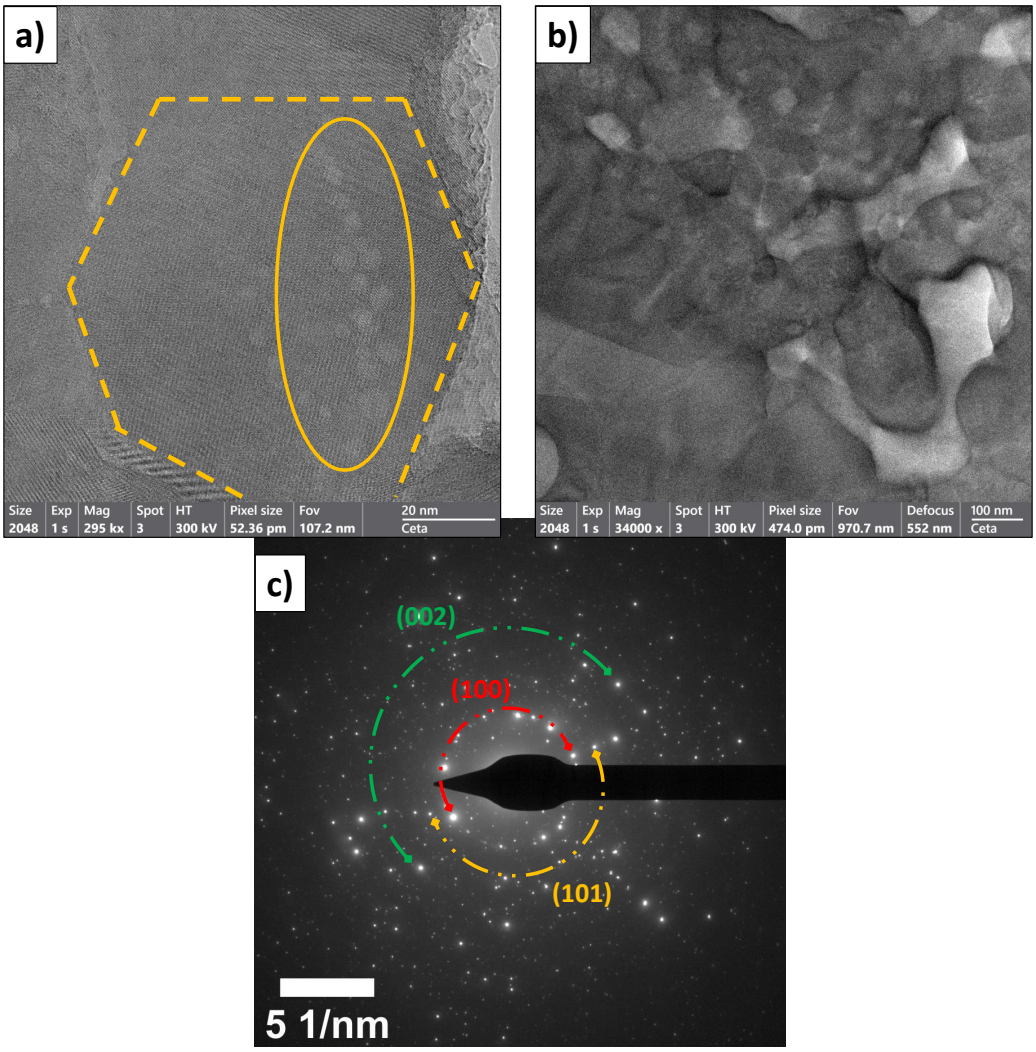

Figure 4.18: HR-TEM images a)-b) and related SADP c) taken from lamellae cut from the sample produced by SPS at 900°C.

The d-spacing corresponding to diffraction spots are compatible with some of the main apatite planes, namely 8.19 Å (1, 0, 0), 5.29 Å (1, 0, 1), and 3.46 Å (0, 0, 2).

Figure 4.19 a) and b) show some examples of d-spacing measurements carried out on EELS-HR micrographs ascribed to apatite and to β-TCP crystal structures, respectively. The presence of both these phases was confirmed by the EDS analysis, whose results are reported in Figure 4.20. Indeed, the ratio between Ca and P peaks intensities was found to be of approximately 1.66 (Figure 4.20 a) and 1.48 (Figure 4.20 b), very close to the nominal values for HA

(1.67) and β-TCP (1.5). The latter findings further testify, coherently with previous analyses, that the samples obtained by SPS from SCSed powders basically consist of these two calcium phosphates, being apatite the main phase present in the bulk in coexistence with β-TCP.

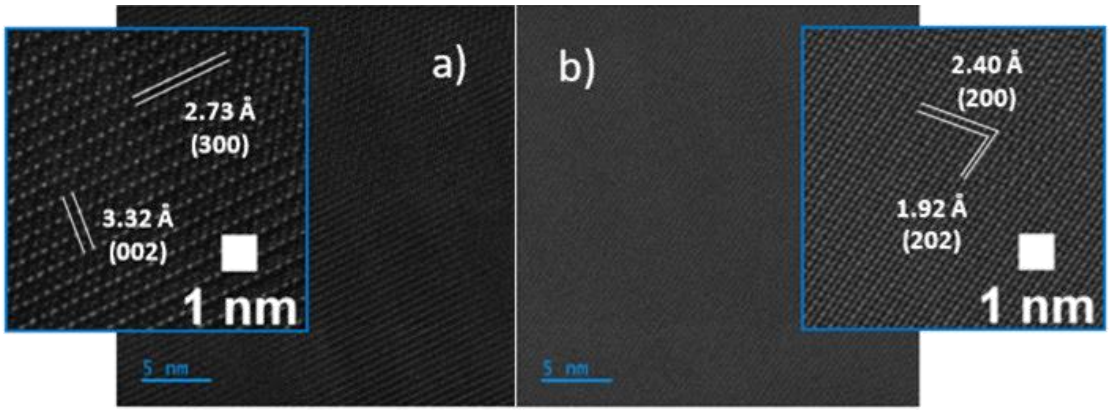

Figure 4.19: EELS-HR micrographs acquired from different parts of the sample produced by SPS at 900°C with the corresponding magnifications reporting d-spacing measurements ascribable to apatite a) and β-TCP b).

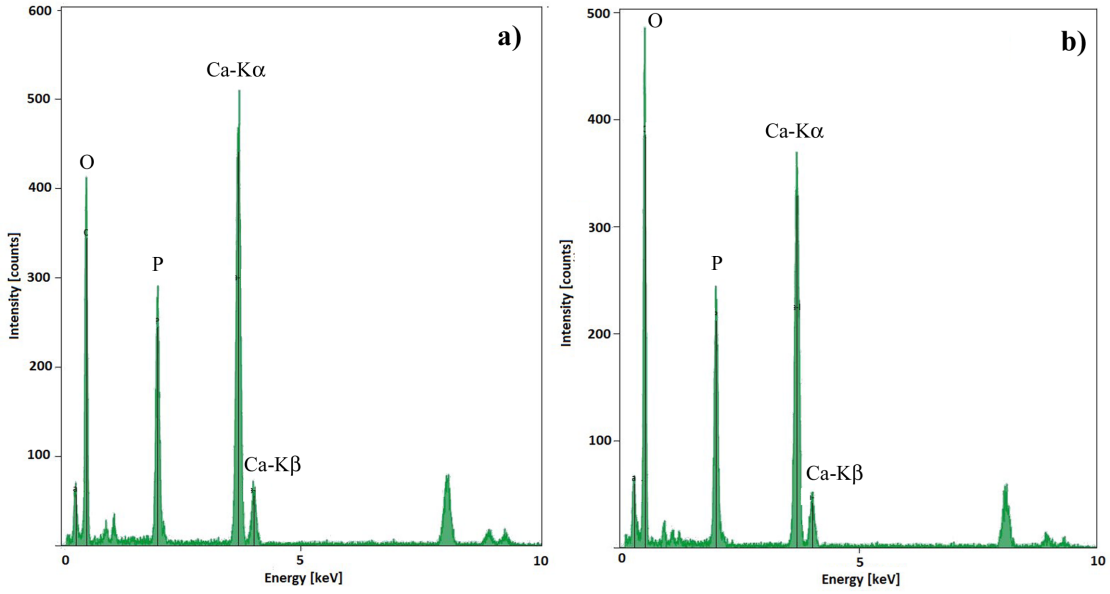

Figure 4.20: EDS analysis performed on different parts of the sample produced by SPS at 900°C.

In conclusion, the obtained bioceramic was very homogeneous and basically maintained the nanostructured nature of the synthesised powders, with apatite grains size growing just slightly above 100 nm. The weakness point is represented by the fact that, due to the vacuum and temperature conditions adopted, the original apatite carbonation is lost during SPS. Future process improvements include powder sintering conducted in an inert environment, instead of vacuum, and the use of higher mechanical loads, to reduce the dwell temperature required to achieve adequate densification levels. Indeed, both would allow to avoid, or retain, the observed decarbonation of apatite as well as grains growth, so that more suitable bioceramics will be produced. Of course, their final performances must be assessed by the required biological characterization, with specific in-vitro tests (both acellular and cellular). Of course, the possibility to incorporate in-situ, during the synthesis process, suitable therapeutic ions in calcium phosphate's structure will be considered. This work should then be seen as a starting point for the fabrication of novel biphasic, as in the present study, or monophasic nanostructured ceramics for biomedical applications with improved biological properties.

Chapter 5

S53P4 Bioactive glass fibres by electrospinning

The work presented in this Chapter was carried out during the candidate's research period in a foreign institution for 6 months. The candidate was hosted at Imperial College of London (ICL, United Kingdom), under the supervision of Prof. Julian R. Jones.

5.1 Introduction

There is a vast interest in biodegradable devices, and among them a particular focus is reserved for the one mimicking the natural structure of the body, being such a feature extremely important when turning to tissue regeneration.

In this sense electrospinning is a suitable technique, being simple and versatile to produce interconnected porous nano- and micro-fibrous structures from various synthetic and natural materials. This is particularly important when turning to mimic some of the key structures of the human body, such as skin [260, 261] or extracellular matrix (ECM) [262, 263]. The sol-gel synthesis, in which the synthesis starts with a solution undergoing a gelation process, can be adopted in combination with electrospinning.

The combination of the sol-gel synthesis and electrospinning has been exploited in the very

recent past to obtain glass fibres of different compositions and for several applications, taking advantage of the features related to both the above-mentioned techniques [264].
In the following, the sol-gel synthesis and the electrospinning procedure are described to underline their advantages. The combination of them to produce bioactive glass fibres will be discussed afterwards.

5.1.1 Sol-Gel synthesis of bioactive glasses

The sol-gel processing technique is a low-temperature processing route where, starting from a solution obtained from chemicals containing the compositional components (sol), a gel is obtained. The gel, a wet inorganic network, results from the occurrence of polymer-type reactions at room temperature, and it is similar to a highly cross-linked short-chain inorganic polymer. The gel is then dried and heated to obtain the final desired product.
Sol-gel is a wet chemistry-based synthesis technique which offers promising and flexible approaches to obtain a variety of novel and functionalized materials, ranging from glasses and ceramics to organic/inorganic hybrids. This flexibility is also empowered by the mild chemical and temperature conditions required for such process [265, 266].
Sol-gel is a reliable and environmentally friendly bottom-up technique, which allows to produce different configurations of the desired materials, such as monoliths, nanoparticles, thin films, foams, fibres (whose case will be discussed later in this Chapter).
The adaptability of the method, regarding both the composition and the resulting properties of the obtained product, also allows for the synthesis of bioactive materials for numerous biomedical applications, with usually improved properties with respect to conventional techniques (such as melt-quenching route in the case of BGs). As indicated before in this work (sections 1.2.4.3.1 and 1.2.4.3.2), the sol-gel method is currently employed to synthesize both HA and BGs.
In the case of Bioactive glasses, the synthesis process usually involves the hydrolysis of alkox-

ide precursors under acidic conditions to create a sol. Regarding silicate-based bioactive glasses, the most common silicate precursor is tetraethyl orthosilicate (TEOS, $Si(OC_2H_5)_4$). If other components apart from silica are required in the glass composition, they are introduced by the addition of either other alkoxides or salts. In the case of phosphorous- and calcium-containing glasses such ions are incorporated by the addition of triethyl phosphate (TEP) and calcium nitrate tetrahydrate ($Ca(NO_3)_2 \cdot 4H_2O$). As stated before, the sol can be considered as a solution of silica species that can undergo polycondensation to form the silica network of $Si-O-Si$ bonds [267]. A gel usually forms within 3 days at ambient temperature, with water and ethanol as by-products of the condensation reaction. The evaporation of such by-products, together with the heat treatment to remove by-products (especially nitrates), are two crucial steps for the completion of the synthesis process. In more details, the steps of the process are described in the following paragraphs.

Stage 1: Mixing Sols are dispersions of colloidal particles (diameters of $1-100$ nm) in a liquid. The stoichiometry of the sol will determine the composition of the resulting glass. In the case of Si-containing glasses, TEOS is the main Si source. It is insoluble in water so that a catalyst is needed to trigger the hydrolysis. In this process, TEOS reacts with water to effectively produce silica tetrahedra (Figure 5.1 a and Figure 5.2 a). The catalyst can be either an acid (e.g. HNO_3) or a base, and this will affect the final properties of the glass. At $pH \leq 2$, the tetrahedra, surfaces of $Si-OH$ groups floating in the water, will come together and the $Si-OH$ groups will condense, forming $O-Si-O$ bridging bonds, with water as a by-product (Figure 5.1 b). The hydrolysis and polycondensation reactions occur simultaneously within the solution during mixing. When sufficient interconnected $Si-O-Si$ bonds are formed, they behave as colloidal particles (Figure 5.2 b). The first small particles that form are named primary particles.

Stage 2: Casting The sol can be cast prior to gelation in air-tight moulds which must be made of material that will not adhere to the gel, usually PTFE. The gelation process can take several days at room temperature, but in some cases, it can be tailored according to the needs

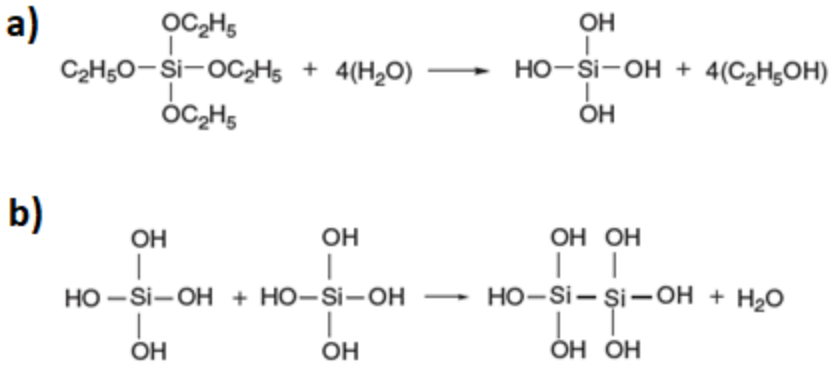

Figure 5.1: a) Hydrolysis reaction occurring during the mixing phase, and b) formation of Si bridging bond with water as by-product.

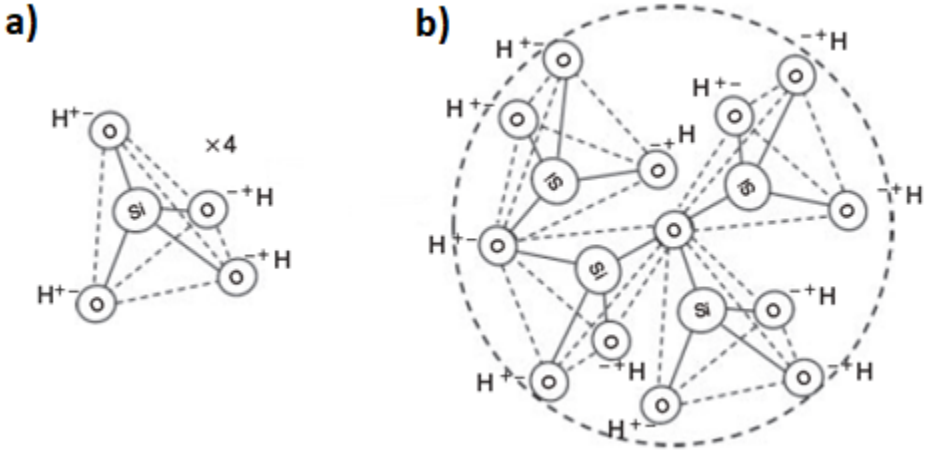

Figure 5.2: a) A silica tetrahedra forming a nanoparticle in a sol and b) particles bonding to form a network, adapted from [268].

of the process.

Stage 3: Gelation The gelation occurs as the primary particles agglomerate. The undergoing condensation will then cause the coarsening of the particles. The viscosity of the gel increases due to the formation of the $O-Si-O$ network, and the reaction proceeds until all the precursors are used up.

Stage 4: Ageing This is an important step, as the condensation reaction continues, and the gel is strengthened by the presence of aqueous by-products. Without this phase, the gel will crack during the next step, the drying phase. The ageing is usually carried out for hours or

days at room temperature, but it can also be done at slightly higher temperatures (e.g. 60 °C).

Stage 5: Drying When the reaction is complete, the by-products must be removed from the gel. The drying phase is meant to evaporate the water and the ethanol formed during the condensation of the silica network, so that the gel leaves behind an interconnected pore network with pores in the nanometer range. As shown in Figure 5.2 b), there are $-OH$ groups on the surface of the resulting particles.

Stage 6: Stabilisation The leftover hydroxyl groups on the pore walls can reduce the network connectivity, as the H^+ can act as network modifier, thus reducing connectivity. A heat treatment can be carried out to remove such hydroxyl groups; this process simultaneously favours the formation of new $O-Si-O$ bonds. In addition, the thermal treatment allows to both incorporate ions into the glass structure, such as Ca and Na, and remove nitrates from chemicals used as precursors, because of their toxicity to cells [119, 268]. To set the proper stabilization temperature one has to take into the glass composition and its properties (e.g., the ions to be incorporated); the adopted temperature is usually around 700 °C.

The abovementioned procedure allows for the synthesis of glasses with a variety of pore structures from the nanometre to the millimetre range, which gives sol-gel glasses great potential in biomedical applications. The sol-gel BGs' surface area per unit mass is approximately 100 times higher than the melt-derived counterpart, implying a much higher dissolution rate [269], and resulting in an increased rate of HCA formation in-vitro. This is caused by the presence of nanoporosity, which can also be tailored to control the degradation rate of the material.

Another improvement on the bioactivity of the materials can be provided by the incorporation of suitable ions (e.g., Ag and Sr [270,271]) into the glass structure, as described previously in this work (section 1.2.4.3.2). In the case of sol-gel glasses, ions release can be tailored by the dissolution rate of the glass itself.

A further advantage is that melt-quenched glasses cannot be bioactive if they have a silica content above 60 mol% (section 1.2.4.3.2). For sol-gel glasses, the Si content can be extended to 90 mol% [272, 273]. The reason for this is the presence of OH groups; the resulting network connectivity is lower than the one which would have been resulting from the melt-quenching route of the same glass composition. Therefore, it has to be underlined that the quantity of OH group decreases after the thermal processing, and so the real composition of the glass changes with the heat treatment [268].

Although their importance in research, industrial and clinical application, very few studies reported successful synthesis of Na-containing bioactive glass formulations, such as 45S5 and S53P4 already described in this work (section 1.2.4.3.2). The main issue in this sense is due to the overlap (at around 600 °C [272]) of the crystallization temperature of the glass and the stabilization temperature required to both remove nitrates and properly incorporate Na into the glass structure. This resulted in the obtainment of glass-ceramics when employing nitrate based precursors [246, 274, 275].

The use of organic precursors, such as calcium and sodium acetates, was also investigated; the authors demonstrated by XRD analysis the degree of crystallinity on the products, but without proving the correct composition [276, 277] or without providing data regarding carbon impurity [276–279]. The investigation to find a solid procedure to synthesize Na-containing glasses by sol-gel route, 45S5 and S53P4 among the others, is an ongoing work at the Materials Department of the Imperial College of London, where this work was carried out. Further improvement in this sense will be discussed later in this Chapter (subsection 5.1.3).

5.1.2 Electrospinning process

The electrospinning (ES) procedure consists in an extrusion through a syringe needle of a polymeric solution having the proper viscosity. An electric field is necessary to be applied between the solution to be spun and the collector. This is done by the application of a high

voltage between the metallic needle and the collector. This causes the charging phenomenon of the solution, resulting in a repulsive Coulomb force which is counterbalanced by the surface tension of the liquid. Once the applied voltage is high enough to induce a repulsion that exceeds the surface tension of the liquid, the solution is stretched to form a filament (in a shape named *Taylor cone*), which moves towards the collector (being such collector grounded or opposite charged). During the travel, the as formed jet, moves randomly, resulting in a random fibre deposition onto the collector. The time spent in the tract from the needle to the collector also causes the drying of the solution. The result of the ideal process is a uniform deposited fibre mat with random orientation of the fibres.

Besides its usage to produce polymeric fibres, ES has also been employed to produce a large variety of materials for different applications, such as in composite materials reinforcement, sensors, filtration, catalysis, protective clothing, space applications (such as solar sails), and micro- and nano-optoelectronics (nanowires, LEDs, photocells, etc.) [280]. Biomedical applications (including wound dressing and scaffolds for tissue engineering, implants, and membranes), usually involve ceramic containing fibres, most commonly in the form of particles dispersed into a polymeric fibre mat. In addition to calcium phosphates and bioactive glasses (whose case will be discussed in more detail in the next section) a variety of ceramics were processed by ES, such as $CaCO_3$ [281–283], and its doping by Si [217,284–289], MgO [290] and amorphous magnesium phosphate [291], among the others.

Fibres obtained by ES usually have diameters ranging from few nanometres to over 1 micrometre (more typically 50-500 nm) and possess unique characteristics, such as very high porosity, good structural and mechanical properties combined with extreme flexibility and a relatively easy processing require to obtain them. Furthermore, they possess an extraordinary high surface area per unit mass (in the order of 1000 m^2/g for the case of fibres having diameters of 100 nm [280]).

The sol-gel transition can be used in this process; the occurrence of gelation causes a variation in the viscosity of the sol. Since viscosity is a crucial parameter in the ES process, the

adaptation of the sol-gel route to obtain the desired viscosity can be a powerful tool for the obtainment of different materials. It is also possible to add a polymer to the sol (such as PVA, PVB etc.), to further improve the control over the viscosity. Such parameter can be a determinant factor in the morphology of the fibres. Usually, higher values result in thicker fibres. In this case, the longer stress-relaxation time could prevent the fracture of the jet during electrospinning. But, on the other hand, very high viscosities cause difficulty in the jet ejection from the polymer solution. Conversely, it has been found that with very low viscosities there is no continuous fibre formation; in this case, the surface tension is the dominant factor and fibres containing beads (or just beads) are usually obtained [261].

In the same way, high surface tensions can inhibit the jet formation and cause instabilities, for instance, droplets spraying [292]. Lower surface tensions can favour the spinning with the application of lower electric fields [293]. A liquid having a surface tension which is too low will result in a drop from the needle.

Once the solution has proper surface tension and viscosity, processing parameters must be considered. The applied voltage is crucial to induce the charging of the solution and so to overcome the surface tension. Usually, the application of higher voltages results in a greater stretching of the solution, causing the formation of thinner fibres [293, 294], but there is no linear correlation between them; it strongly depends on the solution and other process parameters, like the distance between the tip and the collector [295]. The latter is very important, and it must be optimized together with the voltage; the distance should usually increase with increasing voltage values [296]. For this reason, it is useful to consider the electric field (kV/cm) instead of the applied voltage itself [264].

A practical indication for the voltage setting can be obtained by the sol behaviour during the process, as described in Figure 5.3. Considering a fixed value of the distance from the collector, a value of the voltage which is too low may result in drop formation or a drop-containing jet (parts a and b in Figure 5.3). In both cases the deposition is not optimal. When the voltage is properly set, the jet forms and moves through the collector. If the voltage is fur-

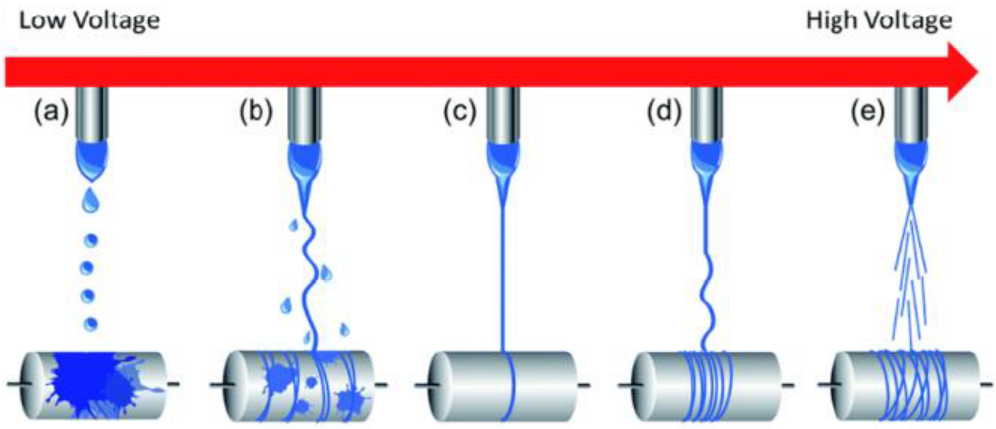

Figure 5.3: Schematization of the behaviour of the sol jet as a function of the applied voltage, reproduced from [297].

ther increased, the jet start to "shake" , resulting more turbulent and eventually breaking in a spray like phenomenon (part e in Figure 5.3).

In addition to the distance between the collector and the needle, the shape of the collector can also influence the process. A flat one allows for a deposition of randomly oriented fibres. The orientation of fibres may be controlled with specific shaped collectors and setups; oriented fibres can be obtained by both cylindrical-rotating collector and parallel metallic plates with a void between them. The feed rate, or else the quantity of solution passing through the needle per unit time, can affect the jet velocity and transfer rate. It has to be properly set so that there is enough time for the evaporation of the solvent. There were few studies systematically investigating the influence of such parameter on the resulting morphology of the fibres [294, 298], but usually high flow rates cause beaded fibres, due to the too short drying time prior to reaching the collector [299–302].

Lastly, the ambient conditions are of particular importance; the temperature can affect the viscosity of the solution while the humidity the drying of the jet prior to fibre deposition. Too low humidity can cause the occlusion of the tip due to too fast solvent evaporation [303], while too high values can result in short fibres with the presence of beads [304]; if the applied voltage is high, electric discharge can occur. Ambient conditions are of particular importance in situations and setups where they cannot be controlled.

5.1.3 Bioactive glass fibres by sol-gel/electrospinning combination

Electrospinning usually provides a 2D structure, when considering a deposition onto a flat surface, but a 3D structure can also be produced. Poologasundarampillai et al. [305] electrospun a sol-gel 70 mol% SiO_2 and 30 mol% CaO (70S30C) bioactive glass directly from the sol to obtain a cotton-wool like structure, with the aim to favour bone bonding and mineralization of a Ca rich scaffold.

Other works were devoted to the development of a solid protocol to produce bioactive glass scaffolds with a 3D porous structure [304], with the deposition of a two component Si-Ca glass. In this work the liquid feeding the electrospinner is formed by a mixture of the sol and an organic binder, Polyvinyl Butyral (PVB, $(C_8H_{14}O_2)_n$) dissolved into ethanol. Such additive was used to control the viscosity of the mixture, being such parameter crucial during electrospinning [306]. Different biphasic Si-Ca composition were investigated, showing that the increase of Ca content (in the range 0-40 mol.%) impacts the 3D structure of the sample; a larger Ca quantity favours the 3D structure of the resulting sample. The FTIR analysis confirmed that the binder was removed during stabilization phase. Moreover, no bands related to the reactants were observed. When the Ca content is equal or higher than 30%, a band associated with CO_3^{2-} was detected in FTIR spectra, with the intensity of the band increasing with Ca content. This was attributed to a carbonation process of the material due to atmospheric CO_2 and moisture [307]. The characterization was carried out for 70S30C and 80S20C, showing a rapid release (between 10 and 24h) of Si and Ca in dissolution studies.

As the glass formulation can have an important influence on its properties and applications, different compositions have been tested by the combination of sol-gel and electrospinning. Indeed, the incorporation of suitable dopants can have beneficial effect on the resulting materials tuned for the specific application [148]. For instance, Liverani et al. [308] elctrospun 80S20C and 80S18C2Cu compositions, in which the latter contained Cu in 2 mol%, with the aim to obtain a cotton-like, Cu-releasing malleable structures for wound healing applications. Indeed, the incorporation of Cu can have beneficial effects on angiogenesis, cellular respira-

tion, bone formation, among the others [148]. Si-Ca bioactive glass-based electrospun fibres were successfully obtained, arranged in the form of a cotton-like macrostructure. The FTIR analysis confirmed the successful elimination of PVB (binder) after heat treatment. Copper-doped BG fibres showed a delayed HCA formation upon immersion in SBF (7 days), respect to undoped fibres (1 day). Both compositions showed cytocompatibility and positive effect on the wound closure rate, assessed by in vitro scratch healing assay [309], confirming their suitability for wound healing applications [308].

On the other hand, despite its importance in terms of properties and applications, only very few studies were devoted to the electrospinning of 45S5 Bioglass®, maybe due to the difficulty to obtain such composition by sol-gel technique [310, 311]. Indeed, the required stabilization phase can cause the crystallization of the glass, as reported by some works obtaining glass-ceramic by this route [275]. Deliormanli and Konyali [310] tried to synthesize 45S5 by sol-gel and subsequently electrospin it together with PVA (Polyvinyl acetate) and a surfactant to obtain glass fibres after stabilization. The XRD results evidenced a marked crystallization caused by stabilization, as expected from the fact that the crystallization temperature is very close, or even lower with respect to the stabilization temperature required to remove by-products such as nitrates. Glass-ceramic fibres were obtained, showing the precipitation of some calcium phosphate after 1 day of immersion in SBF and the subsequent formation of crystalline HA after 30 days of immersion.

Durgalakshmi and Balakumar [311] obtained hollow 45S5 fibres also containing a crystalline phase, for drug delivery applications. Such fibres evidenced the formation of HCA when immersed in SBF for 3 days, and the release of loaded drugs in the range of several hours (from 6 to 18 h).

Beyond 45S5, other glass compositions, like S53P4, are of particular interest because of their properties. As described before (Section 1.4.5.4), such formulation showed to be able to inhibit growth of more than 50 strains of clinically relevant bacteria [130–132] . It is also able to bind to bone and promote bone regeneration, making it a viable material for treating disease

such as osteomyelitis or spine infections [312]. For these, and other reasons presented previously (Section 1.4.5.4), S53P4 is widely studied and even used in commercial products.
As specified before (subsection 5.1.1), even in the case of S53P4 the sol-gel route is problematic, given its crystallization temperature. Some works reporting the sol-gel synthesis of S53P4 [246, 274, 275] either synthesised crystalline glass-ceramic, or glass with incorrect composition. As mentioned before, the determination of a reliable procedure to produce amorphous S53P4 by sol-gel with the proper composition is an ongoing work.
The aim of this work is then to go a step forward and to appropriately modify the sol-gel synthesis procedure to make a sol suitable to be deposited. The main goals of the present work were:

1. to assess the spinnability of the sol and the obtainment of fibres starting from the mixture sol-PVB;

2. the subsequent removal of PVB during the stabilization phase to obtain amorphous S53P4 fibres.

5.2 Experimental setup and procedures

5.2.1 Sol-gel synthesis

Since the sol-gel synthesis is a complex process, it is necessary to investigate the influence of the synthesis parameters on the resulting solution and on its suitability for the electrospinning machine. The preparation of the sol was made by mixing the proper amount of reactants to suit the S53P4 composition and the desired distilled water (DIw) to TEOS ratio (DIw/TEOS). A schematic description of the procedure is reported in Figure 5.4.

TEOS (Tetraethoxysilane 99%, ABCR), TEP (Triethyl phosphate 98+%, Alfa Aesar) and DIw are

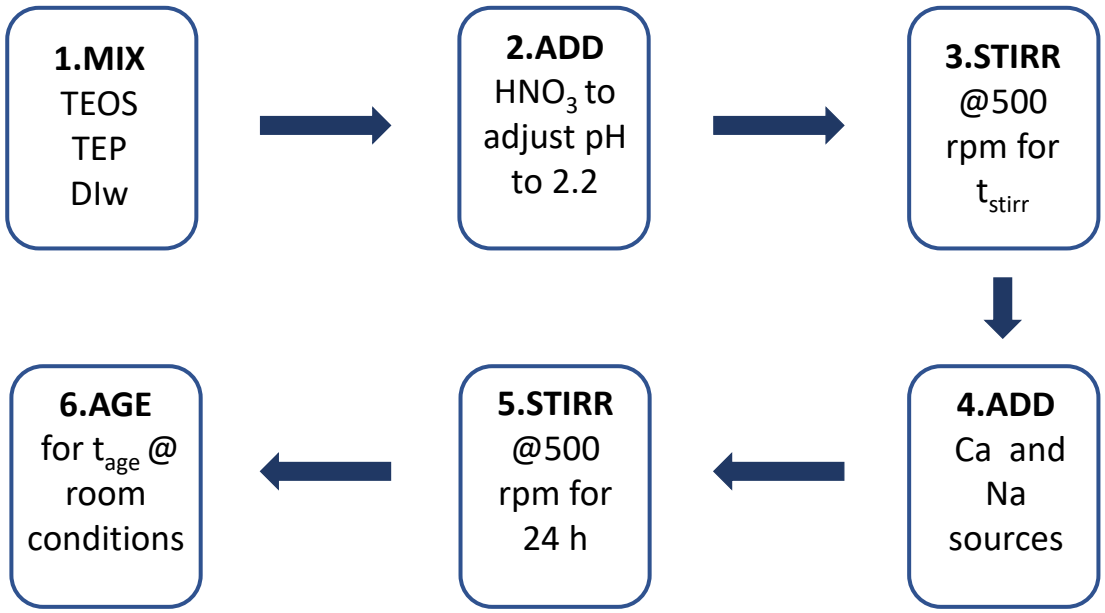

Figure 5.4: Schematic representation of the sol-gel synthesis procedure adopted in this work. TEP (Triethyl phosphate, $(C_2H_5)_3PO_4$), t_{stirr} is the total time of stirring and t_{age} the ageing time.

mixed in a teflon container. While stirring this mixture at 500 rpm, the pH is adjusted to 2.2 by the addition of 1M HNO_3 (Nitric acid, Thermofisher) and the resulting solution is stirred in the same sealed teflon container for the desired amount of time (t_{stirr}). Subsequently, the Ca

and Na salts are added to the solution. The resulting sol is stirred at 500 rpm at room conditions for 24 hours in the same sealed teflon container. Then, the sol is aged at room conditions for the desired amount of time (t_{age}).

As described above in subsection 5.1.1, the reactants can have influence on the resulting glass composition and uniformity; this could also be true for the electrospinning process. For this reason different Ca sources were investigated, to better understand their influence on the procedure and on the resulting products.

As for the present work, it was chosen to investigate the influence of DIw/TEOS, stirring time t_{stirr}, ageing time t_{age} and Ca-containing reactants on the resulting sol and fibres. The values adopted for the previous mentioned parameters are reported in the Table 5.1, whilst the reason for this specific values will be discussed in section 5.3.

Parameter	Adopted values
DIw/TEOS	8, 12
t_{stirr} [min]	10, 20, 30, 60
t_{age} [days]	2, 7

Table 5.1: List of values adopted in this work for the sol-gel synthesis procedure.

5.2.2 Electrospinning

The apparatus reported in Figure 5.5 (Spraybase ® 30kV Electrospinning Starter Kit) allows the regulation of the electrospinning process parameters, namely flow rate (FR), voltage (VO) and distance from the tip to the flat collector (h).

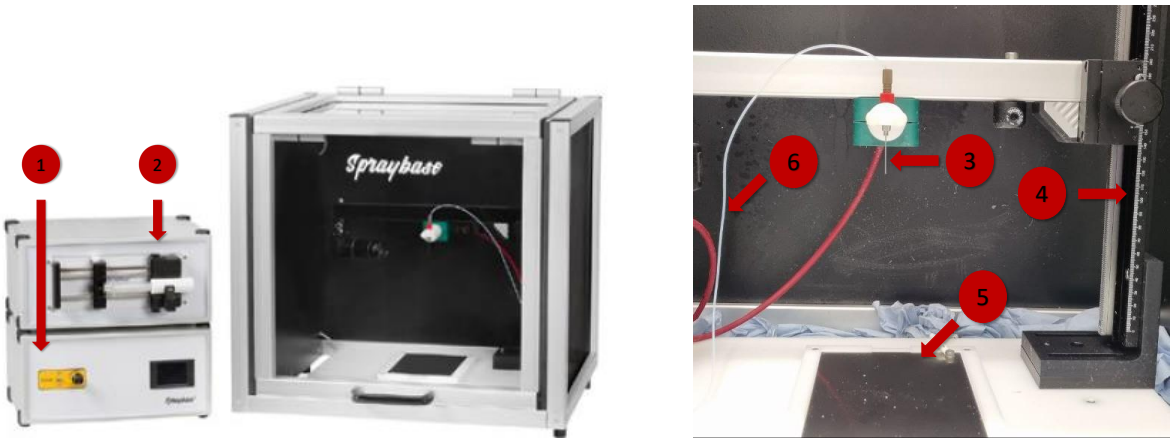

Figure 5.5: Pictures of the electrospinning apparatus. Left side shows the Spraybase® 30kV Electrospinning Starter Kit, while right side the interior part of the safety cover of the same Spraybase ® Kit. **1.** Voltage regulator **2.** syringe pumping motor to regulate FR., **3.** 22G needle **4.** height regulation **5.** metallic flat plate collector **6.** tube bringing solution to the needle.

The room humidity (RH), which plays a crucial role in the electrospinning deposition, is not controllable by this apparatus. All the experiment were carried out whenever RH was in the proper interval, which will be discussed later (section 5.3).

In order to proceed with the electrospinning, the sol has to be mixed with an organic binder. PVB was proven to be suitable for this purpose [304, 308], and so it was chosen for the experiments presented in this work. Its double role is to facilitate the electrospinning process, by making the sol viscous enough for the electrospinning, and to act as a binder for the fibres, once spun [264]. The binder will be later removed by dissociation caused by the high temperatures required for the glass stabilization [313, 314]. The PVB (Sigma Aldrich) was mixed with ethanol (being PVB soluble in such solvent) at different concentrations. Such concentration is an important parameter to tune the viscosity of sol-PVB mixture feeding the electrospinner, and it has influence on the steps following electrospinning, namely heat treatment; lower concentrations should favour the PVB removal.

The desired amount of PVB is dissolved into ethanol and stirred for at least 15 min until a clear solution is obtained. Subsequently, the ethanol-PVB mixture at different concentrations and the sol are mixed together at different sol to binder solution (vol:vol) ratios according to Ta-

ble 5.2, and stirred for another 15 min until the obtainment of an homogenous mixture.
A total of 3 ml of such liquid are placed into a syringe connected to the tip of the electrospinner. The flat collector is then covered with Al foil to facilitate the collection of the samples after the electrospinning process, the distance h is regulated and the flow rate and voltage V are set. The deposition stops once the entire 3 ml are spun.

Parameter	Investigated values
PVB concentration [wt/vol %]	5, 8.8
PVB solution/sol [vol:vol]	1:1, 1:2

Table 5.2: List of adopted values for the binder solution and mixture with the sol.

In the following section, to make the reading easier, the following notation will be adopted:

- DIw/TEOS ratio will be indicated ad w/T
- t_{age}, simply indicated by the number of days, will follow the DIw/TEOS ratio
- 1:1 vol:vol% will become 1:1 vol, and the concentration x of PVB/ethanol solution will be indicated as x PVB

So, for instance, w/T =12, 3, 1:1 vol, 8.8 PVB sample is obtained by using DIw/TEOS ratio of 12 aged for 3 days, mixing the sol with a 8.8 wt/vol% PVB/ethanol mixture at mixing ratio of 1:1 vol:vol.

5.2.3 Characterization

The obtained sample will be characterised by different techniques to investigate whether the adopted procedure is leading to the desired results.
SEM obeservations (JEOL® 6010LA) were carried out to investigate the morphology of the samples using secondary electron imaging (SEI). The FTIR (iS10, Nicolet®) spectra, resulting from an average of 32 measures, were acquired in the range between 400 and 4000 $c\,m^{-1}$ with step size of 0.482 $c\,m^{-1}$. XRD (Xpert Pro, PANalytical ®) patterns in the range between 10°and

60°(3000 steps and scanning time per step 20 s) were recorded (Cu $K\alpha$ radiation at 40 kV and 40 mA was used).

5.3 Results and discussion

The study started by investigating the optimal sol-gel synthesis reaction parameters to obtain a solution suitable for electrospinning. The viscosity of the solution is a crucial parameter for electrospinning process, so the complete gelation must be avoided.

It was chosen to start the experiments adopting a procedure which is being developed for the optimization of the sol-gel synthesis of amorphous S53P4 glass powders, and to modify it in order to have a sol suitable to feed the electrospinner machine. So, the first experiments were carried out with DIw/TEOS = 12, and varying the mixing time t_{stirr}. 60 min stirring resulted in a partially gelled product, making it impossible to fit it in the syringe of the electrospinner. This means that shorter times are required. 30 min resulted in a mixture of a liquid and a denser part, meaning that the sol would immediately deposit the denser fraction at the bottom part of the syringe, causing a non-uniform deposition. On the other hand, both 10 and 20 min resulted in a liquid sol looking suitable to be pumped through the tube and the needle, making this conditions suitable to start electrospinning experiments.

To proceed with such experiments, according to previous work [304] the sol (t_{stirr}=20 min) was mixed in a 1:1 vol:vol ratio with a 8.8 wt/vol% PVB/ethanol solution and stirred according to the procedure reported in section 5.2. Different combinations of process parameters (such as VO and h) were investigated; the electrospinning of glasses (or glass containing systems) is usually carried out with values of the VO/h greater than 1 [296, 304, 305, 308]. In the present work, the proper combination was empirically determined by varying the parameter one at a time, keeping the VO/h ratio greater than 1.5 and the flow rate fixed at 0.75 ml/h, and observing the process. As explained in subsection 5.1.2, the behaviour of the stream can give some important indications on how to find the right conditions for electrospinning. Following this procedure, the optimal conditions, reported in Table 5.3, were determined. Different values lead to spray, drops or non-continuous fibres deposition. If not diffently specified, the results presented below are obtained under such conditions. The optimal values for FR, h and VO

were tested at different RH conditions: it was not possible to obtain fibres whenever the RH was not in the range indicated in Table 5.3.

Parameter	Optimal value
FR [ml/h]	0.75
h [cm]	7
VO [kV]	19
RH [%]	$30 < RH < 40$

Table 5.3: List of optimized parameters adopted for the electrospinning process.

On the other hand the mixture obtained by the 10 min mixed sol resulted in continuous dripping independently from the adopted h and VO, indicating that the solution is too liquid. The value $t_{stirr} = 20min$ has then been chosen as the most suitable among the investigated ones.

Under the optimal conditions reported above, the cotton-like sample reported in Figure 5.6 was obtained. The SEM observations confirmed the presence of uniformly distributed fibres. Before proceeding with the discussion, it should be specified that, after some time from the start of the electrospinning deposition, the mixture contained in the syringe start to separate in a denser part at the bottom and a more liquid one at the top. This fact didn't have an appearent effect on the electrospinning deposition.

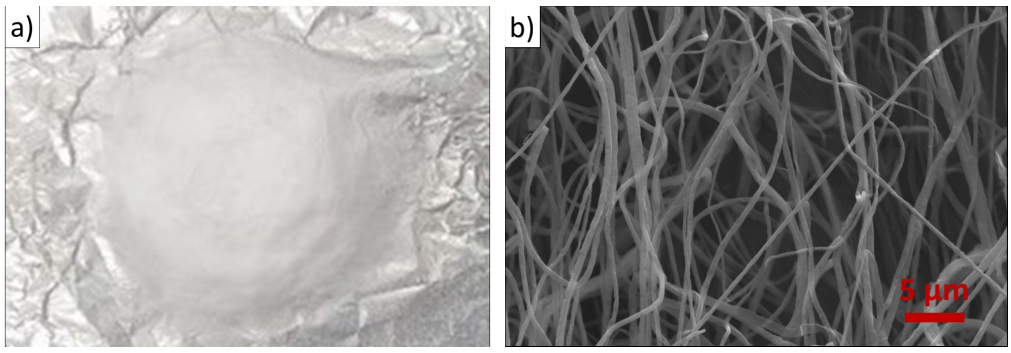

Figure 5.6: a) Picture and b) SEM micrograph of the cotton-like sample obtained by electrospinng the 20 min stirred solution (w/T =12, 2, 1:1 vol, 8.8 PVB) at VO=19kV, h=7cm, 30<RH<40% and FR=0.75 ml/h.

Once the optimal electrospinning parameters has been obtained, it was decided to vary

the DIw/TEOS ratio and the quantity of binder according to what has been said in section 5.2; a lower amount of water may make the sol more viscous possibly requiring less binder. The reduction of binder, on the other hand, can result in an easier and faster binder removal during glass stabilization. For this reason, a sol with DIw/TEOS ratio of 8 was made (lower values of this ratio are not achievable because of the water contained in the calcium salt) and a solution with PVB/ethanol concentration of 5 wt/vol % was made as well. To better investigate the influence of these parameters on the resulting sample, the conditions were varied, one at a time, as described in Table 5.4:

Binder concentration	2 days, 1:1 vol, 8.8 PVB	2 days, 1:1 vol, 5 PVB	2 days, 2:1 vol, 8.8 PVB
DIw/TEOS			
8	Flat deposition (Figure 5.7 a))	Not spinnable	Not spinnable
12	Cotton-like (Figure 5.6 a))	Not spinnable	Not spinnable

Table 5.4: List of adopted values for the binder solution and mixture with the sol.

The reduction of the PVB quantity and the PVB/ethanol solutions resulted in a non-spinnable sol; this may be ascribable to the reduced viscosity due to the lower amount of binder [304], causing the sol to drop instead of forming fibres. On the other hand, the reduction of the quantity of water in the sol resulted in a thin, flat and uniform deposition into the Al foil (Figure 5.7). The fibres can be seen in the right part of the photo, in which they are the white area deposited onto the Al foil. The SEM micrograph evidences the presence of thin fibres and several beads uniformly distributed across the sample. This indicated the fact that the deposition was not carried out under the optimal conditions: the presence of beads make the condition DIw/TEOS = 8 not suitable for the purposes of this work. Due to the previous considerations, this sample was not further characterised. As for the sample w/T =12, 2, 1:1 vol, 8.8 PVB, shown in Figure 5.6, the fibres are thicker with respect to the ones shown in Figure 5.7 and they are more spaced, still randomly oriented, but in this case no bead were observed, making the fibres uniform across their length.

The cotton-like sample shown in Figure 5.6 a) is then constituted by uniform fibres. The

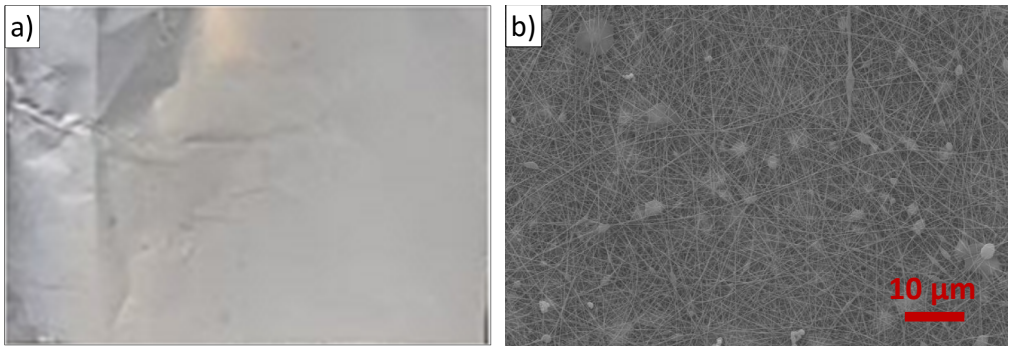

Figure 5.7: a) Picture and b) SEM micrograph of the sample obtained by electrospinng the 20 min stirred solution (w/T =8, 2, 1:1 vol, 8.8 PVB) solution at VO=19kV, h=7cm, 30<RH<40% and FR=0.75 ml/h.

sample was then further characterised by imaging analysis to quantitatively investigate the morphology and FTIR and XRD to assess their composition. The obtained results are reported in Figure 5.8. The diamaters of the fibres were measured by means of the software ImageJ [255]. This kind of analysis was carried out on 3 different micrographs, and the results are reported in Figure 5.8 a). The fibres are distributed around the median value of 402 nm, whilst the average diameter is $424 \pm 109\, nm$, indicating that such value is quite representative, being very close to the median one. A limited amount of information can be extracted from the XRD pattern (Figure 5.8 b), being the signal mainly due to $NaNO_3$ present in the sample.

As well known, the Na incorporation into the glass structure is a critical step which occurs only during stabilization, as described in subsection 5.1.1. In addition the FTIR measures carried out on the same sample (Figure 5.8 c) confirmed the presence of $NaNO_3$ indicated by the presence asymmetric (between 1340 and 1369 cm^{-1}) and symmetric (835 cm^{-1}) stretching of NO_3 group [315]. As expected, PVB is still present after electrospinning, as evidenced by the presence of its characteristic main peaks (Figure 5.8 d); higher temperature will be required to degrade it [314]. No bands relative to the others reactants, such as TEOS, were observed.

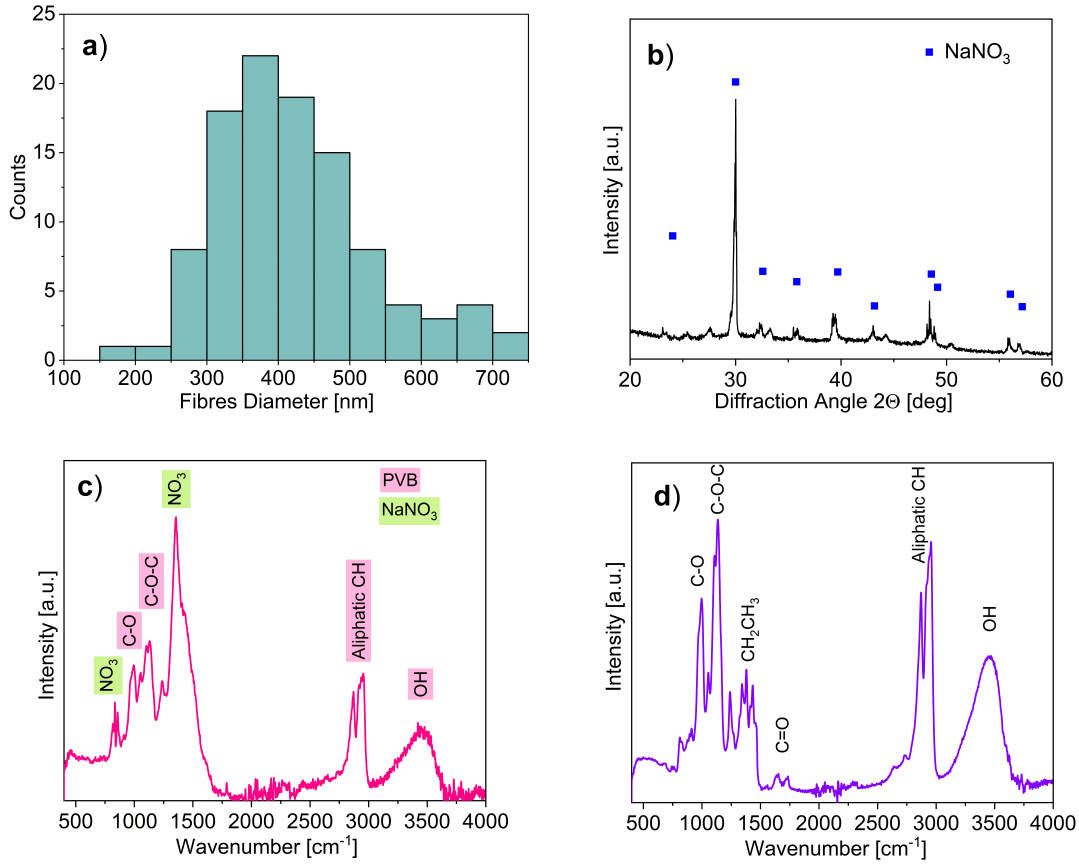

Figure 5.8: a) Fibres diameter distribution (based on measures performed by the software ImageJ on 105 fibres across the sample), b) XRD pattern, and c) FTIR of as spun of w/T =12, 2, 1:1 vol, 8.8 PVB sample (Figure 5.7 b). FTIR of pure PVB d) used in this work is reported as reference.

As explained in subsection 5.1.1, the sol-gel procedure requires drying and stabilization steps to synthesize the glass. In previous experiments on the electrospinning of BG the drying step hasn't been carried out, as the fibres resulting from electrospinning experiments should be dry (or mostly dried). It is a common procedure to directly step through the stabilization phase, usually carried out at 600 or 700 °C for few hours (commonly from 3 to 5) [304, 308]. In the present work it was decided to carry out some tests a very low temperatures (120/130 °C) to assess the behaviour of the samples when heated. This was done by heating a part of the sample right after electrospinning, and the other one after two days. The obtained results are reported in Figure 5.9. The samples shrank immediately when placed into the oven, especially the one treated right after electrospinning, and in both cases they resulted yellowish at

the end of the treatment, as shown in Figure 5.9 e). The SEM micrographs carried out on such samples evidenced a degradation of the fibrous structure observed before. The morphology seems to indicate a melting of the fibres, to form a compact structure. This is more evident in the sample treated right after electrospinning Figure 5.9 a)-b) than that dried for 48 h (Figure 5.9 c)-d), being part of the fibres still visible in the latter. In both cases the results are not acceptable, as the fibre-like structure is lost. In any case, this evidence may be an indication of the fact that the samples may require some time to completely dry after electrospinning process.

Even if the results obtained by the drying process are not optimal, it was decided to heat treat the samples at higher temperature, to assess the behaviour of the fibres during stabilization. As preliminary temperature 350°C was chosen. The obtained samples resulted extremely shrank and with black appearance (Figure 5.10), maybe caused by the incomplete PVB dissociation. The SEM (Figure 5.9 f) showed that the resulting samples are not formed by fibres; the high temperatures needed for the stabilization of the glass are causing the disruption of the fibres.

With the idea to strengthen the fibres to make them more resistant during heat treatment, it was thought to increase the t_{age}; the longer reaction time may cause the enlargement of Si network, ideally strengthening the resulting fibres. The t_{age} was then prolonged to 7 days. The sol was then mixed with PVB and spun. The resulting cotton-like samples are very similar to the ones obtained at $t_{age} = 2$ days. The sample's picture together with the SEM of such sample are reported in Figure 5.11. The sample is formed by fibres uniformly distributed (Figure 5.11 c)-d). Imaging analysis was carried out, and the resulting measured diameter for the fibres was found to be 382 ± 129 nm, with a median value of 361 nm. The obtained distribution is reported in Figure 5.11 b). These values are slightly lower than the one previously reported for samples obtained after 2 days, but the fiber diameters are consistent, also taking into account the wide standard deviation related to the measures.

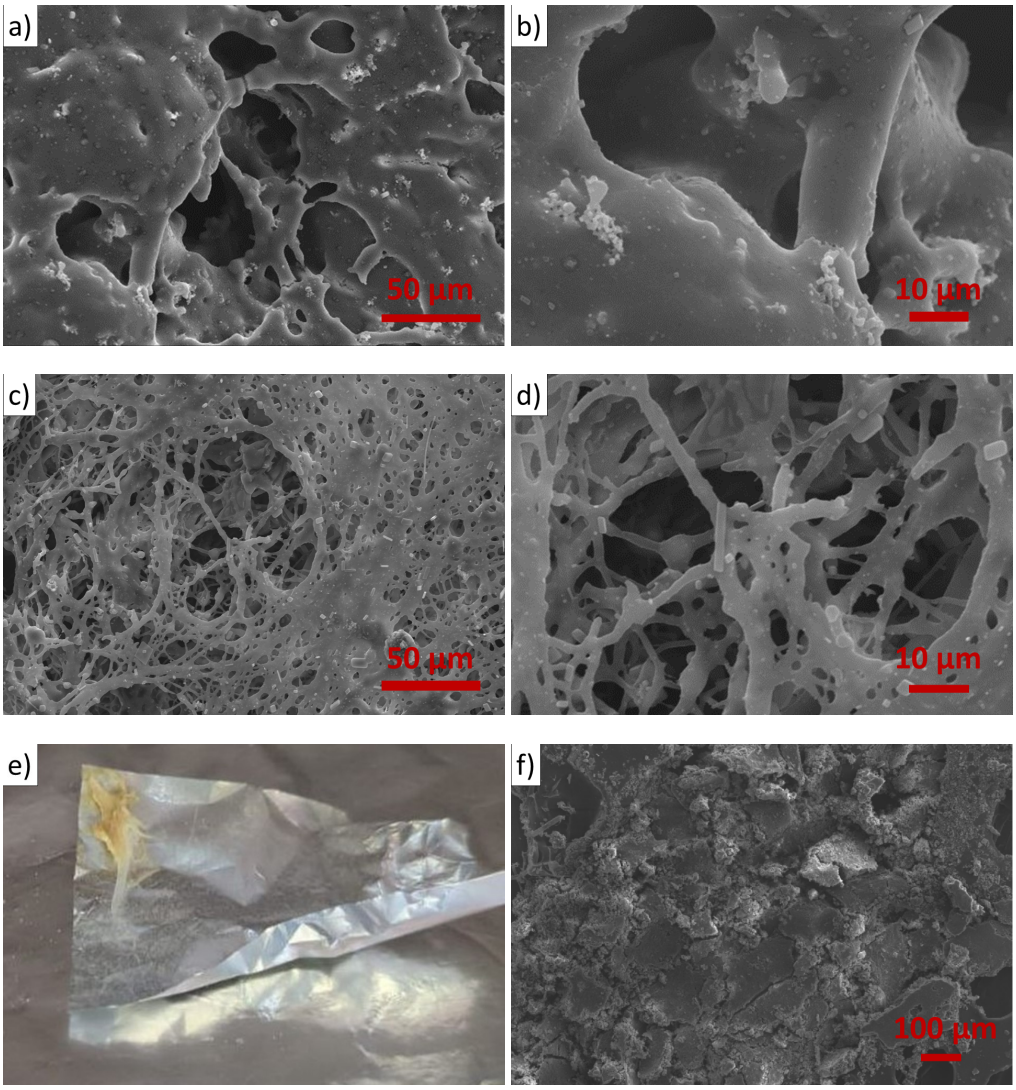

Figure 5.9: SEM of w/T =12, 2, 1:1 vol, 8.8 PVB sample dried at 130 °C right after electrospinning a)-b), and after 48h drying at room conditions c)-d), and corresponding picture of the shrank sample e). f) SEM of the same sample heat treated at 350 °C.

Figure 5.10: Picture of the samples resulting from heat treatment at 350 °C.

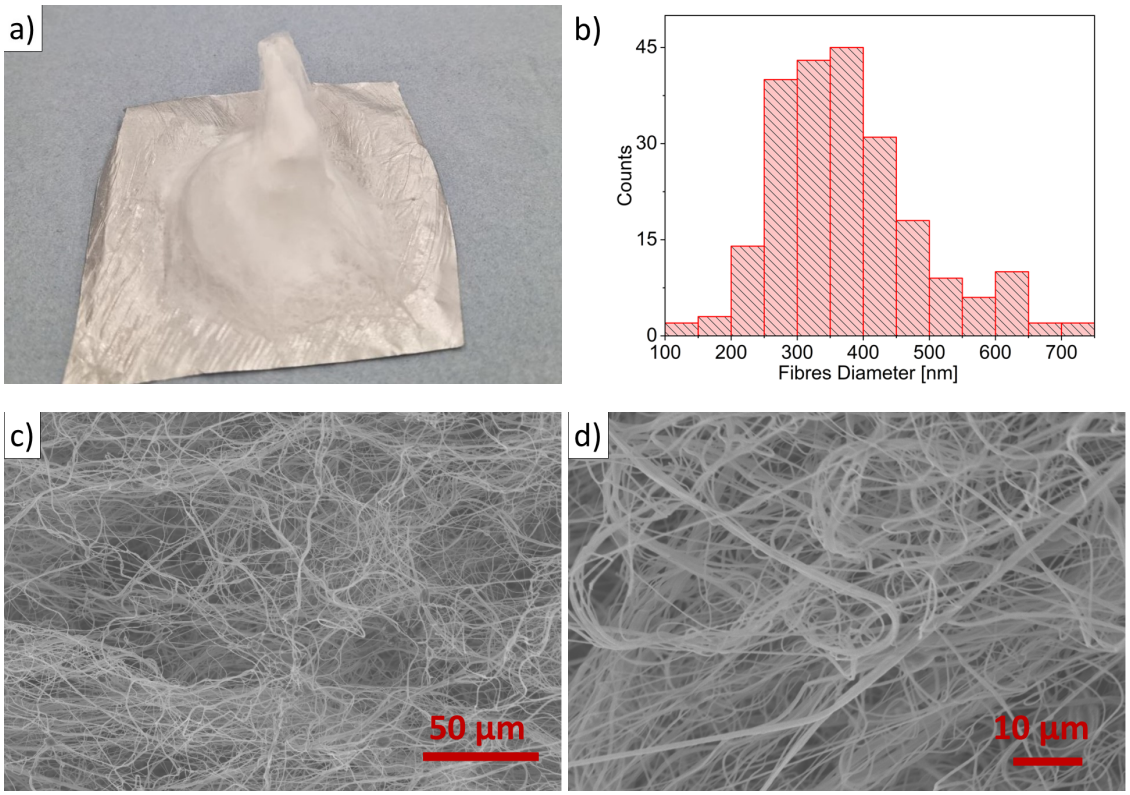

Figure 5.11: a) Picture, b) fibres diameter distribution (based on measures taken by the software ImageJ on 230 fibres across the sample), and c)-d) SEM micrographs of the w/T =12, 7, 1:1 vol, 8.8 PVB sample.

The samples obtained by electrospinning after 7 days of sol-ageing were then heat treated, but the results were the same previously obtained (very similar to the ones reported in Figure 5.10); the t_{age} increase did not show beneficial effects.

Given the previous results, two main hypothesis were formulated:

1. The Si content is too low to allow the formation of a structure strong enough to keep the fibrous form when heated; the vast majority of literature refers to higher Si contents, like 80S20C or 70S30C formulation [304, 305].

2. The Na and Ca reactants are negatively affecting the stability of glass fibres subsection 5.1.3.

Point one would require a more detailed and possibly quantitative analysis, with the additional complication that stabilized glass in the form of fibres is not available for comparison.

The hypothesis at point 2 can be investigated by performing different tests of synthesis and then electrospinning. Since it is well known that the incorporation of Na is non-trivial in sol-gel synthesis, the very first tests were carried out without Na (basically working with a ternary glass) with $Ca(NO_3)_3 \cdot 4H_2O$ as Ca source.

This resulted in very rapid and marked gelation, even after 1 hour from the mixing of the reactants. In addition, even mixing the chemicals all together and then directly mixing the obtained sol with the PVB solution, resulted in a gelled mixture, not suitable to be spun. On the other hand, regarding ternary composition, the usage of $Ca(NO_3)_3 \cdot 4H_2O$ lead to the apparent obtainment of fibres; the results of such tests are reported in Figure 5.12.

As clearly seen, the quality of the fibres is not comparable with the one previously obtained, being such fibres thicker and less uniform (Figure 5.12 c). The FTIR analysis carried out on such sample, reported in figure Figure 5.12 b), evidenced the presence of residual PVB, which main bands (aliphatic groups at 2850 and 3000 cm^{-1} and C-O-C at 1100 cm^{-1}), even if with low intensity, are still visible. This holds also true for $Ca(NO_3)_2$ by asymmetric (around 1350 cm^{-1}) and symmetric (at approximately 820 cm^{-1}) stretching of NO_3 group [316, 317]. In addition, the Si-O oscillation band at 1020 cm^{-1} correspondent to Si-O bond in Q^3 structure of silicate tetrahedron [275], formed during the ageing step, are clearly evident in the spectrum, together with a smaller signal at 800 and 470 cm^{-1} associated with the Si-OH vibrations [304] and bending of oxygen atom in the direction perpendicular to the bisector in Si-O [310], respectively.

The stabilization, carried out at 600 °C caused an important modification of the morphology of the sample, as shown in Figure Figure 5.12 d); also in this case the fibrous structure of the sample is disrupted by the heat treatment. Interestingly, the FTIR spectrum carried out on stabilized sample, shows Si-O stretching bands corresponding to Q^3 (1020 cm^{-1}) and Q^2 (950 cm^{-1}) structures of silicon tetrahedron, together with the band at 470 cm^{-1} associated with the bending of oxygen atom in the direction perpendicular to the bisector in Si-O [310]. Furthermore, the bands associated with NO_3 group are significantly reduced. Additional bands

are present, related to O-C-O at 1440 $c\,m^{-1}$, maybe due to the dissociation of PVB or the presence of CO_3^{2-} ion due to prolonged exposure to air [307]. Lastly, it is important to underline the dissociation of PVB, at least at concentrations below the detectability by FTIR.

In any case, the outcome of such test is not satisfactory, as the sample resulting from stabilization does not show fibres.

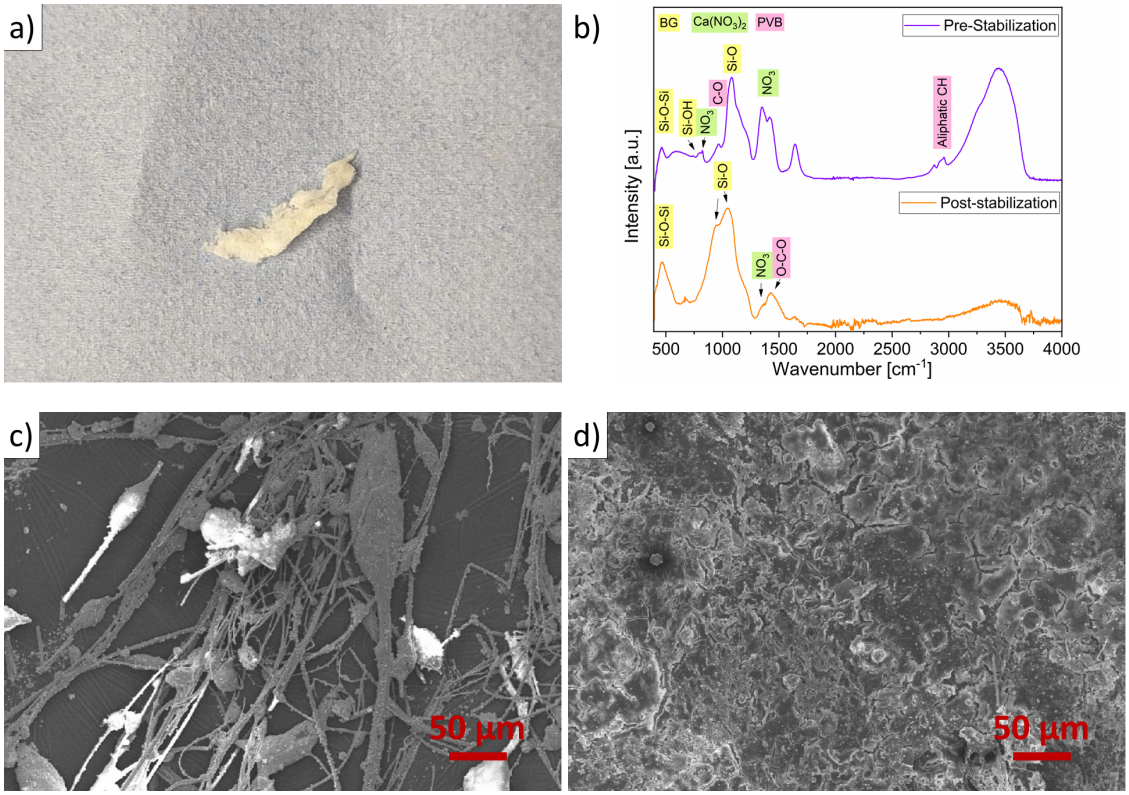

Figure 5.12: a) Picture of the sample obtained by electrospinning with $Ca(NO_3)_3 \cdot 4H_2O$ as Ca source (without Na), b) FTIR spectra before and after stabilization step, SEM micrographs c) before and d) after stabilization at 600 °C.

The spinnability of S53P4 sol-gel derived fibres was assessed. As presented in section 5.3, it was possible to deposit a 3D cotton-wool like sample by electrospinning, by the combination of sol and PVB. Optimal conditions for electrospinning were determined to be VO = 19 kV, h = 70 cm, FR = 0.75 ml/h and RH between 30 and 40 %, allowing to obtain uniformly distributed fibres with an average fibre dimension of 424 ± 109 nm. On the other hand, whenever the samples were exposed to high temperatures, the fibres degraded, independently from the

ageing time and chemicals used for the sol preparation.

In conclusion, regarding the aims of the present work presented in subsection 5.1.3, only the first one was successfully achieved; the stabilization of sol-gel derived fibres and the consequent binder removal were not completely obtained.

Chapter 6

Concluding remarks

In this chapter some final considerations are due to give a clear overview of the research activity presented in this thesis, and to provide a general outline of the work carried out during the whole Ph.D. course. In addition, the very next steps concerning the finalization of the activity performed so far will be indicated.

Chapter 1 provided the introduction and the framework for the research work conducted during the Ph.D., and is the result of deepened literature survey. Furthermore, it was described and briefly discussed the outcome deriving from the active participation to the research activity focused on HA/BG_CaMIX-based FGMs. In this work, two series of highly compacted and crack-free FGMs consisting of 5 superimposed layers, composed of different combinations of HA and bioactive glass, were produced for the first time by SPS. The main results can be sumarized as follows:

- lower temperature and higher-pressure conditions (800 °C/50 MPa) were adopted when considering the BG-rich system, called S2, with respect to those ones (1000 °C/16MPa) applied for the HA-richer counterpart, named S1;
- due to the beneficial role played by BG as sintering aid, a higher compactness was achieved in S2 samples, which is responsible for their superior hardness and Young's modulus, compared to S1;

- S2 system exhibited superior in-vitro bioactivity (assessed by SBF test). This behaviour was ascribed to the fact that crystallisation did not occur in this system during SPS; the combination of two concurrent factors, namely the chemical composition of the BG_Ca/MIX glass, with high crystallization temperature (880 °C), and the milder processing conditions (i.e. 800 °C, 50 MPa) adopted when processing BG-rich system, justify such findings.

As a matter of fact, the fabrication of samples containing both HA and novel formulations of bioactive glass opens intriguing scenarios, since it allows to combine the benefits of the two constituents. Furthermore, the FGMs approach allows for the tuning of the response of the product and controlling the bioactivity/dissolution rate of the sample. In this way, innovative systems with tailored biological properties can be developed. In this context, the SPS technology appears very promising for the fabrication of FGMs for biomedical applications. The full reference of the resulting paper is indicated below (see Appendix).

M. Luginina, **D. Angioni**, S. Montinaro, R. Orrù, G. Cao, R. Sergi, D. Bellucci, V. Cannillo, Hydroxyapatite/bioactive glass functionally graded materials (FGM) for bone tissue engineering, Journal of the European Ceramic Society, https://doi.org/10.1016/j.jeurceramsoc.2020.05.061.

Given the beneficial results obtainable by the employment of bioactive glass formulations with low tendency to crystallize, Chapter 2 focused on the densification by SPS and characterization of the novel BGMS10 glass. The aim of this work was to provide new and useful information regarding such recently developed glass, containing SrO and MgO, for possible application in the biomedical field. Specifically, the effect of the sintering temperature on structural, mechanical, and biological characteristics of the obtained bulk products, was systematically investigated. The outcomes of this study are reported in what follows:

- the characterization carried out on BGMS10 powders confirmed the very low crystallization attitude of this glass, as evidenced by the correspondingly high value of the activation energy (538.9 kJ/mol) compared to other formulations developed so far (for instance 230-338 kJ/mol for the case of 45S5);
- the densification of BGMS10 by SPS performed at 750 °C allowed to obtain nearly fully densified (relative density of 99.7%) and amorphous samples;
- the incipient crystallization of the glass happened at 850°C, while almost completely crystallized ceramics (95 wt.%) were produced at 950 °C;
- the occurrence of crystallization determined a slight decrease of relative density values, the Young's modulus became higher (from 90.9 to 98.4 GPa), whereas the maximum Vickers hardness (719 ± 29) was obtained when considering partially crystallized samples (T_D=850°C) instead of the almost fully crystallized ones (T_D=950°C); this result was explained by the corresponding density decrease;
- in-vitro tests in SBF clearly evidenced that the formation of the silica-gel film preceding apatite nucleation is strongly promoted by the presence of the amorphous glass on the substrate surface.

Based on the results described in Chapter 2, the completely amorphous and dense BGMS10 product displays the most promising characteristics for possible biomedical applications. Indeed, although improved Young's moduli were obtained for crystallized BGMS10 samples, Vickers hardness of the amorphous counterpart is quite high and even better than that of the 95% crystallized sample. In addition, both these properties are much higher than those ones measured for the 45S5 Bioglass® products also processed by SPS.

The research work presented in Chapter 2 resulted in the following scientific publication.

D. Angioni, R. Orrù, G. Cao, S. Garroni, A. Iacomini, D. Bellucci, V. Cannillo, Spark Plasma Sintering, Mechanical and In-vitro Behavior of a Novel Sr- and Mg-Containing Bioactive Glass for Biomedical Applications, J. Eur. Ceram. Soc. 42, (2022), pp. 1776-1783

https://doi.org/10.1016/j.jeurceramsoc.2021.11.061.

In addition, the obtained results were presented in two conferences, as a poster and as an oral presentation.

D. Angioni (speaker), R. Orrù, G. Cao, S. Garroni, A. Iacomini, V. Cannillo, Spark Plasma Sintering and Characterization of an Innovative Sr- And Mg-Containing Bioactive Glass, AIMAT 2021 XVI Convegno Nazionale, Cagliari (Italy), September 15-18, 2021, .

D. Angioni (speaker), R. Orrù, G. Cao, S. Garroni, A. Iacomini, D. Bellucci, V. Cannillo, Spark Plasma Sintering, Crystallization, Mechanical Properties and Biological Behavior of an Innovative SrO- and MgO-containing Bioactive Glass. CIMTEC 2022 - 9th FORUM ON NEW MATERIALS, Perugia (Italy), June 25-29, 2022.

The BGMS10 glass used in Chapter 2 was then employed for the development of novel HA/BGMS10 composites, described in Chapter 3. Three different formulations of the composite were prepared, namely 25HA-75BG, 50HA-50BG and 75HA-25BG. The effect of a ball milling treatment of the composite mixtures prior to SPS was investigated. The most relevant results are summarised in the following.

- the detalied microstructural analysis performed on the 50HA-50BG powders, evidenced that the mechanical treatment produced progressively larger composite agglomerates, an increase of the surface area, and a significantly reduction of HA crystallites size, from the micrometer-submicrometer range, i.e. >200 nm (unmilled), to the nanometer range, i.e. about 70 and 47 nm, for 30 and 120 min milled powders, respectively;
- the optimal SPS conditions, when processing unmilled powders, were found to be 700, 800 and 950 °C for 25HA-75BG, 50HA-50BG and 75HA-25BG, respectively, whereas P = 70MPa. The obtained densities were in the range 89.7%-94.2%;
- the amorphous nature of the glass fraction was preserved for temperatures up to 800 °C, above which glass crystallization occurs, in agreement with outcomes obtained in

Chapter 2 for the individual BGMS10;

- the ball milling treatment was found to affect the microstructural, mechanical and biological (SBF test) characteristics of the sintered samples. In particular, HA crystallites size growth was highly retained (from 70 to 90 nm) during SPS of 30 min milled powders and the obtained samples exhibited superior Young's Modulus (122 GPa), Vickers Hardness (675) and, above all, an extraordinary biological response, being their surface completely covered by HA precipitates just after 7 days immersion in SBF; the extension to 120 min of the BM process is self-defeating, as it results in less dense products with poorer mechanical properties and lower in-vitro bioactivity. The formation of crystalline SiO_2 during SPS is postulated to be responsible for such negative outcome.

The presented results, in particular the extraordinary biological response of the 50HA-50BG SPSed samples derived from 30 min milled powders, makes the combination of formualtion/processing method promising in terms of future applications in biomedicine. The obtained findings relative to the 50HA-50BG composite were described and discussed in a scientific paper (see Appendix), and presented orally in an International Conference, as reported below.

D. Angioni, R. Orrù, G. Cao, S. Garroni, D. Bellucci, V. Cannillo, Bioactivity Enhancement by a Ball Milling Treatment in Novel Bioactive Glass-Hydroxyapatite Composites, Journal of the European Ceramic Society, (2022), https://doi.org/10.1016/j.jeurceramsoc.2022.10.077.

D. Angioni (speaker), R. Orrù, G. Cao, S. Garroni, D. Bellucci, V. Cannillo, Novel Bioactive glass-Hydroxyapatite composites for bone tissue engineering: Processing, Mechanical and in vitro biological properties. BIOCERAMICS32, Mestre (Italy), September 20-23, 2022.

The detailed microstructural, biological and mechanical characterization of the 25HA-75BG and 75HA-25BG composites is in progress and it will be completed soon. Based on the obtained results, a new publication will be submitted in a reputable peer-reviewd journal.

Lastly, given the interesting outcomes reported in the case of HA/BG_CaMIX FGMs, further studies are already planned for the production of HA/BGMS10 FGMs and their characteriza-

tion.

In Chapter 4 a solution combustion route was used for the synthesis of apatite-based ceramics to be consolidated, for the first time by SPS. The most relevant results are summarised below:

- the optimal fuel to oxidizer ratio (ϕ) parameter, in terms of process evolution and composition of the synthesised powders, was 1.1. Apatite was formed as main phase along with other secondary products;
- the latter ones were mostly removed after a heat treatment at 700 °C, with the resulting products composed by apatite (83%) and β-TCP (17%). The apatite crystallite size remained nanometer-sized (about 70 nm) after heat treatment. B-type carbonate substitution is present in the apatite structure, quantified to be approximately 2 wt. %;
- densification by SPS in the temperature range 750-900 °C and (70 MPa, $t_D = 5$ min) resulted in bulk samples with relative densities up to 90%. The 90% dense sample consisted of 78% apatite and the rest β-TCP, with grain size still in the nanoscale (slightly above 100 nm);

The results examined in Chapter 4 allow to state that the SCS route is able to provide apatite based powders that, after a proper heat treatment, still displayed nanoscaled grain dimensions and the preservation of carbonation, at least at the B-site of substitution, both important characteristics of the natural apatite. Such grain dimensions were preserved after densification by SPS. However, no residual carbonation was observed on the apatite-based bulk samples. The data presented in this Chapter will be submitted for pubblication very soon, including the following authors and title:
D. Angioni, R. Orrù, G. Cao, S. Garroni, K. Manukyan, Solution Combustion Synthesis, Spark Plasma Sintering, and Characterization of Apatite-Tricalcium phosphate Nanocomposites.
Following work will be focused on the preservation of carbonation even after SPS, which

needs to be conducted at lower temperature, for instance using higher pressures, and in presence of an inert gas instead of vacuum, which favours decarbonation phenomena. Moreover, the possibility to incorporate suitable dopants into the apatite structure, to better mimic the natural composition and structure, will be investigated.

Chapter 5 describes the results related to the research work carried out at Imperial College of London, in a 6 month-period within the Ph.D. course. The aim of this study was the assessment of the spinnability and the obtainment of sol-gel derived amorphous S53P4 bioactive glass fibres by electrospinning. The obtained results are briefly summarised in the following:

- the optimal mixing time during the synthesis step for the obtainment of a sol suitable to be spun (in combination with PVB as binder) was 20 min;
- the influence of DI water/TEOS ratio and binder quantity on the spinnability of the sol was assesed. Well distributed and randomly oriented fibres were obtained, with average diameter of 424 ± 109 nm, using a DI water to TEOS ratio of 12, 1:1 vol mixing of the sol, and 8.8 wt.% solution of ethanol/PVB;
- both dehydration (130 °C) and stabilization (350 °C) were found to cause the damaging of the fibres. With the aim to improve the fibres stability, the sol-gel ageing time was then prolonged from 2 days to 7 days, but it was shown not to produce beneficial changes;
- the replacement of calcium source with the standard calcium nitrate and the complete removal of Sodium source to produce the sol to be electrospun did not improve the resistance of the obtained fibres.

Due to the restrictions related to the COVID pandemic emergency, the period abroad was postponed at the 3rd and last year of Ph.D., so that the research activity conducted at the Imperial College led only to a partial achievement of the initial aims. However, it must be considered a very initial study for the obtainment of sol-gel derived amorphous S53P4

glass fibres. Moreover, the presented research activity represents only a part of an ongoing collaboration, hopefully resulting soon in scientific outcomes, e.g. a paper.

As a final consideration, the whole work carried out during the Ph.D. was devoted to the study of novel routes to produce innovative materials with suitable properties for the field of biomedicine. In particular, it can be stated that the scientific contribution provided by the present work can give some new insights for the development of bioactive/bioresorbable materials with respect to the state of art. Even if the reported results represent a first step through the validation of such materials and methodologies, some of the obtained findings are very promising regarding the possible development of biomaterials with improved performances regarding tissue applications. In the latter regard, next steps would involve more detailed studies on their biological behaviour. As presented in previous chapters, acellular SBF essay already provided some promising results for the case of the individual BGMS10 bioactive glass and BGMS10-HA composite samples. However, the biological properties of these materials should be assessed also by cellular tests. These will include cytotoxicity and viability test using suitable cell lines typically considered for bone tissue engineering and regenerative medicine,such as SAOS-2, MLO-Y4 cells, or human bone marrow mesenchymal stromal/stem cells (BM-MSCs).

List of Figures

List of Tables

Bibliography

[1] S. Weiner and H. Lowenstam, "Organization of extracellularly mineralized tissues: A comparative study of biological crystal growt," *Critical Reviews in Biochemistry*, vol. 20, no. 4, pp. 365–408, 1986.

[2] C. Slater, "Atlas of anatomy," *South African Medical Journal*, vol. 103, no. 2, 2013.

[3] S. Marksjr and P. Odgren, "Structure and development of the skeleton," *Principles of bone biology*, pp. 3–15, 2002.

[4] B. Clarke, "Normal bone anatomy and physiology," *Clinical Journal of the American Society of Nephrology*, vol. 3, pp. S131–S139, 2008.

[5] D. G. Steele and C. A. Bramblett, "The anatomy and biology of the human skeleton," 1988.

[6] S. M. Ott, "Cortical or trabecular bone: What's the difference?," *American Journal of Nephrology*, vol. 47, pp. 373–375, 2018.

[7] P. A. Downey and M. I. Siegel, "Bone biology and the clinical implications for osteoporosis," *Physical Therapy*, vol. 86, pp. 77–91, 2006.

[8] L. L. Hench, "Bioceramics: From concept to clinic," *Journal of the American Ceramic Society*, vol. 74, no. 7, pp. 1487–1510, 1991.

[9] D. T. Reilly, A. H. Burstein, and V. H. Frankel, "The elastic modulus for bone," *Journal of Biomechanics*, vol. 7, no. 3, pp. 271–275, 1974.

[10] S. Yang, K.-F. Leong, Z. Du, and C.-K. Chua, "The design of scaffolds for use in tissue engineering. part i. traditional factors," *Tissue Engineering*, vol. 7, no. 6, pp. 679–689, 2001.

[11] V. I. Sikavitsas, J. S. Temenoff, and A. G. Mikos, "Biomaterials and bone mechanotransduction," *Biomaterials*, vol. 22, no. 19, pp. 2581–2593, 2001.

[12] U. Wolfram and J. Schwiedrzik, "Post-yield and failure properties of cortical bone," *BoneKEy Reports*, vol. 5, p. 829, 2016.

[13] S. Cowin, G. Gailani, and M. Benalla, "Hierarchical poroelasticity: Movement of interstitial fluid between porosity levels in bones," *Philosophical transactions. Series A, Mathematical, physical, and engineering sciences*, vol. 367, pp. 3401–44, 2009.

[14] A. G. Robling, A. B. Castillo, and C. H. Turner, "Biomechanical and molecular regulation of bone remodeling," *Annual Review of Biomedical Engineering*, vol. 8, no. 1, pp. 455–498, 2006.

[15] R. Florencio-Silva, G. R. da Silva Sasso, E. Sasso-Cerri, M. J. Simoes, and P. S. Cerri, "Biology of bone tissue: Structure, function, and factors that influence bone cells," *BioMed Research International*, vol. 2015, p. 421746, 2015.

[16] M. Capulli, R. Paone, and N. Rucci, "Osteoblast and osteocyte: Games without frontiers," *Archives of Biochemistry and Biophysics*, vol. 561, pp. 3–12, 2014.

[17] T. A. Franz-Odendaal, B. K. Hall, and P. E. Witten, "Buried alive: How osteoblasts become osteocytes," *Developmental Dynamics*, vol. 235, no. 1, pp. 176–190, 2006.

[18] G. Y. Rochefort, S. Pallu, and C. L. Benhamou, "Osteocyte: the unrecognized side of bone tissue," *Osteoporosis International*, vol. 21, pp. 1457–1469, 2010.

[19] X. Feng and J. M. McDonald, "Disorders of bone remodeling," *Annual Review of Pathology: Mechanisms of Disease*, vol. 6, no. 1, pp. 121–145, 2011.

[20] V. Everts, J. M. Delaissé, W. Korper, D. C. Jansen, W. Tigchelaar-Gutter, P. Saftig, and W. Beertsen, "The bone lining cell: Its role in cleaning howship's lacunae and initiating bone formation," *Journal of Bone and Mineral Research*, vol. 17, no. 1, pp. 77–90, 2002.

[21] M. J. Glimcher, "Mechanism of calcification: Role of collagen fibrils and collagen-phosphoprotein complexes in vitro and in vivo," *The Anatomical Record*, vol. 224, no. 2, pp. 139–153, 1989.

[22] F. Nudelman, K. Pieterse, A. George, P. H. H. Bomans, H. Friedrich, L. J. Brylka, P. A. J. Hilbers, G. de With, and N. A. J. M. Sommerdijk, "The role of collagen in bone apatite formation in the presence of hydroxyapatite nucleation inhibitors," *Nature Materials*, vol. 9, pp. 1004–1009, 2010.

[23] F. H. Silver and W. J. Landis, "Deposition of apatite in mineralizing vertebrate extracellular matrices: A model of possible nucleation sites on type i collagen," *Connective Tissue Research*, vol. 52, no. 3, pp. 242–254, 2011.

[24] K. Padian, E. Lamm, and S. Werning, *35 Selection Of Specimens.* University of California Press, 2013.

[25] W. Jong, "La substance minerale dans les os," *Recueil des Travaux Chimiques des Pays-Bas*, vol. 45, pp. 445 – 448, 1926.

[26] H.-M. Kim, C. Rey, and M. J. Glimcher, "Isolation of calcium-phosphate crystals of bone by non-aqueous methods at low temperature," *Journal of Bone and Mineral Research*, vol. 10, no. 10, pp. 1589–1601, 1995.

[27] S. J. Eppell, W. Tong, J. L. Katz, L. Kuhn, and M. J. Glimcher, "Shape and size of isolated bone mineralites measured using atomic force microscopy," *Journal of Orthopaedic Research*, vol. 19, no. 6, pp. 1027–1034, 2001.

[28] W. Tong, M. J. Glimcher, J. L. Katz, L. Kuhn, and S. J. Eppell, "Size and shape of mineralites in young bovine bone measured by atomic force microscopy," *Calcified Tissue International*, vol. 72, pp. 592–598, 2003.

[29] G. Cho, Y. Wu, and J. L. Ackerman, "Detection of hydroxyl ions in bone mineral by solid-state nmr spectroscopy," *Science*, vol. 300, no. 5622, pp. 1123–1127, 2003.

[30] R. Legros, N. Balmain, and G. Bonel, "Age-related changes in mineral of rat and bovine cortical bone," *Calcified Tissue International*, vol. 41, pp. 137–144, 1987.

[31] Y. Wu, J. L. Ackerman, H.-M. Kim, C. Rey, A. Barroug, and M. J. Glimcher, "Nuclear magnetic resonance spin-spin relaxation of the crystals of bone, dental enamel, and synthetic hydroxyapatites," *Journal of Bone and Mineral Research*, vol. 17, no. 3, pp. 472–480, 2002.

[32] M. Vallet-Regí and J. M. Gonzalez-Calbet, "Calcium phosphates as substitution of bone tissues," *Progress in Solid State Chemistry*, vol. 32, no. 1, pp. 1–31, 2004.

[33] C. Rey, B. Collins, T. Goehl, I. R. Dickson, and M. J. Glimcher, "The carbonate environment in bone mineral: A resolution-enhanced fourier transform infrared spectroscopy study," *Calcified Tissue International*, vol. 45, pp. 157–164, 1989.

[34] C. Rey, V. Renugopalakrishman, B. Collins, and M. J. Glimcher, "Fourier transform infrared spectroscopic study of the carbonate ions in bone mineral during aging," *Calcified Tissue International*, vol. 49, pp. 251–258, 1991.

[35] S. V. Euw, Y. Wang, G. Laurent, C. Drouet, F. Babonneau, N. Nassif, and T. Azais, "Bone mineral: new insights into its chemical composition," *Scientific Reports*, vol. 9, pp. 1–11, 2019.

[36] J. A. Buckwalter, M. J. Glimcher, R. R. Cooper, and R. Recker, "Bone biology. part i: Structure, blood supply, cells, matrix, and mineralization," *Journal of Bone and Joint Surgery*, vol. 77, no. 8, pp. 1256–1275, 1995.

[37] S. V. Dorozhkin, "Calcium orthophosphates: Occurrence, properties and major applications," *Apatite: Synthesis, Structural Characterization and Biomedical Applications*, pp. 1–47, 2014.

[38] S. V. Dorozhkin, "Calcium orthophosphates (CaPO4): occurrence and properties," *Progress in Biomaterials*, vol. 5, pp. 9–70, 2016.

[39] W. F. Neuman and M. W. Neuman, "The nature of the mineral phase of bone.," *Chemical Reviews*, vol. 53, pp. 1–45, 1953.

[40] W. F. Neuman and B. J. Bareham, "Further studies on the nature of fluid compartmentalization in chick calvaria," *Calcified Tissue Research*, vol. 17, pp. 249–255, 1975.

[41] M. W. Neuman and W. F. Neuman, "On the measurement of water compartments, ph, and gradients in calvaria," *Calcified Tissue International*, vol. 31, pp. 135–145, 1980.

[42] R. K. Rude, "Magnesium homeostasis," in *Principles of Bone Biology*, pp. 487–513, Elsevier, 2008.

[43] S. Wallach, "Availability of body magnesium during magnesium deficiency," *Magnesium*, vol. 7, no. 5-6, pp. 262–270, 1988.

[44] Y. Wang, S. V. Euw, F. M. Fernandes, S. Cassaignon, M. Selmane, G. Laurent, G. Pehau-Arnaudet, C. Coelho, L. Bonhomme-Coury, M.-M. Giraud-Guille, F. Babonneau, T. Azais, and N. Nassif, "Water-mediated structuring of bone apatite," *Nature Materials*, vol. 12, pp. 1144–1153, 2013.

[45] C. Jager, T. Welzel, W. Meyer-Zaika, and M. Epple, "A solid-state nmr investigation of the structure of nanocrystalline hydroxyapatite," *Magnetic Resonance in Chemistry*, vol. 44, no. 6, pp. 573–580, 2006.

[46] Y.-H. Tseng, Y.-L. Tsai, T. W. . Tsai, C.-P. Lin, S.-H. Huang, C.-Y. Mou, and J. C. Chan, "Double-quantum filtered heteronuclear correlation spectroscopy under magic angle spinning," *Solid State Nuclear Magnetic Resonance*, vol. 31, no. 1, pp. 55–61, 2007.

[47] Y.-H. Tseng, Y.-L. Tsai, T. W. T. Tsai, J. C. H. Chao, C.-P. Lin, S.-H. Huang, C.-Y. Mou, and J. C. C. Chan, "Characterization of the phosphate units in rat dentin by solid-state nmr spectroscopy," *Chemistry of Materials*, vol. 19, pp. 6088–6094, 2007.

[48] S.-J. Huang, Y.-L. Tsai, Y.-L. Lee, C.-P. Lin, and J. C. C. Chan, "Structural model of rat dentin revisited," *Chemistry of Materials*, vol. 21, pp. 2583–2585, 2009.

[49] M. Glimcher, "Bone: Nature of the calcium phosphate crystals and cellular, structural, and physical chemical mechanisms in their formation," *Reviews in Mineralogy & Geochemistry*, vol. 64, pp. 223–282, 2006.

[50] E. H. Schemitsch, "Size matters: Defining critical in bone defect size!," *Journal of Orthopaedic Trauma*, vol. 31, 2017.

[51] E. Roddy, M. R. DeBaun, A. Daoud-Gray, Y. P. Yang, and M. J. Gardner, "Treatment of critical-sized bone defects: clinical and tissue engineering perspectives," *European Journal of Orthopaedic Surgery & Traumatology*, vol. 28, pp. 351–362, 2018.

[52] A. Wiese and H. C. Pape, "Bone defects caused by high-energy injuries, bone loss, infected nonunions, and nonunions," *Orthopedic Clinics of North America*, vol. 41, no. 1, pp. 1–4, 2010.

[53] F. Loi, L. A. Cordova, J. Pajarinen, T. hua Lin, Z. Yao, and S. B. Goodman, "Inflammation, fracture and bone repair," *Bone*, vol. 86, pp. 119–130, 2016.

[54] D. Clark, M. Nakamura, T. Miclau, and R. Marcucio, "Effects of aging on fracture healing," *Current Osteoporosis Reports*, vol. 15, pp. 601–608, 2017.

[55] U. D. o. H. Office of the Surgeon General and H. Services, "Bone health and osteoporosis: a report of the surgeon general," *Reports of the Surgeon General*, 2004.

[56] V. Campana, G. Milano, E. Pagano, M. Barba, C. Cicione, G. Salonna, W. Lattanzi, and G. Logroscino, "Bone substitutes in orthopaedic surgery: from basic science to clinical practice," *Journal of Materials Science: Materials in Medicine*, vol. 25, pp. 2445–2461, 2014.

[57] J. Planell, S. Best, D. Lacroix, and A. Merolli, *Bone repair biomaterials*. Elsevier Inc., 2009.

[58] B. A. Allo, D. O. Costa, S. J. Dixon, K. Mequanint, and A. S. Rizkalla, "Bioactive and biodegradable nanocomposites and hybrid biomaterials for bone regeneration," *Journal of Functional Biomaterials*, vol. 3, no. 2, pp. 432–463, 2012.

[59] R. Langer and J. P. Vacanti, "Tissue engineering," *Science*, vol. 260, no. 5110, pp. 920–926, 1993.

[60] "The european society for biomaterials 9th european conference on biomaterials Chester, UK 9-11th September, 1991 in conjunction with 2nd Consensus Conference on Definitions in Biomaterials 7-8th September, 1991 and IUPAC working party on blood compatibility," *Journal of Materials Science: Materials in Medicine*, vol. 2, p. 62, 1991.

[61] L. Ghasemi-Mobarakeh, D. Kolahreez, S. Ramakrishna, and D. Williams, "Key terminology in biomaterials and biocompatibility," *Current Opinion in Biomedical Engineering*, vol. 10, pp. 45–50, 2019.

[62] D. F. Williams, "Specifications for innovative, enabling biomaterials based on the principles of biocompatibility mechanisms," *Frontiers in Bioengineering and Biotechnology*, vol. 7, 2019.

[63] A. Brydone, D. Meek, S. Maclaine, K. Tanner, and M. Dalby, "Bone grafting, orthopaedic biomaterials, and the clinical need for bone engineering," *Journal of Engineering in Medicine*, vol. 224, pp. 1329–1343, 2010.

[64] W. G. J. De Long, T. A. Einhorn, K. Koval, M. McKee, W. Smith, R. Sanders, and T. Watson, "Bone grafts and bone graft substitutes in orthopaedic trauma surgery: A critical analysis," *The Journal of Bone & Joint Surgery*, vol. 89, pp. 649–658, 2007.

[65] J. Baumhauer, M. S. Pinzur, R. Donahue, W. Beasley, and C. DiGiovanni, "Site selection and pain outcome after autologous bone graft harvest," *Foot & Ankle International*, vol. 35, pp. 104–107, 2013.

[66] G. Kumar and B. Narayan, *Morbidity at Bone Graft Donor Sites*, pp. 503–505. Springer London, 2014.

[67] G. F. Rogers and A. K. Greene, "Autogenous bone graft: Basic science and clinical implications," *Journal of Craniofacial Surgery*, vol. 23, 2012.

[68] F. G. Lakkis and R. I. Lechler, "Origin and biology of the allogeneic response," *Cold Spring Harbor Perspectives in Medicine*, vol. 3, no. 8, 2013.

[69] E. Chiarello, M. Cadossi, G. Tedesco, P. Capra, C. Calamelli, A. Shehu, and S. Giannini, "Autograft, allograft and bone substitutes in reconstructive orthopedic surgery," *Aging Clinical and Experimental Research*, vol. 25, pp. 101–103, 2013.

[70] A. S. Herford, E. Stoffella, and C. M. Stanford, *Bone Grafts and Bone Substitute Materials*. Saint Louis: W.B. Saunders, 2014.

[71] J. Jones and A. Clare, *Bio-Glasses: An Introduction*. 2012.

[72] A. Kulkarni and P. Rao, "2 - synthesis of polymeric nanomaterials for biomedical applications," in *Nanomaterials in Tissue Engineering*, Woodhead Publishing Series in Biomaterials, pp. 27–63, Woodhead Publishing, 2013.

[73] G. Hannink and J. J. Arts, "Bioresorbability, porosity and mechanical strength of bone substitutes: What is optimal for bone regeneration?," *Injury*, vol. 42, 2011.

[74] C. M. J. M. Pypen, K. Dessein, J. A. Helsen, M. Gomes, H. Leenders, and J. D. D. Bruijn, "Comparison of the cytotoxicity of molybdenum as powder and as alloying element in a niobium-molybdenum alloy," *Journal of Materials Science: Materials in Medicine*, vol. 9, pp. 761–765, 1998.

[75] D. R. Haynes, S. D. Rogers, S. Hay, M. J. Pearcy, and D. W. Howie, "The differences in toxicity and release of bone-resorbing mediators induced by titanium and cobalt-chromium-alloy wear particles.," *JBJS*, vol. 75, 1993.

[76] S. Ramakrishna, M. Ramalingam, T. S. Kumar, and W. Soboyejo, *Biomaterials: A Nano Approach*. Saint Louis: CRC Press, 2010.

[77] S. Bose, M. Roy, and A. Bandyopadhyay, "Recent advances in bone tissue engineering scaffolds," *Trends in biotechnology*, vol. 30, pp. 546–54, 2012.

[78] R. Narayan, *Biomedical Materials*. 2009.

[79] W. He and R. Benson, "8 - polymeric biomaterials," in *Applied Plastics Engineering Handbook (Second Edition)* (M. Kutz, ed.), Plastics Design Library, pp. 145–164, William Andrew Publishing, second edition ed., 2017.

[80] M. Vallet-Regí, "Bioceramics: Where do we come from and which are the future expectations," *Key Engineering Materials*, vol. 377, pp. 1–18, 2008.

[81] M. Vallet-Regí, "Evolution of bioceramics within the field of biomaterials," *Comptes Rendus Chimie*, vol. 13, no. 1, pp. 174–185, 2010.

[82] E. Saiz, A. R. Boccaccini, J. Chevalier, and M. Peroglio, "Editorial on bioceramics for bone repair," *Journal of the European Ceramic Society*, vol. 38, pp. 821–822, 2018.

[83] C. Piconi and A. A. Porporati, *Bioinert Ceramics: Zirconia and Alumina*, pp. 59–89. Cham: Springer International Publishing, 2016.

[84] C. Piconi, S. G. Condo, and T. Kosmac, "Alumina and zirconia based ceramics for load-bearing applications,"

[85] S. Best, A. Porter, E. Thian, and J. Huang, "Bioceramics: Past, present and for the future," *Journal of the European Ceramic Society*, vol. 28, no. 7, pp. 1319–1327, 2008.

[86] J. Chevalier, J. Loh, L. Gremillard, S. Meille, and E. Adolfson, "Low-temperature degradation in zirconia with a porous surface," *Acta Biomaterialia*, vol. 7, no. 7, pp. 2986–2993, 2011.

[87] J. Chevalier, L. Gremillard, and S. Deville, "Low-temperature degradation of zirconia and implications for biomedical implants," *Annual Review of Materials Research*, vol. 37, pp. 1–32, 2007.

[88] W. Cao and L. L. Hench, "Bioactive materials," *Ceramics International*, vol. 22, no. 6, pp. 493–507, 1996.

[89] D. M. Eichert, M. Salomé, M. Banu, J. Susini, and C. Rey, "Preliminary characterization of calcium chemical environment in apatitic and non-apatitic calcium phosphates of biological interest by X-ray absorption spectroscopy," *Spectrochimica Acta Part B: Atomic Spectroscopy*, vol. 60, pp. 850–858, 2005.

[90] J. Park, *Bioceramics: Properties, characterizations, and applications*. 2009.

[91] S. V. Dorozhkin, "Calcium orthophosphates as bioceramics: State of the art," *Journal of Functional Biomaterials*, vol. 1, no. 1, pp. 22–107, 2010.

[92] S. V. Dorozhkin, "Calcium orthophosphate-based bioceramics," *Materials*, vol. 6, no. 9, pp. 3840–3942, 2013.

[93] S. Samavedi, A. R. Whittington, and A. S. Goldstein, "Calcium phosphate ceramics in bone tissue engineering: A review of properties and their influence on cell behavior," *Acta Biomaterialia*, vol. 9, no. 9, pp. 8037–8045, 2013.

[94] R. Snyders, D. Music, D. Sigumonrong, B. Schelnberger, J. Jensen, and J. M. Schneider, "Experimental and ab initio study of the mechanical properties of hydroxyapatite," *Applied Physics Letters*, vol. 90, no. 19, p. 193902, 2007.

[95] P. Rulis, L. Ouyang, and W. Y. Ching, "Electronic structure and bonding in calcium apatite crystals: Hydroxyapatite, fluorapatite, chlorapatite, and bromapatite," *Phys. Rev. B*, vol. 70, p. 155104, 2004.

[96] T. J. White and D. ZhiLi, "Structural derivation and crystal chemistry of apatites," *Acta Crystallographica Section B*, vol. 59, no. 1, pp. 1–16, 2003.

[97] A. Sobczak-Kupiec, D. Malina, R. Kijkowska, and Z. Wzorek, "Comparative study of hydroxyapatite prepared by the authors with selected commercially available ceramics," *Digest Journal of Nanomaterials and Biostructures*, vol. 7, pp. 385–391, 2012.

[98] S. Pokhrel, "Hydroxyapatite: Preparation, properties and its biomedical applications," *Advances in Chemical Engineering and Science*, vol. 08, pp. 225–240, 2018.

[99] K. Lin and J. Chang, *Structure and properties of hydroxyapatite for biomedical applications*. Woodhead Publishing Series in Biomaterials, Woodhead Publishing, 2015.

[100] Y. Cai and R. Tang, "Calcium phosphate nanoparticles in biomineralization and biomaterials," *J. Mater. Chem.*, vol. 18, pp. 3775–3787, 2008.

[101] A. Giraldo-Betancur, D. Espinosa-Arbelaez, A. del Real-Lopez, B. Millan-Malo, E. Rivera-Munoz, E. Gutierrez-Cortez, P. Pineda-Gomez, S. Jimenez-Sandoval, and M. Rodriguez-Garcia, "Comparison of physicochemical properties of bio and commercial hydroxyapatite," *Current Applied Physics*, vol. 13, no. 7, pp. 1383–1390, 2013.

[102] M. Bohner and J. Lemaitre, "Can bioactivity be tested in vitro with SBF solution?," *Biomaterials*, vol. 30, no. 12, pp. 2175–2179, 2009.

[103] S. Bertazzo, W. F. Zambuzzi, D. D. Campos, T. L. Ogeda, C. V. Ferreira, and C. A. Bertran, "Hydroxyapatite surface solubility and effect on cell adhesion," *Colloids and Surfaces B: Biointerfaces*, vol. 78, no. 2, pp. 177–184, 2010.

[104] S. Kalita, A. Bhardwaj, and H. Bhatt, "Nanocrystalline calcium phosphate ceramics in biomedical engineering," *Materials Science and Engineering C*, vol. 27, pp. 441–449, 2007.

[105] H. Zhu, D. Guo, L. Sun, H. Li, D. Hanaor, F. Schmidt, and K. Xu, "Nanostructural insights into the dissolution behavior of Sr-doped hydroxyapatite," *Journal of the European Ceramic Society*, vol. 38, 2018.

[106] M. Sadat-Shojai, M. T. Khorasani, E. Dinpanah-Khoshdargi, and A. Jamshidi, "Synthesis methods for nanosized hydroxyapatite with diverse structures," *Acta Biomaterialia*, vol. 9, pp. 7591–7621, 2013.

[107] H. Pan and B. W. Darvell, "Effect of carbonate on hydroxyapatite solubility," *Crystal Growth & Design*, vol. 10, no. 2, pp. 845–850, 2010.

[108] S. V. Dorozhkin, "Multiphasic calcium orthophosphate (CaPO4) bioceramics and their biomedical applications," *Ceramics International*, vol. 42, pp. 6529–6554, 2016.

[109] K. Lin, L. Chen, and J. Chang, "Fabrication of dense hydroxyapatite nanobioceramics with enhanced mechanical properties via two-step sintering process," *International Journal of Applied Ceramic Technology*, vol. 9, no. 3, pp. 479–485, 2012.

[110] W. Suchanek and M. Yoshimura, "Processing and properties of hydroxyapatite-based biomaterials for use as hard tissue replacement implants," *Journal of Materials Research*, vol. 13, no. 1, pp. 94–117, 1998.

[111] L. Sun, C. C. Berndt, K. A. Gross, and A. Kucuk, "Material fundamentals and clinical performance of plasma-sprayed hydroxyapatite coatings: A review," *Journal of Biomedical Materials Research*, vol. 58, no. 5, pp. 570–592, 2001.

[112] S. V. Dorozhkin, "Calcium orthophosphate deposits: Preparation, properties and biomedical applications," *Materials Science and Engineering: C*, vol. 55, pp. 272–326, 2015.

[113] S. C. Cox, R. I. Walton, and K. K. Mallick, "Comparison of techniques for the synthesis of hydroxyapatite," *Bioinspired, Biomimetic and Nanobiomaterials*, vol. 4, pp. 37–47, 2015.

[114] M. Markovic, B. O. Fowler, and M. Tung, "Preparation and comprehensive characterization of calcium hydroxyapatite reference material," *Journal of research of national institute of standards and technology*, vol. 109, pp. 553–568, 2004.

[115] A. Varma, A. S. Mukasyan, A. S. Rogachev, and K. V. Manukyan, "Solution combustion synthesis of nanoscale materials," *Chemical Reviews*, vol. 116, pp. 14493–14586, 2016.

[116] W. hai Huang, Y. Li, M. N. Rahaman, and D. E. Day, "Mechanisms for converting bioactive silicate, borate, and borosilicate glasses to hydroxyapatite in dilute phosphate solution," *Physics and Chemistry of Glasses-european Journal of Glass Science and Technology Part B*, vol. 47, pp. 647–658, 2006.

[117] M. Brink, "The influence of alkali and alkaline earths on the working range for bioactive glasses," *Journal of Biomedical Materials Research*, vol. 36, no. 1, pp. 109–117, 1997.

[118] E. A. Abou Neel, D. M. Pickup, S. P. Valappil, R. J. Newport, and J. C. Knowles, "Bioactive functional materials: a perspective on phosphate-based glasses," *J. Mater. Chem.*, vol. 19, pp. 690–701, 2009.

[119] J. R. Jones, "Review of bioactive glass: From hench to hybrids," *Acta Biomaterialia*, vol. 9, pp. 4457–4486, 2013.

[120] L. L. Hench, "The story of bioglass," *Journal of Materials Science: Materials in Medicine*, vol. 17, pp. 967–978, 2006.

[121] Z. Sultan, M. Khalid, M. Zafar, I. Farooq, R. Khan, and A. Naqvi, "Bioactive glasses and their applications in dentistry," *The Journal of Pakistan Dental Association*, vol. 26, pp. 32–38, 2017.

[122] L. L. Hench and J. R. Jones, "Bioactive glasses: Frontiers and challenges," *Frontiers in Bioengineering and Biotechnology*, vol. 3, 2015.

[123] L. L. Hench, "Chronology of bioactive glass development and clinical applications," 2013.

[124] F. Baino, G. Novajra, V. Miguez-Pacheco, A. R. Boccaccini, and C. Vitale-Brovarone, "Bioactive glasses: Special applications outside the skeletal system," *Journal of Non-Crystalline Solids*, vol. 432, pp. 15–30, 2016.

[125] V. Krishnan and T. Lakshmi, "Bioglass: A novel biocompatible innovation," *Journal of Advanced Pharmaceutical Technology & Research*, vol. 4, no. 2, pp. 78–83, 2013.

[126] I. Gergely, A. Zazgyva, A. Man, S. Zuh, and T. Pop, "The in vitro antibacterial effect of S53P4 bioactive glass and gentamicin impregnated polymethylmethacrylate beads," *Acta Microbiologica et Immunologica Hungarica*, vol. 61, no. 2, pp. 145 – 160, 2014.

[127] L. Drago, C. Vassena, S. Fenu, E. D. Vecchi, V. Signori, R. D. Francesco, and C. L. Romanò, "In vitro antibiofilm activity of bioactive glass S53P4," *Future Microbiology*, vol. 9, no. 5, pp. 593–601, 2014.

[128] R. Detsch, P. Stoor, A. GrÃ¼newald, J. A. Roether, N. C. Lindfors, and A. R. Boccaccini, "Increase in vegf secretion from human fibroblast cells by bioactive glass S53P4 to stimulate angiogenesis in bone," *Journal of Biomedical Materials Research Part A*, vol. 102, no. 11, pp. 4055–4061, 2014.

[129] D. C. Coraća-Huber, M. Fille, J. Hausdorfer, D. Putzer, and M. Nogler, "Efficacy of antibacterial bioactive glass S53P4 against s. aureus biofilms grown on titanium discs in vitro," *Journal of Orthopaedic Research*, vol. 32, no. 1, pp. 175–177, 2014.

[130] L. Drago, E. D. Vecchi, M. Bortolin, M. Toscano, R. Mattina, and C. L. Romano', "Antimicrobial activity and resistance selection of different bioglass S53P4 formulations against multidrug resistant strains," *Future Microbiology*, vol. 10, pp. 1293–1299, 2015.

[131] D. Zhang, O. Lepparanta, E. Munukka, H. Ylanen, M. K. Viljanen, E. Eerola, M. Hupa, and L. Hupa, "Antibacterial effects and dissolution behavior of six bioactive glasses," *Journal of Biomedical Materials Research - Part A*, vol. 93, pp. 475–483, 2010.

[132] O. Lepparanta, M. Vaahtio, T. Peltola, D. Zhang, L. Hupa, M. Hupa, H. Ylanen, J. I. Salonen, M. K. Viljanen, and E. Eerola, "Antibacterial effect of bioactive glasses on clinically important anaerobic bacteria in vitro," *Journal of Materials Science: Materials in Medicine*, vol. 19, pp. 547–551, 2008.

[133] J. Rantakokko, J. P. Frantzén, J. Heinanen, S. Kajander, E. Kotilainen, E. Gullichsen, and N. C. Lindfors, "Posterolateral spondylodesis using bioactive glass S53P4 and autogenous bone in instrumented unstable lumbar spine burst fractures: A prospective 10-year follow-up study," *Scandinavian Journal of Surgery*, vol. 101, no. 1, pp. 66–71, 2012.

[134] K. . Pernaa, I. Koski, K. Mattila, E. Gullichsen, J. Heikkila, A. J. Aho, and N. Lindfors, "Bioactive glass S53P4 and autograft bone in treatment of depressed tibial plateau fractures - a prospective randomized 11-year follow-up," *Journal of Long-Term Effects of Medical Implants*, vol. 21, no. 2, pp. 139–148, 2011.

[135] S. Montinaro, L. Desogus, R. Orrù, S. Garroni, F. Delogu, P. C. Ricci, and G. Cao, "A comprehensive study on compositional and structural changes in 45S5 bioglass products exposed to simulated body fluid," *Journal of the American Ceramic Society*, vol. 101, no. 1, pp. 116–130, 2018.

[136] A. R. Boccaccini, Q. Chen, L. Lefebvre, L. Gremillard, and J. Chevalier, "Sintering, crystallisation and biodegradation behaviour of bioglass-derived glass-ceramics," *Faraday Discuss.*, vol. 136, pp. 27–44, 2007.

[137] X. Chatzistavrou, P. Newby, and A. Boccaccini, "5 - bioactive glass and glass-ceramic scaffolds for bone tissue engineering," in *Bioactive Glasses* (H. O. YlÃ¤nen, ed.), Woodhead Publishing Series in Biomaterials, pp. 107–128, Woodhead Publishing, 2011.

[138] L. Desogus, A. Cuccu, S. Montinaro, R. Orrù, G. Cao, D. Bellucci, A. Sola, and V. Cannillo, "Classical bioglassÂ® and innovative CaO-rich bioglass powders processed by Spark Plasma Sintering: A comparative study," *Journal of the European Ceramic Society*, vol. 35, pp. 4277–4285, 2015.

[139] D. Bellucci, L. Desogus, S. Montinaro, R. Orrù, G. Cao, and V. Cannillo, "Innovative hydroxyapatite/bioactive glass composites processed by spark plasma sintering for bone tissue repair," *Journal of the European Ceramic Society*, vol. 37, pp. 1723–1733, 2017.

[140] S. Montinaro, M. Luginina, S. Garroni, R. Orrù, F. Delogu, D. Bellucci, V. Cannillo, and G. Cao, "Spark plasma sintered CaO-rich bioglass-derived glass-ceramics with different crystallinity ratios: A detailed investigation of their behaviour during biological tests in SBF," *Journal of the European Ceramic Society*, vol. 39, pp. 1603–1612, 2019.

[141] D. Bellucci and V. Cannillo, "A novel bioactive glass containing strontium and magnesium with ultra-high crystallization temperature," *Materials Letters*, vol. 213, pp. 67–70, 2018.

[142] D. Bellucci, E. Veronesi, V. Strusi, T. Petrachi, A. Murgia, I. Mastrolia, M. Dominici, and V. Cannillo, "Human mesenchymal stem cell combined with a new strontium-enriched bioactive glass: An ex-vivo model for bone regeneration," *Materials*, vol. 12, 2019.

[143] K. H. Thompson and C. Orvig, "Boon and bane of metal ions in medicine," *Science*, vol. 300, no. 5621, pp. 936–939, 2003.

[144] P. Habibovic and J. Barralet, "Bioinorganics and biomaterials: Bone repair," *Acta Biomaterialia*, vol. 7, no. 8, pp. 3013–3026, 2011.

[145] J. H. Beattie and A. Avenell, "Trace element nutrition and bone metabolism," *Nutrition Research Reviews*, vol. 5, no. 1, pp. 167–188, 1992.

[146] C. Lang, C. Murgia, M. Leong, L.-W. Tan, G. Perozzi, D. Knight, R. Ruffin, and P. Zalewski, "Anti-inflammatory effects of zinc and alterations in zinc transporter mrna in mouse models of allergic inflammation," *American Journal of Physiology-Lung Cellular and Molecular Physiology*, vol. 292, no. 2, pp. L577–L584, 2007.

[147] L. Esteban-Tejeda, F. Malpartida, A. Esteban-Cubillo, C. PecharromÃ¡n, and J. S. Moya, "Antibacterial and antifungal activity of a soda-lime glass containing copper nanoparticles," *Nanotechnology*, vol. 20, no. 50, p. 505701, 2009.

[148] T. Mehrabi, A. S. Mesgar, and Z. Mohammadi, "Bioactive glasses: A promising therapeutic ion release strategy for enhancing wound healing," *ACS Biomaterials Science and Engineering*, vol. 6, pp. 5399–5430, 2020.

[149] Z. Hong, A. Liu, L. Chen, X. Chen, and X. Jing, "Preparation of bioactive glass ceramic nanoparticles by combination of sol-gel and coprecipitation method," *Journal of Non-Crystalline Solids*, vol. 355, no. 6, pp. 368–372, 2009.

[150] C. Z. Chen, X. G. Meng, H. J. Yu, H. Yang, T. He, D. G. Wang, and S. G. Zhao, "Preparation and development of bioglass by sol-gel method," in *Testing and Evaluation of Inorganic Materials IV*, vol. 591 of *Key Engineering Materials*, pp. 34–39, Trans Tech Publications Ltd, 2014.

[151] R. Li, A. E. Clark, and L. L. Hench, "An investigation of bioactive glass powders by sol-gel processing," *Journal of Applied Biomaterials*, vol. 2, no. 4, pp. 231–239, 1991.

[152] G. Kaur, G. Pickrell, N. Sriranganathan, V. Kumar, and D. Homa, "Review and the state of the art: Sol-gel and melt quenched bioactive glasses for tissue engineering," *Journal of Biomedical Materials Research Part B: Applied Biomaterials*, vol. 104, no. 6, pp. 1248–1275, 2016.

[153] S. E. Lobo and T. Livingston Arinzeh, "Biphasic calcium phosphate ceramics for bone regeneration and tissue engineering applications," *Materials*, vol. 3, no. 2, pp. 815–826, 2010.

[154] J. D. Santos, R. L. Reis, F. J. Monteiro, J. C. Knowles, and G. W. Hastings, "Liquid phase sintering of hydroxyapatite by phosphate and silicate glass additions: structure and properties of the composites," *Journal of Materials Science: Materials in Medicine*, vol. 6, pp. 348–352, 1995.

[155] L. J. Jha, J. D. Santos, and J. C. Knowles, "Characterization of apatite layer formation on P2O5-CaO, P2O5-CaO-na2o, and P2O5-CaO-na2o-al2o3 glass hydroxyapatite composites," *Journal of Biomedical Materials Research*, vol. 31, no. 4, pp. 481–486, 1996.

[156] J. C. Knowles and W. Bonfield, "Development of a glass reinforced hydroxyapatite with enhanced mechanical properties. the effect of glass composition on mechanical properties and its relationship to phase changes," *Journal of Biomedical Materials Research*, vol. 27, no. 12, pp. 1591–1598, 1993.

[157] G. Udupa, S. S. Rao, and K. Gangadharan, "Functionally graded composite materials: An overview," *Procedia Materials Science*, vol. 5, pp. 1291–1299, 2014.

[158] A. Sola, D. Bellucci, and V. Cannillo, "Functionally graded materials for orthopedic applications - an update on design and manufacturing," *Biotechnology Advances*, vol. 34, no. 5, pp. 504–531, 2016.

[159] F. Watari, H. Kondo, S. Matsuo, R. Miyao, A. Yokoyama, M. Omori, T. Hirai, Y. Tamura, M. Uo, N. Ohara, and T. Kawasaki, "Development of functionally graded implant and

dental post for biomedical application," *Materials Science Forum - MATER SCI FORUM*, vol. 423, pp. 321–326, 2003.

[160] D. Lin, Q. Li, W. Li, and M. Swain, "Bone remodeling induced by dental implants of functionally graded materials," *Journal of Biomedical Materials Research Part B: Applied Biomaterials*, vol. 92B, no. 2, pp. 430–438, 2010.

[161] J. Will, L.-C. Gerhardt, and A. R. Boccaccini, *Bioactive Glass-Based Scaffolds for Bone Tissue Engineering*, pp. 195–226. Springer Berlin Heidelberg, 2012.

[162] T. Kokubo, "Surface chemistry of bioactive glass-ceramics," *Journal of Non-Crystalline Solids*, vol. 120, no. 1, pp. 138–151, 1990.

[163] Y. Wu, M. J. Glimcher, C. Rey, and J. L. Ackerman, "A unique protonated phosphate group in bone mineral not present in synthetic calcium phosphates: Identification by phosphorus-31 solid state nmr spectroscopy," *Journal of Molecular Biology*, vol. 244, no. 4, pp. 423–435, 1994.

[164] T. Kokubo and H. Takadama, "How useful is SBF in predicting in vivo bone bioactivity?," *Biomaterials*, vol. 27, no. 15, pp. 2907–2915, 2006.

[165] P. Valerio, M. M. Pereira, A. M. Goes, and M. Leite, "The effect of ionic products from bioactive glass dissolution on osteoblast proliferation and collagen production," *Biomaterials*, vol. 25, no. 15, pp. 2941–2948, 2004.

[166] M. Moshiri, *Integrated process chain for first-time-right mould components production using laser powder bed fusion metal additive manufacturing*. PhD thesis, 2020.

[167] H. Palmour, "Rate controlled sintering for ceramics and selected powder metals," 1989.

[168] G. Muralithran and S. Ramesh, "The effects of sintering temperature on the properties of hydroxyapatite," *Ceramics International*, vol. 26, pp. 221–230, 2000.

[169] S. V. Dorozhkin, "Bioceramics of calcium orthophosphates," *Biomaterials*, vol. 31, no. 7, pp. 1465–1485, 2010.

[170] K. Maca, "Microstructure evolution during pressureless sintering of bulk oxide ceramics," *Processing and Application of Ceramics*, vol. 3, 2009.

[171] N. Loh and K. Sia, "An overview of hot isostatic pressing," *Journal of Materials Processing Technology*, vol. 30, no. 1, pp. 45–65, 1992.

[172] H. V. Atkinson and S. Davies, "Fundamental aspects of hot isostatic pressing: An overview," *Metallurgical and Materials Transactions A*, vol. 31, pp. 2981–3000, 2000.

[173] L. F. Francis, "Chapter 5 - powder processes," in *Materials Processing* (L. F. Francis, ed.), pp. 343–414, Boston: Academic Press, 2016.

[174] R. Orrù, R. Licheri, A. M. Locci, A. Cincotti, and G. Cao, "Consolidation/synthesis of materials by electric current activated/assisted sintering," *Materials Science and Engineering: R: Reports*, vol. 63, no. 4, pp. 127–287, 2009.

[175] A. Cuccu, S. Montinaro, R. Orrù, G. Cao, D. Bellucci, A. Sola, and V. Cannillo, "Consolidation of different hydroxyapatite powders by sps: Optimization of the sintering conditions and characterization of the obtained bulk products," *Ceramics International*, vol. 41, no. 1 Part A, pp. 725–736, 2015.

[176] Z. A. Munir, U. Anselmi-Tamburini, and M. Ohyanagi, "The effect of electric field and pressure on the synthesis and consolidation of materials: A review of the spark plasma sintering method," *Journal of Materials Science*, vol. 41, pp. 763–777, 2006.

[177] L. C. Gerhardt and A. R. Boccaccini, "Bioactive glass and glass-ceramic scaffolds for bone tissue engineering," *Materials*, vol. 3, pp. 3867–3910, 2010.

[178] V. Miguez-Pacheco, L. L. Hench, and A. R. Boccaccini, "Bioactive glasses beyond bone and teeth: Emerging applications in contact with soft tissues," 2014.

[179] Q. Chen, J. Roether, and A. Boccaccini, "Tissue engineering scaffolds from bioactive glass and composite materials," *Topics in tissue engineering*, vol. 4, no. 6, pp. 1–27, 2008.

[180] J. R. Jones, D. S. Brauer, L. Hupa, and D. C. Greenspan, "Bioglass and bioactive glasses and their impact on healthcare," *International Journal of Applied Glass Science*, vol. 7, pp. 423–434, 2016.

[181] L. L. Hench and J. M. Polak, "Third generation biomedical materials," *Science*, vol. 295, pp. 1014–1017, 2002.

[182] S. Grasso, R. K. Chinnam, H. Porwal, A. R. Boccaccini, and M. J. Reece, "Low temperature spark plasma sintering of 45S5 bioglass," *Journal of Non-Crystalline Solids*, vol. 362, pp. 25–29, 2013.

[183] C. Blaess, R. Muller, G. Poologasundarampillai, and D. S. Brauer, "Sintering and concomitant crystallization of bioactive glasses," *International journal of applied glass science*, vol. 10, pp. 449–462, 2019.

[184] D. Bellucci, A. Sola, and V. Cannillo, "Low temperature sintering of innovative bioactive glasses," *Journal of the American Ceramic Society*, vol. 95, pp. 1313–1319, 2012.

[185] D. Bellucci, E. Veronesi, M. Dominici, and C. Valeria, "A new bioactive glass with extremely high crystallization temperature and outstanding biological performance," *Materials Science and Engineering C*, vol. 110, 2020.

[186] R. Sergi, D. Bellucci, R. Salvatori, A. Anesi, and V. Cannillo, "A novel bioactive glass containing therapeutic ions with enhanced biocompatibility," *Materials*, vol. 13, pp. 1–16, 2020.

[187] A. Hoppe, N. S. GÃ¼ldal, and A. R. Boccaccini, "A review of the biological response to ionic dissolution products from bioactive glasses and glass-ceramics," 2011.

[188] A. Pedone, V. Cannillo, and M. C. Menziani, "Toward the understanding of crystallization, mechanical properties and reactivity of multicomponent bioactive glasses," *Acta Materialia*, vol. 213, 2021.

[189] M. Luginina, D. Angioni, S. Montinaro, R. Orrù, G. Cao, R. Sergi, D. Bellucci, and V. Cannillo, "Hydroxyapatite/bioactive glass functionally graded materials (FGM) for bone tissue engineering," *Journal of the European Ceramic Society*, pp. 1–12, 2020.

[190] F. Zhang, K. Lin, J. Chang, J. Lu, and C. Ning, "Spark plasma sintering of macroporous calcium phosphate scaffolds from nanocrystalline powders," *Journal of the European Ceramic Society*, vol. 28, pp. 539–545, 2008.

[191] K. D. Woo, S. M. Kwak, T. Lee, S. T. Oh, and J. N. Woo, "Microstructure and biocompatibility of porous BCP(HA/β-TCP) biomaterials consolidated by sps using space holder," *Korean Journal of Materials Research*, vol. 26, pp. 449–453, 2016.

[192] M. Rizwan, M. Hamdi, W. Basirun, K. Kondoh, and J. Umeda, "Low pressure spark plasma sintered hydroxyapatite and bioglass composite scaffolds for bone tissue repair," *Ceramics International*, vol. 44, no. 18, pp. 23052–23062, 2018.

[193] E. K. Papynov, O. O. Shichalin, I. Y. Buravlev, A. S. Portnyagin, A. A. Belov, V. Y. Maiorov, Y. E. Skurikhina, E. B. Merkulov, V. O. Glavinskaya, A. D. Nomerovskii, A. V. Golub, and N. P. Shapkin, "Reactive spark plasma synthesis of porous bioceramic wollastonite," *Russian Journal of Inorganic Chemistry*, vol. 65, pp. 263–270, 2020.

[194] J. Massera, S. Fagerlund, L. Hupa, and M. Hupa, "Crystallization mechanism of the bioactive glasses, 45S5 and S53P4," *Journal of the American Ceramic Society*, vol. 95, pp. 607–613, 2012.

[195] L. Lutterotti, R. Ceccato, R. Dal Maschio, and E. Pagani, "Quantitative analysis of silicate glass in ceramic materials by the rietveld method," *Materials Science Forum*, vol. 278, pp. 87–92, 1998.

[196] W. Oliver and G. Pharr, "An improved technique for determining hardness and elastic modulus using load and displacement sensing indentation experiments," *Journal of Materials Research*, vol. 7, pp. 1564–1583, 1992.

[197] T. A. Baser, M. Baricco, S. Enzo, G. Vaughan, and A. R. Yavari, "Analysis of crystallization behavior of fe48cr15 mo14y2 c15b6 bulk metallic glass by synchrotron radiation," *Journal of Materials Research*, vol. 23, pp. 2166–2173, 2008.

[198] H. Zhang, B. N. Kim, K. Morita, H. Yoshida, K. Hiraga, and Y. Sakka, "Fabrication of transparent yttria by high-pressure spark plasma sintering," *Journal of the American Ceramic Society*, vol. 94, pp. 3206–3210, 2011.

[199] B. N. Ezealigo, R. Orrù, C. Elissalde, H. E. E. Debeda, D. Debeda, U.-C. Chung, M. Maglione, and G. Cao, "Influence of the Spark Plasma Sintering temperature on the structure and dielectric properties of BaTi (1-x) Zr x O 3 ceramics," *Ceramics International*, vol. 47, pp. 3614–3625, 2021.

[200] D. Bellucci, V. Cannillo, and A. Sola, "An overview of the effects of thermal processing on bioactive glasses," *Science of Sintering*, vol. 42, pp. 307–320, 2010.

[201] S. K. Padmanabhan, F. Gervaso, M. Carrozzo, F. Scalera, A. Sannino, and A. Licciulli, "Wollastonite/hydroxyapatite scaffolds with improved mechanical, bioactive and biodegradable properties for bone tissue engineering," *Ceramics International*, vol. 39, no. 1, pp. 619–627, 2013.

[202] A. R. Boccaccini, Q. Chen, L. Lefebvre, L. Gremillard, and J. Chevalier, "Sintering, crystallisation and biodegradation behaviour of bioglass-derived glass-ceramics," *Faraday Discussions*, vol. 136, pp. 27–44, 2007.

[203] O. Bretcanu, X. Chatzistavrou, K. Paraskevopoulos, R. Conradt, I. Thompson, A. R. Boccaccini, R. Golovchak, H. Jain, S. Bano, and T. Hussain, "Sintering and crystallisation of

45S5 bioglass powder influence of phase separation on the devitrification of 45S5 bioglass effect of processing on microstructure, mechanical properties and dissolution behaviour in SBF of bioglass (45S5) coatings deposited by suspension high velocity oxy fuel (shvof) thermal spray," *Journal of the European Ceramic Society*, vol. 29, pp. 3299–3306, 2009.

[204] S. Koutsopoulos, "Synthesis and characterization of hydroxyapatite crystals: A review study on the analytical methods," 2002.

[205] D. Bellucci, G. Bolelli, V. Cannillo, A. Cattini, A. Sola, C. R. Mariappan, and N. Ranga, "Recommended articles influence of silver on the structure, dielectric and antibacterial effect of silver doped bioglass-ceramic nanoparticles," *Materials characterization*, vol. 62, pp. 1021–1028, 2011.

[206] A. Awonusi, M. D. Morris, and M. M. Tecklenburg, "Carbonate assignment and calibration in the raman spectrum of apatite," *Calcified Tissue International*, vol. 81, pp. 46–52, 2007.

[207] D. Bellucci, A. Sola, A. Anesi, R. Salvatori, L. Chiarini, and V. Cannillo, "Bioactive glass/hydroxyapatite composites: Mechanical properties and biological evaluation," *Materials Science and Engineering: C*, vol. 51, pp. 196–205, 2015.

[208] V. Cannillo and A. Sola, "Different approaches to produce coatings with bioactive glasses: Enamelling vs plasma spraying," *Journal of the European Ceramic Society*, vol. 30, no. 10, pp. 2031–2039, 2010.

[209] A. S. Mao, D. J. Mooney, and J. A. Paulson, "Regenerative medicine: Current therapies and future directions," *PNAS*, vol. 112, 2015.

[210] R. Comesana, F. Lusquinos, J. D. Val, F. Quintero, A. Riveiro, M. Boutinguiza, J. R. Jones, R. G. Hill, and J. Pou, "Toward smart implant synthesis: Bonding bioceramics of different resorbability to match bone growth rates," *Scientific Reports*, vol. 5, 2015.

[211] J. Kolmas, A. Jaklewicz, A. Zima, M. Buccko, B. Bucko, Z. Paszkiewicz, J. Lis, A. S. Losarczyk, and W. Kolodziejski, "Incorporation of carbonate and magnesium ions into synthetic hydroxyapatite: The effect on physicochemical properties," *Journal of Molecular Structure*, vol. 987, pp. 40–50, 2011.

[212] J. D. Santos, P. L. Silva, J. C. Knowles, S. Talal, and F. J. Monteiro, "P205-CaO glasses with Na20, K20 and MgO," *JOURNAL OF MATERIALS SCIENCE: MATERIALS IN MEDICINE*, vol. 7, pp. 187–189, 1996.

[213] D. Tanaskovic, B. Jokic, G. Socol, A. Popescu, I. Mihailescu, R. Petrovic, and D. Janackovic, "Synthesis of functionally graded bioactive glass-apatite multistructures on ti substrates by pulsed laser deposition," *Applied Surface Science*, vol. 254, pp. 1279–1282, 2007.

[214] D. Bellucci, A. Sola, and V. Cannillo, "Bioactive glass-based composites for the production of dense sintered bodies and porous scaffolds," *Materials Science and Engineering C*, vol. 33, pp. 2138–2151, 2013.

[215] S. Mondal, G. Hoang, P. Manivasagan, M. S. Moorthy, T. P. Nguyen, T. T. V. Phan, H. H. Kim, M. H. Kim, S. Y. Nam, and J. Oh, "Nano-hydroxyapatite bioactive glass composite scaffold with enhanced mechanical and biological performance for tissue engineering application," *Ceramics International*, vol. 44, pp. 15735–15746, 2018.

[216] J. A. Rincon-Lopez, J. A. Hermann-Munoz, D. A. Fernandez-Benavides, A. L. Giraldo-Betancur, J. M. Alvarado-Orozco, and J. Munoz-Saldana, "Isothermal phase transformations of bovine-derived hydroxyapatite/bioactive glass: A study by design of experiments," *Journal of the European Ceramic Society*, vol. 39, pp. 1613–1624, 2019.

[217] D. M. Reffitt, N. Ogston, R. Jugdaohsingh, H. F. Cheung, B. A. Evans, R. P. Thompson, J. J. Powell, and G. N. Hampson, "Orthosilicic acid stimulates collagen type 1 synthesis

and osteoblastic differentiation in human osteoblast-like cells in vitro," *Bone*, vol. 32, pp. 127–135, 2003.

[218] M. Dong, G. Jiao, H. Liu, W. Wu, S. Li, Q. Wang, D. Xu, X. Li, H. Liu, and Y. Chen, "Biological silicon stimulates collagen type 1 and osteocalcin synthesis in human osteoblast-like cells through the bmp-2/smad/runx2 signaling pathway," *Biological Trace Element Research*, vol. 173, pp. 306–315, 2016.

[219] C. Suryanarayana, "Mechanical alloying and milling," *Progress in Materials Science*, vol. 46, pp. 1–184, 2001.

[220] D. Maurice and T. H. Courtney, "Milling dynamics: Part ii. dynamics of a spex mill and a one-dimensional mill," *Metallurgic and materials transactions A*, vol. 27A, 1996.

[221] F. Delogu, M. Monagheddu, G. Mulas, L. Sciffini, and G. Cocco, "Impact characteristics and mechanical alloying process by ball milling: experimental evaluation and modelling outcomes," *Int. J. Non-Equilib Process*, pp. 235–269, 2000.

[222] M. Sopicka-Lizer, *High-Energy ball milling: Mechanochemical processing of nanopowders*. Woodhead Publishing Series in Composites Science and Engineering, Woodhead Publishing, 2010.

[223] N. F. Ibrahim, H. Mohamad, and S. N. F. M. Noor, "Effects of milling media on the fabrication of melt-derived bioactive glass powder for biomaterial application," *AIP Conference Proceedings*, vol. 1791, 2016.

[224] G. K. Pouroutzidou, G. S. Theodorou, E. Kontonasaki, L. Papadopoulou, N. Kantiranis, D. Patsiaoura, K. Chrissafis, C. B. Lioutas, and K. M. Paraskevopoulos, "Synthesis of a bioactive nanomaterial in the ternary system sio 2 -CaO-MgO doped with CuO: The effect of ball milling on the particle size, morphology and bioactive behavior," *AIP Conference Proceedings*, vol. 2075, 2019.

[225] D. Bovand, M. R. Allazadeh, S. Rasouli, E. Khodadad, and E. Borhani, "Studying the effect of hydroxyapatite particles in osteoconductivity of Ti-HA bioceramic," *Journal of the Australian Ceramic Society*, vol. 55, pp. 395–403, 2019.

[226] F. Matthews and R. Rawlings, *Composite Materials*. Woodhead Publishing, 1994.

[227] D. Angioni, R. Orrù, G. Cao, S. Garroni, A. Iacomini, D. Bellucci, and V. Cannillo, "Spark plasma sintering, mechanical and in-vitro behavior of a novel Sr- and Mg-containing bioactive glass for biomedical applications," *Journal of the European Ceramic Society*, vol. 42, no. 4, pp. 1776–1783, 2022.

[228] J. K. M. F. Daguano, K. Strecker, E. C. Ziemath, S. O. Rogero, M. H. V. Fernandes, and C. Santos, "Effect of partial crystallization on the mechanical properties and cytotoxicity of bioactive glass from the 3CaO.P2O5-SiO2--MgO system," *Journal of the mechanical behavior of biomedical materials*, vol. 14, pp. 78–88, 2012.

[229] G. Kaur, V. Kumar, F. Baino, J. C. Mauro, G. Pickrell, I. Evans, and O. Bretcanu, "Mechanical properties of bioactive glasses, ceramics, glass-ceramics and composites: State-of-the-art review and future challenges," *Materials Science and Engineering C*, vol. 104, 2019.

[230] L. A. Nunez-Rodriguez, M. A. Encinas-Romero, A. Gomez-Alvarez, J. L. Valenzuela-Garcia, and G. C. Tiburcio-Munive, "Evaluation of bioactive properties of αand βwollastonite bioceramics soaked in a simulated body fluid," *Journal of Biomaterials and Nanobiotechnology*, vol. 09, pp. 263–276, 2018.

[231] F. A. Shah, "Towards refining raman spectroscopy-based assessment of bone composition," *Scientific Reports*, vol. 10, 2020.

[232] E. Canas, M. J. Orts, E. Sanchez, D. Bellucci, and V. Cannillo, "Deposition of bioactive glass coatings based on a novel composition containing strontium and magnesium," *Journal of the European Ceramic Society*, vol. 42, pp. 6213–6221, 2022.

[233] J. Liu, U. A. Glasmacher, M. Lang, C. Trautmann, K. O. Voss, R. Neumann, G. A. Wagner, and R. Miletich, "Raman spectroscopy of apatite irradiated with swift heavy ions with and without simultaneous exertion of high pressure," *Applied Physics A: Materials Science and Processing*, vol. 91, pp. 17–22, 2008.

[234] S. V. Dorozhkin, "Calcium orthophosphate bioceramics," *Ceramics International*, vol. 41, no. 10, Part B, pp. 13913–13966, 2015.

[235] P. Nandha Kumar, S. K. Mishra, R. Udhay Kiran, and S. Kannan, "Preferential occupancy of strontium in the hydroxyapatite lattice in biphasic mixtures formed from non-stoichiometric calcium apatites," *Dalton Trans.*, vol. 44, pp. 8284–8292, 2015.

[236] A. N. Natasha, R. Singh, M. H. Bin Abd Shukor, T. C. Young, J. Purbolaksono, I. Sopyan, and R. Toulouei, "Synthesis and properties of biphasic calcium phosphate prepared by different methods," in *Science and Engineering of Materials*, vol. 970 of *Advanced Materials Research*, pp. 20–25, Trans Tech Publications Ltd, 2014.

[237] A. Eskandari, M. Aminzare, H. Hassani, H. Barounian, S. Hesaraki, and S. Sadrnezhaad, "Densification behavior and mechanical properties of biomimetic apatite nanocrystals," *Current Nanoscience*, vol. 7, no. 5, pp. 776–780, 2011.

[238] E. C. Victoria and F. D. Gnanam, "Synthesis and characterisation of biphasic calcium phosphate," *Trends in Biomaterials and Artificial Organs*, vol. 16, pp. 12+, 2002.

[239] J.-M. Bouler, R. Z. LeGeros, and G. Daculsi, "Biphasic calcium phosphates: Influence of three synthesis parameters on the HA/β-tcp ratio," *Journal of Biomedical Materials Research*, vol. 51, no. 4, pp. 680–684, 2000.

[240] T. Matic, M. L. Zebic, V. Miletic, I. Cvijovic-Alagic, R. Petrovic, D. Janackovic, and D. Veljovic, "Sr,Mg co-doping of calcium hydroxyapatite: Hydrothermal synthesis, processing, characterization and possible application as dentin substitutes," *Ceramics International*, vol. 48, no. 8, pp. 11155–11165, 2022.

[241] M. Ahmadi, G. Dini, M. Afshar, and F. Ahmadpour, "Synthesis, characterization, and bioactivity evaluation of biphasic calcium phosphate nanopowder containing 5.0 mol% strontium, 0.6 mol% magnesium, and 0.2 mol% silicon for bone regeneration," *Journal of Materials Research*, vol. 37, pp. 1916–1928, 2022.

[242] T.-W. Kim, H.-S. Lee, D.-H. Kim, H.-H. Jin, K.-H. Hwang, J. K. Lee, H.-C. Park, and S.-Y. Yoon, "In situ synthesis of magnesium-substituted biphasic calcium phosphate and in vitro biodegradation," *Materials Research Bulletin*, vol. 47, no. 9, pp. 2506–2512, 2012.

[243] S. Kannan and J. M. F. Ferreira, "Synthesis and thermal stability of hydroxyapatite-β-tricalcium phosphate composites with cosubstituted sodium, magnesium, and fluorine," *Chemistry of Materials*, vol. 18, no. 1, pp. 198–203, 2006.

[244] J. Pena and M. Vallet-Regí, "Hydroxyapatite, tricalcium phosphate and biphasic materials prepared by a liquid mix technique," *Journal of the European Ceramic Society*, vol. 23, no. 10, pp. 1687–1696, 2003.

[245] A. Farzadi, M. Solati-Hashjin, F. Bakhshi, and A. Aminian, "Synthesis and characterization of hydroxyapatite/β-tricalcium phosphate nanocomposites using microwave irradiation," *Ceramics International*, vol. 37, no. 1, pp. 65–71, 2011.

[246] Q. Z. Chen and G. A. Thouas, "Fabrication and characterization of sol-gel derived 45S5 bioglass-ceramic scaffolds," *Acta Biomaterialia*, vol. 7, pp. 3616–3626, 2011.

[247] M. Ebrahimi, M. Botelho, W. Lu, and N. Monmaturapoj, "Synthesis and characterization of biomimetic bioceramic nanoparticles with optimized physicochemical properties for bone tissue engineering," *Journal of Biomedical Materials Research Part A*, vol. 107, no. 8, pp. 1654–1666, 2019.

[248] S. K. Ghosh, S. K. Nandi, B. Kundu, S. Datta, D. K. De, S. K. Roy, and D. Basu, "In vivo response of porous hydroxyapatite and β-tricalcium phosphate prepared by aqueous so-

lution combustion method and comparison with bioglass scaffolds," *Journal of Biomedical Materials Research Part B: Applied Biomaterials*, vol. 86B, no. 1, pp. 217–227, 2008.

[249] R. Ramakrishnan, P. Wilson, T. Sivakumar, and I. Jemina, "A comparative study of hydroxyapatites synthesized using various fuels through aqueous and alcohol mediated combustion routes," *Ceramics International*, vol. 39, no. 4, pp. 3519–3532, 2013.

[250] S. Aruna and M. Shilpa, *Solution Combustion Synthesis of Calcium Phosphate-Based Bioceramic Powders for Biomedical Applications*. 2021.

[251] S. V. Dorozhkin, "Nanodimensional and nanocrystalline apatites and other calcium orthophosphates in biomedical engineering, biology and medicine," *Materials*, vol. 2, no. 4, pp. 1975–2045, 2009.

[252] M. Canillas, R. Rivero, R. Garcia-Carrodeguas, F. Barba, and M. A. Rodriguez, "Processing of hydroxyapatite obtained by combustion synthesis," *Boletin de la Sociedad Espanola de Ceramica y Vidrio*, vol. 56, no. 5, pp. 237–242, 2017.

[253] R. Ghosh and R. Sarkar, "Synthesis and characterization of sintered hydroxyapatite: a comparative study on the effect of preparation route," *Journal of the Australian Ceramic Society*, vol. 54, pp. 71–80, 2018.

[254] S. K. Ghosh, S. K. Roy, B. Kundu, S. Datta, and D. Basu, "Synthesis of nano-sized hydroxyapatite powders through solution combustion route under different reaction conditions," *Materials Science and Engineering: B*, vol. 176, no. 1, pp. 14–21, 2011.

[255] C. A. Schneider, W. S. Rasband, and K. W. Eliceiri, "Nih image to ImageJ: 25 years of image analysis," *Nature Methods*, vol. 9, pp. 671–675, 2012.

[256] J. L. Labar, "Consistent indexing of a (set of) single crystal saed pattern(s) with the processdiffraction program," *Ultramicroscopy*, vol. 103, no. 3, pp. 237–249, 2005.

[257] K. Momma and F. Izumi, "*VESTA*: a three-dimensional visualization system for electronic and structural analysis," *Journal of Applied Crystallography*, vol. 41, no. 3, pp. 653–658, 2008.

[258] M. E. Fleet, *Carbonated hydroxyapatite : materials, synthesis, and applications*. 2015.

[259] K. S. Karunadasa, C. Manoratne, H. Pitawala, and R. Rajapakse, "Thermal decomposition of calcium carbonate (calcite polymorph) as examined by in-situ high-temperature x-ray powder diffraction," *Journal of Physics and Chemistry of Solids*, vol. 134, pp. 21–28, 2019.

[260] W. J. Li, C. T. Laurencin, E. J. Caterson, R. S. Tuan, and F. K. Ko, "Electrospun nanofibrous structure: A novel scaffold for tissue engineering," *Journal of Biomedical Materials Research*, vol. 60, pp. 613–621, 2002.

[261] N. Bhardwaj and S. C. Kundu, "Electrospinning: A fascinating fiber fabrication technique," *Biotechnology Advances*, vol. 28, pp. 325–347, 2010.

[262] M. Bao, X. Lou, Q. Zhou, W. Dong, H. Yuan, and Y. Zhang, "Electrospun biomimetic fibrous scaffold from shape memory polymer of pdlla- co -tmc for bone tissue engineering," *ACS Applied Materials and Interfaces*, vol. 6, pp. 2611–2621, 2014.

[263] M. Bao, X. Wang, H. Yuan, Q. Zhao, and Y. Zhang, "HAp incorporated ultrafine polymeric fibers with shape memory effect for potential use in bone screw hole healing," *Journal of Materials Chemistry B*, vol. 4, pp. 5308–5320, 2016.

[264] L. Dejob, B. Toury, S. Tadier, L. Gremillard, C. Gaillard, and V. Salles, "Electrospinning of in situ synthesized silica-based and calcium phosphate bioceramics for applications in bone tissue engineering: A review," *Acta Biomaterialia*, vol. 123, pp. 123–153, 2021.

[265] S. N. Tan, W. Wang, and L. Ge, "Biosensors based on sol-gel-derived materials," *Comprehensive Biomaterials*, vol. 3, pp. 471–489, 2011.

[266] M. R. N. Monton, E. M. Forsberg, and J. D. Brennan, "Tailoring sol-gel-derived silica materials for optical biosensing," *Chemistry of Materials*, vol. 24, pp. 796–811, 2012.

[267] L. L. Hench and J. K. West, "The sol-gel process," *Chemical Reviews*, vol. 90, pp. 33–72, 1990.

[268] J. Jones and A. Clare, *Bio-Glasses: An Introduction*. Wiley, 2012.

[269] P. Sepulveda, J. R. Jones, and L. L. Hench, "In vitro dissolution of melt-derived 45S5 and sol-gel derived 58S bioactive glasses," *Journal of Biomedical Materials Research*, vol. 61, pp. 301–311, 2002.

[270] M. Bellantone, H. D. Williams, and L. L. Hench, "Broad-spectrum bactericidal activity of ag2o-doped bioactive glass," *Antimicrobial Agents and Chemotherapy*, vol. 46, pp. 1940–1945, 2002.

[271] J. Isaac, J. Nohra, J. Lao, E. Jallot, J. M. Nedelec, A. Berdal, and J. M. Sautier, "Effects of strontium-doped bioactive glass on the differentiation of cultured osteogenic cells," *European Cells and Materials*, vol. 21, pp. 130–143, 2011.

[272] L. Lefebvre, J. Chevalier, L. Gremillard, R. Zenati, G. Thollet, D. Bernache-Assolant, and A. Govin, "Structural transformations of bioactive glass 45S5 with thermal treatments," *Acta Materialia*, vol. 55, pp. 3305–3313, 2007.

[273] M. M. Pereira, A. E. Clark, and L. L. Hench, "Effect of texture on the rate of hydroxyapatite formation on gel-silica surface," *Journal of the American Ceramic Society*, vol. 78, pp. 2463–2468, 1995.

[274] J. Faure, R. Drevet, A. Lemelle, N. B. Jaber, A. Tara, H. E. Btaouri, and H. Benhayoune, "A new sol-gel synthesis of 45S5 bioactive glass using an organic acid as catalyst," *Materials Science and Engineering C*, vol. 47, pp. 407–412, 2015.

[275] H. Pirayesh and J. A. Nychka, "Sol-gel synthesis of bioactive glass-ceramic 45S5 and its in vitro dissolution and mineralization behavior," *Journal of the American Ceramic Society*, vol. 96, pp. 1643–1650, 2013.

[276] A. Kumar, S. Murugavel, A. Aditya, and A. R. Boccaccini, "Mesoporous 45S5 bioactive glass: Synthesis,: in vitro dissolution and biomineralization behavior," *Journal of Materials Chemistry B*, vol. 5, pp. 8786–8798, 2017.

[277] A. Lucas-Girot, F. Z. Mezahi, M. Mami, H. Oudadesse, A. Harabi, and M. L. Floch, "Sol-gel synthesis of a new composition of bioactive glass in the quaternary system SiO2--CaO-na2o-P2O5: Comparison with melting method," *Journal of Non-Crystalline Solids*, vol. 357, pp. 3322–3327, 2011.

[278] E. Rezabeigi, P. M. Wood-Adams, and R. A. Drew, "Synthesis of 45S5 bioglass via a straightforward organic, nitrate-free sol-gel process," *Materials Science and Engineering C*, vol. 40, pp. 248–252, 2014.

[279] D. Fernando, N. Attik, M. Cresswell, I. Mokbel, N. Pradelle-Plasse, P. Jackson, B. Grosgogeat, and P. Colon, "Influence of network modifiers in an acetate based sol-gel bioactive glass system," *Microporous and Mesoporous Materials*, vol. 257, pp. 99–109, 2018.

[280] I. S. Chronakis, "Novel nanocomposites and nanoceramics based on polymer nanofibers using electrospinning process - a review," *Journal of Materials Processing Technology*, vol. 167, pp. 283–293, 2005.

[281] P. Wutticharoenmongkol, N. Sanchavanakit, P. Pavasant, and P. Supaphol, "Preparation and characterization of novel bone scaffolds based on electrospun polycaprolactone fibers filled with nanoparticles," *Macromolecular Bioscience*, vol. 6, pp. 70–77, 2006.

[282] Z. Cao, D. Wang, L. Lyu, Y. Gong, and Y. Li, "Fabrication and characterization of PCL/CaCO3 electrospun composite membrane for bone repair," *RSC Advances*, vol. 6, pp. 10641–10649, 2016.

[283] K. Fujihara, M. Kotaki, and S. Ramakrishna, "Guided bone regeneration membrane made of polycaprolactone/calcium carbonate composite nano-fibers," *Biomaterials*, vol. 26, pp. 4139–4147, 2005.

[284] T. Wakita, A. Obata, G. Poologasundarampillai, J. R. Jones, and T. Kasuga, "Preparation of electrospun siloxane-poly(lactic acid)-vaterite hybrid fibrous membranes for guided bone regeneration," *Composites Science and Technology*, vol. 70, pp. 1889–1893, 2010.

[285] A. Obata, T. Hotta, T. Wakita, Y. Ota, and T. Kasuga, "Electrospun microfiber meshes of silicon-doped vaterite/poly(lactic acid) hybrid for guided bone regeneration," *Acta Biomaterialia*, vol. 6, pp. 1248–1257, 2010.

[286] N. Takeuchi, M. Machigashira, D. Yamashita, Y. Shirakata, T. Kasuga, K. Noguchi, and S. Ban, "Cellular compatibility of a gamma-irradiated modified siloxane-poly(lactic acid)-calcium carbonate hybrid membrane for guided bone regeneration," *Dental Materials Journal*, vol. 30, pp. 730–738, 2011.

[287] T. Kasuga, A. Obata, H. Maeda, Y. Ota, X. Yao, and K. Oribe, "Siloxane-poly(lactic acid)-vaterite composites with 3d cotton-like structure," *Journal of Materials Science: Materials in Medicine*, vol. 23, pp. 2349–2357, 2012.

[288] D. Lee, H. Maeda, A. Obata, K. Inukai, K. Kato, and T. Kasuga, "Aluminum silicate nanotube modification of cotton-like siloxane-poly(l-lactic acid)-vaterite composites," 2013.

[289] A. Obata, H. Ozasa, T. Kasuga, and J. R. Jones, "Cotton wool-like poly(lactic acid)/vaterite composite scaffolds releasing soluble silica for bone tissue engineering," *Journal of Materials Science: Materials in Medicine*, vol. 24, pp. 1649–1658, 2013.

[290] A. Suryavanshi, K. Khanna, K. R. Sindhu, J. Bellare, and R. Srivastava, "Magnesium oxide nanoparticle-loaded polycaprolactone composite electrospun fiber scaffolds for bone-

soft tissue engineering applications: In-vitro and in-vivo evaluation," *Biomedical Materials (Bristol)*, vol. 12, 2017.

[291] H. Zhou, M. Nabiyouni, B. Lin, and S. B. Bhaduri, "Fabrication of novel poly(lactic acid)/amorphous magnesium phosphate bionanocomposite fibers for tissue engineering applications via electrospinning," *Materials Science and Engineering C*, vol. 33, pp. 2302–2310, 2013.

[292] M. M. Hohman, M. Shin, G. Rutledge, and M. P. Brenner, "Electrospinning and electrically forced jets. ii. applications," *Physics of Fluids*, vol. 13, pp. 2221–2236, 2001.

[293] A. K. Haghi and M. Akbari, "Trends in electrospinning of natural nanofibers," *Physica Status Solidi (A) Applications and Materials Science*, vol. 204, pp. 1830–1834, 2007.

[294] S. Megelski, J. S. Stephens, D. B. Chase, and J. F. Rabolt, "Micro- and nanostructured surface morphology on electrospun polymer fibers," *Macromolecules*, vol. 35, pp. 8456–8466, 2002.

[295] O. S. Yordem, M. Papila, and Y. Z. Menceloglu, "Effects of electrospinning parameters on polyacrylonitrile nanofiber diameter: An investigation by response surface methodology," *Materials and Design*, vol. 29, pp. 34–44, 2008.

[296] Z. Ghaffarian, A. Faghihimani, A. Doostmohammadi, and M. R. Saeri, "Fabrication, characterization and process parameters optimization of electrospun 58S bioactive glass submicron fibers," *ACERP*, vol. 1, pp. 16–21, 2015.

[297] Y. S. Huang, C. C. Kuo, C. C. Huang, S. C. Jang, W. C. Tsen, F. S. Chuang, B. Y. Chen, J. J. Chen, J. D. Chow, and Y. C. Shu, "Novel highly aligned, double-layered, hollow fibrous polycarbonate membranes with a perfectly tightly packed pentagonal pore structure fabricated using the electrospinning process," *RSC Advances*, vol. 5, pp. 88857–88865, 2015.

[298] X. Zong, K. Kim, D. Fang, S. Ran, B. S. Hsiao, and B. Chu, "Structure and process relationship of electrospun bioabsorbable nanofiber membranes," *Polymer*, vol. 43, pp. 4403–4412, 2002.

[299] L. Wannatong, A. Sirivat, and P. Supaphol, "Effects of solvents on electrospun polymeric fibers: Preliminary study on polystyrene," *Polymer International*, vol. 53, pp. 1851–1859, 2004.

[300] X. Y. Yuan, Y. Y. Zhang, C. Dong, and J. Sheng, "Morphology of ultrafine polysulfone fibers prepared by electrospinning," *Polymer International*, vol. 53, pp. 1704–1710, 2004.

[301] B. Kim, H. Park, S. H. Lee, and W. M. Sigmund, "Poly(acrylic acid) nanofibers by electrospinning," *Materials Letters*, vol. 59, pp. 829–832, 2005.

[302] W. Zuo, M. Zhu, W. Yang, H. Yu, Y. Chen, and Y. Zhang, "Experimental study on relationship between jet instability and formation of beaded fibers during electrospinning," *Polymer Engineering and Science*, vol. 45, pp. 704–709, 2005.

[303] P. K. Baumgarten, "Electrospinning and electrically forced jets. ii. applications," *Journal of Colloid and Interface Science*, vol. 36, pp. 71–79, 1971.

[304] E. Norris, C. Ramos-Rivera, G. Poologasundarampillai, J. P. Clark, Q. Ju, A. Obata, J. V. Hanna, T. Kasuga, C. A. Mitchell, G. Jell, and J. R. Jones, "Electrospinning 3d bioactive glasses for wound healing," *Biomedical Materials (Bristol)*, vol. 15, 2020.

[305] G. Poologasundarampillai, D. Wang, S. Li, J. Nakamura, R. Bradley, P. D. Lee, M. M. Stevens, D. S. McPhail, T. Kasuga, and J. R. Jones, "Cotton-wool-like bioactive glasses for bone regeneration," *Acta Biomaterialia*, vol. 10, pp. 3733–3746, 2014.

[306] S. Sakka and H. Kozuka, "Rheology of sols and fiber drawing," *Journal of Non-Crystalline Solids*, vol. 100, pp. 142–153, 1988.

[307] T. Hayashi and H. Saito, "Preparation of CaO-sio glasses by the gel method," *Journal of Materials Science*, vol. 15, pp. 1971–1977, 1980.

[308] L. Liverani, T. Reiter, K. Zheng, Z. Nescakova, and A. R. Boccaccini, "Copper-doped cotton-like malleable electrospun bioactive glass fibers for wound healing applications," *Materials Letters: X*, vol. 14, 2022.

[309] A. Suarez-Arnedo, F. Torres Figueroa, C. Clavijo, P. Arbelaez, J. C. Cruz, and C. Munoz-Camargo, "An image j plugin for the high throughput image analysis of in vitro scratch wound healing assays," *PLOS ONE*, vol. 15, no. 7, pp. 1–14, 2020.

[310] A. M. Deliormanli, "Preparation and in vitro characterization of electrospun 45S5 bioactive glass nanofibers," *Ceramics International*, vol. 41, pp. 417–425, 1 2015.

[311] D. Durgalakshmi and S. Balakumar, "Phase separation induced shell thickness variations in electrospun hollow bioglass 45S5 fiber mats for drug delivery applications," *Physical Chemistry Chemical Physics*, vol. 17, pp. 15316–15323, 2015.

[312] P. Virolainen, J. Heikkila, A. Yli-Urpo, E. Vuorio, and H. T. Aro, "Histomorphometric and molecular biologic comparison of bioactive glass granules and autogenous bone grafts in augmentation of bone defect healing,"

[313] P. Kumar, N. Khan, and D. Kumar, "Polyvinyl butyral (PVB), versetile template for designing nanocomposite/composite materials:a review," *Green Chemistry and Technology Letters*, vol. 2, pp. 185–194, 2016.

[314] C. Carrot, A. Bendaoud, and C. Pillon, "Polyvinyl butyral," pp. 89–137, 2015.

[315] M. K. Trivedi and A. B. D. Trivedi, "Spectroscopic characterization of disodium hydrogen orthophosphate and sodium nitrate after biofield treatment," *Journal of Chromatography and Separation Techniques*, vol. 06, 2015.

[316] National Institute of standards and Technology, U.S. Department of Commerce, website, “Page title: Nitric acid, calcium salt, tetrahydrate.”

[317] The Conservation and Art Materials Encyclopedia Online (CAMEO), website, “Page title: Calcium nitrate.”

Acknowledgments

I would like to express my deepest gratitude to Professor Cao, for providing me with this opportunity and for your support throughout this experience. To Prof. Roberta Licheri, Dr. Selena Montinaro, and Dr. Ekaterina Pakhomova, thank you for your invaluable support, help and patience through the whole duration of the Ph.D.

I would also like to express my sincerest thanks to my supervisor, Professor Roberto Orrù, for your guidance, mentorship, and support. I am truly grateful for the opportunity to work with you and for everything you have done for me.

I would like to extend my gratitude Professor Julian R. Jones and all the team from Imperial College, for giving me the amazing opportunity to work in your lab and for making me feel at home. I am truly grateful for the experience.

Thank you all for making this journey such a memorable and rewarding experience.